2018-06-01

Art to Engineering: Curved Folding and Developable Surfaces in Mechanism and Deployable Structure Design

Todd G. Nelson
Brigham Young University

Art to Engineering: Curved Folding and Developable Surfaces in Mechanism and Deployable Structure Design

Todd G Nelson

A dissertation submitted to the faculty of
Brigham Young University
in partial fulfillment of the requirements for the degree of

Doctor of Philosophy

Larry L. Howell, Chair
Spencer P. Magleby
Anton E. Bowden
David T. Fullwood
David W. Jensen
Robert J. Lang

Department of Mechanical Engineering

Brigham Young University

ABSTRACT

Art to Engineering: Curved Folding and Developable Surfaces
in Mechanism and Deployable Structure Design

Todd G Nelson
Department of Mechanical Engineering, BYU
Doctor of Philosophy

This work investigates how curved-crease origami and the developable surfaces which compose it can be transitioned to engineering design. Methods for creating flexible, tailorable-property surfaces that function as thick panels in place of paper are presented. Concepts from curved-crease origami and developable surfaces that can describe and extend engineering applications are discussed and demonstrated. These concepts are particularly beneficial to applications where curved surfaces are integral to the function, deployability is desired, and planar manufacturing could be beneficial.

The first part of this work uses arrays of compliant elements to create flexible-tailorable property surfaces. The key feature to these arrays is the alignment of the most flexible bending axis of the individual elements to the ruling line arrangement of a developable surface. This alignment can enable bending of thick panels while maintaining lower stresses, a quality necessary for the transitioning of curved-crease origami into thick materials. The stiffness and stress of these arrays is modeled and physical prototypes are demonstrated. Additionally, shape factors are developed for these compliant arrays (CAs) to facilitate material selection for the panels and understand how the geometry of the array changes the effective properties of the panel.

The second part of this work describes and demonstrates several concepts of curved-crease origami and developable surfaces that can benefit mechanism and structure design, particularly in the context of rolling-contact mechanisms. The design of a rolling-contact joint connected by flexible bands similar to a Jacob's Ladder toy is extended through incorporating curved creases into the design. The resulting design is deployable from a compact state to a functional state and can be manufactured from a single plane and folded into shape.

Mathematical formulations are presented to describe the classes of developable surfaces in terms of properties which are frequently important in mechanism design. These natural equations for a single class of developable surface are conducive to modeling the folding motion of rigid-ruling developables, developables whose ruling lines do change location in a surface during folding. These formulations are used to generalize the design of rolling-contact joints to a family of joints capable of single degree of freedom spatial motions, being manufactured from a plane, and exhibiting a tailorable force response. Finally practical design suggestions for the implementation of rolling-contact joints is given. These include methodology to create sunken flexures which serve to increase the normal force between rolling bodies to prevent slip.

Keywords: developable, curved folding, origami, deployable

ACKNOWLEDGMENTS

I feel an appropriate start to an acknowledgements section would be with the often quoted words of Issac Newton, "If I have seen further it is by standing on the shoulders of giants." Not only have the academic works that this research is built upon been invaluable, but also and perhaps more importantly has been the influence of those I have interacted with face to face while compiling this work.

I would like to thank my PhD committee, Spencer Magleby, Anton Bowden, David Fullwood, David Jensen, Robert Lang, and particularly my advisor Larry Howell. Without their kindness, direction, and willingness to share their experience this work would not have come to pass. I would also like to acknowledge the gracious advising I received from Just Herder during my time in Delft.

My peers in the Compliant Mechanisms Research Group have not only provided constructive insights and discussions, but have created an atmosphere where a strong work ethic, high moral integrity, and positivity had prominent places. It has been a pleasure to associate with them nearly daily. Particularly I would like to thank Jared Bruton, Jason Dearden, Jason Lund, Patrick Walton, Nathan Pehrson, Thomas Evans, Nathan Rieske, Alex Avila, Jared Butler, Jessica Morgan, Jacob Badger, Ezekiel Merriam, Kyler Tolman, John Sessions, Trent Zimmerman, Nichole Cross, Bryce Barker, Alden Yellowhorse, Janette Herron, Peter Schleede, Issac Delimont, and Eric Wilson for the various insights and ideas they have brought to this work. I also appreciated working with the visiting scholars in the group Zhicheng Deng, Liping Zhang, and Guimin Chen. While I was only able to spend a short time with them, I would like to thank my colleagues in the Precision and Microsystems Engineering group at TU Delft for welcoming me there and for the insightful discussions.

The staff and other faculty at Brigham Young University have been phenomenal, with special mention of Kevin Cole, Terri Bateman, Jeffrey Niven, and David Morgan.

I regret that I cannot list all the people personally who have impacted this work whether directly or indirectly, though to some it may seem like I tried. If you feel like you were left out, reach out to me and I'd be happy to thank you personally.

I would like to acknowledge the funding sources that made this work possible. They are the National Science Foundation and the Air Force Office of Scientific Research under NSF Grant EFRI-ODISSEI-1240417 and the National Science Foundation Graduate Research Fellowship Program under Grant No. 1247046. I was also fortunate to participate in the NSF Graduate Research Opportunities Worldwide (GROW) program as part of the National Science Foundation Graduate Research Fellowship Program (NSF GRFP).

I am grateful to my parents for their continual support and patience with my interest in engineering and taking things apart. My wife Kambria and daughter Sofie motivate me to be my best self and I am grateful for their love and encouragement.

Most of all I thank my Father in Heaven and His son Jesus Christ. The peace, purpose, and inspiration they provide is not found anywhere else.

TABLE OF CONTENTS

LIST OF TABLES

LIST OF FIGURES

CHAPTER 1. INTRODUCTION

1.1 Problem Statement

Although origami models were created for art or amusement, they represent the edge of a field consisting of complex mathematical relationships spelled out in a spatial form, kinematic structures made with nearly zero-thickness panels, and avenues towards constructing deployable mechanisms and structures. Furthermore, if certain constraints in traditional origami, such as keeping creases as straight lines, are relaxed then interesting and complex bending surfaces emerge in the paper models. While the aesthetic appeal of origami is well known, mathematicians and engineers have joined artists in investigating what potential origami holds for progressing theory and the creation of real-world products. This thrust prompts the primary hypothesis of the dissertation:

Knowledge from curved-crease origami, and the developable surfaces which form it, can be translated into engineering design, beginning with the development of novel tailorable-property compliant surfaces, and demonstrated through extending rolling-contact joint design.

1.2 Background

The earliest recorded forms of curved-crease origami occurred during an era of napkin or linen folding which peaked during the 17th century [1]. These patterns were used to adorn tables as decorative pieces and eventually became status symbols for high-class society. After the peak of the movement much of the art of napkin folding was lost. Joan Sallas has worked in recreating these techniques from historical records and engravings and published a book about it in 2010 [2].

Early curved-fold origami forms in paper were recorded in the late 1920s at the Bauhaus, a German art school [3]. Bauhaus instructor Josef Albers used curved-crease paper folding as a teaching tool in his classroom. Later other artists would record works utilizing curved creases, including Hiroshi Ogawa and Kurt Londenberg [4, 5].

Rigorous study of curved-fold origami began in the 1960s and 1970s when two computer scientists, David Huffman and Ron Resch, contributed pioneering work. Ron Resch, an artist and computer scientist at the University of Utah, used his background in computational graphics to construct curved-crease surfaces, but published relatively few papers about his curved-folding work [6,7]. David Huffman, who is remembered more often for his data compression contributions, created an expansive body of curved-fold sculptures. Like Resch, he published little about his paper folding [8].

Notwithstanding the many works of curved folding by Resch and Huffman, curved-crease models remain difficult to design and understand. Recently Duks Koschitz documented and categorized Huffman's collection of curved-crease sculptures and notes to illuminate design strategies with curved creases [1]. This comprehensive work includes and expands upon four strategies reviewed by Demaine et al. [9] which are used to understand curved-crease pieces. These strategies are a differential geometric analysis, a constructive geometric approach, the inverse calculation of a crease, and a discrete geometric approach. These strategies represent the current state of the art in understanding curved-crease models, but a general approach to describe the folding process and to be able to generate novel forms is yet to be determined.

To understand these strategies it is necessary to understand curved-crease origami as combinations of developable surfaces. While a more thorough treatment of developable surfaces is provided in the background of Chapter 2, here we mention several key points to introduce the reader to developable surfaces.

Developable surfaces result from bending a plane with no stretching or tearing [10]. Because bending is the only action to form these surfaces it is common to relate a curved or formed developable surface to its planar unrolled or unwrapped state. Distances along the surface are equivalent for both the curved and unrolled states. Another important characteristic of developable surfaces is that a developable surface is composed of straight lines, called ruling lines. Constraining ourselves to three-dimensional space, these ruling lines qualify developable surfaces as a subset of a more general classification of surfaces called ruled surfaces [11]. Somewhat surprisingly, developable surfaces can be decomposed into four fundamental classes. The first class is a plane, where the orientation of ruling lines is arbitrary. The remaining three classes are curved surfaces. These are generalized cylinders, generalized cones, and tangent developables. In generalized cylinders

the ruling lines are parallel to each other. Ruling lines meet at a point for generalized cones. Lastly for tangent developables the ruling lines are tangent to a space curve. When these fundamental classes are joined together by aligning ruling lines, reflection of the surface across a plane, or in some other fashion such that the entire surface remains developable, the surface is referred to as a composite developable, general developable, or discrete developable [12–14].

As curved-crease origami starts with a planar surface and uses only bending to create a folded form, it can be viewed as a method to combine developable surface classes together into a general developable surface.

Using the framework of viewing curved creases as combinations of developable surfaces, each of the four strategies discussed by Demaine et al. [9] will briefly be presented here as they represent the state of the art in understanding curved-crease patterns.

Differential geometric analysis approaches curved-fold origami by investigating how the paper surface behaves locally at a curved crease. Both Resch and Huffman used this approach in designing some of their curved-fold models [6, 8]. Fuchs and Tabachnikov expanded on this approach through explicitly defining differential equations governing the behavior of ruling lines along creases and investigating several observations of how paper creases behave [15]. Duncan et al. provided a mathematical description for folded developable shapes [16].

The constructive geometric approach builds shapes by reflecting a developable surface across a plane. An example of using this approach is a cone inverted upon itself as is found in some compact collapsible umbrellas. The approach is a special case of curved folding, where the curved crease is contained in a single plane. This plane is also called the osculating plane, as it reflects the ruling lines from the incoming developable surface to form the complementary surface moving out of the crease. Jun Mitani has created software based on this approach to synthesize curved-fold origami based on reflections [17, 18].

The inverse calculation of a crease approach defines the final curved shape and works backwards to find the curved crease necessary to achieve the shape [19,20]. A variation of this approach is investigated by Gattas et al. in describing curved-crease Miura-base patterns [21].

The discrete geometric approach is an attempt to generalize a representation for curved surfaces so as to predict behavior without as many assumptions as the other three approaches require. This can be accomplished in a variety of ways including fitting a developable surface to a

generic surface [22], using a PQ mesh coupled with a optimization algorithm to find a ruling [23], and simulating a folding based on a known ruling line pattern in a flat state [24].

These four strategies prove useful in the design of curved-crease origami, yet a general approach to designing novel curved-fold forms still proves elusive.

Curved-crease origami sculptures hold interesting potential not only for decorative art, but for structures and mechanisms in engineering applications. Several qualities of curved-fold origami which would enable unprecedented structures and mechanisms are discussed below.

- Like straight-crease origami, curved-crease origami lends itself towards deployable applications. Complex three dimensional configurations can be moved into a different or flat configuration for storage or transport. Specific applications which have benefitted from deployable configurations in the past include aerospace applications (such as the deployment of solar panels and communication equipment), minimally invasive surgery applications (such as laparoscopic tools), emergency response and outdoor recreational equipment, (such as shelters), conformable body armor, and portable furniture (such as folding tables and chairs).

- Curved-crease origami can inspire structures which are made from planar sheet goods. As origami begins as a sheet of paper, similar folding or bending processes on other sheet goods, such as sheet metal, can be implemented to manufacture origami-inspired products.

- Unlike straight-crease origami, curved creases enable specific curved geometries which can have engineering applications such as drag reduction, wave and signal collection or dispersion, rolling joints, and improved aesthetics.

- Economical and quick prototyping is enabled with curved-fold origami as designs can be rapidly created in various configurations in paper or chosen from an existing large body of origami works.

However, using curved-folding origami to facilitate structures and mechanisms is not without its challenges. Many of these challenges are a result of transitioning curved-fold designs to materials thicker than paper. These challenges, some of which are listed below, are addressed in this research.

- High bending stresses can result in the curved panels of curved-crease patterns when transitioning from paper to thick materials. Failure can result from these stresses both in the panel itself and also in the creases, or hinges, of the pattern. These stresses also prevent many curved-folding patterns from being transitioned into thick deployable applications, as the bending stresses can cause yielding in the material.

- Thick panels can also possess unintended directional stiffness which may resist the movement of the panel into the shape dictated by the curved creases. These opposing forces can alter the final shape from the intended design of the curved-fold-origami pattern.

- There is not currently a general design method for novel curved-fold-origami structures, which inhibits the identification and development of curved-folding principles in engineering design. Addressing this may increase the number of curved-fold-inspired engineering applications.

1.3 Research Hypotheses

Two research hypotheses were formed to investigate first, how curved-fold origami facets, or panels, can be transitioned to thick materials, and second, the potential benefits of curved-folding ideas in engineering design, particularly with the design of rolling joints. These research hypotheses support the fulfillment of the overall research hypothesis described in Section 1.1.

1.3.1 Hypothesis 1

Flexible, tailorable-property surfaces suitable for use as thick curved-crease origami panels can be created and analyzed by employing networks of compliant joints.

Description

A novel approach to morphing surfaces was explored to address the challenge curved folding presents with high bending stresses in panels and the need for specific directional stiffness in the same panels. The field of lamina emergent mechanisms (LEMs) has created mechanisms which are designed to be planar manufactured and supply motion out of plane [25–28]. By placing these

mechanisms into arrays a customizable surface can be created with variable directional bending stiffness, a specified orientation of ruling lines and thus a specific curvature, and a selectable compressive or tensile stiffness. In addition, the bending stresses in the panel at large deflections can be dramatically reduced through the use of lamina emergent arrays.

Chapters Addressing Hypothesis 1

- Chapter 2: Knowledge from compliant mechanisms, particularly lamina emergent mechanisms, is used to construct tailorable morphing surfaces. Methods on how to incorporate these morphing surfaces into curved-crease origami patterns are presented. Models are characterized and validated to describe the stiffness properties of these novel morphing surfaces.
- Chapter 3: Shape factors are presented to quantify the effect of placing compliant arrays in a sheet to create a morphing surface. These factors can be used in conjunction with material property charts to visualize the effects of converting a sheet material into a morphing surface through compliant arrays.

1.3.2 Hypothesis 2

Curved-crease origami concepts and developable surfaces can be used to describe and extend several types of engineering applications, particularly in the design of rolling-contact joints.

Description

Concepts from curved-crease origami and the developable surfaces which compose them can provide pathways towards deployability, compactness, and design-space exploration of mechanisms that rely on curved surfaces to function. To explore this potential, developable surfaces are mathematically modeled in a way conducive to engineering design and analysis. These models are leveraged to explore rolling joints.

Rolling joints, or joints which rely on two surface pairs rolling over one another to achieve motion, are a strong example of how an engineering application can be modeled and theory extended using curved-crease origami concepts. For example, the rolling joint cams can be made

deployable to enable the joint to stow in a flat, collapsed position. Furthermore, the fundamental architecture of a COmpliant Rolling Element (CORE), a rolling joint using interlaced flexible bands to hold the two rolling surfaces together, can be described using concepts of curved-crease origami. This modeling in conjunction with knowledge of curved-crease principles enables designers to explore a new area in the rolling-joint design space where novel architectures, such as conical and tangent-developed rolling joints are developed. In a collaborative work stemming from this research certain characteristics of rolling joints, such as an instantaneous axis of rotation which moves during the joint motion, were leveraged to create a thickness-accommodation technique for folding thick origami models.

Chapters Addressing Hypothesis 2

- Chapter 4: Deployability in rolling joints, particularly the CORE architecture, is achieved through the use of curved-crease origami concepts.
- Chapter 5: A mathematical model of developable surfaces is presented that highlights properties of the surface important in engineering design and analysis. In particular, the curvatures of a prinicpal curve, the cross curve, are used to describe a single-class developable surface. The material in this chapter sets up an exploration of more general rolling-contact joints.
- Chapter 6: The CORE architecture is described in terms of developable surfaces enabling further exploration of the design space of this type of rolling joints. Kinematic and kinetic models of these joints are presented and the specific case of static balancing is discussed.
- Chapter 7: A study is carried out of how rolling joints can be feasibly implemented. This work builds on the work of this dissertation and collaborative work which investigated how custom rolling joints can be leveraged to create a thickness-accommodation technique for folding thick origami models.

1.4 Overview of Organization

This dissertation is composed of chapters that are meant to be able to stand alone. Therefore, each chapter contains its own introduction and conclusions. A section is included at the first of each chapter to provide the reader with extra information about the chapter, such as where the content of the chapter has been published, but also to provide a framework to guide the reader in seeing the connections between the chapters. The notation and terminology is consistent within each chapter. Occasionally there are terms which have evolved as this work has progressed. To provide consistency with the other published versions of the chapters, the terminology has been left to match the other publications with any changes explained in the first section.

CHAPTER 2. FACILITATING DEPLOYABLE MECHANISMS AND STRUCTURES VIA DEVELOPABLE LAMINA EMERGENT ARRAYS

[1]Imagine that as an engineer you've found an exquisite curved-crease origami piece that shows promise as a potential solution to an engineering challenge involving deployable curved surfaces. It won't take long for the elephant in the room to emerge from its corner. While paper is quite an amazing material, it is not the best candidate for many engineering applications. This leads us to a fundamental question for this work and the subject of this chapter: How does one move curved-crease origami out of paper?

2.1 Introduction

The objective of this chapter is to create a method to mathematically model and design large-curvature, developable structures suited to deployable applications using lamina emergent arrays. These arrays are networks of lamina emergent joints, which are compliant joints made from a single layer of material. The principles presented in the chapter enable the construction of developable surfaces in thick or brittle materials which often reside outside the design space when working with sheet material. It also explores how greater elastic deflection can be achieved in sheet products. This increased deflection lends itself towards deployable mechanisms requiring large elastic deflection. These networks of lamina emergent joints can also create a structure that is biased to move along a specific deployment path.

Developable surfaces have emerged as subjects of interest not only to mathematicians, but engineers and artists as flat sheets are morphed into intriguing and complex shapes which can be used in automobiles, boats, architecture, furniture, and clothing construction. Developable surfaces also take a prominent place in origami, specifically curved-fold origami. However, the

[1]This chapter is also published as Nelson, T.G., Lang, R.J., Pehrson, N.A., Magleby, S.P., and Howell, L.L., Facilitating Deployable Mechanisms and Structures via Developable Lamina Emergent Arrays, *Journal of Mechanisms and Robotics*, ASME, Vol. 8, pp. 031006-10, DOI: 10.1115/1.4031901, 2016 [29].

transition between the mathematical descriptions and paper-thin origami into engineering materials and structures presents some unique challenges. These challenges include the high bending stresses that develop when a thick, stiff material is bent to form the desired developable surface. These bending stresses can be reduced by using arrays of previously developed torsional and bending joints. Furthermore, particular placement of the torsion hinge axes along the ruling lines of the developable surface results in a configuration where stresses are reduced effectively. This method thus extends the range of elastic motion for engineering materials utilized in deployable mechanisms and creates a structure that is inclined to moved into a specific shape.

2.2 Background

2.2.1 Developable Surfaces

A developable surface is formed from a flat plane by the process of bending, but not stretching or shrinking [10]. Leonhard Euler and Gaspard Monge pioneered the first of many studies of these intriguing surfaces [30, 31]. These surfaces possess the attribute of being isometric, meaning that a distance between two points on the flat undeveloped plane will be equivalent to the distance between the two corresponding points on the developed surface [10]. Developable surfaces are a subset of ruled surfaces when limited to R^3 space [11]. Ruled surfaces are characterized by the quality that for each point on the surface there exists a straight line, known as a ruling line or generating line, lying upon the surface through the point. The ruling line does not need to characterize one of the principal curvatures at the point in a ruled surface. However, for the surface to be developable, the additional constraint is imposed that the ruling line must be one of the principal curvatures. This leads to the useful mathematical definition of a developable surface that the Gaussian curvature, or product of the two principal curvatures, at all points of a developable surface is zero. Another alternative but useful definition of a developable surface is the normal of the tangent plane to the surface does not change direction when moving along the ruling lines [10]. Lastly, a developable surface can be considered the envelope of a one-parameter family of planes [10].

In addition to the trivial case of the plane, there are three fundamental classes of developable surfaces: generalized cylinders, generalized cones, and tangent developed [32]. These are also referred to as torsal ruled surfaces and are shown in Fig. 2.1. Generalized cylinders contain

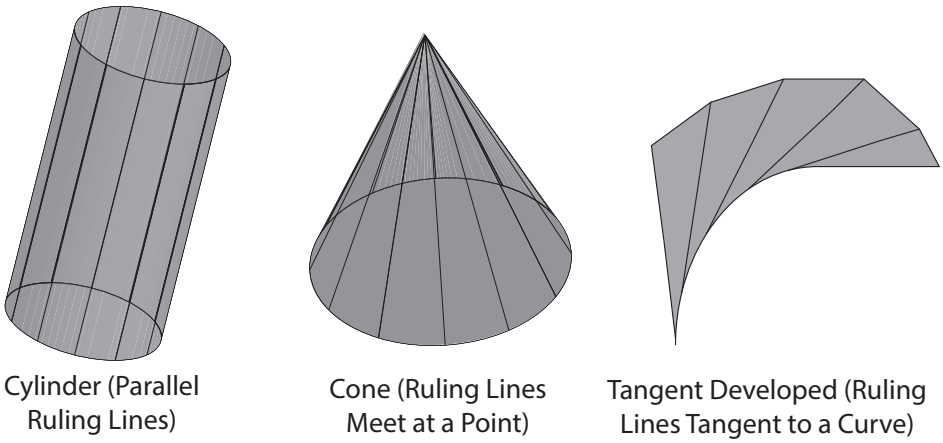

Figure 2.1: The three classes of developable surfaces: cylinder (left), cone (middle), and tangent developed (right).

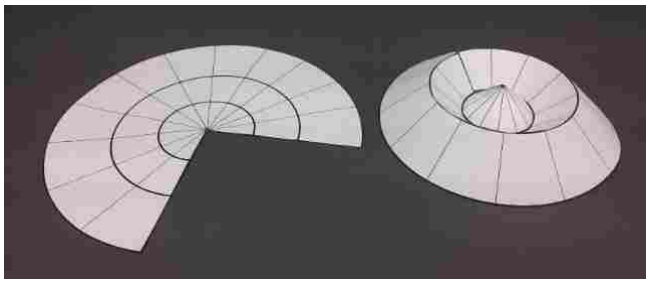

Figure 2.2: Example of a general developable surface in an unfolded and folded configuration with ruling lines shown.

ruling lines parallel to each other. Generalized cones contain ruling lines which meet at a point on or off the actual surface. Tangent developed surfaces consist of ruling lines that correspond to the family of tangent lines of a space curve. More complex developable surfaces can be created by combining the different classes [11]. This is achieved by joining a developable patch of a certain class to another by aligning the ruling lines [33] or reflection of a patch across the osculating plane at each point in a crease [15]. Combinations of torsal ruled surfaces which retain the property of being developable have been named discrete developable surfaces, composite developable surfaces, or general developable surfaces [12–14].

Curved-crease origami is intrinsically tied to developable surfaces because curved creases tie together developable patches. While much of the field of curved folding is yet unexplored, a summary of curved folding research is set forth in an article by Demaine et al. [9] and some of the

best known curved folding work comes from David Huffman [8] and Ron Resch [6]. Mathematical descriptions of curved folding were furthered by Fuchs et al. [15] and Duncan et al. [16]. Recently David Huffman's work has been further analyzed by Demaine et al. and new insights into the design of curve-folded origami have been explained [1, 34, 35].

2.2.2 Lamina Emergent Mechanisms

Like developable surfaces Lamina Emergent Mechanisms (LEMs) are also formed from the flat plane. LEMs are defined as mechanical devices fabricated from planar materials (laminae) with motion that emerges out of the fabrication plane [26]. These mechanisms draw upon flexibility to achieve their motion and are therefore considered a subset of compliant mechanisms, or mechanisms that use flexible members to achieve at least some of their mobility [36]. The main benefits of LEMs include planar fabrication, easily scalable to the micro-level, reduced part counts, lack of friction contacts, and a compact size.

Delimont et al. explored various types of joints suitable for LEMs [27, 28], particularly for origami-inspired mechanisms. This study utilizes several of these joints in specific arrays to create developable surfaces. These joints exhibit a primary motion similar to folding and can be manufactured using two-dimensional geometry. The joints have been modeled with an equivalent stiffness, K_{eq}, to represent the rotational stiffness about the joint where

$$K_{eq}\theta = T \tag{2.1}$$

with T being the torque applied across the joint and θ is the angular deflection of the joint.

A summary will be presented of the geometry and equations of seven joints. Six of the joints are pictured in Figure 2.3 and the seventh joint is a simple groove joint. Figure 2.4 shows the parameters connecting the equations and the geometry for two of the joints. While the geometry of the other joints is defined similarly, the reader is referred to the literature [27, 28] for further clarification of the parameters of the joints not shown in Fig. 2.4.

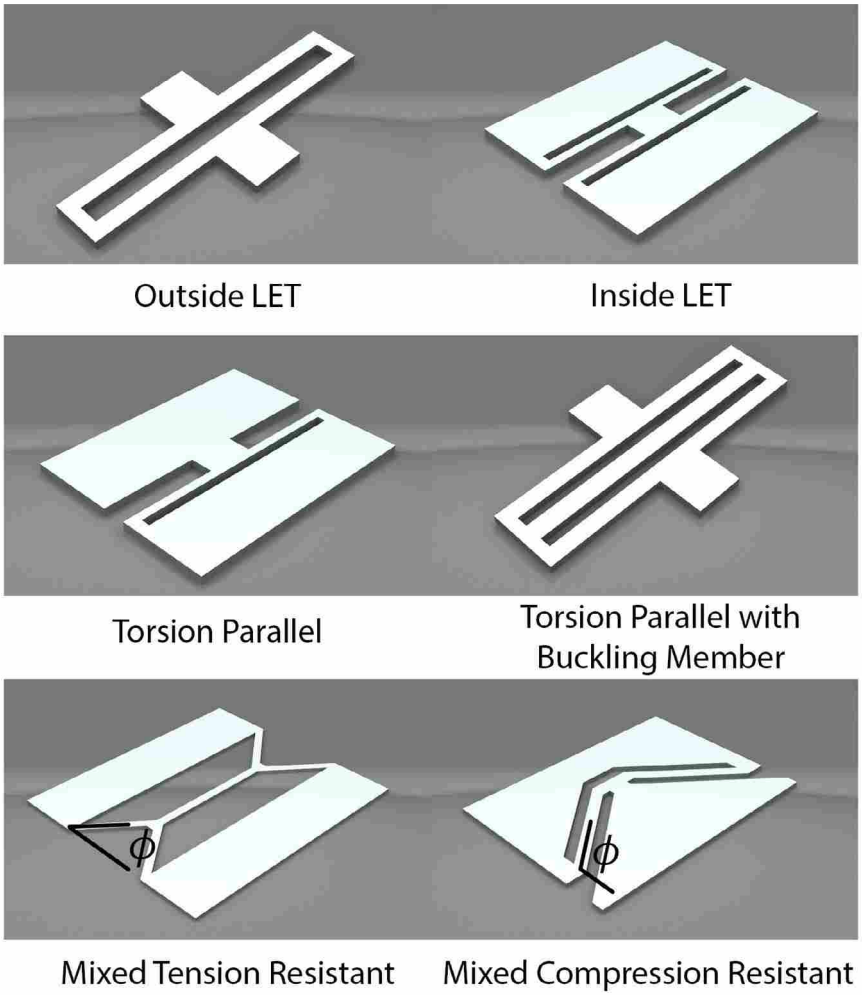

Figure 2.3: A sample of joints suitable for constructing developable surfaces.

The Outside LET Joint

The Outside Lamina Emergent Torsional (Outside LET) joint shown in Fig. 2.3 and Fig. 2.4 enables large angles of rotation in its primary folding direction but is subject to secondary motions of torsion, lateral bending, compression, and tension. It does not have a stable center of rotation in folding. Jacobsen et al. [37] developed a spring model of the joint for a folding motion to find an equivalent stiffness. The equivalent stiffness can be expressed as

$$K_{eq} = \frac{2K_B K_T}{2K_B + K_T} \tag{2.2}$$

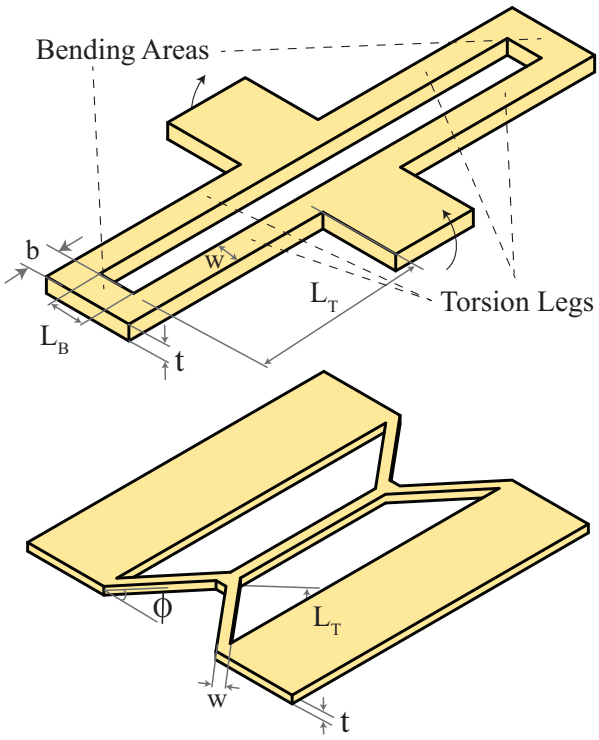

Figure 2.4: Geometric parameters for the Outside LET and Mixed Tension Resistant joints. The regions of bending and torsion are labeled on the Outside LET for the moment loading shown.

The spring constant of the torsion legs, K_T, is

$$K_T = \frac{Gwt^3\left(\frac{1}{3} - 0.21\frac{t}{w}\left(1 - \frac{t^4}{12w^4}\right)\right)}{L_T} \tag{2.3}$$

where $w \geq t$ and G is the shear modulus.

The spring constant of the bending area, K_B, is given by

$$K_B = \frac{EI}{L_B} \quad with \quad I = \frac{bt^3}{12} \tag{2.4}$$

The Inside LET Joint

The Inside Lamina Emergent (LET) joint shown in Fig. 2.3 also exhibits torsion, lateral bending, compression, and tension as secondary motions while allowing for large deflections in the folding motion. With large magnitudes of compression or tension, the Inside LET shows a

stiffer response than the Outside LET. The spring model for the Inside LET yields an equivalent stiffness expressed as

$$K_{eq} = \frac{K_B K_T}{K_B + K_T} \tag{2.5}$$

where K_T and K_B are given by Eq. 2.3 and 2.4.

Torsion Parallel Joint

The Torsion Parallel joint shown in Fig. 2.3 shows an increased stiffness in tension and compression when compared to the Outside or Inside LET joints and also provides a more fixed center of rotation. The stiffness of this joint in folding is given by

$$K_{eq} = \frac{2K_T K_B}{K_B + K_T} \tag{2.6}$$

where K_T and K_B are given by Eq. 2.3 and 2.4.

Torsion Parallel With Buckling Member Joint

The Torsion Parallel with Buckling Member joint shown in Fig. 2.3 provides better resistance to tension and compression loads as compared to the Inside and Outside LET joints by the addition of a member to withstand a buckling motion induced by the loads. The equivalent stiffness of the joint in folding reduces to the same formula as the Inside LET joint as shown in Eq. 2.5 with K_T and K_B being described by Eq. 2.3 and 2.4.

Mixed Tension Resistant Joint

The Mixed Tension Resistant joint, where ϕ ranges from 0 to $\pi/2$ radians, is depicted in Fig. 2.3. This joint is useful when greater resistance to tension than compression is desirable. The stiffness can be characterized by the following equation with ϕ in radians

$$K_{eq} = \left|1 - \frac{2\phi}{\pi}\right|^{0.1096} K_B \cos^2\phi + K_T \sin^2\phi \tag{2.7}$$

with K_B and K_T given by

$$K_B = \frac{2\rho EI}{L_T} \quad with \quad I = \frac{wt^3}{12} \tag{2.8}$$

$$K_T = \frac{2Gwt^3\left(\frac{1}{3} - 0.21\frac{t}{w}\left(1 - \frac{t^4}{12w^4}\right)\right)}{L_T} \tag{2.9}$$

In these equations ρ is commonly approximated as 1.5164 [28], w is the width and t is the thickness of the compliant section with $w \geq t$, E is Young's modulus, G is the shear modulus, and L_T is the length of the compliant section.

Mixed Compression Resistant Joint

When a stiffer resistance to compression is desired, the Mixed Compression Resistant Joint as shown in Fig. 2.3 is a good candidate. The stiffness of this joint can also be described by Eq. 2.7, 2.8, and 2.9 where ϕ ranges from $\pi/2$ to π radians.

Groove Joint

The groove joint is simply an area of reduced cross section in a panel and is simple to create. The center of rotation on a groove joint is relatively stable throughout its bending motion. A living hinge can be considered as a groove joint with a very small stiffness in bending. The expression for the equivalent stiffness of the groove joint is

$$K_{eq} = \frac{GWH^3\left(\frac{1}{3} - 0.21\frac{H}{W}\left(1 - \frac{H^4}{12W^4}\right)\right)}{L} \tag{2.10}$$

where G is the shear modulus, H is the height of the groove, L is the depth of the groove, and W is the length of the groove and panel. For a diagram of these parameters the reader is referred to the literature [28].

2.2.3 Current and Past Applications

Previous research has yielded intriguing methods to create 3D geometry from sheet material. One of the oldest methods of creating 3D structures from sheet material is origami. Origami uses combinations of paper folds to create a 3D structure. You [38] discussed the advantages and challenges of origami in creating folding structures. Dureisseix [39] presented an overview of how origami patterns have been applied in engineering applications, such as deployable structures. Cylinders, spirals, and bi-directional sheets were created using microassembly techniques based on origami by Jamal et al. [40]. Origami metamaterials were investigated Silverberg et al. [41]. Lee et al. [42] explored how the origami waterbomb base, a common origami-fold pattern, could be utilized as a dynamic wheel structure. Energy absorption applications in crushing of thin walled square tubes with origami structures was analyzed by Ma et al. [43]. An interesting method of self-folding origami structures from thin polymer material and controlled heat absorption was presented by Liu et al. [44]. A self folding robot was created by Felton et al. [45]. Kirigami techniques have been used to investigate the creation of custom honeycomb cross sections from flat sheets [46]. Miyashita et al. [47] used self folding with curved creases to create propellers and Gattas et al. [21] explored how curved creases and panels can be used in Miura-derivative prismatic base patterns.

Construction of developable surfaces has received attention from a variety of industries, including ship building, automotive, architecture, clothing and footwear, computer animation, and image processing. A process of designing shoe uppers using triangles and optimizing the surface to make it more developable has been explained by Chung et al. [48]. Kilian et al. [23] created an algorithm to approximate a nearly developable structure as a combination of developable patches, culminating in a case study of a fully developable car body. Pottman et al. [49] approximated freeform architectural surfaces by using developable panels connected together. Further approximation of freeform surfaces was explored using single and doubly curved panels by Eigensatz et al. [50].

This chapter presents a novel method of creating developable surfaces that will enable many of these processes to be applied to thicker materials in addition to allowing a greater elastic range of motion.

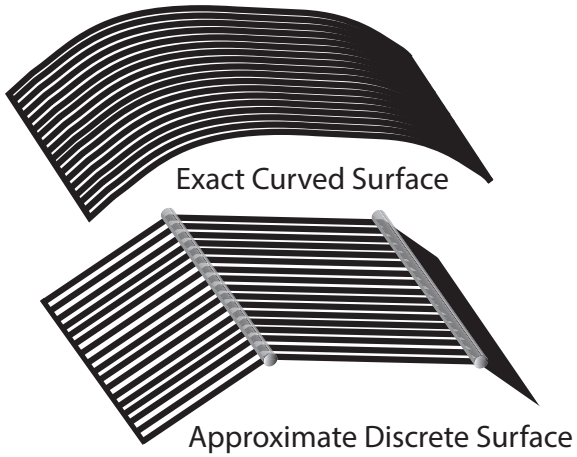

Figure 2.5: Discretized surface model using hinges and panels.

2.3 Method

Each of the joints discussed in Section 2.2.2 can be considered as the fundamental unit of an array. These units can be connected together in parallel, series, or a combination of both. Deployable developable surfaces, that is surfaces which can move back and forth between a flat configuration and a developed surface without yielding, can be created with these joint arrays. It should be noted that while deployable structures normally lock into two positions, the surfaces created by these joint arrays have a single stable position to which the surface wants to return. Additional hardware could be used to lock the surface into the deployed shape. Only an approximation of the surface is possible because the joint arrays cannot create a smooth curved surface but rather a discrete approximation of a surface. This discretization can be roughly modeled as a series of pin joints and rigid panels as shown in Fig. 2.5.

While the design space for arrays of joints used to form a deployable developable surface is vast, several unique properties of developable surfaces cause one specific arrangement to stand out as particularly efficient in terms of achieving the elastic deflection while maintaining stresses below the strength of the material. This configuration consists of aligning the folding axis of the joints to the rules of the developable surface. When the joints are arranged in this fashion, the direction of the primary motion of each joint is matched to the most extreme curvature of the surface. This result can be seen from the following informal proof. At each point of a developable surface the Gaussian curvature vanishes, or restated, the Gaussian curvature is equal to zero. Because

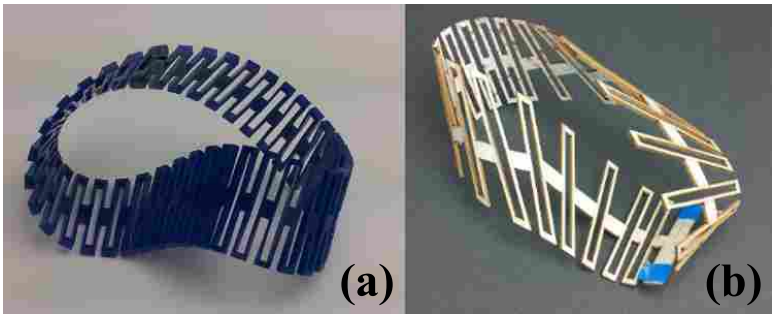

Figure 2.6: Illustration of the method of aligning the axes of the joints to the ruling lines in a Mobius strip: (a) before alignment (b) after alignment.

the Gaussian curvature is the product of the two principal curvatures, one can see that at least one of the principal curvatures at any point is also equal to zero. The direction of this principal curvature corresponds to the direction of the ruling line. As is discussed in [51], the directions of the principal curvatures are orthogonal at any point. Thus the direction of the other principal curvature is orthogonal to the ruling line. The implementation of this method can be seen in Fig. 2.6, where torsion joints of a Mobius strip are not aligned (a) and then aligned to the rules (b).

A finite element analysis (FEA) was performed to investigate the sensitivity of the stress caused by bending to the alignment the joints along the ruling lines of developable surfaces with parallel ruling lines. An array of torsional joints was created as shown in Fig. 2.7 with a thickness of 1.143 mm (0.045 inch) and torsion bars 22.225 mm (0.875 in) long with a width of 1.651 mm (0.065 inch). An isotropic material with a modulus of 207 GPa (30×10^6 psi) and Poisson's Ratio of 0.3 was used. Twelve models were created by varying the angle of the torsional joint axes as measured from the parallel ruling lines from 0 to 20 degrees in increments of 2 degrees. Using ANSYS (Shell 181) the models were fully fixed at one edge and a displacement load of 7.62 mm (0.3 in) was applied to the opposite edge orthogonal to the plane of the initially flat surface. While not a pure bending load, these loading and boundary conditions represent a scenario similar to a cantilever beam with a tip load. The models were stress converged to within a 10% change of Von Mises maximum stress.

A graph of the maximum Von Mises stress for each of the models is shown in Fig. 2.8 along with a reference line which shows the maximum stress of a solid plate without a torsional joint array moved through the same displacement. Images of three cases of the joint arrays (0,

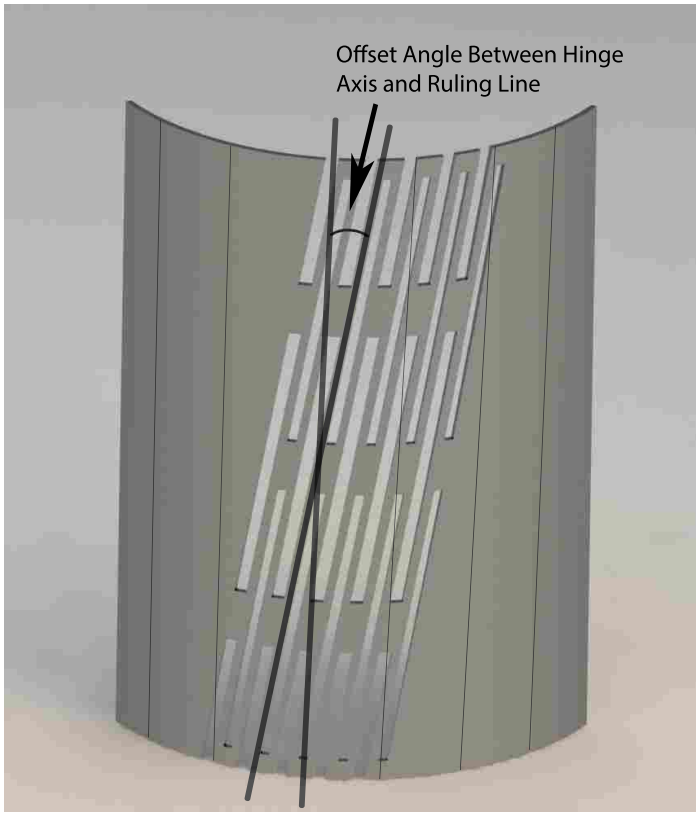

Figure 2.7: CAD model used in FEA to determine the sensitivity of hinge axis alignment to parallel ruling lines.

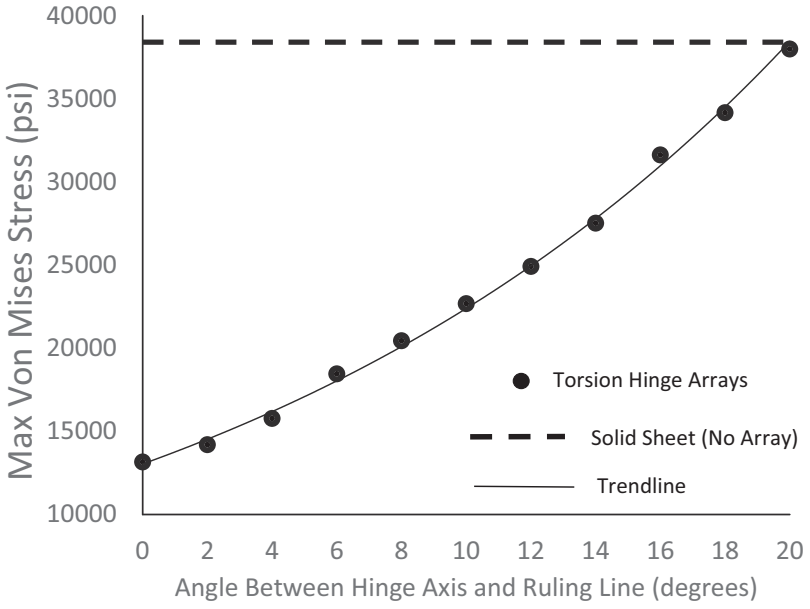

Figure 2.8: Von Mises stress sensitivity to hinge axis alignment for parallel ruling lines.

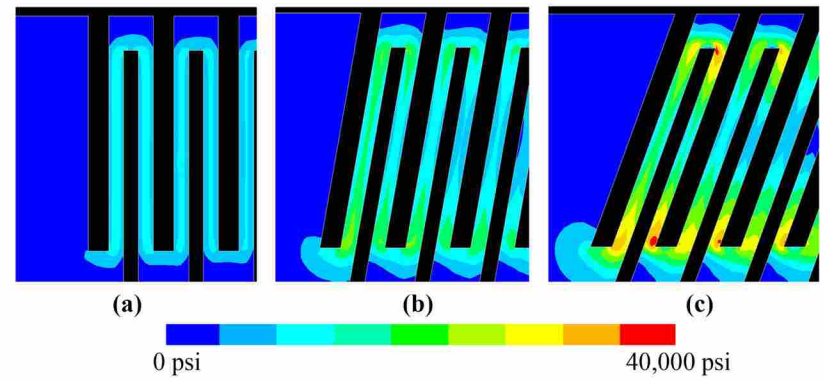

Figure 2.9: Von Mises stress contours of the (a) 0 degree offset model (b) 10 degree offset model and (c) 20 degree offset model.

10, and 20 degree offsets) are shown in Fig. 2.9. As expected from studies of shear stresses in rectangular torsional bars, the maximum stress in the 0 degree offset occurs on the outside of the middle of the wider side of the rectangular torsional beam. In the 10 degree offset model the maximum shear stress has changed locations and occurs at the base of the torsional bar reflecting a stress concentration that has developed due to the hinge axis and ruling line offset. Further, in the 20 degree offset model the maximum stress location has changed to the second torsion member and is similar to the location of the maximum stress of a cantilever beam in bending. As the offset is increased from 0 to 20 degrees, the stresses grow in a exponential manner with an R^2 value of 0.9976.

By using joints which have one axis that is markedly less stiff than any other direction, an array which is aligned to a particular ruling will resist moving away from the path of developable shapes characterized by that ruling during the array's deployment. It may be possible to quantify this reluctance towards deviation from the path through energy methods or through characterizing the stiffness of the arrays for motions other than the primary folding motion.

2.4 Mathematical Model

A relatively straightforward mathematical model was created to describe how arrays of joints function when aligned with the rules of a developable surface. If each joint unit is considered as a torsional spring with a stiffness, K_{eq}, as described for each type of joint in Section 2.2.2, then arrays of these joints can be modeled as a network of torsional springs in parallel and series.

Joints placed along a single ruling line can be considered as torsional springs placed in a parallel arrangement. This can be described by

$$K_p = \sum_{i=1}^{m} K_{eq,i} \tag{2.11}$$

where K_p is the equivalent stiffness of all the joints along the ruling line, m is the number of joints along the ruling line, and $K_{eq,i}$ is the stiffness of the ith joint along the ruling line.

When multiple ruling lines contain joints K_{tot}, the total stiffness of the array in bending, can be found using

$$\frac{1}{K_{tot}} = \sum_{j=1}^{n} \frac{1}{K_{p,j}} \tag{2.12}$$

where n is the number of ruling lines which contain joints and $K_{p,j}$ is the stiffness of the jth ruling line as found from Eq. 2.11.

Knowing the angular displacement of each individual unit facilitates the stress analysis on the torsion bars. Finding this angle is relatively straightforward for parallel ruling lines of generalized cylinders because the angular displacements of the individual units sum to the angular displacement of the entire array in bending. However, in the case of generalized cones and tangent developed surfaces, the combined angular displacement of the individual units is not equal to the angular displacement of the array when the angular displacement of the array is defined about a single axis such as shown Fig. 2.10. Rather the sum of the angular displacements of the individual units represents a total wrapping angle where the axis the angle is measured about changes for each individual joint.

For a generalized cylinder with parallel arrangements of the same stiffness (i.e. constant K_p) and equal spacing between the parallel arrangements, the relationship between the total angular displacement of the array, Θ, and the angular displacement of a parallel arrangement (which is also the displacement of an individual unit, θ) is described by

$$\theta = \frac{\Theta}{n+1} \tag{2.13}$$

where n is the number of ruling lines containing joints.

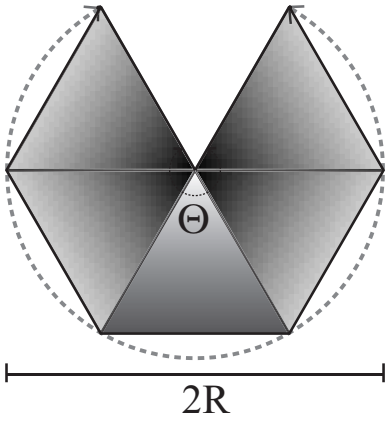

Figure 2.10: Definition of the total angular displacement of a partially formed cone.

For a generalized cone with parallel arrangements of the same stiffness (constant K_p), and equal spacing, the relationship between the total angular sweep of the formed array in degrees, Θ as shown in Fig. 2.10, and the angular displacement of any parallel arrangement in degrees, θ, is dependent upon not only n, the number of ruling lines containing joints, but also γ, the angle swept by the planar undeveloped cone as shown in Fig. 2.11. To facilitate simplicity in the formulas, let

$$\xi = \cos^2\left(\frac{\gamma}{2n+2}\right) + \frac{\cos\left(\frac{\gamma}{n+1}\right) - 1}{2\tan^2\left(\frac{\Theta}{2n+2}\right)} \tag{2.14}$$

The angle of any parallel arrangement in degrees, θ, which is also the displacement of the individual units in the arrangement can be described as

$$\theta = 180 - \arccos\left(\frac{(\xi-1)+(-1-\xi)\cos\left(\frac{\Theta}{n+1}\right)}{(\xi+1)+(1-\xi)\cos\left(\frac{\Theta}{n+1}\right)}\right) \tag{2.15}$$

The geometry of the formed cone where R is the radius of the formed cone and H is the height of the formed cone can be related to ξ and r, the radius of the planar undeveloped cone as shown in Fig. 2.11, by

$$R = r(1-\xi)^{\frac{1}{2}} \tag{2.16}$$

$$H = r(\xi)^{\frac{1}{2}} \tag{2.17}$$

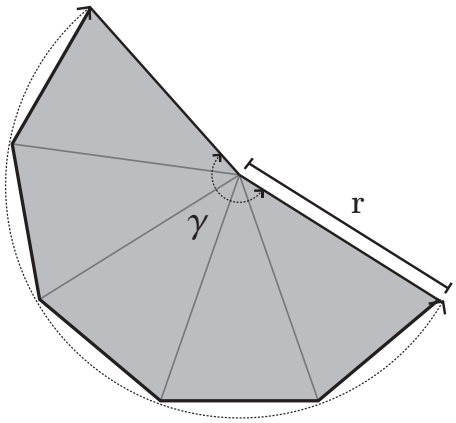

Figure 2.11: Parameters of the planar undeveloped cone.

If the number of joints containing ruling lines is allowed to approach infinity, then the angular displacement of the joints on the ruling lines, θ, goes to zero and the expression for ξ becomes

$$\xi = 1 - \frac{\gamma^2}{\Theta^2} \tag{2.18}$$

2.5 Conical Array Pattern Generation

A technique to generate an array pattern for a conical developable surface using torsional joints is explained in this section. The product of this technique is a network of lines that provide a cut pattern which will form the array. When using the technique the designer is allowed to choose a minimum torsion bar width, which is often one of the critical dimensions in determining the stress present in the developed surface. Using the selected minimum torsion bar width, the technique finds a pattern which maximizes the amount of ruling lines containing torsion joints as well as maximizing the length of the torsion bars in order to minimize the stress present in the developed conical structure.

The steps to generating a conical array pattern are as follows:

- First the designer needs to select a radius for the hole which will be at the top of the cone. As ruling lines collect towards a focal point, interference between hinges will occur if the hole is not present. As the hole becomes larger more torsion bars can be placed in the pattern near the top of the cone and lower stresses will result. Let this radius be called r_1.

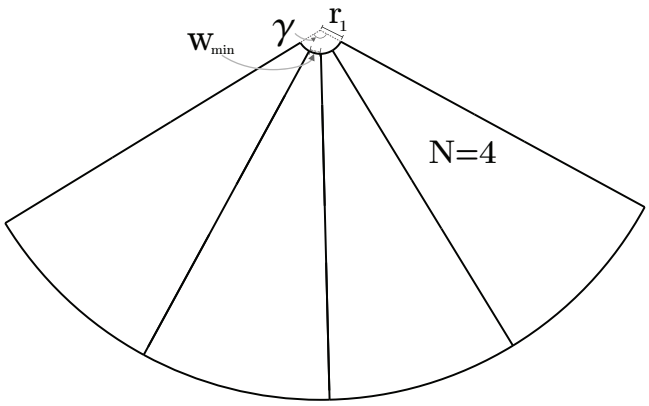

Figure 2.12: Initial geometry of conical cut pattern generation.

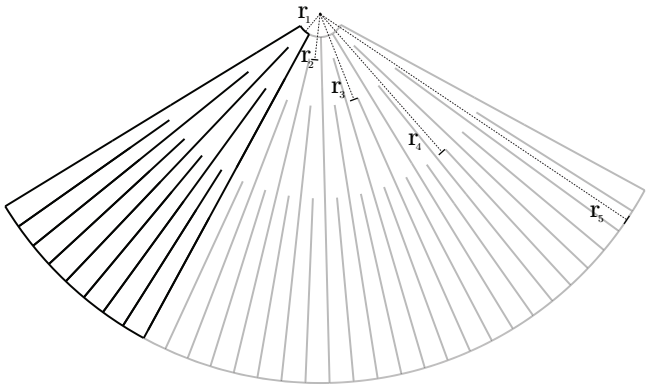

Figure 2.13: Introducing additional levels of cuts.

- Next the number of repeating units, N, in the cut pattern (as shown in Fig. 2.12) should be preliminarily selected. The minimum width of the torsion bars, w_{min}, can be found by applying the Law of Cosines with the result

$$w_{min} = r_1 \left(2 - 2\cos\left(\frac{\gamma}{N}\right)\right)^{\frac{1}{2}} \tag{2.19}$$

where γ is the angle swept by the planar undeveloped cone. The number of repeating units, and consequently the minimum width, can be selected based on the amount of expected deflection of each individual unit in conjunction with a stress analysis of a rectangular bar in torsion.

- More levels of cuts can be introduced along the ruling lines as shown in Fig. 2.13. The radii of the circles at which these cuts can be introduced are described by

$$r_i = r_1 \left(\frac{1 - \cos\left(\frac{\gamma}{N}\right)}{1 - \cos\left(\frac{\gamma}{2^{(i-1)}N}\right)} \right)^{\frac{1}{2}} \tag{2.20}$$

  where r_i is the i^{th} level radius.

- Once these lines have been generated to the desired radius, the designer must choose where to preserve material to create a continuous structure while maintaining the desired stiffness. At least one connection must be made between the repeating units to provide continuity, while more can be put into the pattern to increase resistance to parasitic in-plane movement of the surface. Figure 2.14 shows examples of two patterns where material is preserved to provide continuity. The outermost edge cut of the repeating unit can be interrupted at any point and similar interruptions can occur on at most every other cut line across the pattern to maintain the function of the torsional units. Also, triangular cuts rather than linear cuts can be made to cause the minimum torsion bar width to be utilized as much as possible in the design.

2.6 Structure and Mechanism Examples

Subtractive and additive manufacturing techniques can be used to create structures and mechanisms using lamina emergent arrays in a variety of materials. The arrays can vary widely in appearance depending upon the requirements of each application. When selecting attributes of the arrays, such as n and m, the type of lamina emergent mechanism used as the fundamental unit, and the geometry of the fundamental unit itself, it is useful for the designer to consider factors such as the required displacement of the surface, the material being used, the thickness of the material, and aesthetics. These factors dictate the stress developed in the surface and will help the designer select array attributes which will enable the array to function without failure.

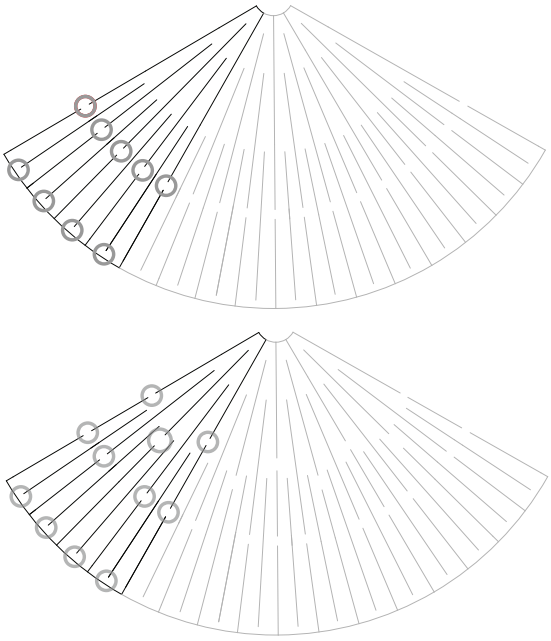

Figure 2.14: Examples of cut patterns adjusted in the circled regions to preserve continuity.

2.6.1 Subtractive Manufacturing

Subtractive manufacturing techniques such as milling, etching, laser cutting, and waterjet cutting can be used to create the lamina emergent arrays in a planar sheet. The two-dimensional geometry in the following four developable structures was created with a laser cutter.

Figure 2.15 (a) shows a cylinder made of 2.54 mm (0.1 in) cold press illustration board using the mixed tension resistant joint. A cone made of 4.8 mm (0.19 in) cherry plywood is shown in (b). This cone uses torsional parallel joints to enable deployment motion and the cut pattern was generated using the technique described in Section 2.5. For this cone $\gamma = 100$ degrees and $\Theta = 360$ degrees with a radius $r = 16.17$ cm (6.37 in) and inside hole radius $r_1 = 0.508$ cm (0.2 in). Each ruling line containing a torsion bar is considered to be a ruling line with a joint giving $n = 80$. The number of repeating units was selected to be $N = 5$. These parameters are shown labeled on the cone in the flat state in Fig. 2.15. From these parameters the height of the formed cone can be calculated as $H = 15.5$ cm (6.11 in) from Eqs. 2.14 and 2.17, the formed radius as $R = 4.49$ cm (1.77 in) from Eqs. 2.14 and 2.16, and the minimum width of a torsion bar as $w_{min} = 1.76$ mm (0.069 in) from Eq. 2.19.

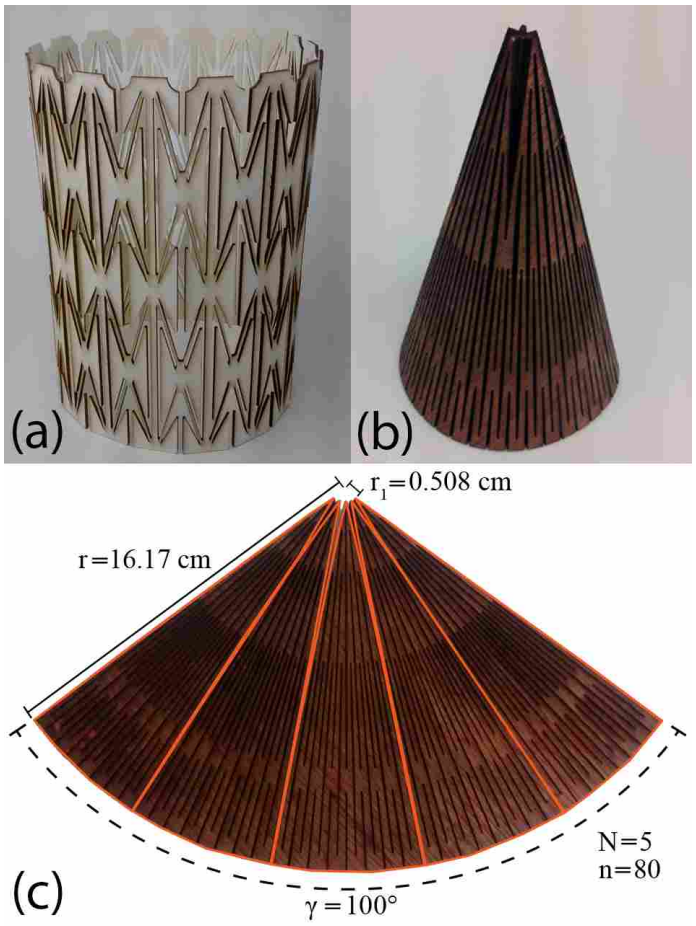

Figure 2.15: Examples of lamina emergent arrays to create developable surfaces in materials other than paper: (a) cylinder (b) cone (c) cone in the flat state with labeled parameters.

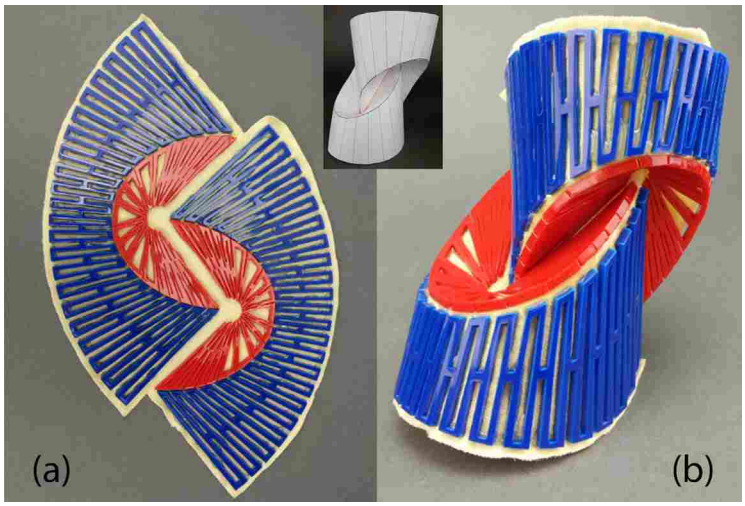

Figure 2.16: Crashing Volcanoes transitioned from paper (origami model is shown in the inset) to acrylic with a fabric backing in its (a) flat state and (b) deployed state.

Figures 2.16 and 2.17 show curved-fold origami models designed by author Lang that have been transitioned into thick material [33]. The model shown in Fig. 2.16 is "Crashing Volcanoes" made of 0.292 cm (0.115 in) acrylic with a fabric backing. This model consists of four conical developable patches which are joined by splicing together ruling lines and reflecting ruling lines over a conic line. A single LET joint was patterned in series across the developable patches to maximize the torsion bar lengths and thus reduce stress in the structure.

The design can be analyzed by separately considering the two distinct conical patches, the outside blue patch and inside red patch. The parameters for these conical patches are shown in Table 2.1. In determining n, the number of ruling lines containing joints, each torsion bar is considered as a joint. For the outside blue patch n is observed to be 44. For the inside red patch a group of torsion bars near both ends of the conical patch were intentionally made short to noticeably stiffen the structure in these regions. The resulting number of ruling lines containing joints was therefore reduced for the inside patch to account for these stiffer ends by only counting torsion bars which had longer torsion bar lengths, resulting in $n = 20$. Assuming that each of the torsion bars have the same angular displacement allows for the computation of the angular displacement of each joint unit using Eq. 2.15. Note that the planar undeveloped radius, r, is not required to compute the displacement of each of the torsion bars. Once again disregarding the stiffer portions of the inside red patch, the geometry of the smallest length torsion bar in both patches is used to calculate the maximum torsion stress, τ_{max}, induced by the joint displacement using equations for torsion of rectangular beams [52]. Table 2.1 reports the material properties used, where G is the shear modulus of the acrylic and S_{sy} is the material's shear yield stress.

Figure 2.17 is Lang's origami model Elliptic Infinity transitioned into 2.692 mm (0.106 in) medium density fiber-board and 22.86 μm (0.9 mils) metallic glass to create the creases. Metallic glass is an amorphous metal with properties that make it a suitable material for compliant structures [53]. The model Elliptic Infinity is based off a single ellipse with ruling lines radiating from the focal points of the ellipse. The technique described in Section 2.5 was adjusted for each conical developable patch to create the pattern of torsion joints with hinge axes that match the ruling lines. The structure in the flat state is approximately 50 cm (19.7 in) wide by 43 cm (16.9 in) tall with a deployed height of 30 cm (11.8 in).

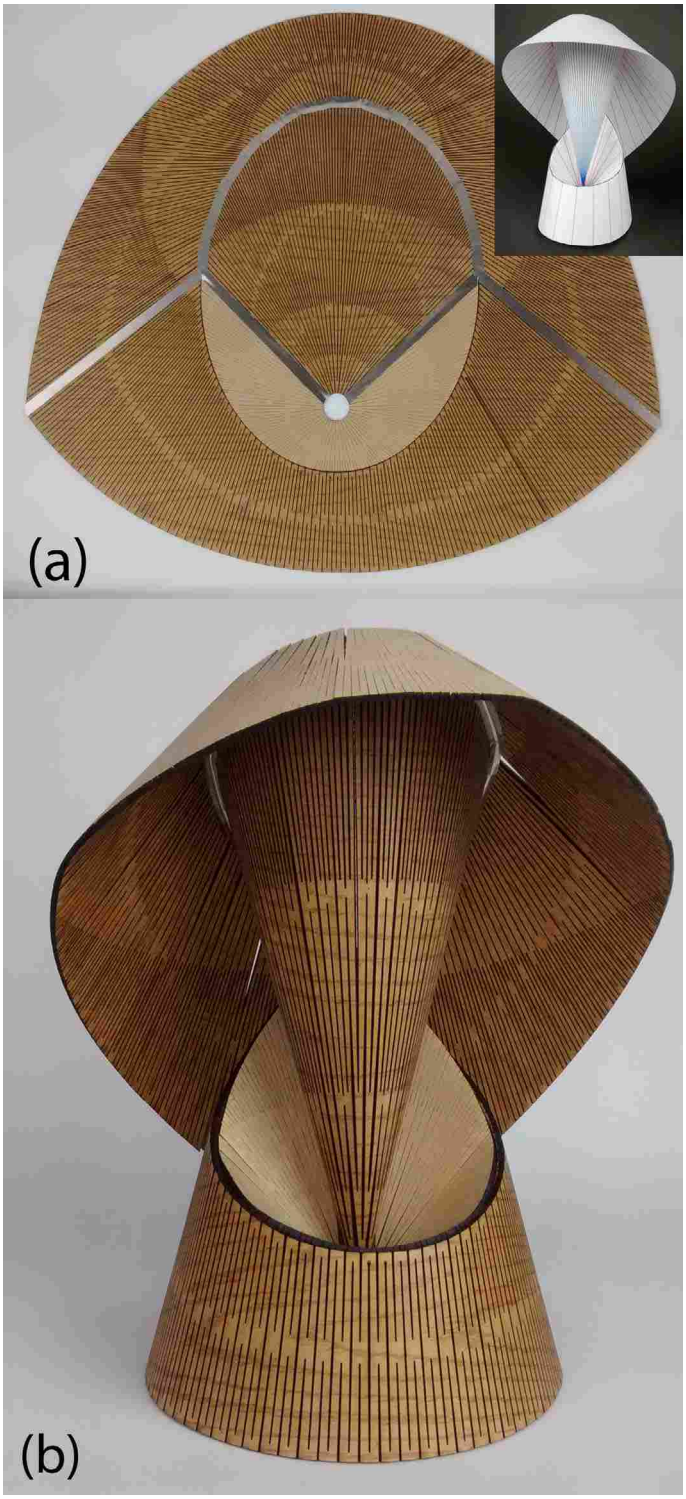

Figure 2.17: Elliptic Infinity transitioned from paper (origami model is shown in the inset) to particle board in its (a) flat state and (b) deployed state.

Table 2.1: Crashing Volcanoes Conical Patch Analysis

	Outside Conical Patch (Blue)	Inside Conical Patch (Red)
Pattern Parameters		
Θ	280 deg	280 deg
γ	96.38 deg	263.74 deg
n	44	20
Calculated Joint Displacement		
θ	5.84 deg	4.49 deg
Joint Geometry		
L_T	1.20 cm (0.472 in)	0.622 cm (0.245 in)
t	0.180 cm (0.071 in)	0.163 cm (0.064 in)
w	0.292 cm (0.115 in)	0.292 cm (0.115 in)
Material Properties		
G	1020 MPa (148 ksi)	1020 MPa (148 kpsi)
S_{sy}	38.5 MPa (5.59 ksi)	38.5 MPa (5.59 ksi)
Calculated Max Shear Stress		
τ_{max}	13.7 MPa (2.00 ksi)	18.9 MPa (2.75 ksi)

2.6.2 Additive Manufacturing (3D printing)

Additive manufacturing has commonly been used to create complex 3D shapes, yet it also has the ability to rapidly create lamina emergent arrays which can be designed to be folded or deployed into a specific shape. Recent research in 3D printing investigates not only how complex shapes can be accomplished with 3D printing, but how assembly and function can be facilitated through the use multiple types of materials, deposition processes, and embedding materials [54, 55]. The following two mechanisms show how developable origami patterns can be transitioned to thick materials using lamina emergent arrays by 3D printing flat designs which are biased to be assembled, or folded, into a certain structure.

The oriceps are an origami-inspired mechanism for use in robotic surgery applications where the instrument must be compact for entry into the body through small incisions and deployed

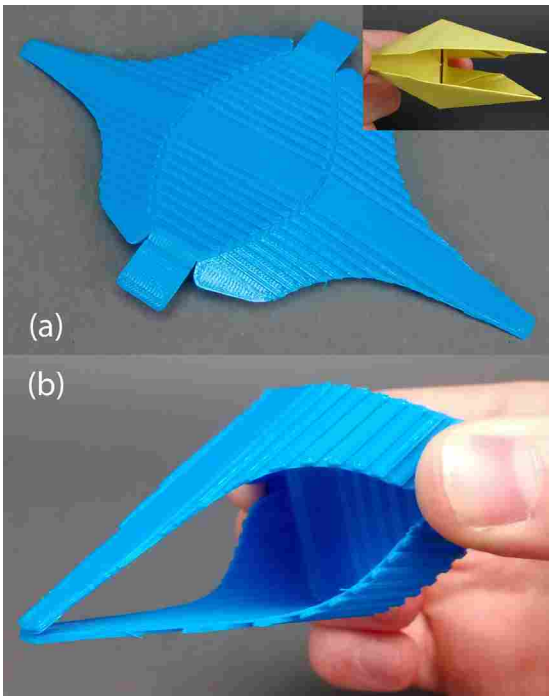

Figure 2.18: 3D printed curved-fold oriceps in its (a) flat printed state (origami model which provided inspiration is shown in the inset) and (b) folded, functional state.

to its functional state after entering the body [56]. The origami pattern used in the oriceps can be adapted to a curved crease pattern which is developable. A lamina emergent array of groove joints can be specified along the ruling lines and curved creases of the pattern. 3D printing was used to create this lamina emergent array as shown in Fig. 2.18 (a) from polylactic acid (PLA) on a Makerbot Replicator 2. The compliant reduced cross sectional area in the groove joints was created by printing two layers of PLA with the tool path orthogonal between the two layers. The build time was 25 minutes and required 5 grams of PLA. The folded, functional oriceps are shown in Figure 2.18.

The deployable compliant rolling contact element (D-CORE) is a curved-crease inspired mechanism which can be planar manufactured and folded into its functional state as a compliant rolling hinge [57]. Groove joints were placed upon the ruling lines and curved creases of this design similar to the oriceps pattern and the flat pattern was 3D printed. Each D-CORE required 3 grams of material and 17 minutes to print in its flat configuration shown in Fig. 2.19 (a). The joints where folded and attached to rigid panels as shown in Fig. 2.19 (b). With the D-CORE hinges the panels can undergo nearly 360 degrees of rotation. The hinged panels from Fig. 2.19 (b) were

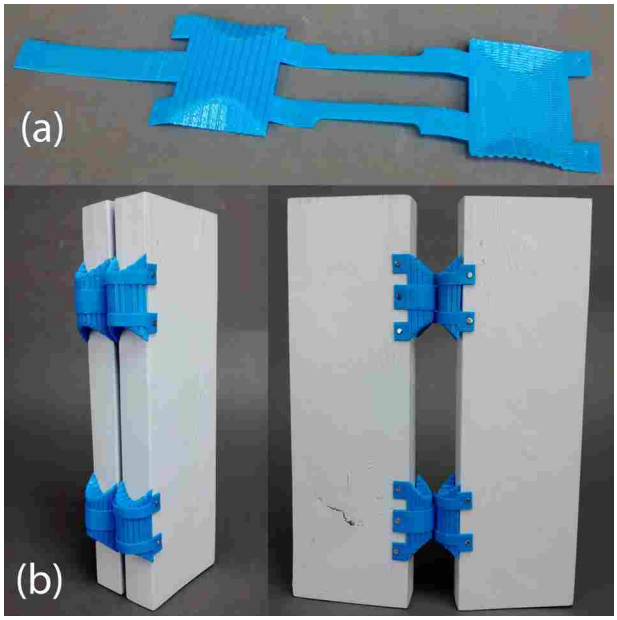

Figure 2.19: 3D printed D-CORES in (a) flat printed state and (b) folded state connecting two panels with nearly 360 degrees of rotation.

compressively loaded with the panels 180 degrees from each other. The hinges failed at a load of approximately 220 newtons (49.5 pounds).

2.7 Conclusion

This chapter has demonstrated a method to create developable structures suited to deployable applications by implementing arrays of lamina emergent joints. Furthermore, the alignment of the axes of these joints to the ruling lines of the surface has been shown to be an efficient configuration in terms of stress reduction in the structure and bias the structure to fold and deploy along a specific path. A mathematical model was developed for finding the stiffness of these types of structures as well as for computing the angular displacement of surfaces with parallel ruling lines and ruling lines which meet at a focus. A technique for generating a cut pattern for a generalized cone was laid out. Using these ideas several example pieces were created.

Using lamina emergent arrays with joint axes aligned to ruling lines provides a vehicle for transitioning curved-fold origami patterns to engineering materials. These ideas can progress applications where storage space is a constraint, such as in devices for minimally invasive surgery, aerospace, and portable outdoor equipment. Particular possible applications include folding an-

tennae, emergency shelters, flexible decorative or functional paneling, morphing surfaces such as wings on UAVs, and conformable protective equipment. Using arrays of lamina emergent joints enables a designer to decouple certain material properties from the modulus of the material. For example, electrical conductivity and the modulus of a material generally increase with each other, but using lamina emergent arrays it may be possible to construct a highly flexible panel that is also electrically conductive.

While this chapter outlines methods for constructing cylindrical and conical surfaces from lamina emergent arrays, future work may include the development of methods to design tangent developable surfaces suited to deployment and to incorporate other types of joints besides those investigated. Intentionally using joints which enable additional motions besides a primary folding motion can possibly facilitate double-curvature or approximately developable shapes to be realized from planar materials. Panels which can stretch and shear in plane, a commonly desired characteristic in applications such as morphing wings, may also be possible. In addition, further methods can be developed in generating conical arrays which enable a designer to begin with various parameters, such as a desired cone shape and maximum stress, and calculate the remaining parameters.

CHAPTER 3. MATERIAL SELECTION SHAPE FACTORS FOR COMPLIANT ARRAYS IN BENDING

[1]While the last chapter introduced a method to accommodate thickness in curved panels using lamina emergent arrays (LEAs), this chapter will build upon the work by setting forth factors that assist in the selection of a material for curved panels in bending. The reader will notice the shift from the term lamina emergent array (LEA) to compliant array (CA) in this chapter. The reason for this is that the term LEA carries a distinct connotation for monolithic planar elements while the term CA is applicable to more general cases where any compliant elements are assembled into networks. In the previous chapter monolithic planar compliant elements were the particular focus in forming the flexible arrays (LEAs). The theory presented in this chapter, while still applicable to LEAs, has a more general scope, prompting the use of the term CAs.

3.1 Introduction

Compliant Arrays (CAs) are panels with geometry consisting of a fundamental unit that is patterned in parallel and series to achieve target material properties, particularly out-of-plane bending stiffness. An example of a CA in acrylic is shown in Figure 3.1. Similar to metamaterials, CAs create responses typically not achievable from a flat panel of a single material. They can be potentially manufactured in micro, meso, or macro scales. Many candidates for the fundamental unit of these arrays come from the field of Lamina Emergent Mechanisms (LEMs). LEMs are mechanical devices fabricated from planar materials (laminae) with motion that emerges out of the fabrication plane [26]. CAs lend themselves towards applications such as deployable or collapsible structures as they enable a larger elastic deformation in out-of-plane bending than is possible with a solid sheet for a given material. Recent developments with the use of patterns similar to those

[1]This chapter is also published as Nelson, T.G., Bruton, J.T., Rieske, N., Walton, P., Fullwood, D.T., and Howell, L.L., Material Selection Shape Factors for Compliant Arrays in Bending, *Materials and Design*, Vol. 110, pp. 865-877, DOI: 10.1016/j.matdes.2016.08.056, 2016 [58].

investigated in this chapter include an array for solar tracking [59], flexible lithium-ion batteries [60], an optical shutter [61], the creation of super-conformable materials for applications such as flexible circuits [62], and creating materials with extreme Poisson's ratios [63, 64]. CAs can also be modified to create thick-material approximations of curved-crease origami patterns used in origami-inspired mechanisms and structures [29]. While the body of work investigating stiff and light panels is extensive and ongoing through a variety of avenues [46,65–73], there is significantly less research describing methods to create panels with a lower, yet selectable, stiffness to enable large amounts of elastic deflection. Recent informative work by Ohshima et al. investigates the analysis and design of slit-based materials [74], which can also be classified as a type of CA. Isobe et al. also characterize motions of a kirigami pattern which could be considered a CA [75].

Shape factors were developed to show the effect of a variable cross section for beams [76]. Also known as a shape transformer, a shape factor is defined as the ratio of a geometric quantity for a specific cross section over the same geometric quantity of a reference cross section [77, 78]. Shape factors can be used to compare properties of a component or structure as a combination of geometry and material simultaneously. They provide a way to represent the properties of a shaped component as a 'new'material through modification of the material properties. Comparison to other materials and geometries is then facilitated in the material selection process. Elastic bending shape factors have been previously developed for a variety of cross sections [79, 80], yet shape factors have not been developed to describe the impact of panels with patterns that can be described by planar geometry, such as those found in CAs. This chapter characterizes elastic bending shape factors and strength efficiency shape factors associated with two types of CAs. These factors function as design guidelines in selecting materials for applications requiring large magnitudes of elastic bending.

3.2 Background

3.2.1 Compliance

CAs rely on the fundamental principles of compliant mechanisms to function. Compliant mechanisms "gain at least some of their mobility from the deflection of flexible members rather than from movable joints only" [36]. Using compliant mechanisms to achieve the lamina-emergent

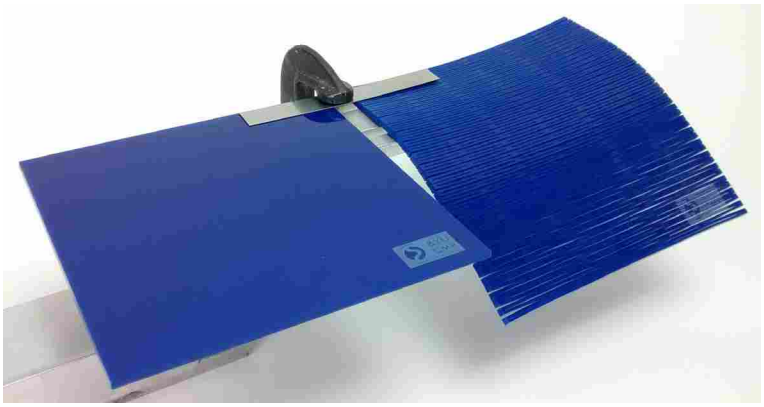

Figure 3.1: An acrylic compliant array (CA), shown on the right, bending under its own weight with a reference panel of same material, thickness, and area shown on the left.

function has several advantages over using traditional mechanisms, including simplified manufacturing, reduced wear, and reduced part count. In many cases, a lamina-emergent mechanism can have a part count of one, a quality retained by a CA. Because a CA consists of a single part, it can also be viewed as a modified material rather than strictly a mechanism. For a CA to function, the array must be able to deflect without failing by undergoing some combination of torsion and/or bending. As such, a fundamental unit consisting of different members that bend or twist can be developed to be used in arrays. Multiple individual units that can bend or deflect elastically to a certain displacement can be arrayed in series to achieve the desired elastic range of motion.

3.2.2 CA Applications: Deployable Structures and Developable Surfaces

Because CAs can be designed to achieve a large elastic range of motion, they are good candidates to be incorporated into deployable structures. Deployable structures have been used in space technology [81], portable shelters [82], microelectromechanical systems (MEMS) [83], outdoor equipment, and furniture. They come in a variety of sizes, shapes, and materials. These structures are commonly composed of developable surfaces because of planar manufacturing or storage requirements. While developable surfaces can be rigorously described by mathematics [10, 15, 16] and design guidelines for specific deployable applications exist [84], limited investigation of guidelines for material selection for deployable mechanisms has been conducted. Characterizing the elastic bending and strength efficiency shape factors of CAs provides material selection guidelines that can be incorporated into bending applications and deployable structure design.

CAs are particularly suited for transitioning curved-fold origami into thicker materials to create mechanisms and structures. This is because curved-fold origami results in a combination of curved surfaces joined by creases which Solomon [14] classifies as a general developable surface. While much of the field of curved folding is unexplored, several recent papers have presented design guidelines utilizing principles from optics for the creation of developable curved-fold designs [1, 33, 35]. The transition between paper-thin curved-fold origami to thicker engineering materials presents a unique set of challenges, including the high bending stresses introduced by the large possible curvatures of the surfaces. The majority of origami designs that have been transitioned to engineering materials fall into the category of rigidly foldable [85] as seen in the self-folding design of Felton et al. [45], where the panels do not flex or bend, thus facilitating physical construction. CAs can provide a path to creating curved-fold designs in thick materials [29].

3.2.3 Shape Factors and Material Selection

The concept of dimensionless shape factors and how they can be incorporated into material selection was first investigated by Ashby [76]. These shape factors enable designers to see the effect of shape on effective material properties. For example, an extruded aluminum I-beam can be considered a "new"material that is stiffer and stronger than a square aluminum beam. Shape factors describe how the material properties, such as modulus and yield strength, can be modified to achieve the effective properties of the "new"material. This chapter will examine two shape factors in particular. The elastic bending shape factor for bending about a particular axis, ϕ_B^e, is used to describe relative stiffness gain for a shape as compared to a reference shape of the same area and material. This shape factor can be expressed as [79]

$$\phi_B^e = \frac{S}{S_o} \tag{3.1}$$

where S is the stiffness of the shape and S_o is the stiffness of the reference shape. For example, steel I-beams can have elastic bending shape factors ranging from approximately 1 to 65 [86]. This can be interpreted as the I-beam being a "new"material which has an effective modulus that is 1 to 65 times as stiff as the modulus of the material for a square beam of an equivalent cross-sectional area.

Another shape factor, the strength efficiency shape factor ϕ_B^f, is a measure of how much stronger a shape is in bending compared to a reference shape of the same area and material. The strength efficiency shape factor is described [79] by

$$\phi_B^f = \frac{M_{max}}{M_{o,max}} \tag{3.2}$$

where M_{max} is the bending moment at failure of the shape and $M_{o,max}$ is the bending moment at failure of the reference shape. Similarly, an I-beam made of aluminum of cross-sectional area, A, with a strength efficiency shape factor of 5 can be considered a "new"material with an effective yield strength 5 times as large as the yield strength of a square aluminum beam of the same cross-sectional area.

Shape factors have been characterized for many common cross-sectional shapes of beams [79]. Elastic bending shape factors for solid cross sections of circles, squares, and other regular polygons are typically close to one. Elongated, hollow, and I-shaped cross sections can have elastic bending shape factors of 50 or more. It is rare to find real components with shape factors above 65 due to manufacturing constraints and the onset of local buckling as the predominant failure mode [86]. The possible range of shape factors can also vary significantly from material to material. Several methods exist to incorporate shape factors into material selection processes. These include the method developed by Birmingham [87] to link material property charts with shape-efficiency charts, developing material indices (measures of material performance in a specific engineering situation) with shape factors included, and modifying material property charts by plotting a "new"material that is possible with shape factors. [79] The application of material indices to facilitate material selection has recently been introduced into the field origami-inspired structures, as seen in the research by Tolman et al. [88]

3.3 Methods

3.3.1 Compliant Array Geometry

The geometry of CAs can vary greatly as CAs are formed by linking together multiple units of a lamina emergent mechanism or multiple types of lamina emergent mechanisms. In this study

two particular CAs have been chosen to illustrate general methods for CA shape factor analysis. These two CAs also demonstrate how a reduction in out-of-plane bending stiffness can be achieved in particular directions determined by the geometry of the array. The bending stiffness of an array about a particular axis, $K_{array,axis}$, will be defined such that the angular rotation about the axis, Θ, is related to the moment applied across the axis, M, by the equation

$$M = K_{array,axis}\Theta \tag{3.3}$$

Unidirectional CA

The Unidirectional CA is formed with the Outside Lamina Emergent Torsion joint (Outside LET) [89] as the fundamental unit, as illustrated in Figure 3.2. This array maintains a stiff bending axis, the x-axis, which can be nearly as stiff as a solid panel. It also enables a compliant bending axis offset by 90 degrees from the stiff bending axis, the y-axis. Its name, Unidirectional CA, is derived from this property of having one bending direction that sees a marked decrease in stiffness. When a moment is applied about the flexible axis, the y-axis, the four legs function as torsion bars. When a moment is applied about the stiff axis, the x-axis, the fundamental unit's four legs function as bending beams, which can retain much of the original solid panel's stiffness.

The stiffness of the Outside LET unit is characterized using a model similar to the torsion spring model developed by Jacobsen et al. [37] The bending stiffness about the y-axis, k_y, can be expressed using the geometry definitions of Figure 3.2 as

$$k_y = \frac{k_b k_t}{k_b + k_t} \tag{3.4}$$

or if k_b is much greater than k_t (at least two orders of magnitude)

$$k_y = k_t \quad if \;\; k_b \gg k_t \tag{3.5}$$

The spring constant of the torsion legs, k_t, equivalent to a rectangular beam in torsion [52], is expressed as

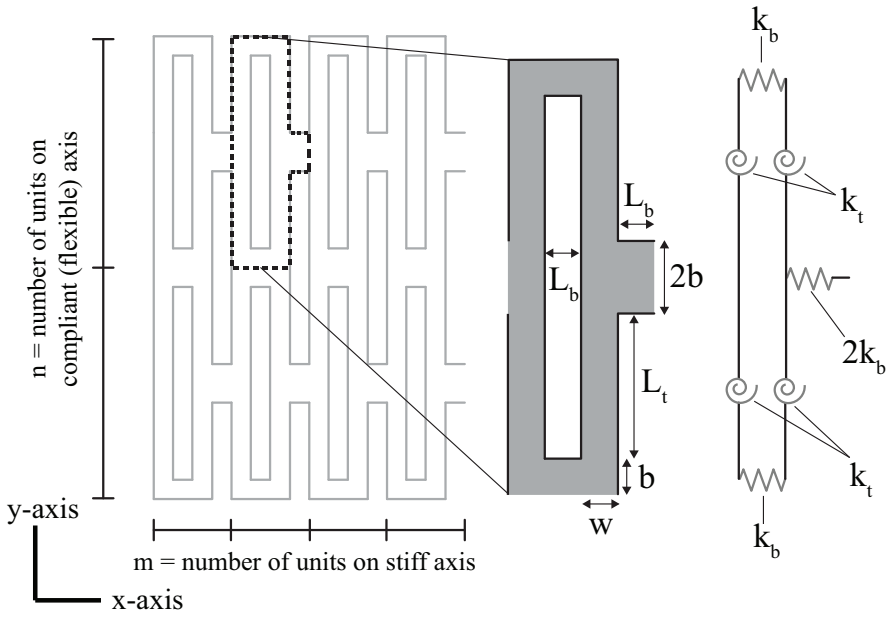

Figure 3.2: The Unidirectional CA geometry and parameters with a detailed fundamental unit and its corresponding spring model for bending across the y-axis.

$$k_t = \frac{Gwt^3\left(\frac{1}{3} - 0.21\frac{t}{w}\left(1 - \frac{t^4}{12w^4}\right)\right)}{L_t} \tag{3.6}$$

where t is the thickness of the sheet, $w \geq t$, and G is the shear modulus. This symbolic expression for the torsional stiffness of a rectangular beam where $w \geq t$ is an approximation of the infinite series solution derived from elasticity theory [52, 90]. Comparisons of the approximate equation solution to the series solution show error of less a half a percent [37]. The spring constant of the bending regions, k_b, is given by

$$k_b = \frac{EI}{L_b} \quad with \quad I = \frac{bt^3}{12} \tag{3.7}$$

where E is Young's modulus. This stiffness is used to relate the moment applied to the joint about the y-axis, M, and the resulting angular deflection of the joint about the y-axis, θ, as

$$M = k_y\theta \tag{3.8}$$

These definitions for the fundamental unit can be extended to the Unidirectional CA by considering each fundamental unit as a torsion spring connected to the neighboring units in parallel

and series. By letting m be the number of units along the x-axis and n be the number of units along the y-axis, the total stiffness of the Unidirectional CA across the y-axis, $K_{uni,y}$, can be expressed as

$$K_{uni,y} = \left(\frac{n}{m}\right) k_y \tag{3.9}$$

As explained in Equation 3.3, the total angular displacement of the array, Θ, is related to the moment applied to the array about the compliant bending axis, M, by

$$M = K_{uni,y}\Theta \tag{3.10}$$

In a similar manner, the rotational stiffness of the fundamental unit about the x-axis, k_x, can be expressed as

$$k_x = \frac{Ew\left(w + \frac{1}{2}L_b\right)t^3}{6\left(4bw + 2wL_t + L_bL_t\right)} \tag{3.11}$$

where E is Young's modulus. This expression was derived by accounting for each leg of the fundamental unit as a spring in bending (as none of the legs act in torsion for loading across the x-axis) and combining the legs together as springs in parallel and series to find an expression for the total rotational stiffness for bending around the x-axis. The form for the bending stiffness of each leg resembles Equation 3.7, with variation in the expression for I and in the denominator of the stiffness expression for k_b corresponding to the geometry of each leg.

The total stiffness of the Unidirectional CA across the x-axis can be expressed as

$$K_{uni,x} = \left(\frac{m}{n}\right) k_x \tag{3.12}$$

where once again m is the number of units along the y-axis and n is the number of units along the x-axis.

Bidirectional CA

The Bidirectional CA uses a variation of the Outside LET joint as its fundamental unit to provide a reduction in stiffness in two orthogonal directions as shown in Figure 3.3. Across the

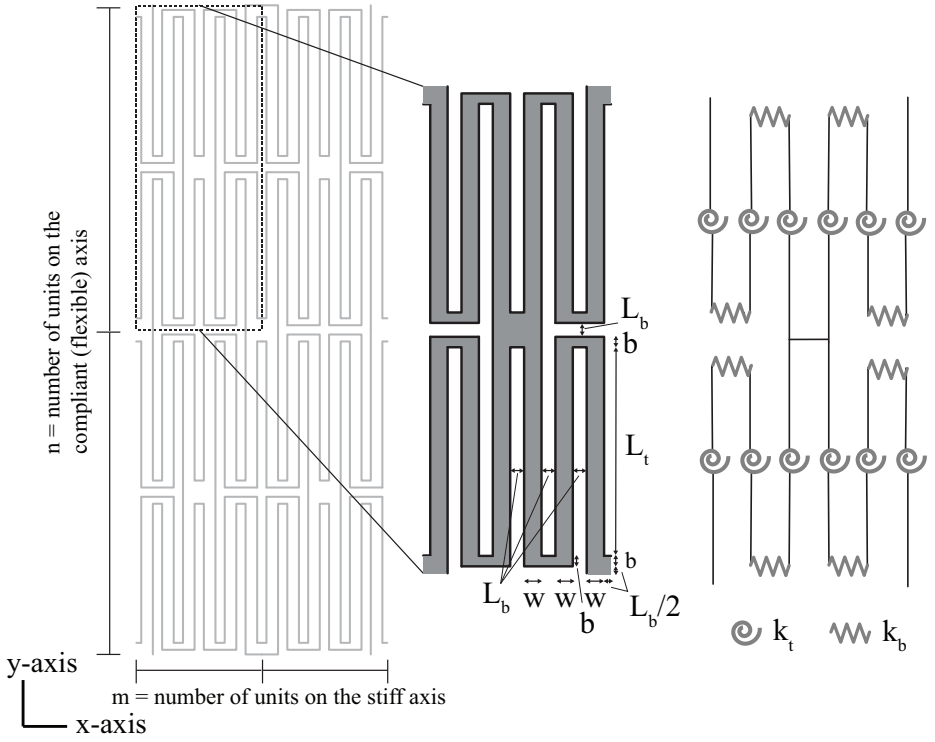

Figure 3.3: Bidirectional CA geometry and parameters with a detailed fundamental unit and its corresponding spring model for bending across the y-axis.

compliant bending axis, the y-axis, the legs of the fundamental units function as torsion bars while across the stiffer bending axis, the x-axis, they are placed in bending.

The bending stiffness of the fundamental unit about the y-axis, k_y, for the Bidirectional CA can be expressed as

$$k_y = \frac{k_b k_t}{3k_b + 2k_t} \tag{3.13}$$

or if k_b is at least two orders of magnitude greater than k_t

$$k_y = \frac{k_t}{3} \quad if \;\; k_b \gg k_t \tag{3.14}$$

where k_t and k_b are described by Equation 3.6 and Equation 3.7. The middle portion of the fundamental unit is considered to be rigid for bending about the y-axis as it is stiffer than all other areas of the joint in this bending mode. Equation 3.8 describes the relationship of the angular deflection of the unit, the bending stiffness of the unit, and the moment applied to the unit.

The total stiffness of the Bidirectional CA across the y-axis, $K_{bi,y}$, can be expressed as

$$K_{bi,y} = \left(\frac{n}{m}\right) k_y \tag{3.15}$$

where m represents the number of units along the x-axis and n represents the number of units along the y-axis.

By modeling each leg of the joint as a spring, the expression for the bending stiffness of the fundamental unit of the Bidirectional CA across the x-axis, k_x, is

$$k_x = \frac{Ew\left(w + \frac{1}{2}L_b\right)t^3}{6\left(2wb + 3L_t\left(L_b + 2w\right) + 2w\left(L_b + 2b\right)\right)} \tag{3.16}$$

where E is Young's modulus. Similar to the way Equation 3.11 was derived, this expression was found by considering each leg of the fundamental unit to be in bending, calculating the bending stiffness of each leg as is shown in Equation 3.7, and then combining the stiffnesses of all the legs together using rules for springs in parallel and series to find an equivalent total stiffness for the fundamental unit. It should be noted that the middle portion of the Bidirectional CA is not considered to be rigid for computing the stiffness across the x-axis as it was for computing the stiffness across the y-axis. This is because the middle portion is no longer much stiffer compared to the other areas of the joint. The total stiffness of the Bidirectional CA across the x-axis, $K_{bi,x}$, can be expressed as

$$K_{bi,x} = \left(\frac{m}{n}\right) k_x \tag{3.17}$$

Examples of the Unidirectional and Bidirectional arrays were created through laser cutting 0.292 cm (0.115 in) thick acrylic and 0.114 cm (0.045 in) thick steel. These are shown in Figure 3.4.

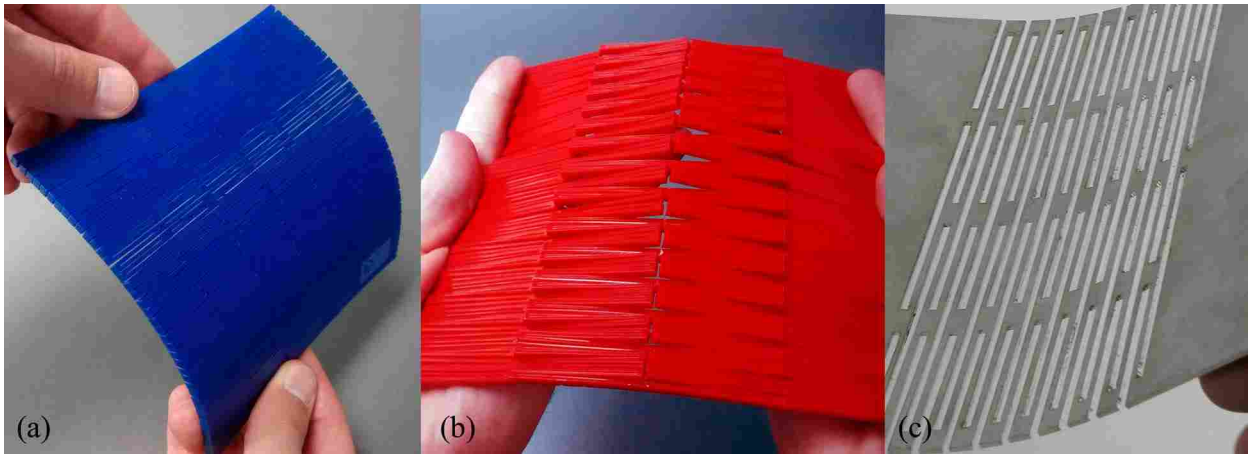

Figure 3.4: Examples of (a) Unidirectional CA in acrylic bending about its y (compliant) axis, (b) Bidirectional CA in acrylic bending about its x (stiff) axis, and (c) Unidirection CA in steel bending about its y (compliant) axis.

3.3.2 Analytical Characterization of Bending Shape Factors and Strength Efficiency Factors

Bending Shape Factors

The shape factor and strength efficiency shape factor for the Unidirectional and Bidirectional CAs can be analytically determined for both the compliant and stiff bending axes. Using the elastic bending shape factor definition from Equation 3.1, the elastic bending shape factor for the Unidirectional array across the y-axis with a moment loading can be expressed as

$$\phi_B^e = \frac{S_y}{S_{o,y}} = \frac{K_{uni,y}}{\frac{EI_{o,y}}{L_{o,y}}} \tag{3.18}$$

where $I_{o,y}$ is the second moment of area for the cross section of the reference shape and is expressed as

$$I_{o,y} = \frac{n\,(4b + 2L_t)\,t^3}{12} \tag{3.19}$$

and $L_{o,y}$ is the length of the reference shape perpendicular to the bending axis and is expressed as

$$L_{o,y} = m\,(2w + 2L_b) \tag{3.20}$$

Typically, elastic bending shape factors are most useful when they are only a function of geometry. To minimize the number of properties affecting the shape factor, Equations 3.4, 3.6, 3.7, 3.9 and

$$G = \frac{E}{2(1+\nu)} \tag{3.21}$$

are combined. Note that Equation 3.21 is only valid for isotropic materials where G is the shear modulus, E is Young's modulus, and ν is Poisson's ratio. Combining these equations results in

$$\phi_B^e = \frac{\frac{6bw(w+L_b)}{(2b+L_t)}\left(\frac{1}{3} - 0.21\left(\frac{t}{w}\right)\left(1-\frac{t^4}{12w^4}\right)\right)}{(1+\nu)\,bL_t + 6L_b w\left(\frac{1}{3} - 0.21\left(\frac{t}{w}\right)\left(1-\frac{t^4}{12w^4}\right)\right)} \tag{3.22}$$

If $k_b \gg k_t$, then the equation simplifies to

$$\phi_B^e = \frac{6w\,(w+L_b)}{(1+\nu)\,L_t\,(2b+L_t)}\left(\frac{1}{3} - 0.21\frac{t}{w}\left(1-\frac{t^4}{12w^4}\right)\right) \tag{3.23}$$

By approximating ν by 0.3, which is common for metals and many isotropic materials [91], this equation can be expressed as

$$\phi_B^e = \frac{4.615w\,(w+L_b)}{L_t\,(2b+L_t)}\left(\frac{1}{3} - 0.21\frac{t}{w}\left(1-\frac{t^4}{12w^4}\right)\right) \tag{3.24}$$

The elastic bending shape factor about the x-axis for the Unidirectional array can be found in a similar manner as follows

$$\phi_B^e = \frac{S_x}{S_{o,x}} = \frac{K_{uni,x}}{\frac{EI_{o,x}}{L_{o,x}}} \tag{3.25}$$

where

$$I_{o,x} = \frac{m\,(2w+2L_b)\,t^3}{12} \tag{3.26}$$

and

$$L_{o,x} = n\,(4b+2L_t) \tag{3.27}$$

Table 3.1: Bending Shape Factors for CAs with $w \geq t$.

		Unidirectional CA	
Bending about y-axis,	ϕ_B^e	In general,	$\frac{\frac{6bw(w+L_b)}{(2b+L_t)}\left(\frac{1}{3}-0.21\left(\frac{t}{w}\right)\left(1-\frac{t^4}{12w^4}\right)\right)}{(1+\nu)bL_t+6L_bw\left(\frac{1}{3}-0.21\left(\frac{t}{w}\right)\left(1-\frac{t^4}{12w^4}\right)\right)}$
		if $k_b \gg k_t$	$\frac{6w(w+L_b)}{(1+\nu)L_t(2b+L_t)}\left(\frac{1}{3}-0.21\frac{t}{w}\left(1-\frac{t^4}{12w^4}\right)\right)$
		if $\nu = 0.3$ and $k_b \gg k_t$	$\frac{4.615w(w+L_b)}{L_t(2b+L_t)}\left(\frac{1}{3}-0.21\frac{t}{w}\left(1-\frac{t^4}{12w^4}\right)\right)$
Bending about x-axis,	ϕ_B^e	$\frac{w(2w+L_b)(2b+L_t)}{(w+L_b)(4bw+2wL_t+L_bL_t)}$	
		Bidirectional CA	
Bending about y-axis,	ϕ_B^e	In general,	$\frac{\frac{6bw(w+L_b)}{(2b+L_t+L_b)}\left(\frac{1}{3}-0.21\left(\frac{t}{w}\right)\left(1-\frac{t^4}{12w^4}\right)\right)}{(1+\nu)bL_t+4L_bw\left(\frac{1}{3}-0.21\left(\frac{t}{w}\right)\left(1-\frac{t^4}{12w^4}\right)\right)}$
		if $k_b \gg k_t$	$\frac{6w(w+L_b)}{(1+\nu)L_t(2b+L_t+L_b)}\left(\frac{1}{3}-0.21\frac{t}{w}\left(1-\frac{t^4}{12w^4}\right)\right)$
		if $\nu = 0.3$ and $k_b \gg k_t$	$\frac{4.615w(w+L_b)}{L_t(2b+L_t+L_b)}\left(\frac{1}{3}-0.21\frac{t}{w}\left(1-\frac{t^4}{12w^4}\right)\right)$
Bending about x-axis,	ϕ_B^e	$\frac{w(2w+L_b)(2b+L_t+L_b)}{3(w+L_b)(6bw+2wL_b+3L_tL_b+6L_tw)}$	

Substitutions from Equations 3.11 and 3.12 allow the shape factor about the x-axis for the Unidirectional array in bending to be written as a function of geometry as

$$\phi_B^e = \frac{w\,(2w+L_b)\,(2b+L_t)}{(w+L_b)\,(4bw+2wL_t+L_bL_t)} \tag{3.28}$$

The procedure for finding the elastic bending shape factor for the Bidirectional array is similar to that of the Unidirectional array. Similarly, elastic bending shape factors can be written for both arrays when $t \geq w$ by swapping t and w in Eq. 3.6 during the derivation. The elastic bending shape factors for both arrays are summarized in Table 3.1 for $w \geq t$ and in Table 3.2 for $t \geq w$.

Table 3.2: Bending Shape Factors for CAs with $t \geq w$.

		Unidirectional CA
Bending about y-axis, ϕ_B^e	In general,	$\frac{\frac{6bw^3(w+L_b)}{(2b+L_t)}\left(\frac{1}{3}-0.21\left(\frac{w}{t}\right)\left(1-\frac{w^4}{12t^4}\right)\right)}{(1+\nu)bL_tt^2+6L_bw^3\left(\frac{1}{3}-0.21\left(\frac{w}{t}\right)\left(1-\frac{w^4}{12t^4}\right)\right)}$
	if $k_b \gg k_t$	$\frac{6w^3(w+L_b)}{(1+\nu)L_tt^2(2b+L_t)}\left(\frac{1}{3}-0.21\frac{w}{t}\left(1-\frac{w^4}{12t^4}\right)\right)$
	if $\nu = 0.3$ and $k_b \gg k_t$	$\frac{4.615w^3(w+L_b)}{L_tt^2(2b+L_t)}\left(\frac{1}{3}-0.21\frac{w}{t}\left(1-\frac{w^4}{12t^4}\right)\right)$
Bending about x-axis, ϕ_B^e		$\frac{w(2w+L_b)(2b+L_t)}{(w+L_b)(4bw+2wL_t+L_bL_t)}$

		Bidirectional CA
Bending about y-axis, ϕ_B^e	In general,	$\frac{\frac{6bw^3(w+L_b)}{(2b+L_t+L_b)}\left(\frac{1}{3}-0.21\left(\frac{w}{t}\right)\left(1-\frac{w^4}{12t^4}\right)\right)}{(1+\nu)bL_tt^2+4L_bw^3\left(\frac{1}{3}-0.21\left(\frac{w}{t}\right)\left(1-\frac{w^4}{12t^4}\right)\right)}$
	if $k_b \gg k_t$	$\frac{6w^3(w+L_b)}{(1+\nu)L_tt^2(2b+L_t+L_b)}\left(\frac{1}{3}-0.21\frac{w}{t}\left(1-\frac{w^4}{12t^4}\right)\right)$
	if $\nu = 0.3$ and $k_b \gg k_t$	$\frac{4.615w^3(w+L_b)}{L_tt^2(2b+L_t+L_b)}\left(\frac{1}{3}-0.21\frac{w}{t}\left(1-\frac{w^4}{12t^4}\right)\right)$
Bending about x-axis, ϕ_B^e		$\frac{w(2w+L_b)(2b+L_t+L_b)}{3(w+L_b)(6bw+2wL_b+3L_tL_b+6L_tw)}$

Strength Efficiency Shape Factors

The strength efficiency shape factor as defined in Equation 3.2 can be found for a moment load across the y-axis for the Unidirectional CA with the following procedure. Using standard mechanics equations, the maximum bending moment of the reference panel, $M_{o,max}$, can be expressed as

$$M_{o,max} = \frac{\sigma_y I_{o,y}}{c} \quad with \quad I_{o,y} = \frac{n\,(4b+2L_t)\,t^3}{12} \tag{3.29}$$

where c is the distance furthest from the neutral axis of the cross section of the panel and σ_y is the yield stress of the material.

The maximum moment of the Unidirectional CA about the y-axis, $M_{max,y}$, is equal to the maximum moment that one torsion bar of the fundamental unit can withstand before failure multiplied by $2n$, as the maximum moment of the entire array is divided into load paths through $2n$

torsion bars. This reasoning holds only when using ductile materials. With ductile materials the stress concentrations at the joints between the torsion and bending regions of the fundamental units can be disregarded as localized strengthening occurs from plastic strain. Thus for ductile materials the maximum moment the CA can withstand before failure can be expressed as [92]

$$M_{max,y} = 2n\tau Q \quad with \quad Q = \frac{8\left(\frac{wt}{4}\right)^2}{3\left(\frac{w}{2}\right)+1.8\left(\frac{t}{2}\right)} \tag{3.30}$$

where τ is the maximum shear stress of the material and $w \geq t$. If a brittle material is used to construct the CA, an appropriate stress concentration factor should be applied which will in effect reduce the value of τ.

Substitution of Equations 3.29 and 3.30 into Equation 3.2 results in

$$\phi_B^f = \frac{2n\tau Q}{\frac{\sigma_y I_{o,y}}{c}} \tag{3.31}$$

For this array $c = \frac{t}{2}$ and the approximation of $\tau = 0.577\sigma_y$ [92] can be used to simplify the equation to contain only geometric factors resulting in

$$\phi_B^f = \frac{0.577nQt}{I_{o,y}} \tag{3.32}$$

Further substitution for $I_{o,y}$ and Q and simplifying gives the following expression of the strength efficiency shape factor for out-of-plane bending about the y-axis of the Unidirectional array where $w \geq t$.

$$\phi_B^f = \frac{1.154w^2}{(w+0.6t)(2b+L_t)} \tag{3.33}$$

The strength efficiency shape factor for bending about the x-axis with a moment load for the Unidirectional array can similarly be found. The maximum moment of the reference panel, $M_{o,max}$, can be expressed as

$$M_{o,max} = \frac{\sigma_y I_{o,x}}{c} \quad with \quad I_{o,x} = \frac{m(2w+2L_b)t^3}{12} \tag{3.34}$$

Table 3.3: Strength Efficiency Shape Factors for CAs with $w \geq t$.

		Unidirectional	Bidirectional
Strength Efficiency about y-axis	(ϕ_B^f)	$\frac{1.154w^2}{(w+0.6t)(2b+L_t)}$	$\frac{0.3846w^2}{(w+0.6t)(2b+L_t+L_b)}$
Strength Efficiency about x-axis	(ϕ_B^f)	$\frac{w}{w+L_b}$	$\frac{w}{3(w+L_b)}$

where c is the distance furthest from the neutral axis of the cross section of the panel and σ_y is the yield stress of the material. The maximum moment of the Unidirectional CA about the x-axis, $M_{max,x}$, is equal to $2m$ times the maximum moment which the bending bars of the fundamental unit can withstand before failure when using ductile materials. Beam mechanics equations can be used to express $M_{max,x}$ as

$$M_{max,x} = \frac{2m\sigma_y I_{u,x}}{c_u} \quad with \quad I_{u,x} = \frac{wt^3}{12} \tag{3.35}$$

where σ_y is the yield stress of the material and c_u is the distance furthest from the neutral axis of the cross section of the bending portion of the fundamental unit. Substituting Equations 3.34 and 3.35 into Equation 3.2 results in

$$\phi_B^f = \frac{2mI_{u,x}c}{I_{o,x}c_u} \tag{3.36}$$

Making further substitutions for $I_{u,x}$ and $I_{o,x}$ and noting that $c = c_u = \frac{t}{2}$ for the array, the strength efficiency shape factor for the Unidirectional array with moment load about the x-axis and $w \geq t$ can be expressed in geometrical parameters as

$$\phi_B^f = \frac{w}{w+L_b} \tag{3.37}$$

A similar procedure can be carried out to find the strength efficiency shape factors of the Bidirectional array about the x and y axes. In addition, expressions for strength efficiency factors for both arrays when $t \geq w$ can be found by swapping t and w in Eq. 3.30 during the derivation. The results are summarized in Table 3.3 for $w \geq t$ and in Table 3.4 for $t \geq w$.

Table 3.4: Strength Efficiency Shape Factors for CAs with $t \geq w$.

		Unidirectional	Bidirectional
Strength Efficiency about y-axis	(ϕ_B^f)	$\frac{1.154w^2}{(t+0.6w)(2b+L_t)}$	$\frac{0.3846w^2}{(t+0.6w)(2b+L_t+L_b)}$
Strength Efficiency about x-axis	(ϕ_B^f)	$\frac{w}{w+L_b}$	$\frac{w}{3(w+L_b)}$

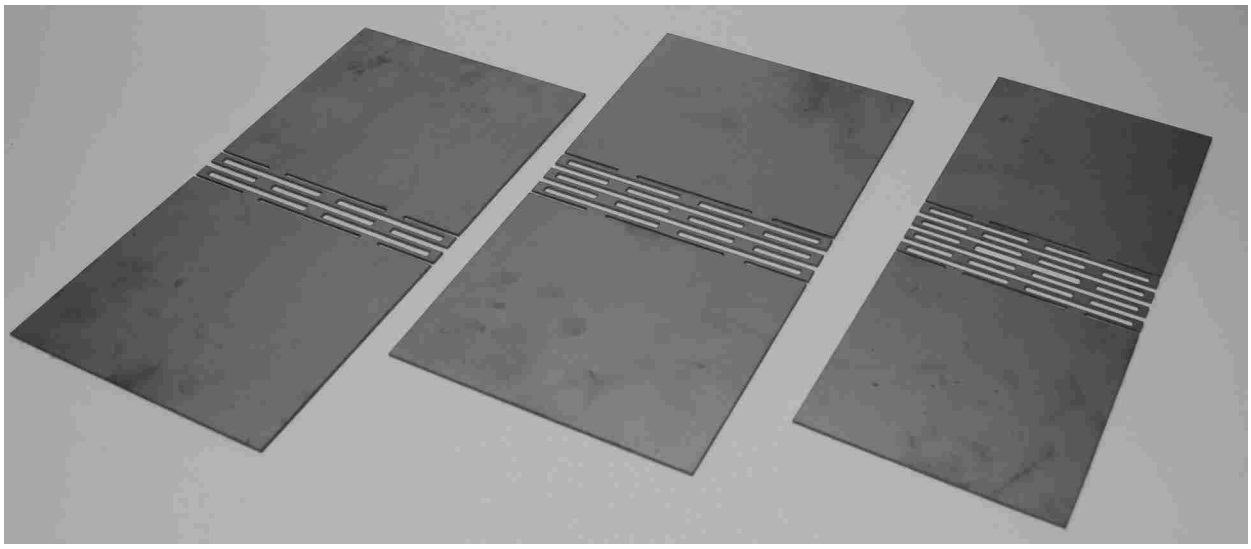

Figure 3.5: Three stainless steel prototypes of the Unidirectional CA: left 2x2 array, middle 3x2 array, right 4x2 array.

3.3.3 Experimental Verification

Physical testing of the Unidirectional CA for bending about the y-axis was conducted to verify the method used to derive the shape factors described in this chapter. Three unidirectional CA patterns were cut into 1.22 mm (0.048 in) thick stainless steel sheet using a water jet and described by the number of fundamental units used in the array (*mxn*). Two prototypes, the 2x2 array and the 3x2 array, had all geometry of a fundamental unit the same (with small variation due to tolerances on the water jet). The third prototype was the largest array, a 4x2 array, with different geometry parameters than the first two prototypes. These prototypes are shown in Figure 3.5.

A four-point bending test performed on a hydraulic tensile test machine (Instron Model 1321 with a 200 lb load cell) was used to approximate a constant moment loading of the CAs

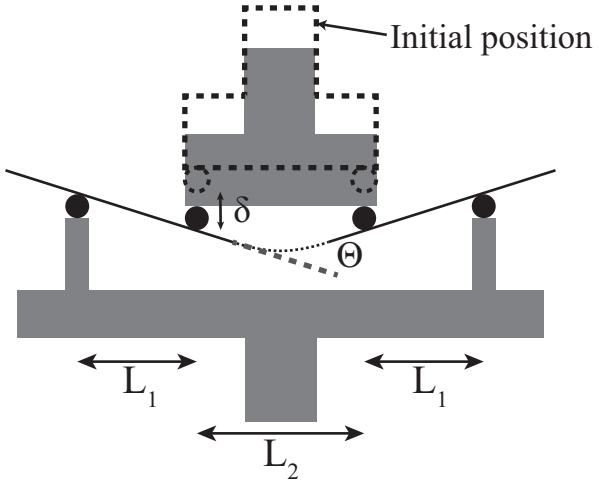

Figure 3.6: Four point bending test parameters.

across the y-axis. The rotational stiffness for each of the patterns, $K_{uni,y}$, was calculated using the elastic portion of the force displacement data from each of the tests as described next.

The moment imposed on the array by the four-point bending test, M_{4point}, can be calculated as follows

$$M_{4point} = \frac{PL_1}{2} \tag{3.38}$$

where P is the measured applied force and L_1 is the length between the outside roller and closest middle roller, as shown in Figure 3.6.

The rotational deflection was calculated by assuming the stainless steel plate area without the CA to be rigid. This assumption is only appropriate when the bending stiffness of the CA is much less than that of the plate (a large shape factor), as is the case for each of the three geometries used in the prototypes. With this assumption the rotational deflection of the CA, Θ, can be computed from the measured linear deflection, δ, using the following formula derived from the diagram in Figure 3.6.

$$\Theta = 2\sin^{-1}\frac{\delta}{L_1} \tag{3.39}$$

where L_1 is the length between the outside roller and closest middle roller.

Using Eqs. 3.38 and 3.39 and fitting a linear line to a plot of M_{4point} and Θ gives the stiffness of the array, $K_{uni,y}$.

The reference stiffness of a panel without the CA, S_o, is calculated by Eqs. 3.18, 3.19, and 3.20. The flexural modulus, E, used in this equation was obtained for this particular stainless steel through a four-point bending test on a solid panel with the following equation derived from deflection equations from the shear moment diagrams:

$$E = \left(\frac{P}{\delta}\right) \frac{L_1^2(2L_1 + 3L_2)}{12I_s} \tag{3.40}$$

where P is the measured applied force, L_1 is the length between the outside and closest middle roller, L_2 is the distance between the two middle rollers, I_s is the second moment of area for the sample in bending, and δ is the measured deflection. The measured modulus was $E = 193$ GPa (28.0 Mpsi).

The experimental bending shape factors can now be computed using Eq. 3.18. The experimental shape factors for each of the three CAs are shown in Table 3.5 along with the analytically determined shape factors using the general shape factor equations from Table 3.1.

The strength efficiency shape factor was also measured experimentally for the three arrays. The moment at failure, $M_{max,y}$ was estimated from the recorded force-deflection plots by identifying the approximate force at yield and using Eq. 3.38. The maximum moment of the reference panel was calculated using Eq. 3.29 where σ_y, the yield stress, was measured from a four-point bend test on a solid panel using Eqs. 3.29 and 3.38. The measured yield stress was 254 MPa (36.9 kpsi) for the stainless steel.

The experimental strength efficiency shape factors were computed using Eq. 3.2 for each of the three CAs. These experimental strength efficiency factors are shown in Table 3.5 with the analytically determined shape factors computed from Table 3.3. The analytical and experimental results agree reasonably well.

Table 3.5: Comparing experimentally determined and analytical shape factors for stainless steel Unidirectional CA prototypes.

			Experimental	Analytical
2x2 array	Bending about y-axis	ϕ_B^e	0.010	0.014
	Strength Efficiency about y-axis	ϕ_B^f	0.049	0.055
3x2 array	Bending about y-axis	ϕ_B^e	0.011	0.013
	Strength Efficiency about y-axis	ϕ_B^f	0.051	0.055
4x2 array	Bending about y-axis	ϕ_B^e	0.008	0.010
	Strength Efficiency about y-axis	ϕ_B^f	0.039	0.043

3.4 Results and Discussion

3.4.1 CA Shape Factor Analysis

The elastic bending shape factors for the Unidirectional and Bidirectional arrays are summarized by the geometric parameters in Table 3.1. The strength efficiency shape factors are summarized for these two arrays in Table 3.3. Careful examination of the tables shows that the elastic bending shape factors for bending about the y-axis for the Unidirectional and Bidirectional CAs are nearly equivalent. The marked difference between the two arrays can be seen in bending about the x-axis where the Bidirectional CA contains a larger denominator and thus smaller bending shape factor than the Unidirectional CA.

These shape factor expressions also show the independence of the shape factor from the scale of the shape. Multiplying all the geometric parameters by a constant scaling factor creates no variation in the expressions of the shape factors. Similarly, adding elements to the array in parallel and series as described by m and n has no effect on the shape factor as the shape of the fundamental unit remains the same. Only changing the ratio of geometric parameters to each other, and consequently changing the shape of the fundamental unit, causes the shape factor to change in value. This is seen in the results from the experimental prototypes as shown in Table 3.5. The 2x2 and 3x2 arrays have nearly equivalent shape factors with small variation due to manufacturing tolerances that effected the shape slightly. The 4x2 array has different ratios of the geometric

parameters and thus a different shape of the fundamental unit than the other prototypes. This differing shape is reflected in the change in the shape factor value.

It should be noted, as a small I-beam and larger scaled I-beam may share the same shape factor, the values of the stiffness and the load they can carry are not the same. Similarly, a CA with a larger scaled fundamental unit will have a larger stiffness and load carrying capacity than a CA with an equivalent shape factor on a smaller scale. The efficiency of the shapes in modifying the stiffness and strength are the same. This relationship is clearly seen in Equations 3.1 and 3.2 where the scale factors cancel out in the right side of the equations. However, if the equations are rearranged to find the stiffness and strength of a shape at a particular scale, the scale factor dictates the magnitude of the values.

A range of shape factor values for CAs made of metals and polymers were generated by placing limits based on current manufacturing techniques and tolerances on the geometrical parameters used to define the arrays.

Laser cutting was found to be one of the most effective manufacturing methods in achieving the largest range of limits for these types of arrays. The parameters were then varied within these limits to establish a range of shape factors. In addition, a constraint was imposed to ensure the torsion bars would deflect in the intended torsion mode rather than a bending mode. This constraint can be described as $k_{b,uni} > 2k_t$ for the Unidirectional array and $k_{b,bi} > 2k_t$ for the Bidirectional array. In these constraints k_t is described by Eq. 3.6 and $k_{b,uni}$ and $k_{b,bi}$ are the bending stiffness corresponding to the torsion bars for the Unidirectional array and Bidirectional array, respectively, and can be calculated for $w \geq t$ as

$$k_{b,uni} = \frac{E\,(4b + 2L_t)\,t^3}{12w} \tag{3.41}$$

$$k_{b,bi} = \frac{E\,(4b + 2L_t + 2L_b)\,t^3}{12w} \tag{3.42}$$

The constraints can also be formulated for $t \geq w$ by swapping t and w in the above expressions and in Eq. 3.6.

An optimization routine was used to generate the extreme values for the shape factors with geometry still in the manufacturable ranges and satisfying the model assumption constraint.

Table 3.6: Range of manufacturable shape factors, geometrical parameter limits, and constraints for metals and polymers.

Unidirectional Array Shape Factor Ranges				
Geometric Parameters	Limits (m)	Constraint	Shape Factor Ranges	
L_b	0.0003 to 0.01	$k_{b,uni} > 2k_t$	ϕ_B^e about y-axis	1.26e-5 to 0.964
b	0.0015 to 0.01		ϕ_B^e about x-axis	0.137 to 0.984
w	0.0015 to 0.01		ϕ_f^e about y-axis	0.0023 to 0.822
L_t	0.0003 to 0.05		ϕ_f^e about x-axis	0.131 to 0.971
t	0.0001 to 0.015			
Bidirectional Array Shape Factor Ranges				
Geometric Parameters	Limits (m)	Constraint	Shape Factor Ranges	
L_b	0.0003 to 0.01	$k_{b,bi} > 2k_t$	ϕ_B^e about y-axis	1.25e-5 to 0.9837
b	0.0015 to 0.01		ϕ_B^e about x-axis	0.018 to 0.210
w	0.0015 to 0.01		ϕ_f^e about y-axis	6.83e-4 to 0.2710
L_t	0.0003 to 0.05		ϕ_f^e about x-axis	0.044 to 0.324
t	0.0001 to 0.015			

Table 3.6 lists the imposed limits, constraint equation, and the resulting shape factor values for a range of manufacturable arrays. It was seen that the length of the torsion bar, L_t, played the most dramatic role in determining the reduction of stiffness in bending about the y-axis. This was expected as L_t, most easily seen in the simplified shape factor equations, appears as a squared term in the denominator of the elastic bending shape factor expression about the y-axis whereas other parameters appear in a linear form. Similarly, when considering the strength efficiency shape factor for bending about the y-axis it is expected and was found that the parameter w, the width of the torsion bar, has the most dramatic impact in preserving bending strength.

Besides establishing the extreme values for the shape factors with a optimization routine, Latin hypercube sampling [93] of the five geometric parameters of the arrays was used to generate a visual depiction of the design space for both bending and strength efficiency factors. This space is shown in Figure 3.7 for bending about both the y and x axes for the Unidirectional array and in Figure 3.8 for the Bidirectional array.

These plots for the elastic bending shape factors and strength efficiency factors show that while the stiffness in a particular bending direction can be decreased by using the Unidirectional and Bidirectional arrays, the bending strength for that direction is also decreased. It is also clear

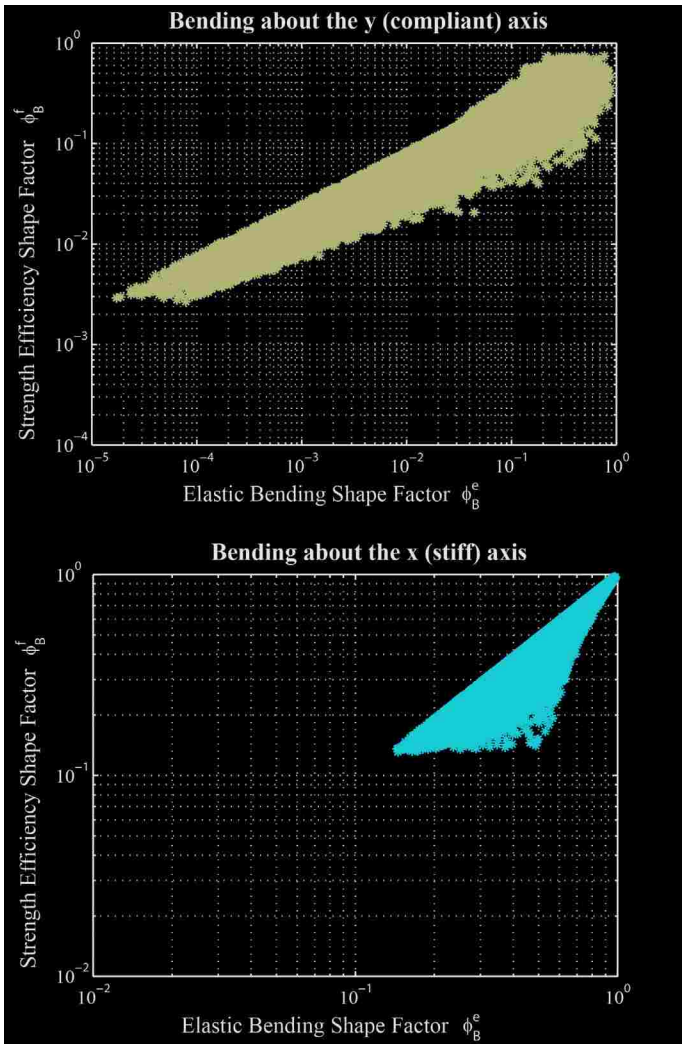

Figure 3.7: Shape Factor Design Space for Unidirectional Array.

in the plots that the x-direction bending shape factor is smaller for the Bidirectional array than the Unidirectional array.

3.4.2 Material Selection with CAs

The shape factors for the Unidirectional and Bidirectional CAs can be used in conjunction with Ashby charts of material properties to understand how the CA geometry affects the effective material properties of a component. Because CAs are generally employed to reduce bending stiffness, charts which include stiffness on at least one axis are most applicable for CA design. For example if a designer is concerned about mass and bending stiffness, the chart of Young's

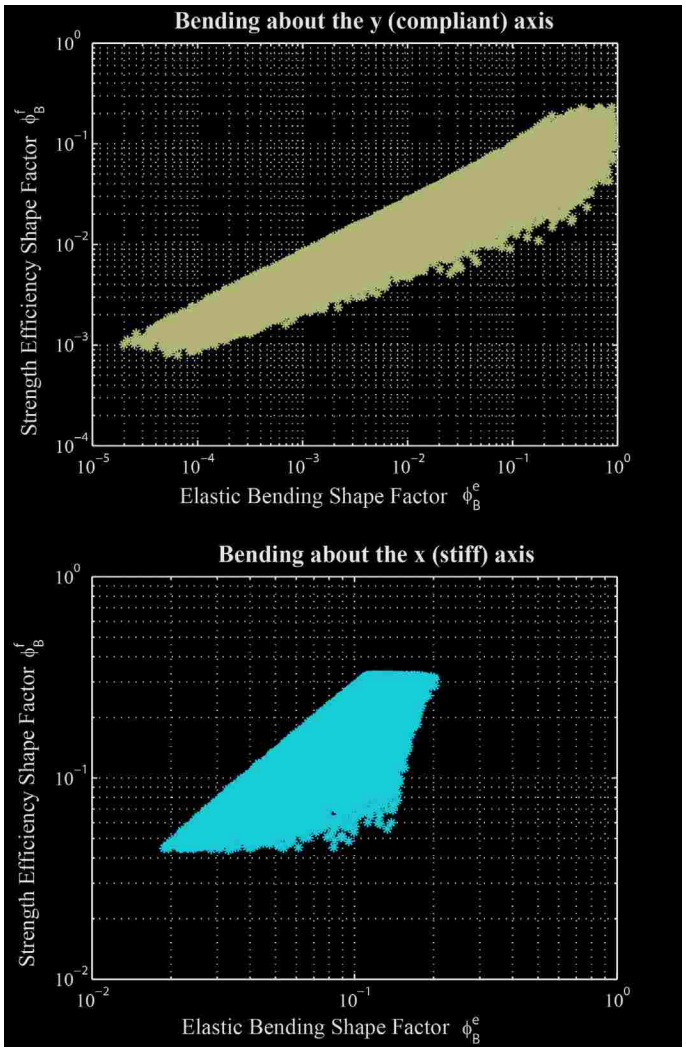

Figure 3.8: Shape Factor Design Space for Bidirectional Array.

Modulus vs. Density can be used as shown in Figure 3.9. To see the effect of the elastic bending shape factor for bending about the y-axis of the Unidirectional CA, the chart can be modified by the corresponding shape factor and reference shape parameters. This is accomplished by scaling the axis with Young's modulus by the constant, $\frac{I_0}{L_0}$, where I_o is the second moment of area of the reference shape about the bending axis and L_o is the length of array perpendicular to the bending axis. By scaling this axis the chart now shows the stiffness of the reference panel, $\frac{EI_o}{L_o}$, for each material on the chart plotted against the density of the material. The shape factor for elastic bending about the y-axis can now be applied to the chart by taking any point of interest and multiplying the y coordinate, (the stiffness of the reference panel), by the shape factor. The resulting point is

the stiffness of the CA made of the same material as the point of interest and with an equivalent cross-sectional area as the reference panel.

Using this method, the material envelopes of the Ashby chart can be expanded to show the effects of the shape factors on the effective material properties. The effects of the shape factor for elastic bending about the y-axis for the Unidirectional array according to the manufacturable range for metals and polymers are shown in Figure 3.10. It should be noted that while these expanded envelopes are accurate for metals and polymers, they are extrapolated to other types of materials, such as ceramics, where the ability to physically manufacture the CA geometry needs to be considered before using the chart.

While scaling the modulus axis of a material property chart by the constant $\frac{EI_o}{L_o}$ presents a straightforward representation of how the stiffness of a panel changes depending on the material and shape factor, it can also be useful to think of the shape factor as representing a "new"material with a modulus, $\phi_B^e E$. With this thought process a designer can look at a material property chart such as that in Figure 3.9 and plot a "new"material with modulus $\phi_B^e E$ and the original density, ρ.

The same type of approach can be employed to show the effect of the strength efficiency shape factor on the material property elastic yield strength for bending applications. The elastic yield strength can be multiplied by the constant $\frac{I_o}{c}$, where I_o is the second moment of area of the reference shape about the bending axis and c is the farthest distance from the neutral axis of the reference shape in bending. This scaling of the axis modifies the chart to show the maximum bending moment carried by the reference shape plotted against the density. The shape factor for strength efficiency can be applied in the same way as with the elastic bending. In addition, the CA again can be considered a "new"material with an effective yield strength of $\phi_B^f \sigma_y$ in bending. The modified Ashby chart of elastic yield strength plotted against density with the effects of the strength efficiency shape factors of the manufacturable range for polymers and metals in bending about the y-axis for the Unidirectional array is shown in Figure 3.11.

To maximize angular deflection of a panel, which is often the impetus for using a CA, a designer is interested in maximizing the ratio of yield strength over bending stiffness. For this case, the Ashby plot for yield strength vs. Young's modulus is used. Figure 3.12 shows how a single point on the chart can be moved about the material property space using various geometries of the Unidirectional CA within the manufacturable range for polymers and metals in bending about the

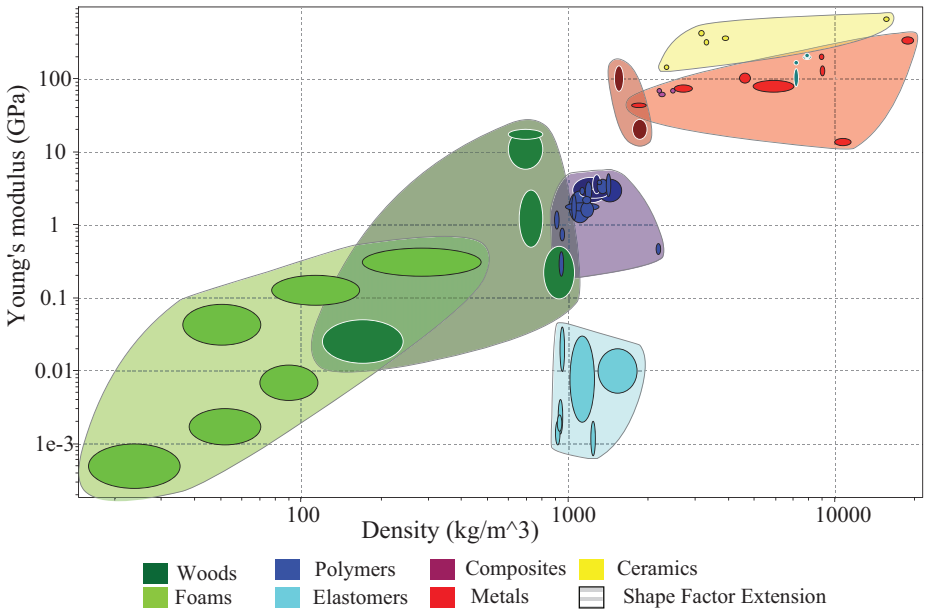

Figure 3.9: The Ashby chart of Young's modulus vs. density.

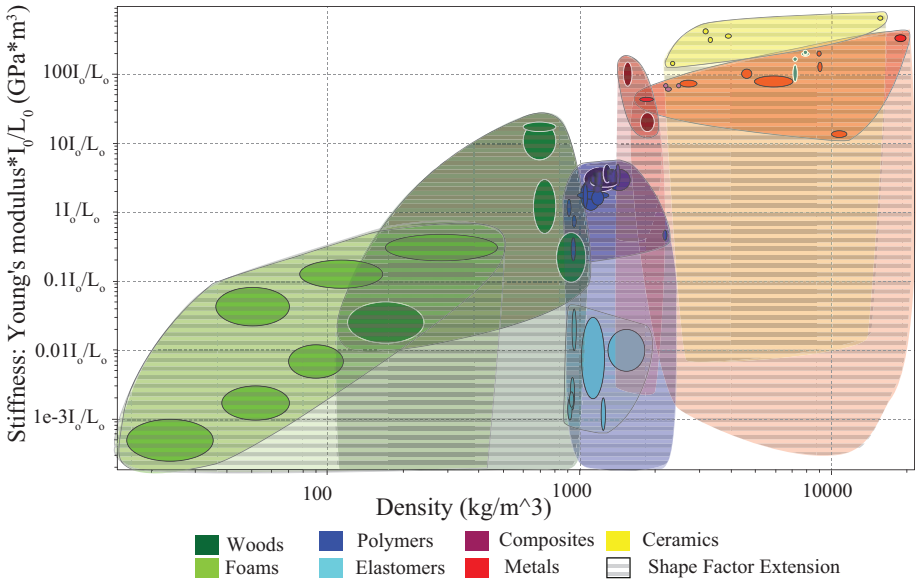

Figure 3.10: The Ashby chart of Young's modulus vs. density modified to show bending stiffness about the y-axis for a panel and shape factor effects for the Unidirectional CA.

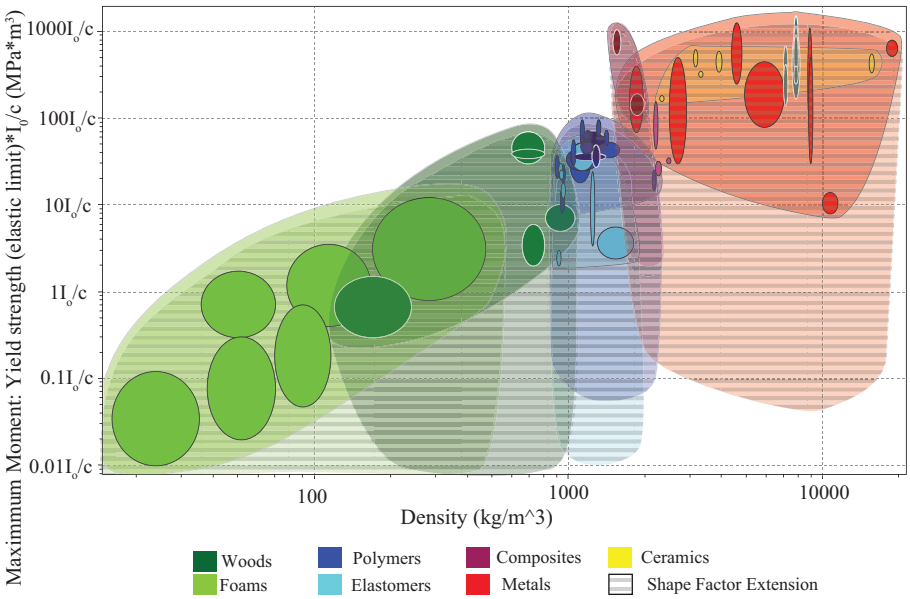

Figure 3.11: The Ashby chart of elastic yield strength vs. density modified to show the effect of the shape factor on the maximum moment withstood in bending about the y-axis for the Unidirectional CA.

y-axis. The possible area to where the point can be moved in the material property space correlates with the possible shape factor space shown in Figure 3.7.

Other material property charts, such as the electrical conductivity vs. modulus chart in Figure 3.13, provide examples of how a reduction in stiffness by a CA can enable a designer to access previously empty sections of the material property charts. The electrical conductivity chart shows a trend where an increase in conductivity is accompanied by an increase in modulus. Here if a designer desires a flexible panel which is still electrically conductive, such as in a flexible circuit, a CA can be used to achieve this decrease in stiffness.

3.5 Conclusions

This chapter demonstrates how the notion of shape factors can be extended to flexible panels characterized by planar geometries. It describes how the specific geometry of two CAs, the Unidirectional and Bidirectional, can be captured in shape factors for elastic bending and strength efficiency. These shape factors help to show the tradeoff between a reduction in bending stiffness and a reduction in bending strength. Realistic ranges of these shape factors were determined and

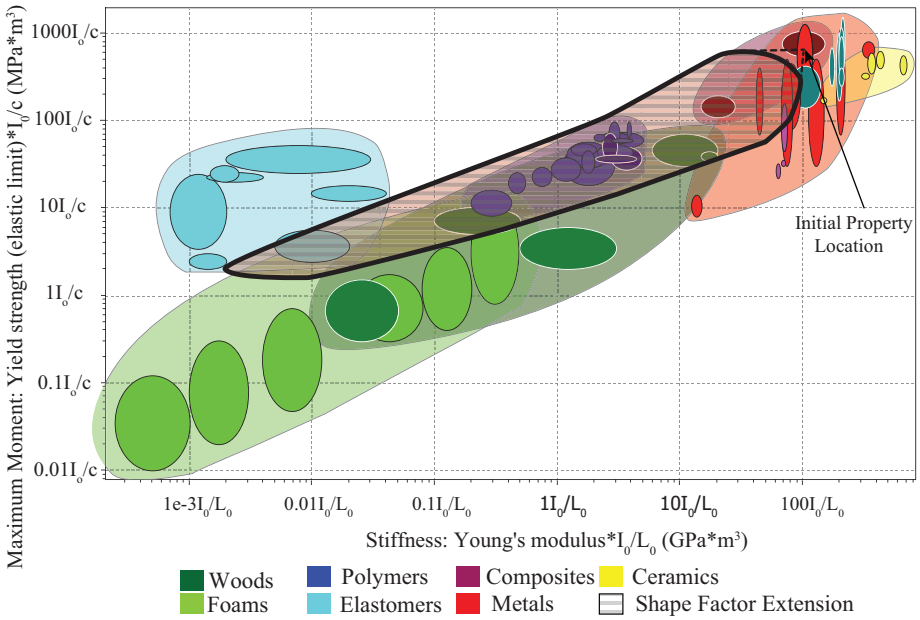

Figure 3.12: The Ashby chart of yield strength vs. Young's modulus with modified axes and examples of how single material property points can be moved about the chart as a consequence of using a Unidirectional CA in bending about the y-axis.

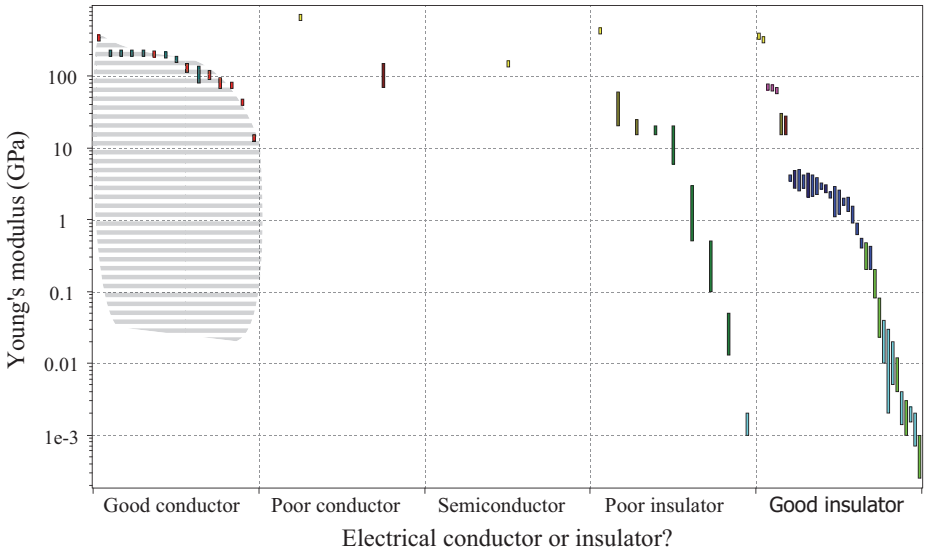

Figure 3.13: The Ashby chart of Young's modulus vs. qualitative electrical conductivity with the shaded region showing shape factor effects on good conductor panels shaped as Unidirectional CAs placed in bending about the y-axis.

plotted on several Ashby material property charts. These charts show the previously inaccessible spaces which now can be accessed through the use of the compliant array. The designer can use the CA to decouple properties which are commonly linearly connected, such as electrical conductivity and stiffness. The expressions for the CA shape factors in conjunction with Ashby material charts provide a succinct way for designers to easily explore the benefits and drawbacks of using Unidirectional and Bidirectional CAs for particular bending applications.

CHAPTER 4. CURVED-FOLDING-INSPIRED DEPLOYABLE COMPLIANT ROLLING-CONTACT ELEMENT (D-CORE)

[1]The past two chapters addressed how thickness can be accommodated and material selection can be informed for curved panels of curved-origami-inspired mechanisms. This chapter begins our exploration of how curved-crease origami and developable-surface principles can be leveraged to enhance the performance of mechanisms and enable the creation of novel mechanisms. We begin by looking at a rolling-contact element (specifically the CORE). By incorporating curved-origami principles into this mechanism's design we add the strengths of origami, such as deployability and the ability to be manufactured from a planar sheet, to the mechanism's capabilities.

4.1 Introduction

This chapter draws upon curved-folding techniques from origami to create a compliant rolling-contact element (CORE) [94] with the capability of being deployed from a planar state to a deployed state. CORE joints are large-displacement angle, compliant, multi-stable, revolute joints [94]. CORE joints and other types of revolute joints have been investigated to mitigate the challenges encountered by traditional pin-joints such as backlash and wear. Wear can intensify undesired motion as the clearance between the pin and the hole increases with use. Traditional bearings present another alternative but can significantly increase cost, weight, and size. The CORE uses compliant flexures that join two cams together, as shown in Figure 4.1. The tension in the flexures holds the cams together as they roll across each other.

While still preserving the desirable properties of CORE joints to reduce undesired motion and wear, deployable CORE (D-CORE) joints enable the joint to be stored in a compact position

[1]This chapter is also published as Nelson, T.G., Lang, R.J., Magleby, S.P., and Howell, L.L., Curved-Folding-Inspired Deployable Compliant Rolling-contact Element (D-CORE), *Mechanism and Machine Theory*, Vol. 96, pp. 225-238, DOI:10.1016/j.mechmachtheory.2015.05.017, 2016 [57].

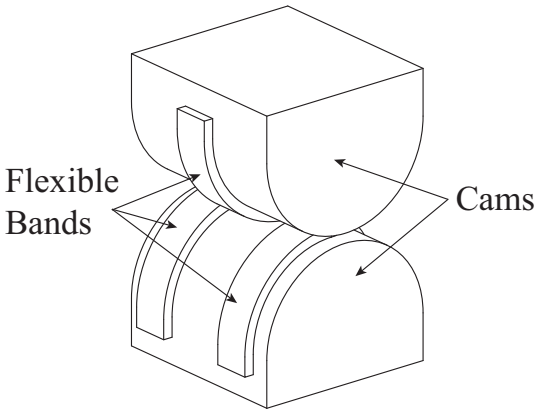

Figure 4.1: A CORE with circular cams.

before and after use. This facilitates use of the joint in applications where space is a constraint before or after the joint is to function. This constraint is commonly seen in spacecraft, aircraft, minimally invasive surgery devices, and stowable furniture. The ability of the D-CORE to be manufactured from a single sheet of material and assembled through folding make it a low cost alternative to a traditional joint. The D-CORE, as well as the CORE, differ from traditional pin joints as the axis of rotation moves during the rotation of the joints. While this prohibits the use of the D-CORE or CORE in some precision movement applications where a fixed axis of rotation is required, the movement of the axis of rotation is calculable enabling predicted motion paths. Another desirable property of one of the D-CORE configurations discussed in this chapter is the ability to be a zero-degree-of-freedom static structure in its stowed, planar state and to transition to a one-degree-of-freedom mechanism in its deployed state. This type of mechanism is known as a metamorphic mechanism [95].

4.2 Background

The use of compliant flexures in the D-CORE and CORE to join two rigid bodies together is reminiscent of a single unit in a Jacob's ladder toy. The D-CORE is created using curved-fold origami techniques to construct the curved surfaces of the cams. This enables the joint to maintain the advantages of the CORE while adding the capability of the joint to be deployed to and from a flat position.

4.2.1 Jacob's Ladder

The underlying mechanism of the CORE is also what creates the optical illusion of a falling block in a Jacob's Ladder. The Jacob's Ladder is an ancient toy [96] that consists of ribbons connected in a specific pattern to wooden blocks, as shown in Figure 4.2. When the top block of a Jacob's Ladder is rotated, the illusion of a falling block is created as each block flips in alternating directions one after another. Similar to the study of the underlying mechanism of a color changing toy ball by Ding et al. [97], insights into mechanism design can be gained from an investigation of the Jacob's Ladder.

By isolating a single unit of the Jacob's ladder one can see how two rotational axes are present about which the top block can revolve, as shown in Figure 4.3. All of the degrees of freedom are constrained through either contact of the faces of the block and the ribbon or tension in the ribbon. Similarly, in the CORE all degrees of freedom besides the rolling motion are constrained through contact of the flexures and the cams or tension in the flexures. However, the introduction of a curved surface as the cam face rather than a flat surface as in the Jacob's Ladder causes the instantaneous axis of rotation to follow the curvature of the cam throughout the motion rather than switching between two stable axes of rotation. This difference in location of the instantaneous axis of rotations during the joint motions is shown in Figure 4.4.

4.2.2 Compliant Mechanisms

The CORE is a compliant mechanism, whose motion is derived at least partly from flexing members [36]. Compared to traditional mechanisms, compliant mechanisms can offer cost reduction due to lower part count and assembly time, simplified manufacturing processes, performance improvement through increased precision and reliability, and reduced wear, weight, and maintenance [36]. In the CORE, there is no need for lubrication, wear is dramatically reduced, and the compliance of the CORE enables design for specific force-deflection properties and an ease of miniaturization.

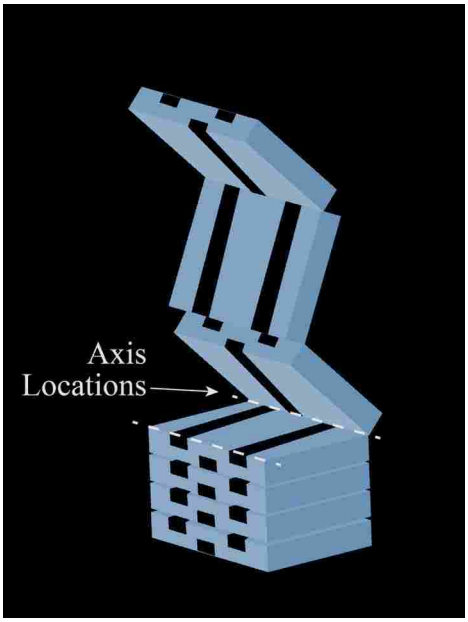

Figure 4.2: A Jacob's Ladder toy with hinge axis locations shown.

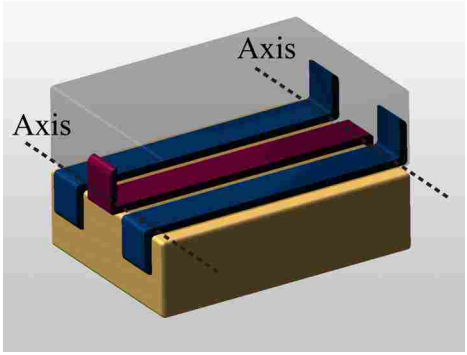

Figure 4.3: A single functional unit of a Jacob's Ladder in a closed position with hinge axes shown. The top block is transparent to show the attachment scheme of the bands.

4.2.3 Contact-Aided Rolling Joints

The development of the CORE was preceded by similar mechanisms that utilize the mechanism described in the Jacob's Ladder. The Rolamite concept was developed in the 1960's [98]. This design used a band between two rollers to create linear displacement with little friction. Further development of the Rolamite has occurred as seen in the creation of analysis techniques of the joint [99], implementation of the concept in a prosthetic knee joint [100], and more recently using the concept to create variable joint stiffness [101].

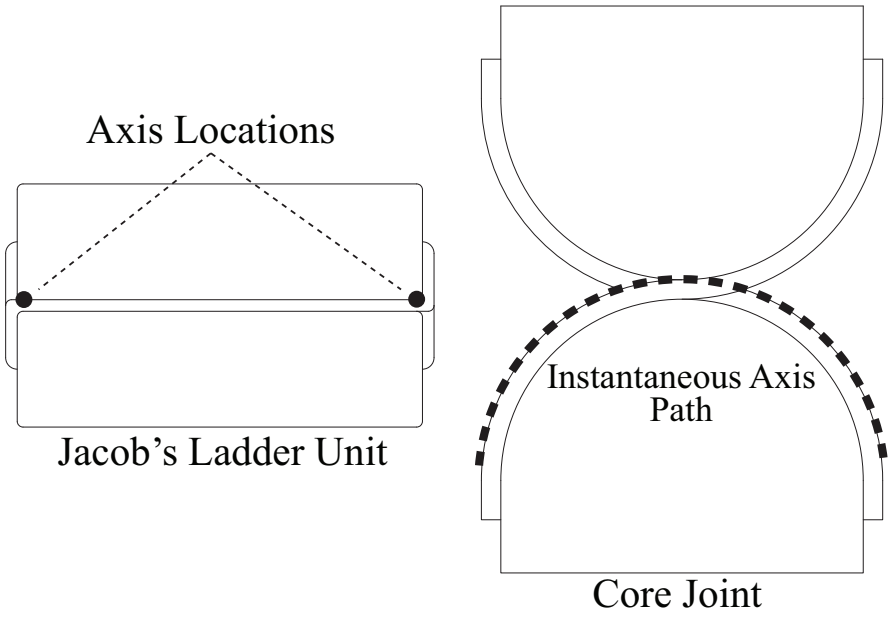

Figure 4.4: Location of the instantaneous axis of rotation of the Jacob's Ladder fundamental unit and a CORE through the joint motion.

The CORE [94] uses flexible bands to join two rolling surfaces similar to the Rolamite. However, while the Rolamite joint provides a linear displacement, the CORE allows the two rolling surfaces to roll over top of each other creating a motion similar to a revolute joint. Halverson et al. [94] used a strain energy approach to derive models for the CORE. Their work particularly examines tension-based multi-stable CORE joints and develops equations to describe the angular velocities of the cams, stress in the joint, strain of the flexures, and retaining forces (forces in the flexures) for these joints. A variation of this joint was used to create an artificial disc implant for the human spine designed to mimic the motion and stiffness characteristics of a human spinal disc [102].

The ability to scale the CORE and mechanisms similar to it has resulted in their use in medical devices for minimally invasive surgery [103] and robotic components such as a bio-mimetic finger [104].

4.2.4 Origami Inspired Mechanisms

Origami constructions have inspired the study of a variety of mechanisms and folding structures [38] including planar-spherical over-constrained mechanisms [105] and queer-square mech-

anisms with multi-furcation qualities [106]. Folding techniques have been used to formulate a systematical approach to carton folding [107]. Most of these origami constructions used in mechanism analysis are prismatic, where the straight creases can be modeled as revolute joints and the panels as links as is the case in the development of a systematic approach to modeling carton folding [107]. Kirigami, which uses cutting as well as folding, has also inspired mechanism design [108].

Curved-fold origami is intrinsically tied to curved surfaces. When paper is folded along a curved crease, the two surfaces created are developable surfaces [15]. Developable surfaces are sometimes called singly-curved surfaces as at every point of the surface one of the principle curvatures is zero [10, 49]. They are a subset of ruled surfaces, or surfaces where a straight line, or ruling line, can be used to generate the surface [10]. Three types of developable surfaces exist: generalized cylinders, generalized cones, and tangent-developable surfaces [32]. Curved-fold origami can thus be thought of as a combination of developable surface patches that are joined through curved creases. David Huffman [8] [1] and Ron Reusch [6] pioneered a rigorous approach to curved folding with their work in the 1970's. Recent work by Lang [33] and Demaine et al. [9] has demonstrated methods to design curved-fold structures by treating the ruling lines of the developable surfaces as optics lines and curved-creases as lenses. Curved-folding techniques are used in this chapter to create the curved surfaces of the CORE. In addition, curved-folding enables the CORE joint to be stowed in a flat position and gives the possibility of the joint to be self-deployed.

4.3 Deployable CORE (D-CORE)

4.3.1 Description

The deployable CORE (D-CORE) is made of two flat panels with curved creases that form the cams of the joint when deployed and three flexible bands which hold the two panels together. These components are chained together alternating between panels and flexible bands as is shown in Figures 4.5 and 4.6. The two flat panels that form the cams also require curved cut edges if the angle between the cam sides and cam's contact surface varies from 90 degrees. The geometry of the curved cut edges and curved creases is discussed in Section 4.3.1. Two configurations of the D-CORE are presented below. Configuration 1 enables motion in the undeployed state while

Configuration 2 does not. Both configurations can be manufactured from a single sheet, assembled by folding and one point of attachment, and are three layers thick in the assembled but undeployed state. Anchoring either configuration of D-COREs to rigid bodies can be achieved through sliding fits to accommodate for the motion of deployment. These sliding fits are discussed in Section 4.3.1 as an anchoring solution.

Configuration 1

Configuration 1 of the D-CORE enables a Jacob's ladder like motion when the joint is in its undeployed state and full CORE motion in the deployed state. It can be manufactured in a planar state (Figure 4.5(a)), folded into an assembled but undeployed flat state (Figure 4.5(b)), and deployed into the CORE geometry (Figure 4.5(c)). The length of the panels that form the cam surfaces, L, is equivalent to the length of the flexible bands, L_{band}, when the bands are thin. The joint can be cut out of a single sheet or assembled from multiple components. If a single sheet is used for fabrication, one attachment point is required to complete a chain where the single flexible band passes between the two parallel flexible bands.

Configuration 2

The second configuration of the D-CORE is a static structure in its undeployed state and shows full CORE motion in its deployed state. Similar to the Configuration 1, Configuration 2 can be manufactured in a planar state (Figure 4.6(a)), folded into an assembled but undeployed flat state (Figure 4.6(b)), and deployed into the CORE geometry (Figure 4.6(c)). Configuration 2 is constrained from motion in the undeployed state by placing hard stops on the panel's edges. One pair of these hard stops on each panel can be folded over themselves to accommodate for the thickness of the bands. This causes the panels to interfere with one another if the joint tries to rotate in the undeployed state. The addition of these hard stops slightly decreases the range of motion of the joint in the deployed position.

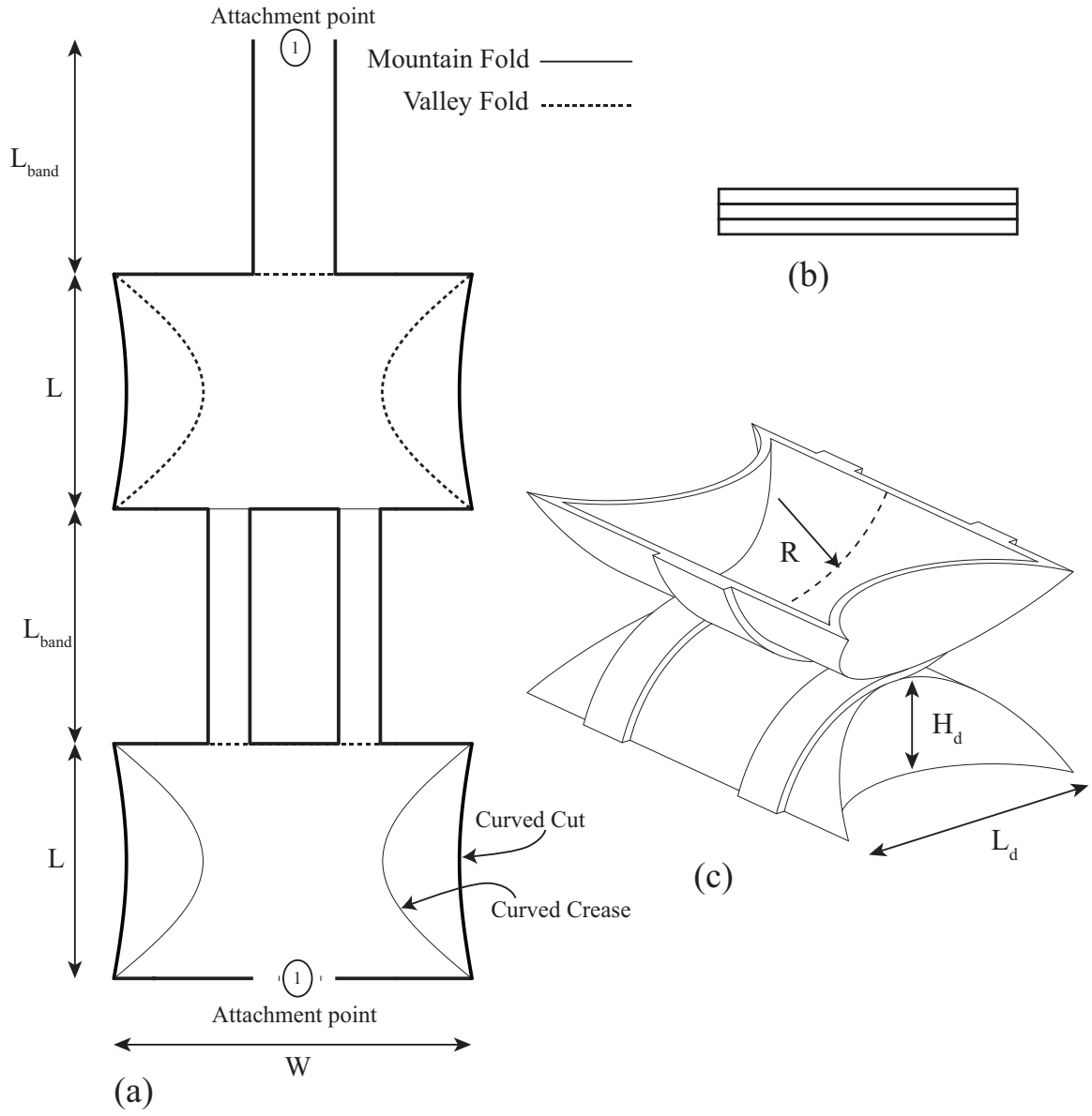

Figure 4.5: Configuration 1 of the D-CORE shown in its (a) planar, as-manufactured state, (b) folded undeployed state, and (c) deployed state.

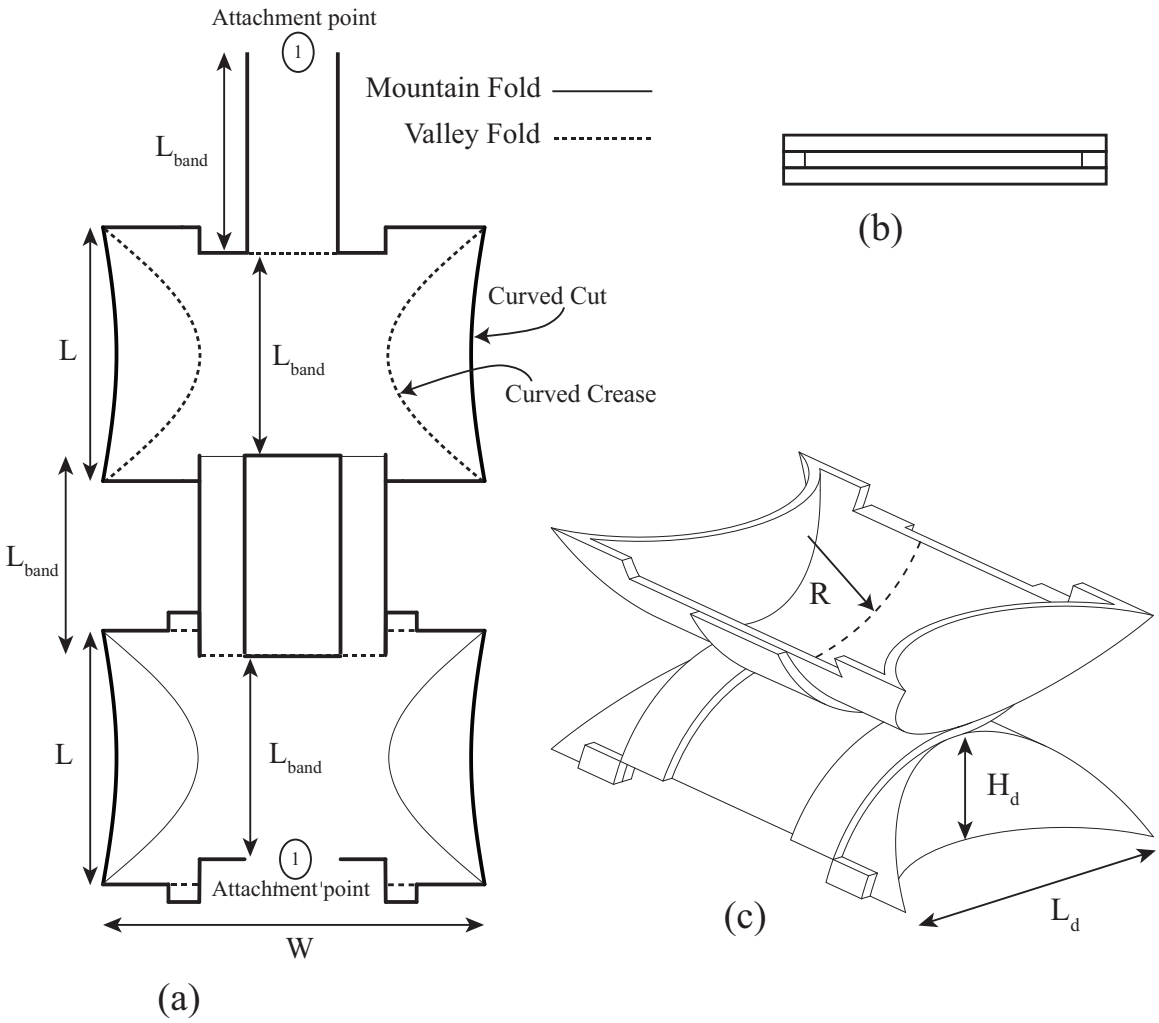

Figure 4.6: Configuration 2 of the D-CORE shown in its (a) planar as-manufactured state, (b) folded undeployed state, and (c) deployed state.

Cam Construction Using Curved Creases

Configurations 1 and 2 both draw upon curved creases to create the cam surfaces. The geometry of the curved creases used to form the cams as well as the length of the flexible bands of the D-CORE determines the range of motion for the angular deflection of the joint and the radius of the cam. The crease geometry can be determined by considering the intersection of cylinders where the cam face is modeled as a section of a cylinder and the two cam side panels are also modeled as sections of cylinders, as shown in Figure 4.7. Apostol et al. [20] show that the intersection curve between a cylinder and a plane is an elliptical cross section and when the cut cylinder is unwrapped

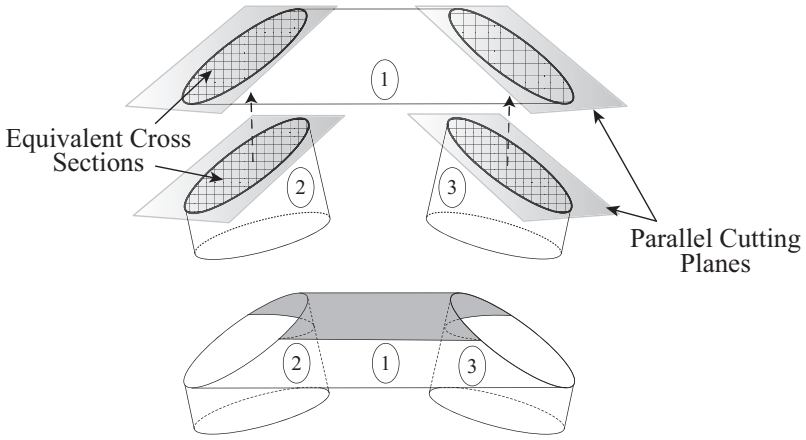

Figure 4.7: Modeling the CORE cam shown in gray as a combination of three oblique cylindrical sections intersected with one another.

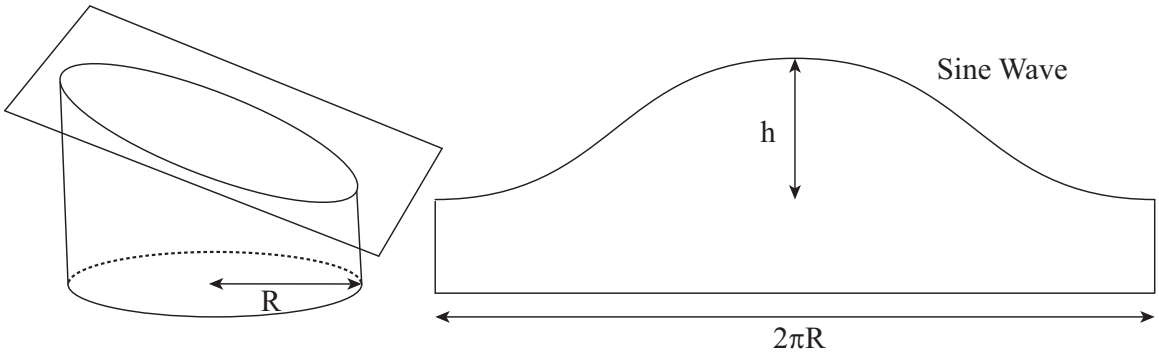

Figure 4.8: Intersection geometry for a cylinder and a cutting plane with the resulting unwrapped cylinder.

the profile of the cut edge is a sine wave, as shown in Figure 4.8. To form a deployable CORE cam, the cutting planes of three cylinders are placed on top of one another and the elliptical cross sections are aligned as shown in Figure 4.7. When any cylinder is unwrapped the profile of the cut edge forms the geometry of the curved crease. If the angle between the face and sides of the deployed cam, α, differs from $\pi/2$ the panels that form the cams will need to have an additional curved cut edge to enable the joint to sit on a flat plane in the deployed state.

The equations describing the relationship between the range of angular deflection of the joint in radians, Θ, the radius of a cylindrical cam, R, the angle between the face and sides of the deployed cam in radians, α, and the geometry of the curved crease and curved cuts expressed as functions, $y_{crease}(x)$ and $y_{cut}(x)$, can be determined for deployable joints with cylindrical side

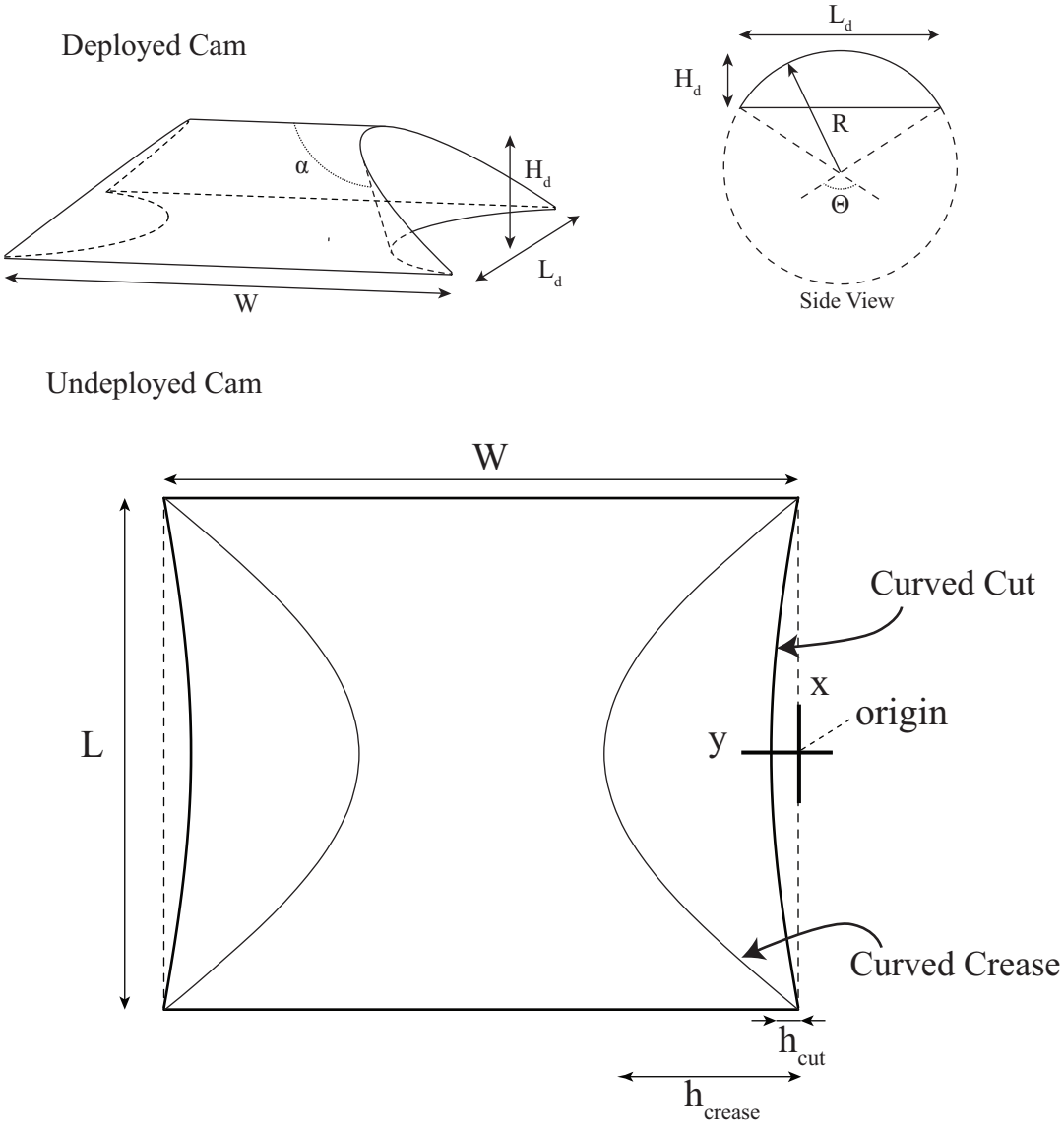

Figure 4.9: Parameters for a cylindrical cam with cylindrical side panels in the undeployed and deployed states.

panels of the cams as is described in the next section. Figure 4.9 shows the parameters which will be used in the expressions.

Deployable CORE Model for Design

The following relationships were developed for the D-CORE such that the radius of the cam, R, the deflection of the joint, Θ, the angle between the cam sides and face, α, and the width of the cam, W, are selected and all other parameters of the D-CORE are computed. After selecting

the radius of the cylindrical cam, R, and the desired angular deflection of the joint, Θ, which can range from 0 to π, the required panel length, L, can be calculated by

$$L = R\Theta \tag{4.1}$$

It should be noted that the addition of the hard stops in Configuration 2 causes the effective angular deflection of the joint to be decreased to

$$\Theta_{config2} = \frac{L_{band}}{R} \tag{4.2}$$

Using the selected angle in radians between the cam face and side panels in the deployed state, α, the height of the crease, h_{crease}, is computed as follows

$$h_{crease} = R\tan\left(\frac{\alpha}{2}\right)\left(1-\cos\frac{\Theta}{2}\right) \tag{4.3}$$

The height of the curved cut edge of the panel, h_{cut}, when α is in radians is described as

$$h_{cut} = R\tan\left(\alpha-\frac{\pi}{2}\right)\left(1-\cos\frac{\Theta}{2}\right) \tag{4.4}$$

The crease geometry, which corresponds to the unwrapped curve of a cylinder cut by a plane, can then be expressed by the following equation with the coordinate system placed as shown in Figure 4.9.

$$y_{crease}(x) = R\tan\left(\frac{\alpha}{2}\right)\left(\cos\frac{x}{R}-\cos\frac{\Theta}{2}\right) \tag{4.5}$$

where the domain for x is from $-\frac{L}{2}$ to $\frac{L}{2}$. This expression was derived in a manner similar to that described by Apostol et al. [20] for unwrapping curves from cylinders. Similarly, the curved cut edge geometry, which also corresponds to the unwrapped curve of a cylinder, can be expressed by the following equation where the coordinate system is placed as shown in Figure 4.9

$$y_{cut}(x) = R\tan\left(\alpha-\frac{\pi}{2}\right)\left(\cos\frac{x}{R}-\cos\frac{\Theta}{2}\right) \tag{4.6}$$

The length of the deployed cam, L_d, is expressed as

$$L_d = 2R\sin\frac{\Theta}{2} \tag{4.7}$$

The height of the deployed cam, H_d, is computed from

$$H_d = R\left(1-\cos\frac{\Theta}{2}\right) \tag{4.8}$$

The length of the bands are shown in Figures 4.5 and 4.6 for the two configurations.

While the D-CORE cams created with these equations are circular cylindrical cams in the final deployed state, the surfaces are not guaranteed to remain as circular cylinders during the deployment of the cam from a flat state. The shape the surface of the cam takes during the deployment process can be investigated using the process outlined by Apostol et al. [20] of finding the shape of a generalized cylinder cut by a plane where the unwrapped curve of intersection is known. The generalized cylindrical shape can be considered as the profile of the cam while the plane shown in Figure 4.7 can be considered the cutting plane. The unwrapped curve of intersection is the cam's crease geometry as described in Equation 4.5. This crease geometry is constant for any stage of the deployment process.

Anchoring the D-CORE to Rigid Bodies

The joint boundaries move during deployment which complicates anchoring the D-CORE to rigid bodies. One method of anchoring the joint while still allowing for the deployment motion is to use sliding fits as shown in Figure 4.10. These fits are joined to the cam panels with a crease. The length of the sliding fit is $(L-L_d)/2$ to accommodate the deployment motion. If the anchor points can be placed underneath the deployed cam, the range of motion of the joint will not be affected, yet the undeployed folded state will be an additional two layers thick. If the anchor points are placed on the outside of the cam, the range of motion will be decreased due to interference of the anchors at the extreme positions of the joint. Also, if the angle between the sides of the cam and the cam's contact surface, α, falls between the range of 0 to $3\pi/4$, interference can occur during deployment as the sides of the cam swing below the anchoring plane. To ensure clearance, appropriate cuts can be made in the panels to which the D-CORE is anchored.

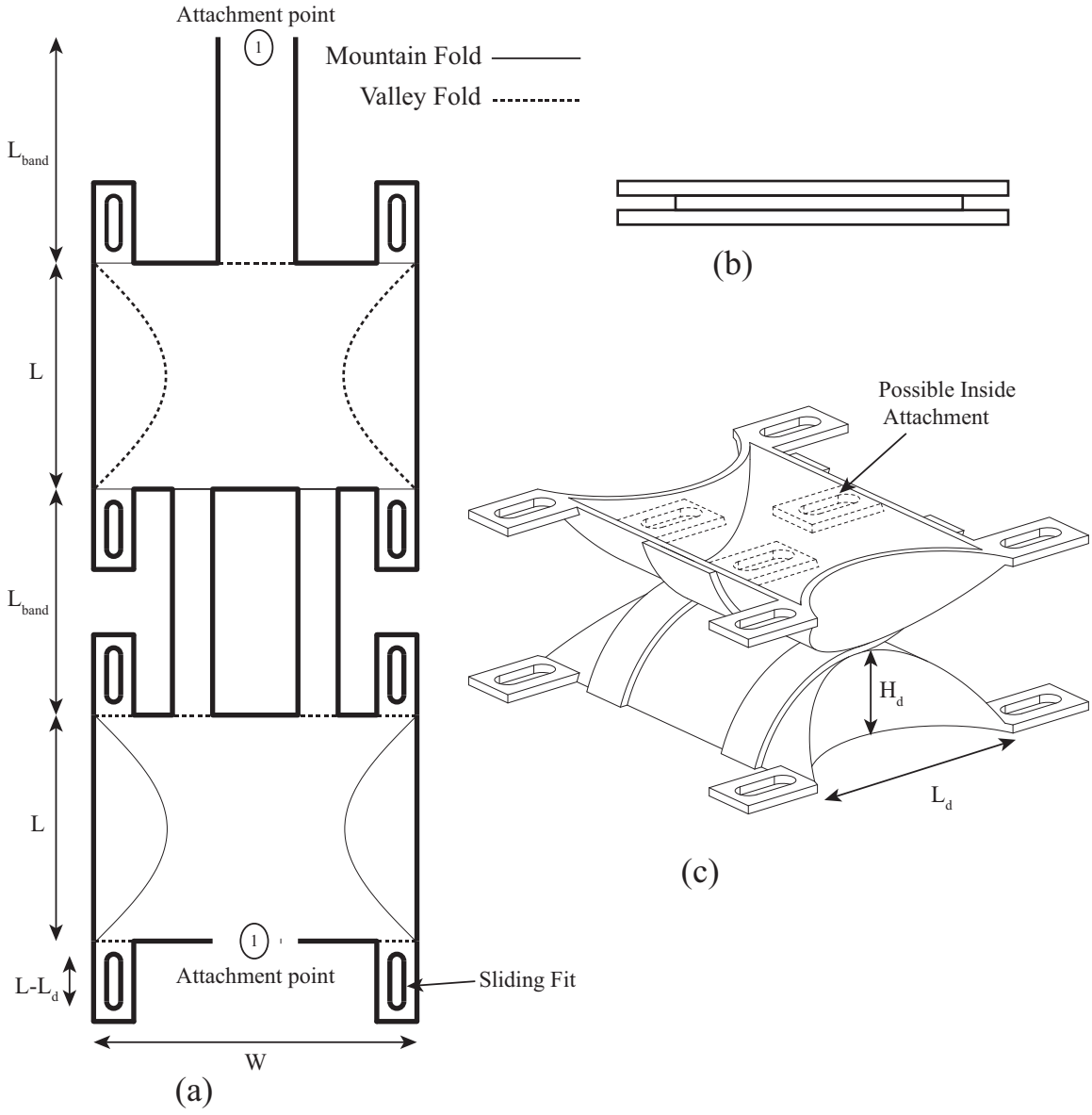

Figure 4.10: Anchoring the D-CORE using sliding fits shown in a position for (a) planar manufacture, (b) a folded undeployed state, and (c) a deployed state.

Stiffness and Stress Characteristics of the D-CORE

The D-CORE manufactured from a single sheet is unlikely to have the same performance in compression as a solid CORE. However, the deployability of the D-CORE gives it advantages besides compressive strength which can make the joint suitable to applications requiring a small stowed volume or low-cost manufacturing. The development of a simple analytical model for stiffness and stress of the D-CORE under various loading conditions is challenging because of the combined effects of stress from deployment and the stress induced by the joint loading. As such, prototype testing and finite element analysis methods are recommended for determining the stiffness and stress characteristics for particular applications of the D-CORE.

Despite the difficulty in developing a simple analytical model, insight can be gained by comparing finite element models of hollow CORE and D-CORE cams with the same dimensions, material, and compressive loads. Two finite element models (ANSYS, BEAM 188) were created to represent hollow CORE and D-CORE cams. The hollow CORE cam was modeled as an initially curved beam fixed at both ends as shown in Figure 4.11. The cam of the D-CORE was modeled as an initially flat beam which was morphed into its deployed shape using moment loads on either end of the beam. As the curved creases of the D-CORE cam force the initially flat center panel to take the same circular shape as the moment loading, this method to create the deployed stresses was considered as a reasonable approximation. Once in the deployed shape the ends of the beam were fixed and compressive loadings were applied at various locations around the cam as described by the load location parameter γ. The variation in the load location parameter was used to simulate the variation in the compressive loading location as the joint rolls through its range of motion.

These two finite element models were stress converged to within a 5% change in maximum Von Mises stress for two loading locations. The maximum Von Mises stress developed under the compressive loads at various locations is shown in Figure 4.12 for both the hollow CORE and D-CORE cams. The prestress component from the deployment of the D-CORE cam is reflected in the higher stresses present in the D-CORE cam for all of the loading locations. The deflection of the point where the compressive loading was applied was also plotted for both the hollow CORE and D-CORE cams in Figure 4.13. Interestingly the D-CORE cam shows a slight improvement in the stiffness at this point over the hollow CORE cam. While these finite element models give insight to general characteristics of the D-CORE performance under compressive loadings compared to a

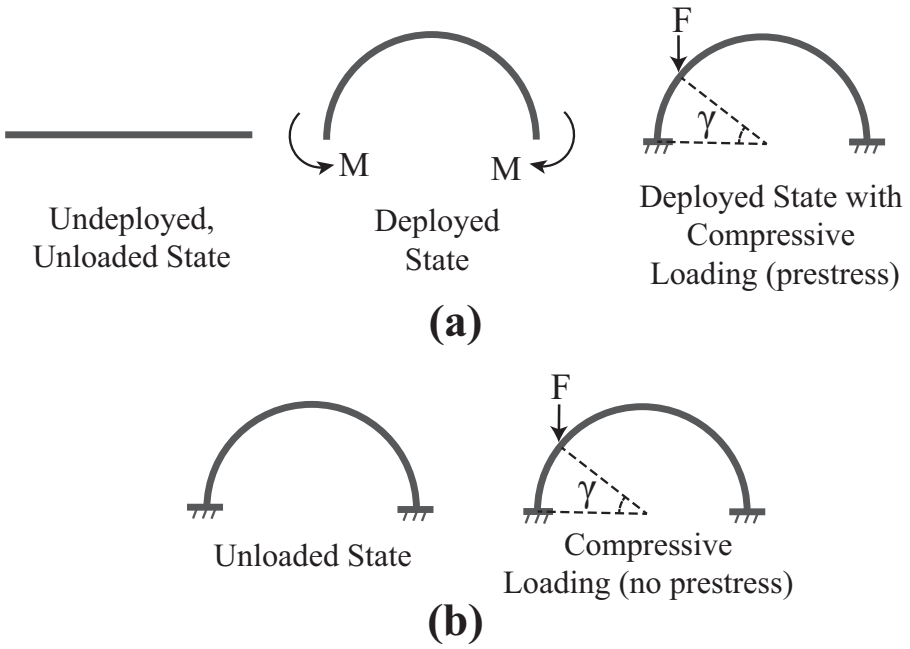

Figure 4.11: Finite element model set up for (a) the D-CORE and (b) hollow CORE cams illustrating the presence of a prestress condition from deployment of the D-CORE and definition of the compressive load location parameter, γ.

hollow CORE, further work would need to be conducted for specific applications. Also, analysis of the local stresses developed in the curved creases of the D-CORE rather than the curved panels during the loaded states needs to be explored.

4.3.2 Physical Models

Physical models of Configurations 1 and 2 were constructed out of a range of materials to demonstrate the transition from paper to engineering materials. Figure 4.14 shows a family of Tyvek® models with common radius of the cylindrical cam, R, but varying values of the angle between the sides and contact surface of the cam, α, and range of motion, Θ. Tyvek® is made from fusing together finely spun high density polyethylene fibers into a web. This results in a paper-like material that is tough, water resistant, and yet still maintains the ability to hold creases [109].

Configuration 1 was also constructed out of 0.38 mm (0.015 in) thick polycarbonate panels with 0.023 mm (9 mils) thick metallic glass hinges as shown in Figure 4.15. Bulk metallic glasses are metallic alloys which fail to crystallize during solidification. This gives them a unique combi-

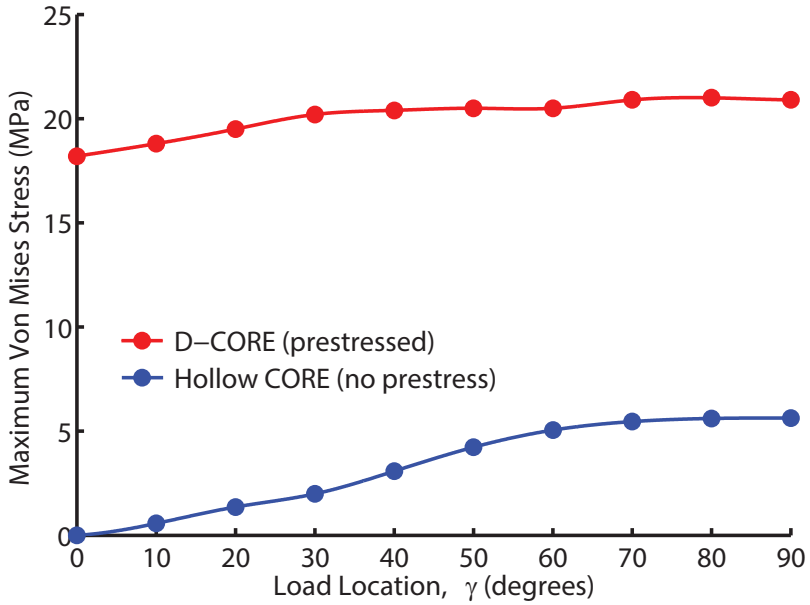

Figure 4.12: Maximum Von Mises Stress developed under compressive loadings at various locations for the hollow CORE and D-CORE cams.

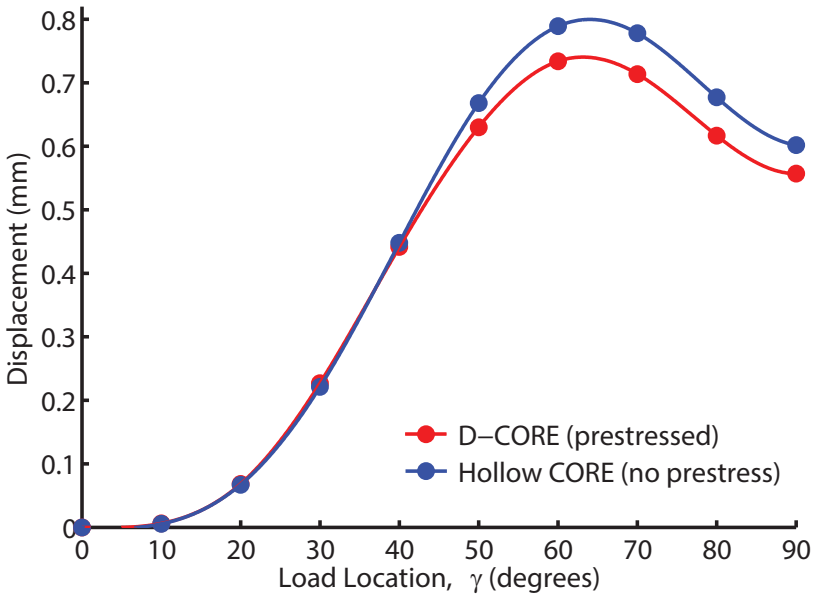

Figure 4.13: Displacement of the point where the compressive loading is applied for various loading locations for the hollow CORE and D-CORE cams.

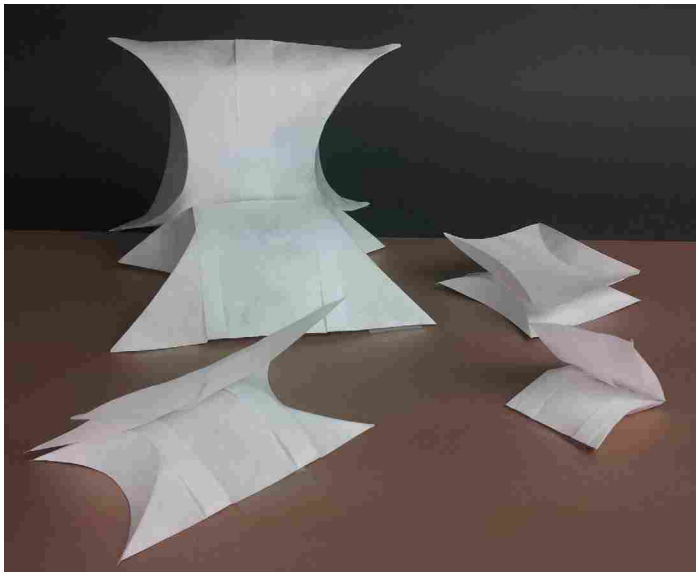

Figure 4.14: Tyvek® models of Configuration 1 with varying values of α and Θ and a common radius, R, of 5 cm.

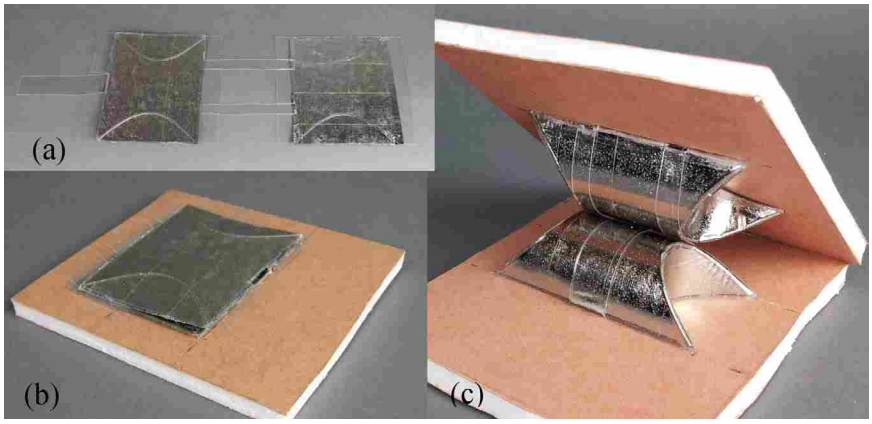

Figure 4.15: Configuration 1 made of polycarbonate panels and metallic glass hinges shown (a) during planar manufacture, (b) in a folded undeployed state without the top panel, and (c) in a deployed state.

nation of properties including high elastic strain and strength, making them a good candidate for compliant applications [53]. The metallic glass was secured with adhesive transfer tape between two layers of polycarbonate panels from which material in the curved crease regions had been removed. The joint was anchored to the foamboard panels by polycarbonate tabs that were inserted into slits in the foamboard.

Figure 4.16: Configuration 2 made of polypropylene anchored to wood panels shown (a) during planar manufacture, (b) in a folded undeployed state, and (c) in a deployed state.

A 0.81 mm (0.032 in) polypropylene sheet was used to construct Configuration 2 of the D-CORE. The polypropylene sheet was cut as shown in Figure 4.16(a). The curved creases and creases where the bands and sliding fits connect to the cam panels were created by using an embossing tool to remove material to form living hinges in the polypropylene. The polypropylene was folded and secured to wooden panels with nails to complete the sliding fits. Figure 4.16(b) and 4.16(c) show the D-CORE in the undeployed and deployed state. Polypropylene tabs on the base of the cams were inserted into grooves in the wood panels to lock the joint into the deployed state. The deployed joint functioned under a 100 N (22.5 lb) compressive load before visually detectable deformation of the cams occurred.

4.4 Deployable Translating Platform

4.4.1 Description

By using two or more inverted D-CORE joints and adjusting the cam profile to be a half circle to enable 180 degrees of angular rotation, a deployable translating platform can be formed. The deployable translating platform has the ability to be stored flat with effectively no degrees of freedom and to deploy to a state where linear translation is facilitated. This change in the degrees of freedom between the stored and deployed state qualifies the translating platform as a metamorphic mechanism [95].

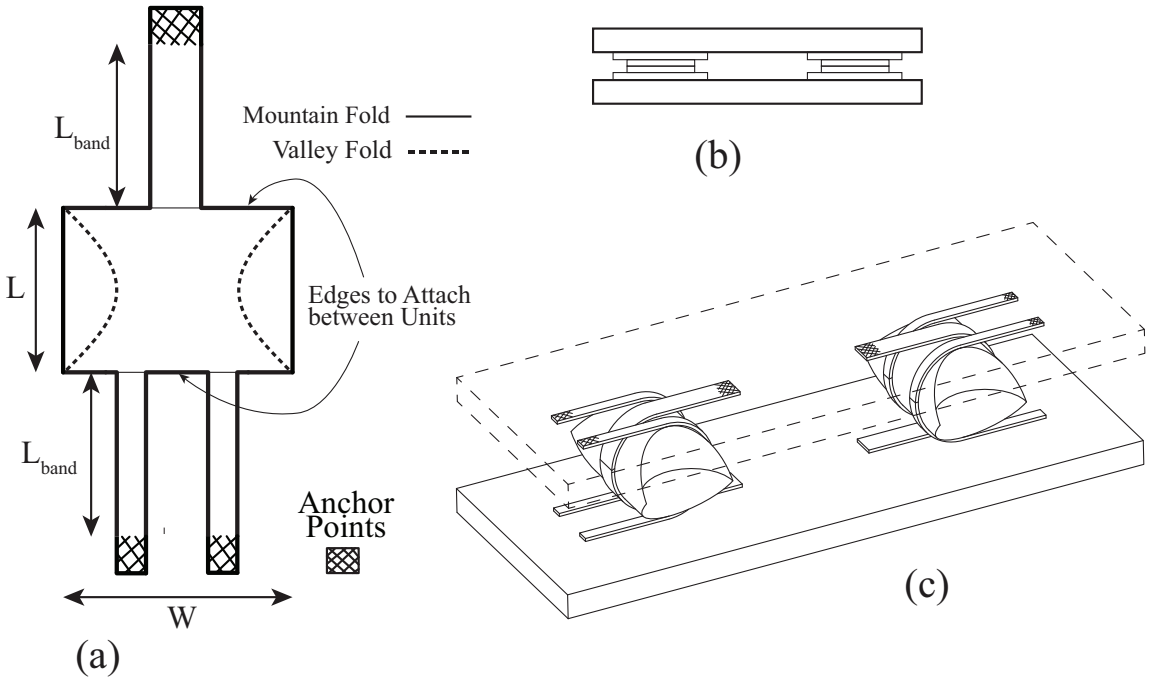

Figure 4.17: Translating platform geometry shown in (a) a planar state for manufacturing, (b) the assembled but undeployed state, and (c) the functioning deployed state.

Figure 4.17 shows the geometry of the translating platform. Each of the joint units can be made from two identical pieces that are placed on top of one another and joined along the opposite edges of the panels which form the cams, as shown in Figure 4.17(a). These units are attached to the platforms by the flexible bands. The undeployed state is four layers thick (see Figure 4.17(b)). The deployed state of the platform is shown in Figure 4.17(c).

The range of linear translation, δ, can be expressed in terms of the radius of the cam cylinder, R, as

$$\delta = \pi R \tag{4.9}$$

This range can be easily adjusted to a shorter length by shortening the length of the flexible bands. The cam geometry and curved crease geometry are described by Equations (4.1),(4.3),(4.5),(4.7), and (4.8) where $\Theta = \pi$. If $\alpha < 3\pi/4$, the two cam units joined together will need to be actuated at separate times to avoid interference of the cam side panels. If $\alpha \geq 3\pi/4$ the cams can be actuated simultaneously and furthermore all edges of the cam units can be joined together instead of only the opposite edges shown in Figure 4.17(a). The motion that occurs during deployment of the

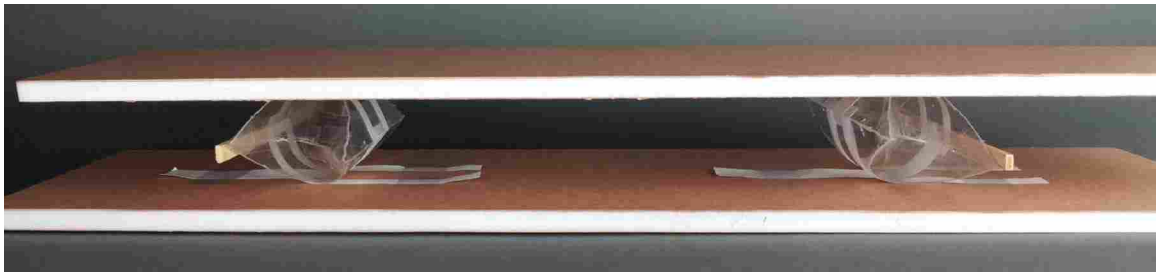

Figure 4.18: Translating platform constructed of polycarbonate cams attached to translating panels via Tyvek® flexible bands.

translating platform does not require sliding fits to anchor the joint units to the translating panels because the joint units can be anchored to the translating panels by the flexible bands.

4.4.2 Physical Model

A model of the translating platform was constructed from deployable cams made of 0.38 mm (0.015 in.) polycarbonate sheets and connected to foamboard translating panels via Tyvek® flexible bands. A small piece of wood and mono-filament lines were used to lock the mechanism into the deployed position. Figure 4.18 shows the physical model of the translating platform in the deployed state.

4.5 Discussion

As the D-CORE can be stowed in a flat configuration it can be used in applications where space constraints would limit the use of a traditional CORE. These applications include minimally invasive medical implants, space applications, and stowable furniture. However, when the cams of the CORE are made to be deployable, the compressive strength of the joint decreases.

Actuation of the joint can be accomplished through a force which pulls the edges of the deployable cams together or through forces which fold the creases to the appropriate angles. Springs or hand actuation, as was used with the models in this chapter, are two methods of deploying the joint by forcing the edges of the deployable cam together. Shape memory alloys and thermally actuated contractile polymers [45, 110] also present possible methods of self-folding or deployment of the joints. Inflation is a possible actuation method for the cams of the translating platform if $\alpha \geq 3\pi/4$ and all edges of the cam units are joined together.

4.6 Conclusion

This chapter applied curved-fold origami techniques to create the geometry of a D-CORE that is manufacturable from a single sheet. Two configurations were presented which have the ability to be stored in a flat state and deploy to a functioning state, making them suitable for space-constrained applications such as medical devices and in aerospace. The crease geometry was mathematically related to key properties of the D-CORE to facilitate design of the joint. These relations were used to create physical prototypes of the D-CORE. A deployable translating platform was presented as a derivative of the D-CORE.

This chapter outlines how the geometry of the D-CORE is created for a cylindrical radius. It may be possible to characterize other profiles which can be created using curved creases. These non-cylindrical profiles could be used to create multiple stable positions of the joint and also to change the location of the instantaneous axis of rotation.

CHAPTER 5. NATURAL EQUATIONS FOR RIGID-RULING SINGLE-CLASS DEVELOPABLE SURFACES

Now we have had the chance to see an example of the potential of curved-crease origami and developable-surface principles at work in mechanism design in the previous chapter, it's time to take a step back and cast the mathematical representations of developable surfaces into a form that is based on properties which have significant meaning for the design of mechanisms containing developable surfaces. In particular, this chapter sets forth a representation for developable surfaces based on curvatures of a principal curve, or cross curve, on the surface. This form of representing developable surfaces makes it convenient to differentiate between and relate all the rigid-ruling states of a surface, that is all the possible folded states that share a common ruling. We call this form the natural equations for a rigid-ruling developable surface. With the cross-curve curvatures explicitly defined, engineering quantities such as bending stresses which are proportional to one of the curvatures can be found in a straightforward manner.

One purpose of this chapter is to introduce fundamentals of differential geometry applicable for this work to an audience who may not be as familiar with the field. It is the hope that these fundamentals and results will prepare the reader to more fully utilize developable surfaces in engineering design by giving concise mathematical descriptions that are especially applicable to a specific category of developable surfaces, rigid-ruling developables. Rigid-ruling developables are developable surfaces where the ruling lines do not change location in a surface during folding. While we didn't call it by this name, this category of developables has already been encountered in this work where the compliant arrays define the ruling-line locations in a surface and force a rigid-ruling folding motion. We will also find in the following chapter that the natural equations for a ruling-rigid developable surface clearly show the requirements for developable surfaces to roll on each other.

5.1 Introduction

Developable surfaces, surfaces which can be formed by bending a plane with no stretching or tearing [10], have been studied to facilitate efficient forming of 3D shapes from planar stock materials. With the recent interest in origami-inspired engineering [111–116], and more particularly curved-crease origami [1, 21, 34, 35, 117], which is composed of developable surfaces, there is renewed interest in developable surfaces to model folding for deployable applications. In particular, some of the forms of creating thick developable surfaces involve the fixing of ruling-line locations in a panel through lines of decreased stiffness in the ruling-line directions [29, 118]. In past work these surfaces have been commonly represented by specific forms of the generalized parametrization for ruled surfaces and more recently other parameterizations such as using lines of curvature [12, 119–122]. In this chapter we present an equation form for rigid-ruling single-class developable surfaces. The ruling lines in a rigid-ruling developable do not change location in the surface [118]. A single-class developable surface refers to the surface being either a generalized cylinder, generalized cone, or tangent developable where the edge of regression is C^1 continuous. The contributions of this chapter are

- Recasting developable surface equations into a natural equation form where properties containing information about folding and bending stress analysis of a curved surface are identified and explained. These properties are coordinate system independent and are thus natural properties. These natural equations can describe all possible folded forms for rigid-ruling single-class developable surfaces.

- Conditions are defined for the natural properties which readily communicate to which developable class the surface belongs.

- Osculating shapes are described to further physical intuition of the natural property of ruling curvature.

- Explicit formulas are written to find the principal curvatures at any point on a surface from its natural properties.

- Equations to move between the traditional and natural equations of a developable surface are listed to facilitate design of surface using the form most conducive to a particular application.

The natural equations presented give a concise and simple description of both the formed and developed states of a rigid-ruling surface using properties often essential to engineering and manufacturing applications. This representation can be useful for computer graphic models of developable surfaces, in further understanding curved-crease origami, and in curved-crease origami applications such as self-assembling propellers [47] and new metamaterials [123]. This method of expressing developable surfaces can also be beneficial in manufacturing processes, such as rolling, to create specific developable surfaces by defining the desired surface concisely in terms of its natural properties. These natural properties can be used to control the process, such as the speed and angle of the rollers, to create the desired shape. Examples of developable surface classes described by their natural equations will be explained and graphically plotted.

5.2 Background

5.2.1 Natural Equations of Curves

Natural, or *intrinsic*, equations for curves can be used to specify the geometry of a planar or space curve irrespective of the coordinate system in which the curve is placed [10, 124]. Consequently these equations are written in terms of natural properties, that is quantities or properties that are invariant to the choice of coordinate system. Typically these include arc length (s), curvature (κ), tangential angle (θ), and torsion (τ) or a combination of these properties [124].

Euler described curves with natural equations in terms of arc length and curvature as part of a work presented to the St. Petersburg Academy in 1735 [10, 125]. Since this time other natural measures have been used to write natural equations for curves [126–128]. The Fundamental Theorem of Space Curves states that the natural measures of curvature and torsion define a unique space curve [10]. Frenet and Serret developed the following formulas, now known as the *Frenet-Serret Formulas*, to relate curvature and torsion to the tangent, normal, binormal frame (**TNB** frame) [129, 130]:

$$\begin{aligned}\frac{\mathrm{d}\mathbf{T}}{\mathrm{d}s} &= \kappa\mathbf{N} \\ \frac{\mathrm{d}\mathbf{N}}{\mathrm{d}s} &= -\kappa\mathbf{T} + \tau\mathbf{B} \\ \frac{\mathrm{d}\mathbf{B}}{\mathrm{d}s} &= -\tau\mathbf{N}\end{aligned} \tag{5.1}$$

where $\mathrm{d}/\mathrm{d}s$ is the derivative with respect to arc length s, κ is the curvature of the space curve, and τ is the torsion of the space curve.

5.2.2 Intrinsic properties of surfaces

Surfaces have been described using intrinsic properties. For surfaces, *intrinsic* properties are defined as properties that are constant for all isometries (distance preserving transformations) of a surface [131]. For example, cylinders and planes are related isometrically to each other and thus share intrinsic properties. The first fundamental form is an intrinsic measure of a surface and can be used in determining arc lengths of curves on a surface, angles between curves on a surface, and areas [132].

While there is much utility in intrinsic measures (isometric equivalence) in describing surfaces, the goal of this chapter is to describe specific rigid-ruling folding states of developable surfaces and thus differentiate between surfaces which have isometric equivalence. As developable surfaces share equivalent intrinsic properties, natural measures which are not necessarily intrinsic measures will be identified to write natural equations for each of the three curved classes of developable surfaces. These natural measures still do not depend on the coordinate system in which a surface is placed.

5.2.3 Normal, Principal, Geodesic, and Gaussian Curvatures

Several curvatures of curves on an arbitrary surface will be important in this chapter. The *normal curvature* of a curve on an arbitrary surface is the curvature of the projected curve on the plane containing the tangent vector of the curve and surface normal vector [10]. When considering all possible curves through a given point, the maximum and minimum values of the normal

curvature are the *principal curvatures* of the surface at that point. The principal curvatures are orthogonal to each other. The *Gaussian curvature* is the product of the two principal curvatures. Gauss showed that remarkably this curvature is an intrinsic property [133].

The *geodesic curvature* of a curve on a surface is the curvature of the projected curve on the surface's tangent plane. The geodesic curvature represents the deviation of a curve from a geodesic on a surface, which is a straight line for developable surfaces in their developed (planar) state. While the geodesic curvature is not an intrinsic property for developable surfaces, it is a constant property for all forms of a rigid-ruling developable surface.

The sign of the geodesic and normal curvatures are meaningful when the direction of the surface normal is selected. A positive geodesic curvature denotes counterclockwise rotation of the tangent line of the projected curve on the surface's tangent plane with the surface normal pointing towards the observer. A negative geodesic curvature denotes clockwise rotation. A positive normal curvature of a curve on a surface denotes that the projected curve on the plane containing the curve's tangent vector and the surface normal curves in the direction of the surface normal, with negative normal curvature denoting curvature of the projected curve in the opposite direction of the surface normal.

5.2.4 Darboux Frame (T, L, U frame)

A *Darboux frame* moves across a surface along a curve [133]. This frame will be used in explaining how to move between natural equations of developable surfaces and canonical parametric representations of the surfaces in Cartesian coordinates. Let unit vectors **T**, **L**, and **U** define the Darboux frame. **T** is the tangent vector to the curve, **U** is the normal vector to the surface, and **L** the tangent normal vector ($\mathbf{U} \times \mathbf{T}$). This frame is shown in Fig. 5.1.

Similar to the Frenet-Serret Formulas are the Darboux formulas [133]:

$$\begin{bmatrix} \mathbf{T}' \\ \mathbf{L}' \\ \mathbf{U}' \end{bmatrix} = \begin{bmatrix} 0 & \kappa_g & \kappa_n \\ -\kappa_g & 0 & \tau_g \\ -\kappa_r & -\tau_g & 0 \end{bmatrix} \begin{bmatrix} \mathbf{T} \\ \mathbf{L} \\ \mathbf{U} \end{bmatrix} \tag{5.2}$$

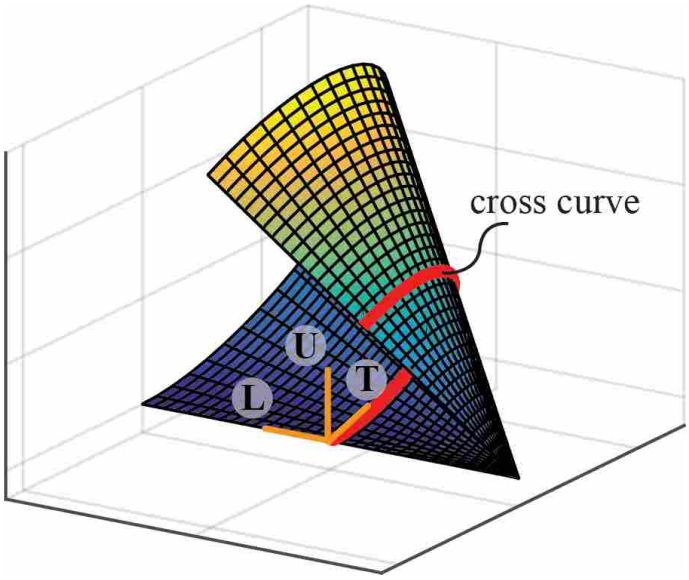

Figure 5.1: The Darboux frame (**T**, **L**, **U** frame) following a principal curve on a developable surface.

where κ_g, κ_n, and τ_g are the geodesic curvature, normal curvature, and geodesic torsion of the curve along which the Darboux frame travels. The *geodesic torsion* is the rate of rotation of the tangent plane to the surface about the tangent to the curve the frame is following [132].

5.2.5 Developable Surfaces

A developable surface is characterized by zero Gaussian curvature at any point on the surface [10]. Zero-Gaussian curvature at a point is the result of one, or both in the trivial case of a plane, principal curvatures being zero. Furthermore, developable surfaces are a subset of ruled surfaces, and can be described using straight lines called ruling or generator lines [11]. Four primary classes of developable surfaces exist: planes, generalized cylinders, generalized cones, and tangent developables [32]. The three curved classes are shown in Figure 5.2. Generalized cylinders are created by translating a constant-direction line to sweep out the surface. Generalized cones are created by rotating a line about a point to generate a surface. Finally, tangent developable surfaces correspond to the family of tangent lines extending away from a space curve, called the edge of regression, such that no intersection of the tangent lines occurs. The four primary classes of developable surfaces can be joined together to create general or composite developable surfaces

[13]. In these general surfaces, as with each class of surface, the ruling lines cannot cross one another.

Parametric equations have traditionally been used to represent these surfaces [134]. Any ruled surface, $\mathbf{r}$, has the form

$$\mathbf{r}(t,u) = \alpha(t) + u\beta(t) \tag{5.3}$$

where t and u are the parameters of the surface, $\alpha(t)$ is the directrix of the surface, and $\beta(t)$ is the direction of the ruling lines. Notice that t specifies which ruling line a point lies on in addition to the direction of the ruling line, while u specifies the position along a ruling line. A generalized cylinder is represented more specifically with the form

$$\mathbf{r}(t,u) = \alpha(t) + u\beta \tag{5.4}$$

where the directrix, $\alpha(t)$, is the cross section of the generalized cylinder. The director, β, is a vector in the direction of all the parallel ruling lines of the generalized cylinder. A generalized cone has the form

$$\mathbf{r}(t,u) = \alpha + u\beta(t) \tag{5.5}$$

where the directrix is the cone-apex position vector, α, and the curve defining the direction of the ruling lines, $\beta(t)$ is the curve defining the cross section of the cone. This equation shows that the ruling lines intersect at the apex of the cone. Since developable surfaces cannot have intersecting ruling lines, this point defines a boundary of a developable surface. Thus, the parametric equation for a generalized cone depicts two conical developable surfaces separated at a shared apex. We can denote a single generalized conical developable surface by limiting the parameter u to the domain $[0,\infty)$ or $(-\infty,0]$. We will call a generalized cone with $u \in [0,\infty)$ the forward parametrization, $\mathbf{r}_f(t,u)$, and with $u \in (-\infty,0]$ the reverse parametrization, $\mathbf{r}_r(t,u)$.

Lastly, a tangent developable surface commonly takes the form

$$\mathbf{r}(t,u) = \alpha(t) + u\alpha'(t) \tag{5.6}$$

where $\alpha(t)$ is the equation of the edge of regression off of which tangent lines radiate to form the ruling lines of the surface. The direction of the ruling lines and tangent lines to the edge of regression are equivalent, as seen in the relation of $\beta(t) = \alpha'(t)$. The edge of regression and apex of generalized cones are sometimes referred to as focal curves of the surface [135]. Here we assume $\alpha(t)$ has C^1 continuity. If $\alpha(t)$ is not C^1 continuous, we consider the tangent developable to be a combination of two or more tangent developables where $\alpha(t)$ is C^1 continuous.

As with the generalized cone parametric equation, allowing u to vary from $(-\infty, \infty)$ results in intersecting ruling lines from two tangent developable surfaces. By limiting the domain of u to $[0, \infty)$ or $(-\infty, 0]$ we can separate the two tangent developable surfaces. We will denote these, as with generalized cones, as the forward and reverse parametrizations respectively. Observe that a forward parametrization of a tangent developable has the ruling line direction and edge of regression tangent collinear, while in a reverse tangent developable parametrization the ruling lines radiate away from the edge of regression in the direction opposite the edge of regression tangent. These two parametrizations for tangent developable surfaces are shown in Fig. 5.3. This differentiation will be useful later in the chapter.

A unit surface normal vector exists for orientable developable surfaces (which includes all topological discs) [136]. The standard unit normal [136] can be found using

$$\mathbf{U}(t,u) = \frac{\mathbf{r}_t(t,u) \times \mathbf{r}_u(t,u)}{\|\mathbf{r}_t(t,u) \times \mathbf{r}_u(t,u)\|} \tag{5.7}$$

where $\mathbf{r}_t(t,u)$ and $\mathbf{r}_u(t,u)$ are the partial derivatives of the surface $\mathbf{r}(t,u)$ with respect to t and u, respectively. While $-\mathbf{U}(t,u)$ also represents an equally valid surface normal, to avoid ambiguity Eq. 5.7 is used to specify a particular side of a surface with a positive surface normal. Also, for developable surfaces the surface normal does not vary along a ruling line and thus u does not appear on the right side of Eq. 5.7. Therefore we will sometimes write the surface normal as a function of a single parameter, $\mathbf{U}(t)$. In this chapter, whenever a surface normal for a parametrically defined surface is referred to, it will be the standard unit normal following the form of Eq. 5.7.

As developable surfaces describe many 3D objects created from planar stock materials, various computational representations and approximations for these surfaces have been created such as in [23, 137]. One method that is related most closely to this chapter is approximating devel-

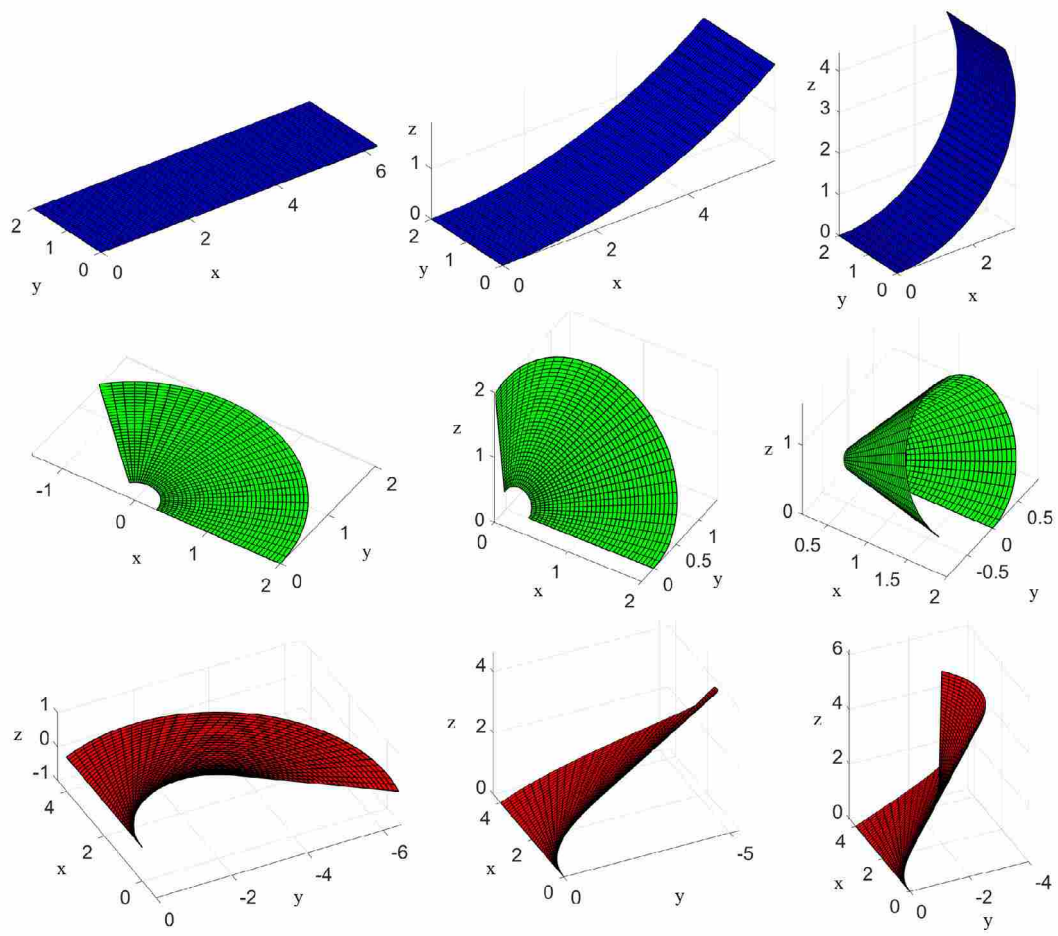

Figure 5.2: The three curved classes of developable surfaces: generalized cylinder (blue), generalized cone (green), and tangent developable (red) shown folding (increasing the magnitude of the ruling curvature) from left to right.

opable surfaces with cone splines [138, 139]. In this work osculating cones are defined and used to approximate developable surfaces and manipulate them. Another work uses both the Darboux and Frenet-Serret frames to describe parametrically defined ruled surfaces and investigates some interesting properties of these surfaces such as the pitch and angle of pitch of the surface [140].

5.3 Natural Equations of Rigid-Ruling Single-Class Developable Surfaces

For the set of natural equations that is developed in this chapter we desire to have a single natural measure for the direction of the ruling lines in a developable surface and another measure describing the rigid-ruling folding of the developable surface from a plane. These two measures take the form of the geodesic curvature and ruling (principal) curvature of a cross curve.

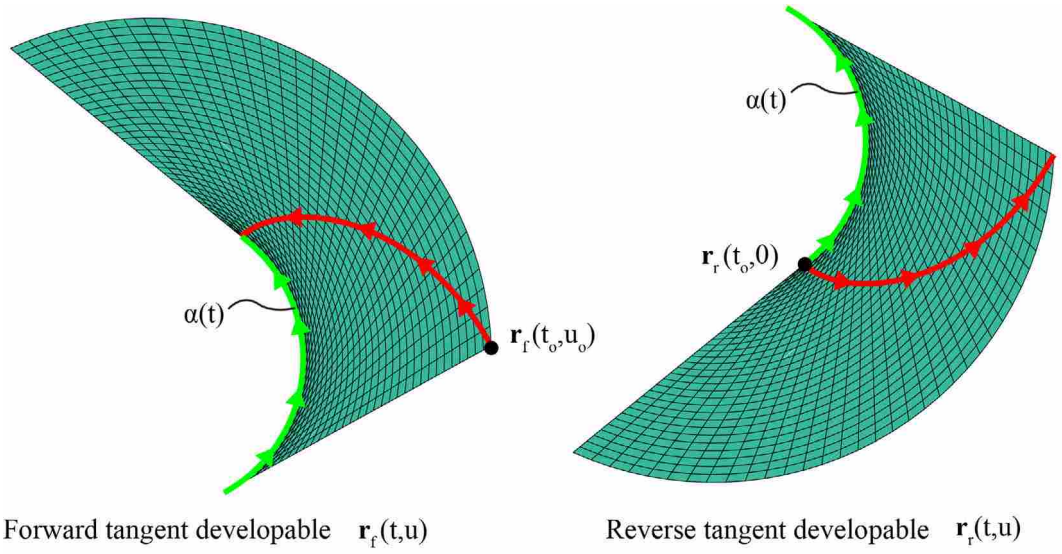

Figure 5.3: Forward and reverse parametrizations for tangent developable surfaces where the direction of the edge of regression (green) and cross curves (red) are shown with arrows.

5.3.1 Cross Ruling Principal Curves (Cross Curves)

A developable surface contains an infinite family of principal curves which cross orthogonally to the ruling lines. A *cross ruling principal curve* (cross curve) is a single curve of our choosing in this family. The geodesic curvature, κ_g, of a cross curve gives the direction of the ruling lines in the developable surface. The geodesic curvature of a cross curve is constant for all folded forms of a rigid-ruling pattern. It is helpful to visualize how the geodesic curvature determines the direction of the ruling lines in the surface by thinking about developing or unrolling the surface into a plane. The geodesic curvature of a cross curve is equivalent to the curvature of the planar (developed) cross curve. Because a cross curve is a principal curve we can draw the ruling lines of the surface by drawing lines orthogonal to this planar curve. Let us look at how the ruling lines are described by the geodesic curvature for each class of developable surface.

For a generalized cylinder the geodesic curvature of a cross curve is $\kappa_g = 0$. A single cross curve is shown in Fig. 5.4 where on the left the surface is developed (so κ_g is the curvature of the planar curve resulting in a straight line) and is in the formed shape on the right.

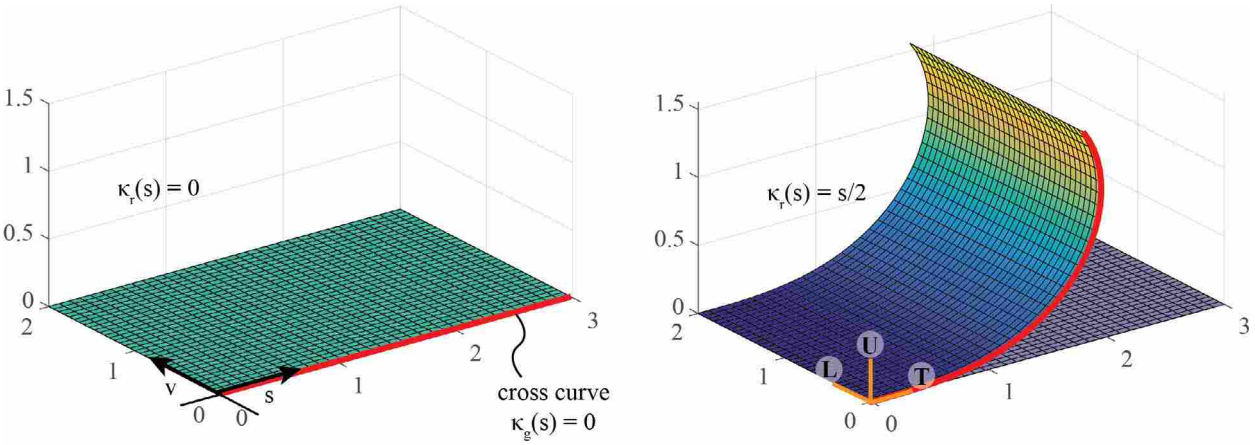

Figure 5.4: Generalized cylinder flat (left) and formed (right) with a cross curve (red) and the Darboux frame (orange).

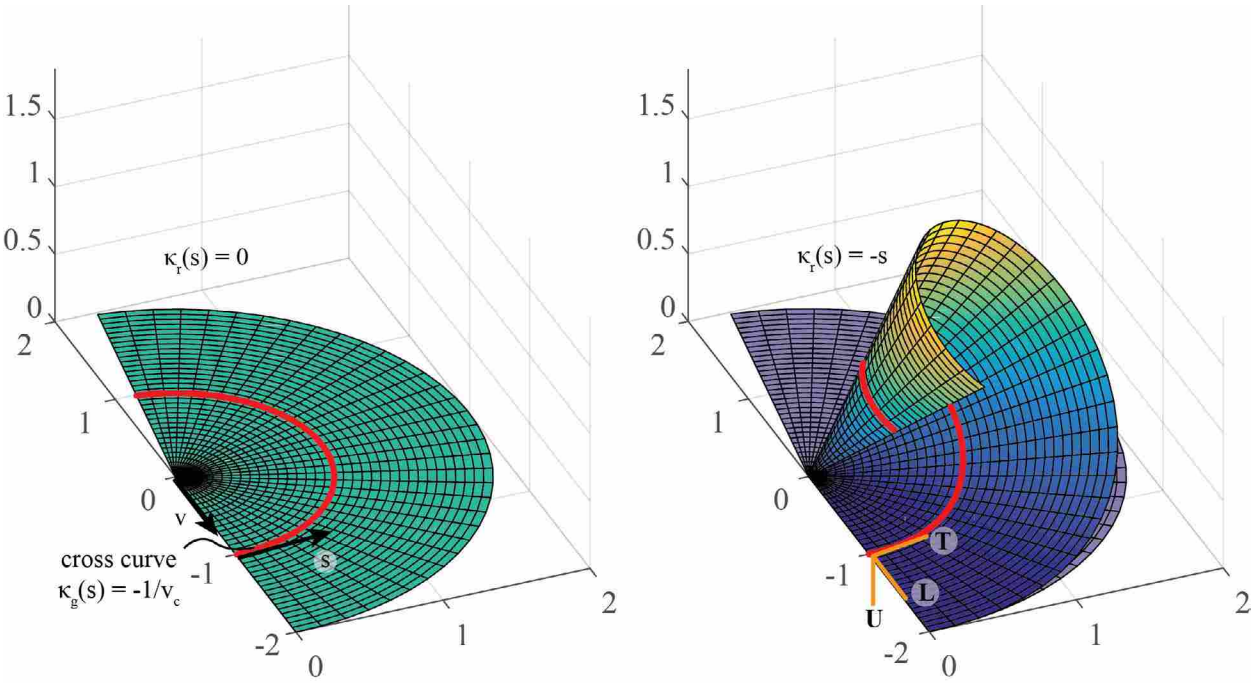

Figure 5.5: Generalized Cone flat (left) and formed (right) with a cross curve (red) and the Darboux frame (orange).

For a generalized cone $\kappa_g = 1/v_c$ where v_c is the distance from the apex of the cone to a cross curve. This cross curve is an arc of constant radius v_c when the surface is developed and is shown on the left side of Fig. 5.5 and in the 3D form on the right.

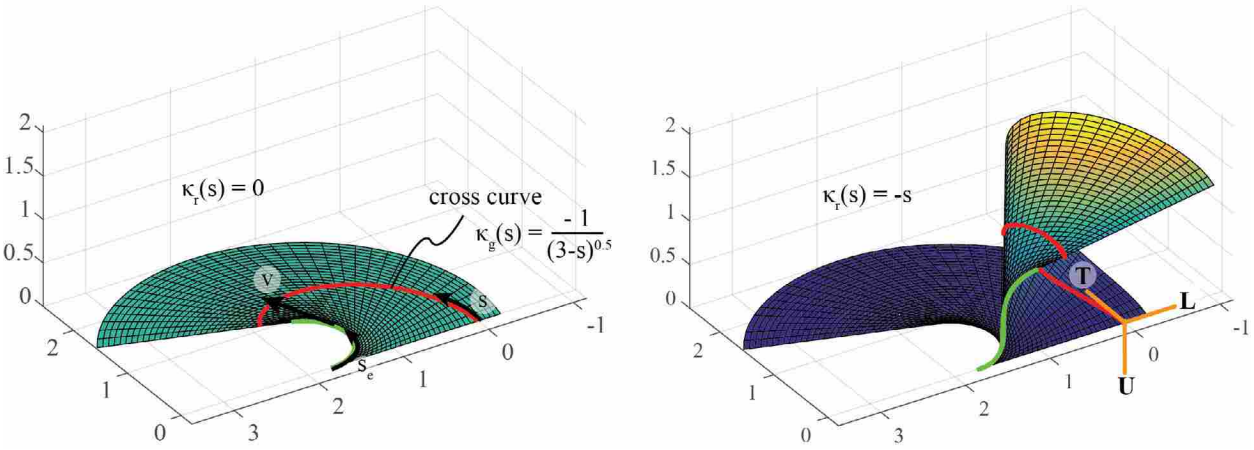

Figure 5.6: Tangent developable flat (left) and formed (right) with a cross curve (red) and the Darboux frame (orange).

For a tangent developable surface a cross curve of arc length s has geodesic curvature $\kappa_g(s)$. This function should have C^1 continuity, be increasing or decreasing, and should not change signs as the edge of regression which will be derived from this function should be convex or concave to form a single tangent developable surface. A cross curve with $\kappa_g(s) = -1/(3-s)^{0.5}$ with $s \in [0, 2.9]$ for a tangent developable is shown on the left side of Fig. 5.6 in the developed state and on the right in a formed state.

We will see later that we can either select a cross curve on a surface to write a set of natural equations for a surface or alternatively write the natural equations for a cross curve to generate a developable surface. The choice of which cross curve to use with the natural equations can be made by looking at which curve will be most convenient for a particular application.

5.3.2 Canonical Developable Parametrizations

It is useful to adjust the parametrizations given by Eqs. 5.4, 5.5, or 5.6 in Sec. 5.2.5 to create a *canonical parametrization* [118]. For this parametrization we require an arc-length parametrization for parameter u. By examining Eq. 5.3 we see that it is impossible to write an arc-length parametrization for both parameters of a ruled surface as the two parameters interact with each other. However, we can write an arc-length parametrization for u easily for any ruled surface by normalizing $\beta(t)$, denoting the normalized vector as $\hat{\beta}(t)$. Let us denote the arc length along a ruling line with the parameter v. Additionally we require certain conditions for $\alpha(t)$ and represent the

new canonical directrix as $\hat{\alpha}(t)$. For generalized cylinders $\hat{\alpha}(t)$ is perpendicular to $\hat{\beta}(t)$. For cones $\hat{\alpha}(t)$ is the cone-apex position vector. Lastly for tangent developables $\hat{\beta}(t) = \hat{\alpha}'(t)$. In summary, the canonical parametrization for developable surfaces symbolically is

$$\mathbf{r}(t,v) = \hat{\alpha}(t) + v\hat{\beta}(t) \tag{5.8}$$

where v is the arc length measured along the ruling lines from the directrix.

For this chapter's purposes we are interested in letting $\mathbf{r}(t, c_v(t))$ correspond to a cross curve where $c_v(t)$ is a function describing the distance along the ruling line at t from the directrix to the cross curve. This is accomplished with the expression

$$c_v(t) = \frac{-1}{\kappa_g(t)} \tag{5.9}$$

where $\kappa_g(t)$ is the signed geodesic curvature of a cross curve. The surface normal used to define the sign of the geodesic curvature is the standard unit surface normal from Eq. 5.7 applied to Eq. 5.8.

For generalized cylinders since $\kappa_g = 0$ Eq. 5.9 is undefined. We can interpret this to mean that for generalized cylinders $c_v(t)$ can be equal to any constant and still describe a cross curve with $\kappa_g = 0$. This is because with generalized cylinders all cross curves have the same geodesic curvature (zero).

For a parametric equation in the form of Eq. 5.8 with the surface normal given by Eq. 5.7 a forward generalized cone parametrization has a negative κ_g or equivalently v_c. If κ_g or equivalently v_c is positive we have a reverse generalized cone parametrization.

For parametric equations in the form of Eq. 5.8 where $\hat{\beta}(t) = \hat{\alpha}'(t)$ with the surface normal given by Eq. 5.7 forward tangent developable parametrizations have a negative $\kappa_g(t)$, reverse tangent developable parametrizations have a positive $\kappa_g(t)$, while both parametrizations have a negative $\kappa_g'(t)$, the derivative of $\kappa_g(t)$ with respect to t. If these conditions are not met for $\kappa_g(t)$ it is impossible to describe the surface in the form of Eq. 5.8 where $\hat{\beta}(t) = \hat{\alpha}'(t)$ with the surface normal given by Eq. 5.7.

5.3.3 Ruling Curvature

With the direction of the ruling lines in the surface defined with a cross curve's geodesic curvature, it is useful to define another natural measure for a cross curve, the *ruling curvature*. The ruling curvature measures the formed or folded shape of a rigid-ruling developable surface. As bending can only occur across a ruling line we define the ruling curvature of a cross curve, $\kappa_r(t)$, to describe the deviation of a surface from a plane as we move transversely across a ruling lines along a cross curve. While this curvature is equal to the non-zero principal curvature of a developable surface at a point we give it a name, the ruling curvature, to emphasize it is a curvature for a curve rather than a surface curvature as well as to emphasize importance for theoretical as well as practical purposes.

Since the ruling curvature of a cross curve is the non-zero principal curvature it can be calculated the same way as the principal curvature of a surface. This process involves finding the roots of a characteristic equation from a determinant composed of the coefficients of the first and second fundamental forms of a parametric surface as described in [141]. We can also find the ruling curvature along a specific cross curve, $\mathbf{r}(t, c_v(t))$ as

$$\kappa_r(t) = -\frac{1}{\dot{s}} \frac{\mathrm{d}\mathbf{U}(t)}{\mathrm{d}t} \cdot \mathbf{T}(t) \tag{5.10}$$

where $\mathbf{U}(t)$ is the unit surface normal as one moves along the cross curve, $\mathbf{T}(t)$ the unit tangent vector to the cross curve, and $\dot{s}$ is the curve speed of the cross curve ($\dot{s} = \|\dot{\mathbf{r}}(t, c_v(t))\|$) where $dotr$ is the derivative with respect to t. Because the cross curve is orthogonal to the ruling lines, the vector $\frac{\mathrm{d}\mathbf{U}(t)}{\mathrm{d}t}$ and $\mathbf{T}$ are aligned. Since $\mathbf{T}(t)$ is a unit vector the ruling curvature has a magnitude equal to the magnitude of vector $\frac{\mathrm{d}\mathbf{U}(t)}{\mathrm{d}t}$.

The sign of the ruling curvature behaves like that of the normal and principal curvatures. A positive ruling curvature denotes that the surface curves towards the direction the surface normal is pointing. A negative ruling curvature denotes that the surface bends away from the direction the surface normal points. Figure 5.1 shows a conical developable surface with positive ruling curvature.

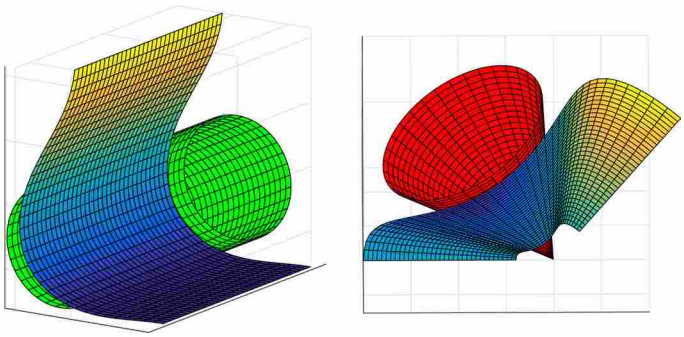

Figure 5.7: On the left a generalized cylinder with the osculating cylinder (green) shown for a single ruling line and on the right a generalized cone with the osculating cone (red) shown for a single ruling line.

5.3.4 Osculating Shapes

Intuition for the ruling curvature measure can be developed by examining physical interpretations of the non-zero principal curvature, κ_1, for each class of developable surface as the ruling curvature at a point on a cross curve is equal to the non-zero principal curvature at that point.

For a generalized cylinder κ_1 can be related to an osculating right circular cylinder, much as an osculating circle is related to the curvature of a curve. An osculating cylinder of a generalized cylinder at a given ruling line can be defined as a right circular cylinder that shares the given ruling line, has the same tangent plane along the ruling line as the generalized cylinder, and has the same maximum principal curvature along that ruling line as the generalized cylinder. Figure 5.7 shows an osculating cylinder for a single ruling line of a generalized cylindrical surface. The radius of the osculating cylinder, $R(t)$, for every ruling line in a generalized cylinder is (see A.1.1 for derivation)

$$R(t) = \pm \frac{1}{\kappa_r(t)} \tag{5.11}$$

For a generalized cone it can be shown that the non-zero principal curvature of a cone varies as $1/v$ from the apex of the cone. Therefore the curvature defines an osculating right circular cone. This osculating cone of a generalized cone at a given ruling line is a right circular cone that shares the given ruling line and conical apex, has the same tangent plane along the ruling line as the generalized cone, and has the same maximum principal curvature variation along the ruling line as the generalized cone. Note that the maximum principal curvature along ruling lines decreases as one moves away from the apex of the cone. This decrease is equivalent for the shared ruling line

of both the generalized conical surface and the osculating cone. Figure 5.7 shows an osculating right circular cone for a single ruling line on a generalized conical surface.

The osculating cone can be characterized by the angle between the osculating cone's ruling lines and cone axis, ϕ. This angle is related to the ruling curvature of a cross curve $\kappa_g(t) = 1/v_c$ as (see A.1.2 for derivation)

$$\phi(t) = \tan^{-1}\left(\frac{-1}{v_c(\kappa_r(t))}\right) \tag{5.12}$$

Similar to a generalized cone, κ_1 along a tangent developable surface can be shown to vary along a ruling line as $1/v$. Therefore, we can use the ruling curvature to define either an osculating helical tangent developable or an osculating cone [142]. Figure 5.8 shows a tangent developable surface patch with the osculating circular helical tangent developable for a single ruling line. There exists a family of osculating helical tangent developables for a given ruling line in a tangent developable surface. This family is characterized by a constant ratio of τ/κ where τ is the torsion and κ the unsigned curvature of the helix corresponding to the edge of regression of the osculating helical tangent developable. We can find this ratio with the expression (see A.1.3 for derivation)

$$\frac{\tau(t)}{\kappa(t)} = \frac{\kappa_r(t)}{\kappa_g(t)} \tag{5.13}$$

The osculating cone for a tangent developable surface characterized by the angle between the osculating cone's ruling lines and cone axis, ϕ, is (see A.1.4 for derivation)

$$\phi(t) = \tan^{-1}\left(\frac{-\kappa_g(t)}{\kappa_r(t)}\right) \tag{5.14}$$

An osculating cone for a tangent developed surface is shown in Fig. 5.8.

5.3.5 Ruling Curvature Related to Principal Curvature Variation

The ruling curvature of a cross curve can be used to describe the variation in the principal curvature as one moves along a ruling line for all three curved classes of developable surfaces. The principal curvature is often of interest in engineering applications as it is proportional to the

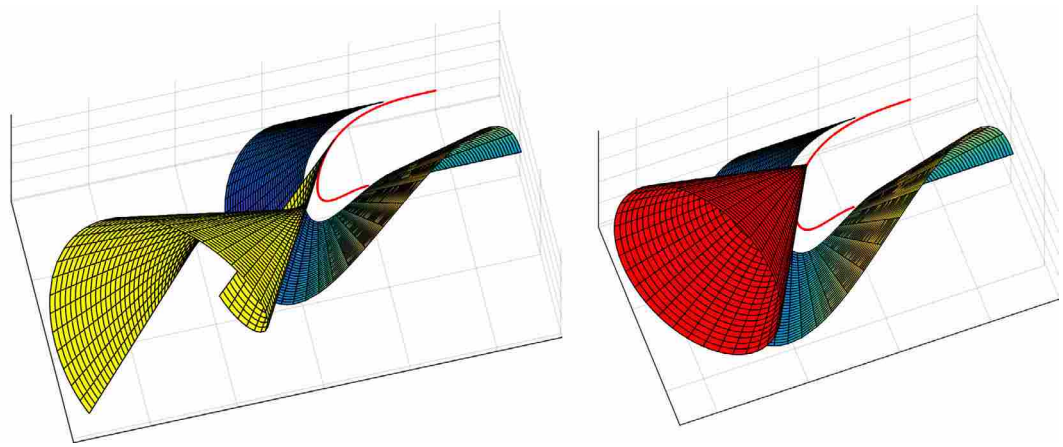

Figure 5.8: A tangent developable surface patch (the edge of regression for the surface is the red curve) with the osculating helical tangent developed (orange) shown for a single ruling line and the equivalent osculating cone (red).

bending stress in a surface [29]. A.1.5 contains derivations for the equations in this section. For generalized cylinders there is no variation in the principal curvature along a ruling line so the ruling curvature is the principal curvature along a ruling line.

For conical surfaces the variation of the principal curvature as one moves along a ruling line at t is

$$\kappa_1(v) = -\kappa_r(t)v_c\left(\frac{1}{v}\right) \tag{5.15}$$

where κ_1 is the non-zero principal curvature of the developable surface, $\kappa_r(t)$ is the ruling curvature of the cross curve at t, v_c is the radius of the cross curve, and v is the position along the ruling line. Or in terms of the osculating cone's opening half angle ϕ

$$\kappa_1(v) = \cot(\phi)\left(\frac{1}{v}\right) \tag{5.16}$$

For a tangent developable surface the variation of the principal curvature as one moves along a ruling line at t is

$$\kappa_1(v) = -\frac{\kappa_r(t)}{\kappa_g(t)}\left(\frac{1}{v}\right) \tag{5.17}$$

Or in terms of the osculating helical tangent developable

$$\kappa_1(v) = -\frac{\tau(t)}{\kappa(t)}\left(\frac{1}{v}\right) \tag{5.18}$$

where κ and τ are the parameters for the helix which is the edge of regression of the osculating helical tangent developable, and v is the position along the ruling line.

5.3.6 Developable Surface Formulas

We can write a simplified version of the Darboux formulas for the **T**, **L**, **U** frame moving along a cross curve in terms of natural properties for a developable surface. Because a cross curve is a principal curve and a principal curve points in the principal direction [16, 133] we can write

$$\tau_g = 0 \tag{5.19}$$

Because $\tau_g = 0$ the Darboux frame moving along a principal curve also qualifies as a rotation-minimizing frame [143].

Further we note that the normal curvature κ_n along a principal curve is one of the principal curvatures (and also ruling curvature) so

$$\kappa_n = \kappa_r \tag{5.20}$$

Simplifying the Darboux formulas in this way give what we will call the developable surface formulas and they are written symbolically as

$$\begin{aligned}
\frac{\mathrm{d}\mathbf{T}}{\mathrm{d}t} &= \dot{s}\left(\kappa_g\mathbf{L} + \kappa_r\mathbf{U}\right) \\
\frac{\mathrm{d}\mathbf{L}}{\mathrm{d}t} &= -\dot{s}\kappa_g\mathbf{T} \\
\frac{\mathrm{d}\mathbf{U}}{\mathrm{d}t} &= -\dot{s}\kappa_r\mathbf{T}
\end{aligned} \tag{5.21}$$

where $\mathrm{d}/\mathrm{d}t$ is the derivative with respect to parameter t, κ_r is the ruling curvature of a cross curve, κ_g is the geodesic curvature of the same cross curve, and $\dot{s}$ is the curve speed of the cross curve.

This set of equations can be written concisely in matrix form as

$$\begin{bmatrix} \mathbf{T}' \\ \mathbf{L}' \\ \mathbf{U}' \end{bmatrix} = \dot{s} \begin{bmatrix} 0 & \kappa_g & \kappa_r \\ -\kappa_g & 0 & 0 \\ -\kappa_r & 0 & 0 \end{bmatrix} \begin{bmatrix} \mathbf{T} \\ \mathbf{L} \\ \mathbf{U} \end{bmatrix} \tag{5.22}$$

where the derivative of the vectors is with respect to the parameter t of the cross curve and the matrix is noted to be skew symmetric.

5.3.7 Natural Equations for Generalized Cylinders

A generalized cylinder can be expressed with two natural equations using the natural measures of ruling curvature and geodesic curvature of a chosen cross curve as

$$\begin{aligned} \kappa_g &= 0 \\ \kappa_r &= \kappa_r(s) \end{aligned} \tag{5.23}$$

where κ_g is the geodesic curvature of the cross curve (zero) and $\kappa_r(s)$ is the ruling curvature as a function of the arc length of the cross curve s.

Figure 5.4 shows how each of these natural equations characterize a generalized cylinder. A cross curve, which defines the direction of ruling lines in the developable surface, is a straight line ($\kappa_g = 0$) of length s for a planar surface ($\kappa_r = 0$). The ruling curvature describes how much the surface bends from a planar state, or in other words how folded the developable surface is into a 3D state. In the left of the figure the generalized cylinder is shown with $\kappa_r(s) = 0$ while on the right of the figure the generalized cylinder is shown folded from its flat state (shown in blue) to its formed state with $\kappa_r(s) = s/2$.

Generalized Cylinders: From Natural Equations to a Canonical Parametrization

We move from the natural equations of a generalized cylinder to a canonical parametrization given by Eq. 5.8 using the developable surface formulas given by Eqs. 5.21. This system of first order ordinary differential equations can be solved (numerically if need to be) to find **T**, **L**, and **U** as functions of s. Note that since the geodesic and ruling curvature functions were defined

using the arc length of the cross curve s, our curve speed $\dot{s} = 1$. We can then relate these vectors to the canonical parametric equation for a developable surface given in Eq. 5.8 by

$$\begin{aligned} \hat{\alpha}(s) &= \hat{\alpha}(s_o) + \int_{s_o}^{s} \mathbf{T}(w)\, dw \\ \hat{\beta}(s) &= \mathbf{L}(s) \end{aligned} \tag{5.24}$$

where $\hat{\alpha}(s_o)$ is an arbitrary vector determining the initial location of the directrix. Once we have Eq. 5.8 we can locate the surface in a coordinate system using Euclidean transformations.

5.3.8 Natural Equations for Generalized Cones

A generalized cone can be expressed using the natural equations

$$\begin{aligned} \kappa_g &= \frac{1}{v_c} \\ \kappa_r &= \kappa_r(s) \end{aligned} \tag{5.25}$$

where κ_g is the geodesic curvature of a cross curve, v_c is the radius of the cross curve, and $\kappa_r(s)$ is the ruling curvature as a function of the arc length of the cross curve s. As mentioned previously, a negative κ_g results in a forward parametrization while a positive κ_g results in a reverse parametrization with the surface normal defined by Eq. 5.7.

Figure 5.5 shows a planar generalized cone ($\kappa_r = 0$) with a cross curve defining the cone's ruling lines on the left and then shows how this cone is formed into a 3D shape controlled by the ruling curvature equation on the right.

Generalized Cones: From Natural Equations to a Canonical Parametrization

To move from the natural equations given by Eq. 5.25 to a canonical parametrization of a generalized cone we use the developable surface formulas given by Eqs. 5.21. Like with the natural equations for generalized cylinders this system of first order ordinary differential equations can be solved to find $\mathbf{T}$, $\mathbf{L}$, and $\mathbf{U}$ as functions of s. These vector valued functions are related to the canonical equation for a developable surface from Eq. 5.8 by

$$\begin{aligned}\hat{\alpha}(s) &= \hat{\alpha} \\ \hat{\beta}(s) &= \mathbf{L}(s)\end{aligned} \tag{5.26}$$

where $\hat{\alpha}$ is a vector to the desired cone tip location.

5.3.9 Natural Equations for Tangent Developables

A tangent developable surface can be expressed using the natural equations

$$\begin{aligned}\kappa_g &= \kappa_g(s) \\ \kappa_r &= \kappa_r(s)\end{aligned} \tag{5.27}$$

where $\kappa_g(s)$ is geodesic curvature of a cross curve and $\kappa_r(s)$ is the ruling curvature both as functions of arc length of the cross curve s. As mentioned before to form a tangent developable surface $\kappa_g(s)$ must not change sign, have C^1 continuity, and be always increasing or decreasing. Further for a canonical parametrization with the surface normal defined by Eq. 5.7 with $\hat{\beta}(t) = \hat{\alpha}'(t)$ a negative $\kappa_g(s)$ results in a forward tangent developable parametrization, a positive $\kappa_g(s)$ gives a reverse tangent developable parametrization, and both have a negative $\kappa'(g)$.

Figure 5.6 shows a cross curve for a flat tangent developed surface on the left and shows how the ruling curvature equation causes the surface to fold into a 3D shape on the right.

Tangent Developables: From Natural Equations to a Canonical Parametrization

Similar to both generalized cylinders and cones we use the developable surface formulas given by Eqs. 5.21 to solve for **T**, **L**, and **U**. We can use these results to write a canonical parametric equation for the tangent developed surface in the form of Eq. 5.8 as

$$\begin{aligned}\hat{\alpha}(s) &= \mathbf{C}(s_o) + \int_{s_o}^{s} \mathbf{T}(w)\, dw + \frac{1}{\kappa_g(s)}\mathbf{L}(s) \\ \hat{\beta}(s) &= \mathbf{L}(s)\end{aligned} \tag{5.28}$$

where $\mathbf{C}(s_o)$ is an arbitrary vector to the location of the cross curve's initial point.

Sometimes it is desirable to write a canonical parametric equation for tangent developable surface patches where the edge of regression is written in an arc-length parametrization rather than the cross curve. This can be accomplished through traditional methods of integrating the magnitude of the derivative of the directrix, $\hat{\alpha}(s)$, and inverting the expression. However, we can use the unique relation of a cross curve being an involute of the edge of regression to obtain the relation between arc lengths of a cross curve, s, and arc length of the edge of regression, s_e. For a forward tangent developed surface the relationship is

$$s_e = \frac{1}{\kappa_g(s)} - \frac{1}{\kappa_g(s_o)} \tag{5.29}$$

where $\kappa_g(s_o)$ is the geodesic curvature of a cross curve at the starting point of the cross curve (see Fig. 5.3 point $\mathbf{r}_f(t_o, u_o)$).

For a reverse tangent developable surface the relationship is

$$s_e = \frac{1}{\kappa_g(s)} \tag{5.30}$$

These relations can be solved for s and substituted into the canonical parametric equation given by Eq. 5.8 to give an arc-length parametrization for the edge of regression rather than the principal curve.

5.3.10 From a Surface to its Natural Equations

It is not uncommon to start with a known curved developable surface and to desire information about its unfolded flat state or how it folds in a rigid-ruling fashion to its formed state. This information can be found in the surface's natural equations. If one knows the parametric equations of a formed developable surface in the form of Eqs. 5.4, 5.5, or 5.6 a set of natural equations can be found as described below.

A cross curve $\mathbf{C}(t)$ is selected on the surface by letting the parameter describing the position along the ruling lines, u, be equal to a constant of one's choice for generalized cylinders and cones.

For tangent developables a particular cross curve is chosen by writing the equation for an involute of the edge of regression, $\hat{\alpha}$. For forward tangent developables a cross curve passing through the point $\mathbf{r}(t_o, u_o)$ is

$$\mathbf{C}(t) = \hat{\alpha}(t) + (u_o - s(t_o, t))\hat{\alpha}'(t) \tag{5.31}$$

where u_o is the distance to the selected cross curve at t_o (as shown in Fig. 5.3), and $s(t_o, t)$ is the arc length function of $\hat{\alpha}(t)$. For reverse tangent developables a cross curve passing through the point $\mathbf{r}(t_o, 0)$ is written as

$$\mathbf{C}(t) = \hat{\alpha}(t) - s(t_o, t)\hat{\alpha}'(t) \tag{5.32}$$

where t_o specifies the point at which the cross curve intersects the directrix (see Fig. 5.3).

The set of natural equations for the chosen cross curve on the surface is found using Eq. 5.10 and

$$\kappa_g(t) = -\frac{1}{\dot{s}}\frac{\mathrm{d}\mathbf{L}(t)}{\mathrm{d}t} \cdot \mathbf{T}(t) = -\frac{1}{\dot{s}}\frac{\mathrm{d}(\mathbf{U}(t) \times \mathbf{T}(t))}{\mathrm{d}t} \cdot \mathbf{T}(t) \tag{5.33}$$

where $\mathbf{T}(t)$ is the unit tangent to the cross curve, $\mathbf{U}(t)$ is the unit surface normal along the cross curve, and $\dot{s}$ is the cross curve speed.

With these equations one now knows the planar state of the developable as described by the planar cross curve with the parameter $\kappa_g(t)$ and a measure of how folded the formed surface is with $\kappa_r(t)$.

5.4 Results and Discussion

The natural equations for developable surfaces presented in this chapter provide a concise and meaningful way to describe a developable surface of a single-class. In many instances developable surfaces are used as they can be manufactured in a plane and folded into shape. However, information for the planar state of a developable surface and its rigid-ruling folding can be difficult to access directly from the traditional parametrization for representing developable surfaces. The natural equations presented here can provide a new tool for use in industries where developable surfaces play a critical role such as curved-fold origami, boat hull design, clothing and shoe con-

struction, sheet metal rolling, architecture, and recent applications such as mechanism design [57] and folding of 3D printed medical structures [144].

By using the geodesic curvature and ruling curvature of a cross curve as the natural measures in the natural equations of developable surfaces, a designer can have a strong understanding of how to mathematically describe and also manufacture a desired surface. For example, designers can connect the flat, or developed, surface which forms into a desired 3D surface by letting the ruling curvature equation be equal to zero and computing the planar surface. The rigid-ruling folding of the surface can be modeled and visualized by allowing the ruling curvature to increase to its final desired values.

There is a strong parallel between the developable surface formulas given by Eqs. 5.21 and the Frenet-Serret Formulas. Careful selection of the Darboux frame enabled this parallel where the natural equations of developable surfaces in terms of the geodesic curvature and ruling curvature of a cross curve correspond to space curves being denoted by their curvature and torsion. This formulation helps to see how this description of rigid-ruling developable surfaces fits between the natural equations for a space curve and the fundamental forms which are expressed in natural measures describing an arbitrary surface.

A collection of surfaces given by natural equations are shown in their flat and folded states in Fig. 5.9. This figure shows a sampling of the variety of surfaces that can be concisely described and easily mapped to their developed state using natural equations.

The first row of Fig. 5.9 shows surfaces whose ruling curvature is defined with a cosine function. The second row shows the three curved classes of developable surfaces where the ruling curvature is the curvature of a logarithmic spiral with the polar equation

$$r = e^{0.4\theta} \tag{5.34}$$

The equation for the third row's ruling curvature was generated by fitting a curve to points describing the relationship between the arc length and curvature of a parabola with the distance from the focal point to the base of the parabola as a variable a. This curve fit was parametrized such that it has an error of less than $\pm 5 \times 10^{-4}/a$ for κ_r (which is to the curvature of the parabola) for arc lengths $s \leq 27.8075a$. This curve fit is given by

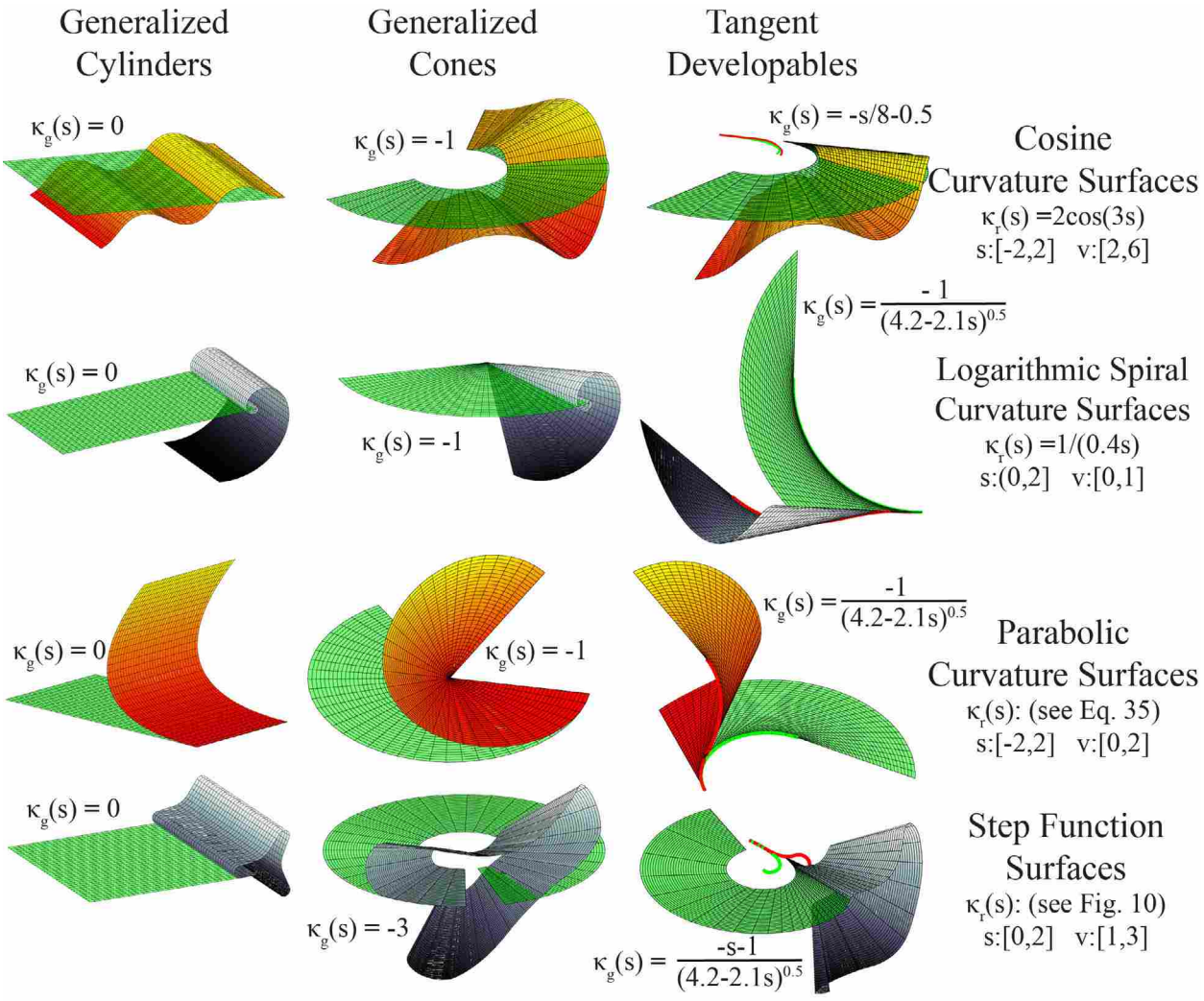

Figure 5.9: A collection of developable surfaces expressed by their natural equations in both their formed states ($\kappa_r = \kappa_r(s)$) shown with the colored surfaces and their planar states ($\kappa_r = 0$) shown with the transparent green surfaces. Four types of functions for $\kappa_r(s)$ as listed on the right were plotted for each of the three curved classes of developable surfaces. For the tangent developables the edge of regression is shown for the planar state in green and for the formed state in red. The range plotted for the parameters s and v is also given.

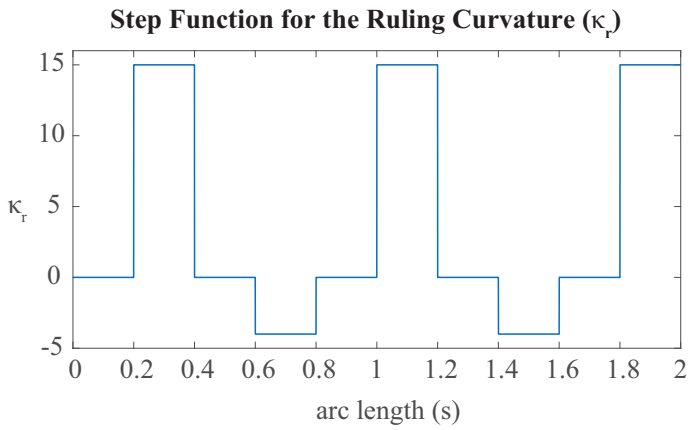

Figure 5.10: The step function used as $\kappa_r(s)$ in the fourth row of Fig. 5.9.

$$\kappa_r(s) = \frac{0.07264\,|s| + 1.272a}{s^2 + 0.1371\,|s|\,a + 2.544a^2} \tag{5.35}$$

where a is the distance from the focal point to the base of the parabola. In creating Fig. 5.9 we chose $a = 0.3$.

The fourth row surfaces in Fig. 5.9 were generated with a step function as the ruling curvature function. This step function is shown in Fig. 5.10.

5.5 Conclusions

Specific developable surfaces for each of the three curved classes of developable surfaces can be expressed concisely using natural equations in terms of the geodesic curvature of a cross curve to describe the arrangement of the ruling lines and the ruling curvature of the same cross curve to describe the bending of the surface about the ruling lines. While this chapter investigates natural equations for a single class of developable surfaces, further work can be done to concisely express composite developable surfaces (surfaces made of two or more classes of developable surfaces joined together). The natural measures used in the natural equations set forth in this chapter carry physical meanings that enable strong intuition between the natural equations and the physical shape they create. These equations can provide succinct representations and straightforward rigid-ruling folding modeling for many applications which rely on developable surfaces ranging from computer graphics to sheet metal rolling.

CHAPTER 6. DEVELOPABLE COMPLIANT-AIDED ROLLING-CONTACT MECHANISMS

[1]With the natural equations of developable surfaces presented in the last chapter we are prepared to use this representation to extend the design space of rolling-contact joints. When a specific class of developable surface is used in a mechanism or structure, it presents an opportunity for the designer to explore new variations and even new functionality by considering other classes or combined classes of developable surfaces in place of the surface presently in use. The natural equations for developable surfaces present a convenient tool to facilitate this exploration for not only all the classes or developable surfaces, but every possible folded shape of the surface.

We also introduce in this chapter the idea of adding stiffness, prestress, and/or changing geometry to the components of rolling-contact joints to achieve specific force-displacement responses.

6.1 Introduction

Rolling-contact mechanisms are characterized by surfaces exhibiting pure rolling relative to each other to create relative motion between bodies. These types of mechanisms have proven useful in applications where unique motion paths are required, friction needs to be kept to a minimum, and under high compressive loads. For example, an artificial disc replacement rolling mechanism was created for degenerated vertebral discs that mimics the motion of a healthy disc [102]. Compliant-aided rolling-contact mechanisms use flexible bands or segments to help enforce the rolling constraint. Existing compliant-aided rolling-contact mechanisms commonly utilize cylindrical rolling surfaces to achieve motion [94, 145, 146]. Recently rolling-contact joints created from generalized cylindrical surfaces, surfaces formed from translating a generator line such that all ruling lines on the surface are parallel to each other, were employed to create the required panel

[1]This chapter has been accepted for publication as Nelson, T.G., Herder, J.L., Developable Compliant-Aided Rolling-Contact Mechanisms, *Mechanism and Machine Theory*, MECHMT_2018_146, (Accepted April 14, 2018)

offsets for a thickness accommodation technique for origami vertices [147]. In addition Lang et al. set forth theorems for 3D rolling motion [147]. This chapter presents a method that illustrates how developable surfaces can be used to design a family of compliant-aided rolling-contact mechanisms with both planar and 3D motion. Specific kinetic responses can also be designed by modifying the stiffness of the flexible bands and curvature of the rolling surfaces [99].

In Section 6.2 we give a brief background of rolling mechanisms and developable surfaces. In Section 6.3 we set forth a mathematical notation for developable surfaces convenient for rolling contacts, discuss how rolling-contact mechanisms can be created using developable surfaces as a basis, give kinematic and kinetic models, and discuss a special case force response, static balance. In Section 6.4 we show several rolling-contact mechanisms and discuss their construction. Lastly we close with a final discussion and mention areas of potential future work.

6.2 Background

6.2.1 Rolling-contact Mechanisms

Mechanisms incorporating rolling into their motion can provide unique benefits for engineering applications. For example, ball and other rolling bearings have been commonly used to reduce friction during movement in the past [148] and continue to be researched [149]. Cams and followers provide specific cyclic motion and have been highly utilized in engines [150]. Cylinders rolling on each other, implemented in forms such as gears, can create dramatic changes in mechanical advantage and change directions of motion [151].

One class of rolling-contact mechanisms uses compliant flexures to enforce a rolling constraint between two surfaces. For example, a Jacob's Ladder toy can be considered a compliant-aided rolling-contact mechanism [96]. The compliant rolling-contact element (CORE) [152] and X_r joint [146] use the same type of flexure architecture as the Jacob's Ladder toy to create a joint with two rolling-contact surfaces which curve away from each other, such as two circles. Multiple stable locations can be built into these compliant-aided rolling-contact joints [94]. Another flexure arrangement is seen in the Rolamite joint, which exhibits linear motion with low friction [99]. Advantages of elliptical rolling-contact joints over circular joints are explored by Mon-

tierth et al. [153]. An interesting analysis of planar rolling-contact mechanisms has been written by Kuntz [154].

It should be noted that compared to a traditional revolute joint where the axis of rotation is stationary throughout the motion, rolling-contact mechanisms have an instantaneous axis of rotation which continuously moves locations as the surfaces roll across each other [155]. This quality gives rise to unique motion paths, but also can complicate actuation and implementation.

In addition, rolling-contact mechanisms have the ability to take complex motions which are normally two degrees of freedom (translation and rotation), and reduce the system to a single degree of freedom, provided that a no-slip condition is enforced during the rolling motion [154].

Compliant-aided rolling-contact mechanisms have been used in multiple applications. Many of these applications involve some degree of biomimicry, as rolling motions are readily seen in biological joints. A prosthetic knee joint was designed by Hillberry and Hall [156]. More recently rolling joints were used to mimic the motion of a knee in the creation of a knee prosthesis and brace [157–159]. Finger joints have been constructed out of cylindrical rolling elements joined by flexible bands [104, 145]. Rolling joints were employed in the creation of a human-oriented biped robot [160]. Steerable surgical tools have utilized rolling architectures to facilitate small part sizes [103, 161]. A grapser with force perception was designed using compliant-aided rolling contacts [162]. A deployable compliant-aided rolling-contact joint was created by employing curved-folding origami techniques [57]. Folding plate structures have been facilitated using rolling-contact mechanisms [163]. Pellegrino et al. created a compliant-aided rolling-contact joint suited to deploying structures in space using a tape spring for actuation [164].

Recent work on a thickness accommodation technique for origami patterns used compliant-aided rolling-contact mechanisms to create offsets between panels as they moved into a stacked position [147]. As part of this work two rolling-contact theorems were set forth. The first describes how relative planar motion between two bodies that is well-behaved, meaning the motion never is pure translation, but is always coupled with a rotational component, can be accomplished through two translationally symmetric surfaces rolling on each other. These translationally symmetric surfaces are ruled surfaces and can furthermore be described as generalized cylinders. The second theorem states that relative 3D motion between two bodies that is well behaved and satisfies a no-lateral sliding condition can be created through rolling two ruled surfaces upon each other. Besides

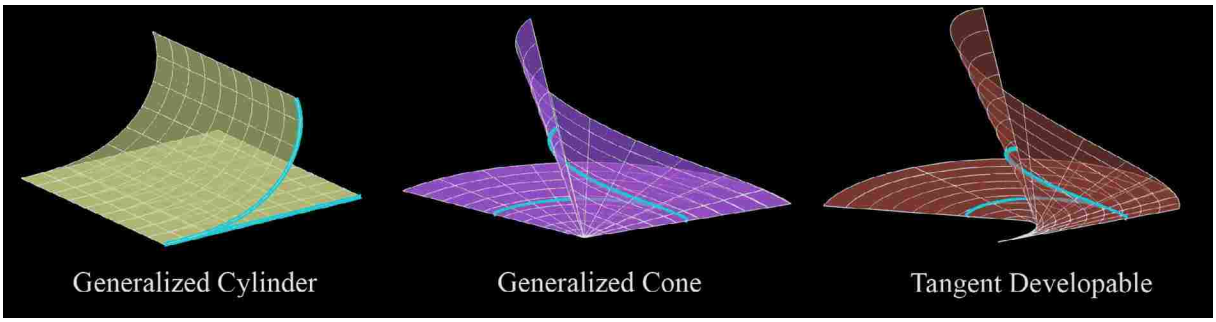

Figure 6.1: Three classes of developables shown flat and with curvature. A single cross curve for each class is shown in red in both the curved and developed states.

stating these two general theorems, their application was shown in the paper through the design of rolling surfaces which match the kinematics of origami vertices.

6.2.2 Developable Surfaces

Rather than creating specific rolling-contact pairs which satisfy origami-vertex kinematics, in this chapter we will discuss how developable surfaces can be used to create a family of compliant-aided rolling-contact pairs. A developable surface is a surface that can be created by bending a plane without any stretching or tearing [10]. Developable surfaces are composed of ruling lines (straight lines) making them also ruled surfaces [11]. Planes, generalized cylinders, generalized cones, and tangent developables are the four basic classes of developable surfaces [32]. The three classes other than planes are shown in Fig. 6.1. General or composite developable surfaces can be created by splicing these classes together using ruling lines or curved creases [1, 13].

The traditional parametric representation of developable surfaces takes the form of

$$\mathbf{r}(t,u) = \alpha(t) + u\beta(t) \tag{6.1}$$

where t and u are the parameters of the surface, $\alpha(t)$ is the directrix of the surface, and $\beta(t)$ is the direction of the ruling lines.

Its often convenient to represent developable surfaces with their *canonical parametrization* $\mathbf{r}(t,v) = \hat{\alpha}(t) + v\hat{\beta}(t)$ [118]. In this form we require $\hat{\beta}(t)$ be a unit vector and change u to v to reflect that v is now an arc length along a ruling line. Additionally for generalized cylinders $\hat{\alpha}(t)$ (representing a cross section of the cylinder) is orthogonal to $\hat{\beta}(t)$, a constant. For generalized

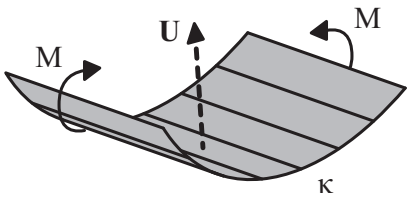

Figure 6.2: Positive notation for curvature and moments acting on a surface in relation to the standard unit normal of the surface.

cones $\hat{\alpha}(t)$ is a constant vector pointing to the apex of the cone. Finally for tangent developables $\hat{\alpha}(t)$ is the equation for the edge of regression with $\hat{\beta}(t) = \hat{\alpha}'(t)$.

We also note that while the canonical parametrization for a generalized cylinder is valid for the interval $v \in (-\infty, \infty)$, the generalized cone and tangent developable parametrizations represent two developable surfaces, one where $v \in [0, \infty)$ which we call the forward parametrization and one where $v \in (-\infty, 0]$ which we call the reverse parametrization.

The standard unit normal, which will be used in this chapter, for all orientable developable surfaces [136] can be found using

$$\mathbf{U}(t,u) = \frac{\mathbf{r}_t(t,u) \times \mathbf{r}_u(t,u)}{\|\mathbf{r}_t(t,u) \times \mathbf{r}_u(t,u)\|} \tag{6.2}$$

where $\mathbf{r}_t(t,u)$ and $\mathbf{r}_u(t,u)$ are the partial derivatives of the surface $\mathbf{r}(t,u)$ with respect to t and u.

Using the standard unit normal for an orientable developable surface we can define a positive notation that will be used through the rest of this chapter. This notation is shown in Fig. 6.2 where a positive moment results in positive curvature which curves the surface towards the direction of the standard unit normal.

A particular family of curves on developable surfaces, the principal curves, are helpful in analyzing and designing developable rolling contacts. Principal curves follow the principal curvatures of a surface. On a developable surface the ruling lines form one set of principal curves while the curves crossing perpendicular to the ruling lines (which we call cross curves for short) form the other set. A single cross curve is highlighted for each of the three classes of developable surfaces in Fig. 6.1. With the canonical parametrization of developable surfaces the family of cross

curves can be written with t being the parameter of the curve and w differentiating one cross curve from another as [118]

$$\mathbf{c}(t,w) = \begin{cases} \hat{\alpha}(t) + w\hat{\beta}(t) & \text{(generalized cylinder),} \\ \hat{\alpha}(t) + w\hat{\beta}(t) \text{ for } w > 0 \text{ or } w < 0 & \text{(generalized cone),} \\ \hat{\alpha}(t) + s(t,w)\hat{\beta}(t) \text{ for } w > t \text{ or } w < t & \text{(tangent developable),} \end{cases} \tag{6.3}$$

where $s(t,w)$ is the arc length along the edge of regression from t to w. For the planar (developed) mapping of a developable surface the cross curves are straight lines for generalized cylinders, circular arcs (and a point at the cone tip extreme) for generalized cones, and the involutes of the edge of regression for tangent developables.

6.3 Methods

While planar motion using rolling contacts has been extensively investigated and used in various applications, 3D motion using rolling-contact joints has been limited. Examples of 3D rolling motion are most often seen in gears, such as hyperboloid gears or bevel gears. These are special case scenarios where fixed, skewed axes exist between two rolling bodies. Analytic studies were conducted for spherical motions using conical cams [165, 166] and designing for motion paths using instantaneous screw axes has been investigated [167]. Developable surfaces can help further illuminate the design space available with rolling-contact joints, especially for complex 3D motions.

Planar rolling-contact joint surfaces can be described using generalized cylinders. Rolling-contact joint surfaces that produce 3D motion can be described with generalized cones and tangent developable surfaces, or combinations of the primary classes of developable surfaces (general developables). It should be noted that not all rolling surfaces producing 3D motion are developable. Some ruled surfaces, such as those that create hyperboloid gears, are not developable and still produce a rolling motion. This chapter will focus on how developable shapes can be used to design rolling contacts to access a large portion, but not the entire design space, of rolling-contact joints

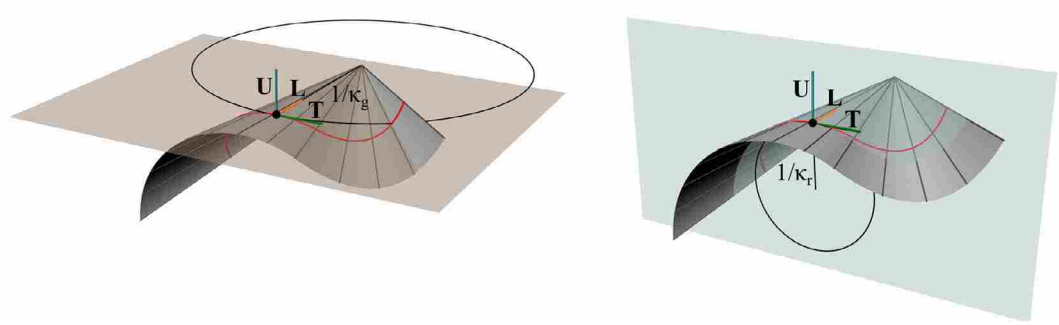

Figure 6.3: On the left is an illustration of the geodesic curvature κ_g at a point along a cross curve shown in red with its osculating circle of radius $1/\kappa_g$ in the plane containing the ruling line direction **L** and the tangent to the cross curve **T**. On the right is an illustration of the ruling curvature κ_r at the same point with its osculating circle in the plane containing the surface normal **U** and tangent to the cross curve **T**.

producing 3D motion. First we discuss a mathematical notation for developable surfaces conducive to rolling-contact mechanism design.

6.3.1 Representing Developable Surfaces for Rolling Contacts

We will see in the following sections that geodesic curvature and ruling curvature of a chosen cross curve highlight several properties important in rolling-contact mechanism design. The geodesic curvature of a curve is a measure of twist about the unit normal of the surface a curve is embedded in. The ruling curvature is a measure of the twist about a ruling line for a curve embedded in a surface. For a cross curve the ruling curvature is the non-zero principal curvature of the surface. These two curvatures with their osculating circles are shown in Fig. 6.3 for a point along a cross curve of a generalized cone. The importance of these two parameters for a chosen cross curve leads to two scenarios of interest for representing developable surfaces. The first is that the canonical parametrization of a developable surface is known leaving the designer to chose a specific cross curve for analysis of the geodesic and ruling curvatures. The second is that a designer has desired functions for geodesic and ruling curvatures and is interested in finding a parametrization of the developable surface for which these are valid. We present both directions of work flow below.

From Canonical Parametrizations of Developables to Geodesic and Ruling Curvatures

From the canonical parametrization we choose a single cross curve $\mathbf{c}(t)$ by using Eq. 6.3 and setting w equal to a value. We can then calculate the geodesic curvature and ruling curvature as

$$\kappa_g(t) = -\frac{1}{\dot{s}} \frac{\mathrm{d}(\mathbf{U}(t) \times \mathbf{T}(t))}{\mathrm{d}t} \cdot \mathbf{T}(t) \tag{6.4}$$

$$\kappa_r(t) = -\frac{1}{\dot{s}} \frac{\mathrm{d}\mathbf{U}(t)}{\mathrm{d}t} \cdot \mathbf{T}(t) \tag{6.5}$$

where $\mathbf{T}(t)$ is the unit tangent vector to the cross curve $\mathbf{c}(t)$, $\mathbf{U}(t)$ is the standard unit normal to the surface computed from Eq. 6.2, and $\dot{s}$ is the curve speed of the cross curve ($\dot{s}(t) = \|\dot{\mathbf{c}}\|$).

From Geodesic and Ruling Curvatures to Canonical Developable Parametrizations

Similar to the way a space curve can be uniquely defined using its curvature and torsion, we can describe a specific developable surface with the geodesic curvature κ_g and ruling curvature κ_r of a cross curve. As mentioned previously, while κ_r for a cross curve is equal to the non-zero principal curvature of a developable surface, we call it the ruling curvature to specify it as a measure of curvature of a curve lying on a surface rather than a surface curvature. The geodesic and ruling curvatures are independent of each other with the geodesic curvature containing information about the direction of ruling lines within the surface while the ruling curvature describes the deviation of the surface from a plane as one moves along the cross curve.

As the geodesic curvature of a cross curve contains information about the direction of the ruling lines within the surface, we can determine the class of developable surface by it. Let $\kappa_g(s)$ be a function of the geodesic curvature defining a cross curve where s is the arc length along the cross curve. The conditions on $\kappa_g(s)$ for every class is summarized in Table 6.1. For generalized cones v_c is a positive constant corresponding the distance from the cone's apex to the cross curve.

Our chosen desired geodesic curvature function determines a single cross curve of a developable surface and consequently the full ruling pattern.

Table 6.1: Summary of Geodesic Curvature Functions and the Corresponding Class of Developable Surface

	Forward Parametrization $v \in [0,\infty)$	Reverse Parametrization $v \in (-\infty,0]$
Generalized Cylinder	$\kappa_g(s) = 0$	$\kappa_g(s) = 0$
Generalized Cone	$\kappa_g(s) = -\frac{1}{v_c}$ (negative constant)	$\kappa_g(s) = \frac{1}{v_c}$ (positive constant)
Tangent Developable	$\kappa_g(s) = C^1$ continuous decreasing function with $\kappa_g(s) \in (-\infty,0)$	$\kappa_g(s) = C^1$ continuous decreasing function with $\kappa_g(s) \in (0,\infty)$

Now we can choose a function for the ruling curvature along the cross curve, $\kappa_r(s)$. The continuity of this function is equivalent to the continuity of the developable surface and a change in sign is reflected as a change in concavity in the surface.

With these two functions we can write a simplified version of the Darboux formulas (also called the moving-frame equations [168]) because the geodesic torsion for a cross curve is zero [16, 133] and the ruling curvature is equal to the normal curvature as

$$\begin{bmatrix} \mathbf{T}' \\ \mathbf{L}' \\ \mathbf{U}' \end{bmatrix} = \begin{bmatrix} 0 & \kappa_g & \kappa_r \\ -\kappa_g & 0 & 0 \\ -\kappa_r & 0 & 0 \end{bmatrix} \begin{bmatrix} \mathbf{T} \\ \mathbf{L} \\ \mathbf{U} \end{bmatrix} \tag{6.6}$$

where the vectors $\mathbf{T}$, $\mathbf{L}$, $\mathbf{U}$ form a Darboux frame and are the unit tangent vector to the cross curve, the unit vector in the direction of the ruling lines, and the unit surface normal, respectively. The derivative of the vectors is with respect to the arc length s of the cross curve and the matrix is noted to be skew symmetric. This system of first order ordinary differential equations can be solved (numerically if need be) to find $\mathbf{T}$, $\mathbf{L}$, and $\mathbf{U}$ as functions of s with a set of initial conditions $\mathbf{T}(s_o)$, $\mathbf{L}(s_o)$, and $\mathbf{U}(s_o)$.

The canonical parametrizations $\{\hat{\alpha}(s) + v\hat{\beta}(s)\}$ in terms of the arc length of the cross curve s can the be written for each type of surface with

$$\begin{cases} \hat{\alpha}(s) = \hat{\alpha}(s_o) + \int_{s_o}^{s} \mathbf{T}(t)\,dt & \text{(cylinder)}, \\ \hat{\alpha}(s) = \hat{\alpha}(s_o) & \text{(cone)}, \qquad \hat{\beta}(s) = \mathbf{L}(s) \quad \text{(all classes)} \\ \hat{\alpha}(s) = \hat{\alpha}(s_o) + \int_{s_o}^{s} \mathbf{T}(t)\,dt + \frac{1}{\kappa_g(s)}\mathbf{L}(s) - \frac{1}{\kappa_g(s_o)}\mathbf{L}(s_o) & \text{(tangent developable)}, \end{cases} \tag{6.7}$$

where $\hat{\alpha}(s_o)$ is an arbitrary vector determining the initial location of the directrix.

We can relate our original choice of $\kappa_g(s)$ to a specific cross curve described by w from Eq. 6.3 by

$$\begin{aligned} w &= -\tfrac{1}{\kappa_g(s)} \quad \text{(generalized cones)} \\ s(t,w) &= -\tfrac{1}{\kappa_g(s)} \quad \text{(tangent developables)} \end{aligned} \tag{6.8}$$

where it is noted that because cross curves for cylinders are straight lines and do not have unique curvature, $\kappa_g(s)$ could apply to any cylindrical cross curve.

6.3.2 Designing Rolling-Contact Mechanisms with Developable surfaces

Architecture Modeling

While both convex and concave rolling surfaces can be described with developable surfaces, this chapter will focus on pairs of surfaces that curve away from each other. Maintaining a rolling constraint between two bodies with compliant flexures, such as is seen in the Jacob's ladder joint, requires two surfaces to curve away from each other. If an attempt is made to move these rolling bodies away from each other, tension forces develop in the bands resisting the motion. A relationship where two surfaces curve in the same direction for rolling bodies with flexures of negligible stiffness does not exhibit this behavior as slack in the flexures enables the rolling bodies to move away from each other. It may be possible to prestress the bands between surfaces which curve in the same direction such that the no-slip condition is enforced up to a specific force threshold.

Figure 6.4 shows a generalized architecture for compliant-aided rolling-contact mechanisms such as the CORE joint and X_r joint. In this architecture two developable surfaces are held together by interwoven flexible bands. Part (a) of Fig. 6.4 shows how separating the mechanism at a single point and unfolding the developable surfaces to a flat state produces an arrangement where all components are contained in a single plane. In some cases where no overlap occurs between bands and surfaces, this arrangement could be used for monolithic manufacture and subsequent folding of the mechanism. Part (b) of Fig. 6.4 shows what the mechanism would look like when folded, but keeping the developable surfaces and bands in a flat configuration. In this arrange-

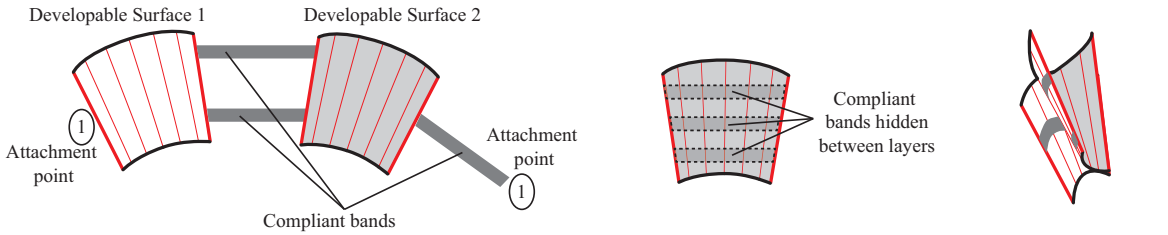

(a) Planar Separated (b) Planar Stacked (c) Formed (3D)

Figure 6.4: Generalized architecture for a compliant-aided rolling-contact mechanism made of a single developable class shown in an (a) planar separated state, (b) planar stacked state and (c) formed functional state.

ment 3 layers exist (the two unfolded developable surfaces composing of the outside layers and the bands creating the inside layer). Finally, part (c) shows the folded and formed mechanism where the developable shapes have taken their final form and rolling motion is exhibited.

In Figures 6.4 and 6.5 the ruling lines are shown by thin red lines. The edges of the developable that correspond to ruling lines, which we will call the ruling line edges, are shown by thick red lines. The thick black boundaries can be arbitrary selected for the application without consequence to the fundamental rolling motion.

Rolling without slip of two surfaces maintaining line-contact (rather than point-contact) throughout the motion results in equivalent ruling patterns, or rulings, for the two surfaces. This means that we are limited to creating line-contact rolling mechanisms where a generalized cylinder rolls on a generalized cylinder, generalized cone on a generalized cone, or a tangent developable on a tangent developable. It is possible to join developable surface classes together to create a general developable shape which can be used in rolling-contact mechanisms, however developable classes will always be rolling on a member of their own class. An architecture using general developables connected by flexible bands is shown in Fig. 6.5. Connecting developable classes together to form a general developable surface can be accomplished by connecting the classes by a common ruling line.

We call the shared ruling pattern of both rolling surfaces the base ruling. If we select any cross curve on the base ruling we note that the geodesic curvature, κ_g along this curve is shared by all possible developable shapes that can roll on each other with line contact. The variation in these shapes can be quantified using the ruling curvature κ_r along the cross curve.

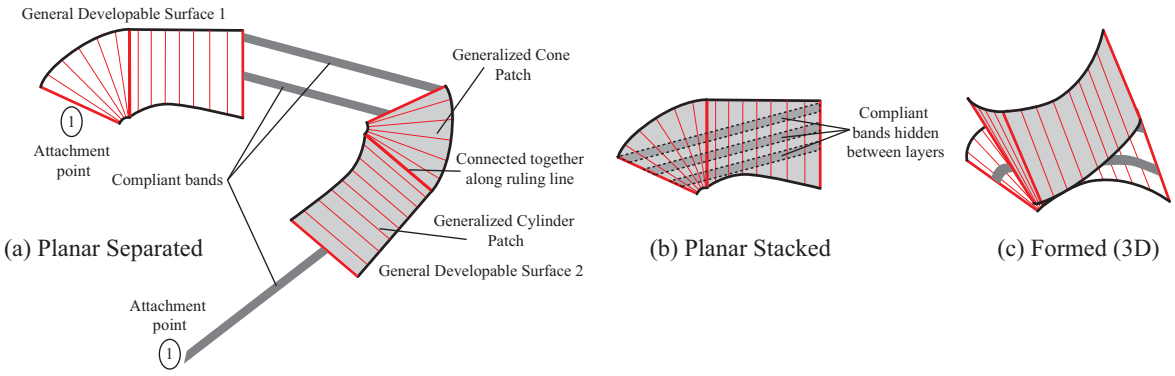

Figure 6.5: Generalized architecture for a compliant-aided rolling-contact mechanism made of general developables shown in an (a) planar separated state, (b) planar stacked state and (c) formed functional state.

There is some flexibility when choosing the path of the compliant bands used to connect two rolling developable surfaces, which we will call the construction bands. To create the necessary rolling constraint conditions with the construction bands, the bands must correspond to common geodesics of the two rolling surfaces which connect the ruling line edges of the surfaces together. When the bands correspond to the geodesics, any motion introduces tensile forces which hold the two rolling surfaces in contact. If the bands do not correspond to a common geodesic of both surfaces, then the bodies connected by the bands can move relative to each other without introducing band tension.

It is convenient to view developable surfaces in a planar state when determining the path for the flexible bands, as a geodesic in a plane corresponds to a straight line. In this arrangement construction bands can be chosen as any straight lines connecting the ruling edges that do not leave the surface and do not cross one another, or when the bands have thickness, the bands do not overlap. If a smaller range of motion is desired, construction bands can be connected between the two ruling lines that correlate to the lines of contact for the two most extreme positions. In the case where full rotation is possible with the two surfaces, that is the ruling line edges of the surfaces are connected together when the surfaces are formed, as is the case with a full cylinder rotating on a full cylinder, the bands can be extended to allow for a larger range of motion. This can be accomplished by lengthening the bands within the envelope created by connecting multiple instances of the surface together as is shown in Fig. 6.6. It should be noted that some paths chosen

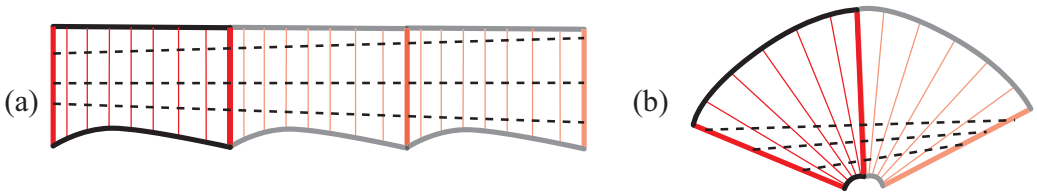

Figure 6.6: Compliant construction band path possibilities enabling more than 360 degrees of rotation, where multiple instances of the planar shape (shown in the lighter colors) are pieced together by ruling lines and the bands are connected from one ruling edge to the other extreme ruling edge in straight lines without crossing or overlapping.

for bands which provide more than 360 degrees of rolling motion can result in overlap of the bands wrapping multiple times around the surfaces.

Kinematic Modeling

The kinematics of rolling contacts has been extensively studied for point-contact rolling rigid bodies as well as line-contact rolling [147, 169–172]. In the following kinematic modeling we present a sequence of steps particularly suited to tracking the position of any point on a body during rolling motion for developable shapes which curve away from each other.

Let $\mathbf{r}_g(t,v)$ be a canonical parametrization of a developable surface which is grounded. Let $\mathbf{r}_1(t,v)$ be a canonical parametrization of a developable surface curving away from $\mathbf{r}_g(t,v)$ which can roll on $\mathbf{r}_g(t,v)$. As explained in a previous section for the rolling condition to be met $\mathbf{r}_1(t,v)$ must have an equivalent ruling pattern as $\mathbf{r}_g(t,v)$ and thus the geodesic curvature of the cross curves $\mathbf{c}_g(t,w)$ and $\mathbf{c}_1(t,w)$ will be equivalent for all w. Furthermore, we require $\mathbf{r}_g(0,v) = \mathbf{r}_1(0,v)$, which represents the initial line of contact between the two surfaces, and the standard unit normals for $\mathbf{r}_g(t,v)$ and $\mathbf{r}_1(t,v)$ found from Eq. 6.2 at $t = 0$ are equivalent giving equivalent tangent planes at the initial line of contact. This initial configuration is shown in Fig. 6.7(a) for cylindrical rolling surfaces and Fig. 6.8(a) for conical rolling surfaces.

While it can be difficult to find pairs of canonical parametrizations which meet these criteria other than for simple cases, it is straightforward to write a pair of canonical parametrizations by defining a shared base ruling with a function $\kappa_g(s)$ and allowing the two surfaces to have differing ruling curvature functions $\kappa_r(s)$ (one negative and one positive if two surfaces are to curve away

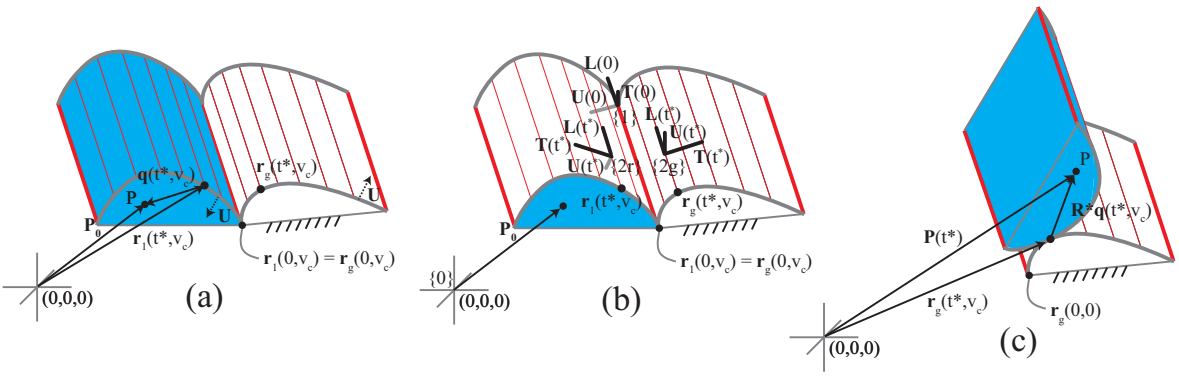

Figure 6.7: Cylindrical rolling surfaces showing (a) the initial position (b) the frames used to develop the rotation matrix (c) the rolled state at t^*.

from each other enabling a compliant band architecture). This procedure was discussed previously in Section 6.3.1.

Let P denote any point on the rolling body containing the surface $\mathbf{r}_1(t,v)$. We will track the motion of this point throughout rolling $\mathbf{r}_1(t,v)$ on the grounded $\mathbf{r}_g(t,v)$. Let $\mathbf{P}_0$ to be the vector from the origin to the point P when $t = 0$.

To establish the position of point P throughout the rolling motion we can write vector, $\mathbf{q}$, from a point lying on the line of contact to point P as

$$\mathbf{q}(t,v_c) = -\mathbf{r}_1(t,v_c) + \mathbf{P}_0 \tag{6.9}$$

where v_c is an arbitrarily chosen constant to define a reference point along a ruling line. We will show how to formulate a rotation matrix, $\mathbf{R}$ which will rotate $\mathbf{q}$ to the appropriate angle for a particular state of rolling. We can then translate the rotated vector to its appropriate position during rolling as shown in Fig. 6.7(c) and 6.8(c). The rotation matrix $\mathbf{R}$ is formulated by combining the contributions of both the ground and rolling surfaces to the change of the angle of the vector $\mathbf{q}$. We can define a particular position during the rolling with $t = t^*$. Because the parameter t describes movement from ruling line to ruling line, which is also how the rolling motion progresses, this single parameter is sufficient to define the position of the rolling body.

The contribution of each surface to the rotation of vector $\mathbf{q}$ is calculated with the following method. We call the world coordinate frame $\{0\}$ as shown in Figs. 6.7(b) and 6.8(b). We create a

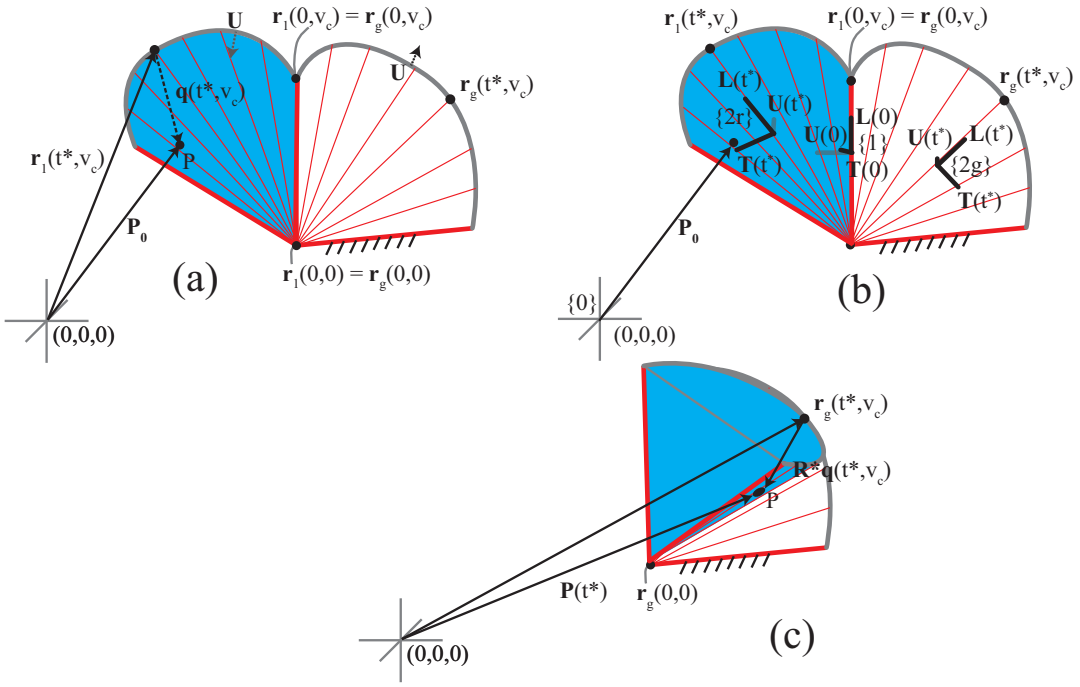

Figure 6.8: Conical rolling surfaces showing (a) the initial position (b) the frames used to develop the rotation matrix (c) the rolled state at t^*.

coordinate frame $\{1\}$ at the initial line of contact, $t = 0$, aligned with $\mathbf{T}(0)$, $\mathbf{L}(0)$, and $\mathbf{U}(0)$. These vectors are computed in the world frame using Eq. 6.2 for $\mathbf{U}(0)$ and

$$\mathbf{T}(0) = \frac{\dot{\mathbf{c}}(0)}{\|\dot{\mathbf{c}}(0)\|}$$

$$\mathbf{L}(0) = \mathbf{U}(0) \times \mathbf{T}(0)$$

where $\dot{\mathbf{c}}(t)$ is the derivative of a cross curve of either surface for a chosen w.

The rotation matrix $\mathbf{R}_1^0$ to rotate frame $\{0\}$ to frame $\{1\}$ is

$$\mathbf{R}_1^0 = \begin{bmatrix} \mathbf{T}(0) & \mathbf{L}(0) & \mathbf{U}(0) \end{bmatrix} \tag{6.10}$$

We create frames $\{2g\}$ and $\{2r\}$ at the position $t = t^*$ on the ground surface and rolling surface, respectively. Frames $\{2g\}$ and $\{2r\}$ are not shared between the two surfaces unlike Frame $\{1\}$. Frame $\{2g\}$ is aligned with unit vectors $\mathbf{T}(t^*)$, $\mathbf{L}(t^*)$, and $\mathbf{U}(t^*)$ where $\mathbf{U}(t^*)$ is found from Eq. 6.2 using the ground surface $\mathbf{r}_g$ and

$$\mathbf{T}(t^*) = \frac{\dot{\mathbf{c}}_g(t^*)}{\left\|\dot{\mathbf{c}}_g(t^*)\right\|}$$

$$\mathbf{L}(t^*) = \mathbf{U}(t^*) \times \mathbf{T}(t^*)$$

where $\dot{\mathbf{c}}_g(t)$ is the derivative of a cross curve of the ground surface for a chosen w.

The rotation matrix $\mathbf{R}^0_{2g}$ to rotate frame $\{0\}$ to frame $\{2g\}$ is

$$\mathbf{R}^0_{2g} = \begin{bmatrix} \mathbf{T}(t^*) & \mathbf{L}(t^*) & \mathbf{U}(t^*) \end{bmatrix} \tag{6.11}$$

Frame $\{2r\}$ and rotation matrix $\mathbf{R}^0_{2r}$ is found in a similar manner using the rolling surface rather than the ground surface t compute $\mathbf{T}(t^*)$, $\mathbf{L}(t^*)$, and $\mathbf{U}(t^*)$.

With these rotation matrices we can compute the contribution of the ground surface $\mathbf{R}_g$ and of the rolling surface $\mathbf{R}_r$ to the rotation of vector $\mathbf{q}$ as

$$\mathbf{R}_g = \mathbf{R}^0_{2g}\mathbf{R}^{0^T}_1 \tag{6.12}$$

$$\mathbf{R}_r = \mathbf{R}^0_{2r}\mathbf{R}^{0^T}_1 \tag{6.13}$$

Finally the full rotation matrix, $\mathbf{R}$ for rotating vector $\mathbf{q}$ with both the rolling and grounded surface contributions is defined by

$$\mathbf{R} = \mathbf{R}_g\mathbf{R}^T_r \tag{6.14}$$

We can write the vector $\mathbf{P}$ to point P at t^* as

$$\mathbf{P}(t^*) = \mathbf{r}_g(t^*, v_c) + \mathbf{R}\mathbf{q}(t^*, v_c) \tag{6.15}$$

These equations enable us to track the position of a point on the rolling body for any class of developable surface pair rolling on each other. By writing the rotation matrices as functions of t it is possible to differentiate Eq. 6.15 to find the velocity and acceleration of any point during the motion.

We can use Euclidean transformations applied to the parametric equation representation of the rolling surface to express how the entire surface changes rather than a single point. We accomplish this by tracking the origin of the parametric equation using the procedure above to obtain rotation matrix **R** and vector **P**. These are applied to the rolling surface parametric equation as

$$\mathbf{r}_{t^*}(t,v) = \mathbf{R}\hat{\alpha}(t) + v\mathbf{R}\hat{\beta}(t) + \mathbf{P} \tag{6.16}$$

to find $\mathbf{r}_{t^*}$, the parametric surface representation of the rolling surface when the line of contact is at the ruling line specified by t^*. Note that this expression rotates the directrix, $\hat{\alpha}(t)$, about the origin. It is oftentimes desirable to rotate the directrix about its initial point. This can be accomplished by using the following equation

$$\mathbf{r}_{t^*}(t,v) = \mathbf{R}(\hat{\alpha}(t) - \hat{\alpha}(t_o)) + \hat{\alpha}(t_o) + v\mathbf{R}\hat{\beta}(t) + \mathbf{P} \tag{6.17}$$

where $\alpha(t_o)$ is the vector to the initial point of the directrix.

Kinetic Modeling

Stiffness can be introduced into a rolling-contact mechanism joined with compliant flexures by adding additional bands with non-negligible bending stiffness, or by adding stiffness to the construction bands themselves. Adding stiffness can enable a designer to choose a desired moment-rotation response throughout the rolling-contact motion.

The kinetic modeling developed here for rolling-contact mechanisms will describe the moment required to roll the rolling body about the grounded body. Moon et al. describe the kinetic modeling for a rolling mechanism synthesized from an equivalent four-bar linkage [104]. Here the kinetic modeling will utilize the vector equations employed in the kinematic modeling of the previous section and extend the analysis to conical and tangent developable rolling surfaces.

Let's consider first generalized cylindrical surfaces rolling on each other. Figure 6.9 shows a free body diagram of the two rolling bodies midway through the rolling motion with a cut made to the bands with stiffness at t^* and the rolling bodies moved apart for clarity. Band g represents all the bands connected to the grounded surface on the ruling line $\mathbf{r}_g(0,v)$ and then to the rolling

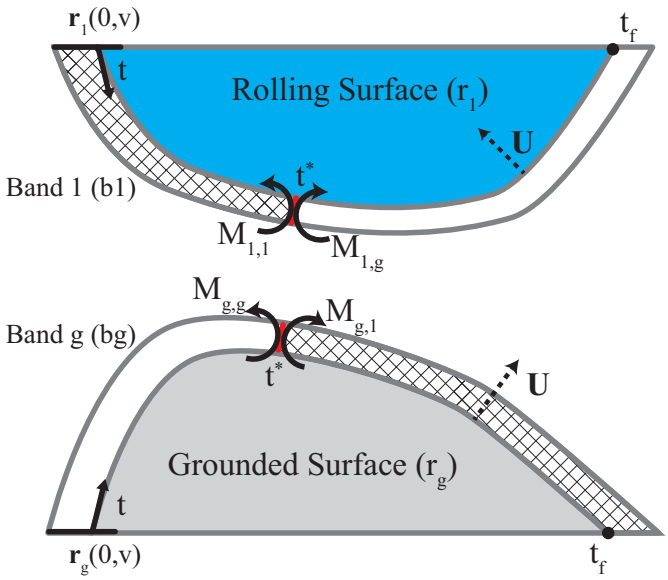

Figure 6.9: Kinetic model for generalized cylinder surfaces which curve away from each other.

surface $\mathbf{r}_1(t_f, v)$ where t_f is the endpoint of the rolling surface. This representative band is shown in white in Fig. 6.9. Similarly, Band 1 represents all bands connected to the rolling surface on the ruling line $\mathbf{r}_1(0, v)$ and then to the grounded surface on the ruling line $\mathbf{r}_g(t_f, v)$. This band is shown with the cross hatchings. The resulting moments from cutting the bands at t^* are shown and labeled in the figure using the positive notation set forth earlier.

From the figure we can write the total moment exerted on the body with the rolling surface by summing the moments where the counterclockwise direction is positive as

$$M_{tot} = -M_{g,g} + M_{g,1} - M_{1,g} + M_{1,1} + M_g \tag{6.18}$$

where M_g is the moment caused by the weight of the body of the rolling surface.

The Bernoulli-Euler relation for beams in bending can be used to write the moment expression in terms of the geometry and material properties of the bands and the geometry of the rolling surfaces. This relation for a beam in bending is expressed as

$$M = \frac{EI}{R} = EI\kappa_1 \tag{6.19}$$

where M is the moment induced by bending, E is Young's modulus of the material, I is the second moment of area for the axis in bending, and R is the radius of curvature of the deformed beam (the inverse of the non-zero principal curvature, κ_1).

By applying the Bernoulli-Euler relation to Eq. 6.18 we have the following expression for the total moment exerted on the rolling surface, $\mathbf{r}_1$ as

$$M_{tot}(t) = -\frac{E_{bg}I_{bg}(t)}{R_g(t)} + \frac{E_{b1}I_{b1}(t)}{R_g(t)} - \frac{E_{bg}I_{bg}(t)}{R_1(t)} + \frac{E_{b1}I_{b1}(t)}{R_1(t)} + M_g(t) \tag{6.20}$$

where E_{bg} and E_{b1} are the material moduli of Band g and Band 1 respectively, $I_{bg}(t)$ and $I_{b1}(t)$ are the second moment of area about the bending axis for Band g and Band 1 respectively, $R_g(t)$ and $R_1(t)$ are the radii of curvature (whose signs are determined by the surface normals shown in Fig. 6.9) for the ground surface $\mathbf{r}_g$ and the rolling surface $\mathbf{r}_1$ respectively, and $M_g(t)$ is the moment caused by the weight of the body with the rolling surface.

It is possible to add a stiffness response to the rolling-contact joint through pre-curving the stiffness bands. In this case Eq. 6.20 becomes

$$M_{tot}(t) = -\frac{E_{bg}I_{bg}(t)}{R_g(t) - R_{bg}(t)} + \frac{E_{b1}I_{b1}(t)}{R_g(t) - R_{b1}(t)} - \frac{E_{bg}I_{bg}(t)}{R_1(t) - R_{bg}(t)} + \frac{E_{b1}I_{b1}(t)}{R_1(t) - R_{b1}(t)} + M_g(t) \tag{6.21}$$

where $R_{bg}(t)$ and $R_{b1}(t)$ are the radii of precurvature of Band g and Band 1 respectively where the sign is determined from the unit normals shown in Fig. 6.9.

By examining Eq. 6.21 we can see that the force response of a rolling joint can be specified by choosing a combination of the curvature of the rolling surfaces, precurvature of the flexible bands, and stiffness of the bands either through geometry and material choice or both.

For generalized cones and tangent developable rolling-contact surfaces a kinetic model can also be developed to describe the moment required to roll one surface over the other. For generalized conical and tangent developable surfaces it should be noted that the model becomes more complex as the curvature of the surface changes as one moves along a single ruling line causing the moment developed in the band to vary along the ruling lines.

We can find this variation of curvature along a ruling line in terms of κ_g and κ_r of a cross curve using the first and second fundamental forms as described in [141] with the canon-

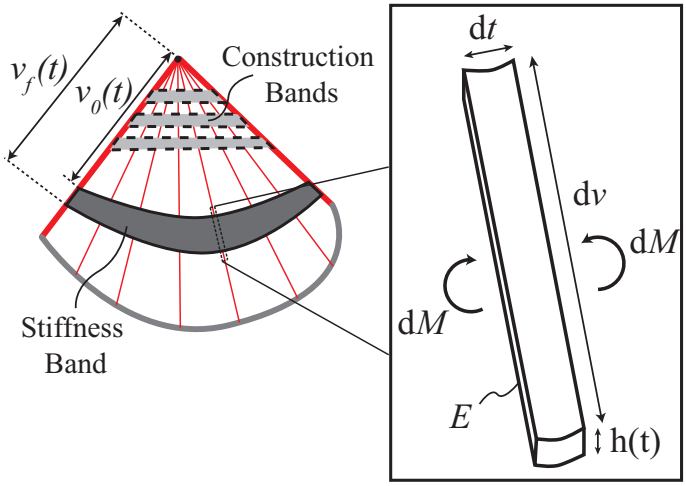

Figure 6.10: Diagram of a conical surface with construction and stiffness bands with a differential element of the stiffness band shown in detail. The standard unit normal is coming out of the page.

ical parametrization of a surface. For conical and tangent developable surfaces this results in the variation of the principal curvature as one moves along a ruling line at t as

$$\kappa_1(v) = -\frac{\kappa_r(t)}{\kappa_g(t)}\left(\frac{1}{v}\right) \tag{6.22}$$

With the variation of the curvature along a ruling line we are prepared to write an expression for the differential moment produced by a differential piece of a stiffness band as shown in Fig. 6.10. Using the Bernoulli-Euler relationship of Eq. 6.19 we can write

$$\mathrm{d}M = E\frac{(\mathrm{d}v)h(t)^3}{12}\kappa_1(v) \tag{6.23}$$

where $\mathrm{d}M$ is the differential moment, E is Young's modulus of the band, $\mathrm{d}v$ is the differential length along the ruling line, $h(t)$ is the height of the stiffness band at t, and $\kappa_1(v)$ is the principal curvature as a function of v. Integrating this expression gives

$$M(t) = \frac{Eh(t)^3}{12}\int_{v_0(t)}^{v_f(t)} \kappa_1(v)\mathrm{d}v \tag{6.24}$$

where $v_0(t)$ and $v_f(t)$ are the positions along the ruling line where the stiffness band begins and ends as a function of t.

If the stiffness band is initially curved we can write the moment equation as

$$M(t) = \frac{Eh(t)^3}{12} \int_{v_0(t)}^{v_f(t)} \kappa_1(v) - \kappa_{1,b}(v) \mathrm{d}v \tag{6.25}$$

where $k_{1,b}(v)$ is the variation of the non-zero principal curvature for the band's initial shape.

A figure similar to Fig. 6.9 can be constructing for conical and tangent developable rolling surfaces. Similarly, the relationship of Eq. 6.18 is valid for these types of surfaces. With this equation we can write an expression for the total moment exerted on a rolling body by the stiffness bands for conical and tangent developable surfaces using Eq. 6.24 or Eq. 6.25 if the bands are precurved. For example, to write the expression for $M_{1,g}$ of Eq. 6.18 for a conical rolling surface without precurved stiffness bands we use Eq. 6.24 where $k_1(v)$ is determined from Eq. 6.22 for the rolling surface $\mathbf{r}_1$ and $h(t)$, $v_0(t)$, $v_f(t)$, and E, are determined from Band g.

Special Case Force Response, Static Balance

One special case of a force-displacement response potentially available with these rolling-contact mechanisms is that of static balance, or a zero-force response. As suggested by its name, static balance refers to a condition where the rolling-contact mechanisms requires no force (if friction is considered to be negligible) to quasi-statically move from one position to a finitely separated other position. Mechanisms that are statically balanced can greatly reduce the size of actuators required to cause movement, increase energy efficiency, and provide accurate force feedback [173, 174].

Static balance of rolling-contact mechanisms can be achieved by adjusting the geometry, pre-curvature, and materials affecting Eq. 6.18 such that $M_{tot}(t)$ is equal to zero for every value of t. This approach could provide statically balanced rolling-contact mechanisms that exhibit complex large-range 3D motions with the addition of compact static balancing elements that minimally increase the size or weight of the rolling joint. In comparison, other common static balancing methods of adding additional linear or compliant springs connected to particular locations between moving bodies or the addition of counterweights to provide the balancing force can substantially increase the size or weight of the mechanism. An example of statically balancing a rolling-contact mechanism will be shown in results and discussion section of this chapter.

6.4 Results and Discussion

This section will show and discuss several prototypes demonstrating the methodology explained above for creating rolling-contact mechanisms using developable surfaces and show an example of designing a statically balanced rolling-contact mechanism created by tailoring the mechanism's force response. The accuracy of the kinematic modeling was verified by computing motion paths of points on the rolling bodies for the prototypes constructed and comparing the behavior to the physical models. Additionally, simple cases of rolling-contact pairs where the motion paths of points on the rolling body are known were computed with the kinematic model and compared. Both approaches yielded good agreement. The accuracy of the kinetic modeling was tested by measuring the performance of the statically balanced rolling-contact mechanism presented in this section and the findings are discussed.

6.4.1 Generalized Cylinder Parabolic Rolling-Contact Mechanism

A rolling-contact mechanism with rolling surfaces comprised of generalized cylinders in the form of parabolas was 3D printed (Makerbot 2) with polylactic acid (PLA) and is shown in Fig. 6.11. The rolling surfaces were combined using flexible canvas bands. The parabolic rolling surfaces for this mechanism are defined by the canonical parametrization

$$\mathbf{r}(t,v) = \begin{bmatrix} t \\ 0 \\ t^2/a \end{bmatrix} + v \begin{bmatrix} 0 \\ 1 \\ 0 \end{bmatrix} \tag{6.26}$$

where a, the distance from the base of the parabola to the focal point, is 19.05 mm (0.75 in), $t \in [-63.5, 63.5]$ mm ($[-2.5, 2.5]$ in), and $v \in [0, 50.8]$ mm ($[0, 2]$ in). This particular rolling-contact mechanism results in a straight line path for the focus of one of the parabolic surfaces as it rolls across the other anchored parabolic surface. Motion paths calculated from the procedure described in the methods section for ten other points on the rolling body are shown in Fig. 6.11.

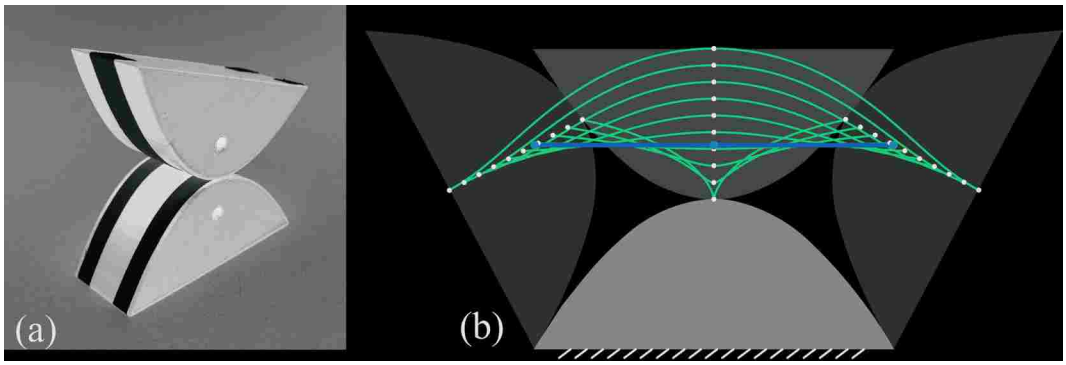

Figure 6.11: (a) Generalized cylinder (parabolic surfaces) rolling-contact mechanism and (b) the kinematic paths of 11 points on the rolling body with the straight line path emphasized in orange.

6.4.2 Developable Compliant-Aided Rolling-Contact Mechanisms from Planar Sheets

Two paper models were constructed for rolling-contact mechanisms using developable surfaces. These were constructed by designing the mechanism in the flat state where the construction bands are straight lines and then increasing the ruling curvature of the surface while holding the ruling line positions fixed to make the formed 3D shape.

A generalized conical mechanism with constant ruling curvature in shown in Fig. 6.12. In this prototype three red paper construction bands are used to connect the two conical surfaces. Each component starts in a flat form as shown in Fig. 6.12(a). The mechanism is folded together as shown in Fig. 6.12(b) and Fig. 6.12(c) and the final attachment of the middle construction band is made at the location shown in the figure. The conical surfaces are formed into their 3D shape and secured using adhesive to create the functional mechanism in Fig. 6.12(d). This joint has a large range of motion where the rolling cone is able to rotate 360 degrees about the grounded cone as shown in the series of pictures in Fig. 6.12(e).

A second interesting paper rolling-contact mechanism was created from a convex hull of two disks, similar to an oloid. The width of the developed (flat) pattern of this shape is $4R$ where R is the radius of the semicircle caps, and the height $3.535R$ as shown in Fig. 6.13. This shape is a general developable (using two or more types of the four fundamental developable surfaces) and a rolling developable as it develops its entire surface on a plane as it rolls [175]. Figure 6.13 also shows a folded paper prototype of this oloid-like rolling-contact mechanism constructed with $R = 38.1$ mm (1.5 in).

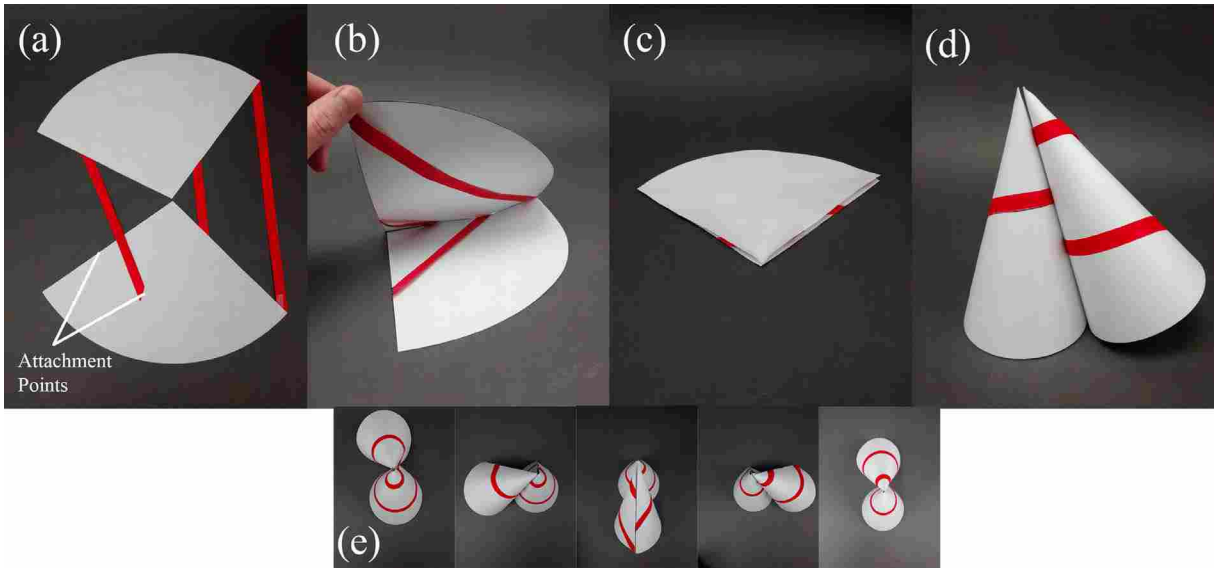

Figure 6.12: A generalized conical mechanism formed from paper (a) in a planar separated state, (b) being folded into a planar stacked state (c) in a planar stacked state, and (d) in the final formed state. The bottom pictures (e) show the range of motion where one cone is able to rotate 360 degrees about the grounded cone.

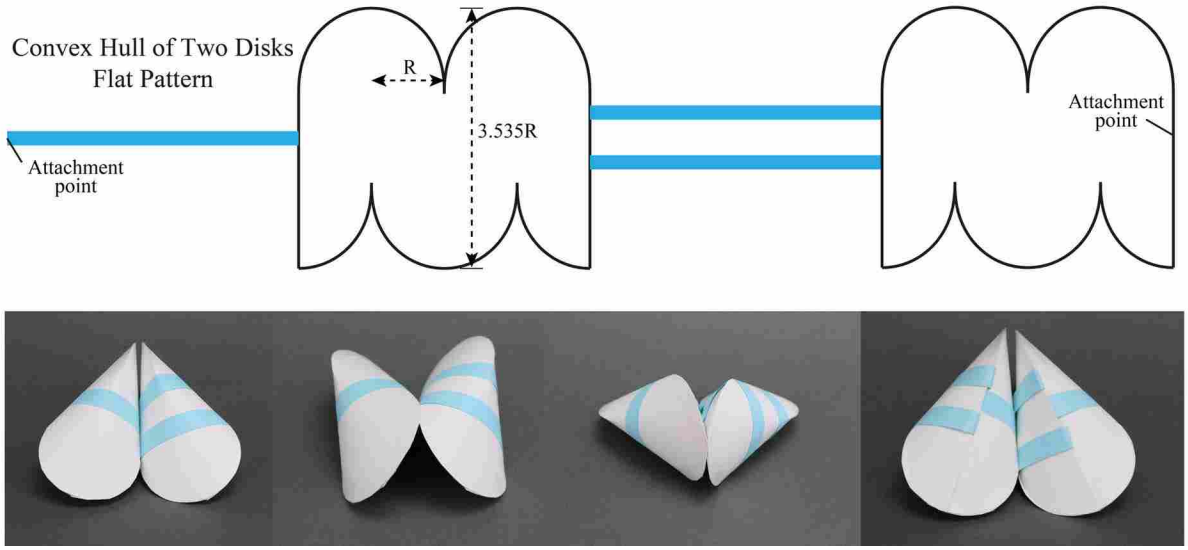

Figure 6.13: The flat pattern of a general developable (convex hull of two disks similar to an oloid) rolling-contact mechanism (top) and the mechanism constructed of paper in four rolled states (bottom).

Figure 6.14: 3D printed generalized conical rolling-contact mechanism in multiple positions demonstrating the range of motion.

Figure 6.15: 3D printed tangent developable rolling-contact mechanism in multiple positions demonstrating the range of motion.

6.4.3 Rolling-Contact Mechanisms with Rolling Surfaces of Differing Ruling Curvatures

A generalized conical rolling-contact mechanism and tangent developable rolling-contact mechanism were created to demonstrate the principle that two rolling surfaces can still roll on each other with differing ruling curvatures as long as the geodesic curvatures are equivalent.

A generalized conical mechanism was 3D printed out of PLA with braided filament utilized in the three construction bands (SpiderWire Stealth-Braid 36.2 kg (80 lb) test). Bead crimps and small 3D printed blocks were used to appropriately tension the bands. The 3D printed blocks were inserted underneath the bands on the backsides of the rolling surfaces and twisted into place to create tension in the bands. The grounded surface is a partial cone with constant ruling curvature while the rolling surface has a variable ruling curvature. The joint is shown in Fig. 6.14 in multiple positions.

A tangent developable rolling-contact mechanism was also constructed in the same manner and is shown in Fig. 6.15. In this mechanism four construction bands were used. The tangent developable surface making up the grounded surface has zero ruling curvature (a planar surface), while the tangent developable surface rolling on it has a variable ruling curvature. The geodesic curvature and equivalently edge of regression of both of these tangent developable surfaces are the same enabling the mechanism's function.

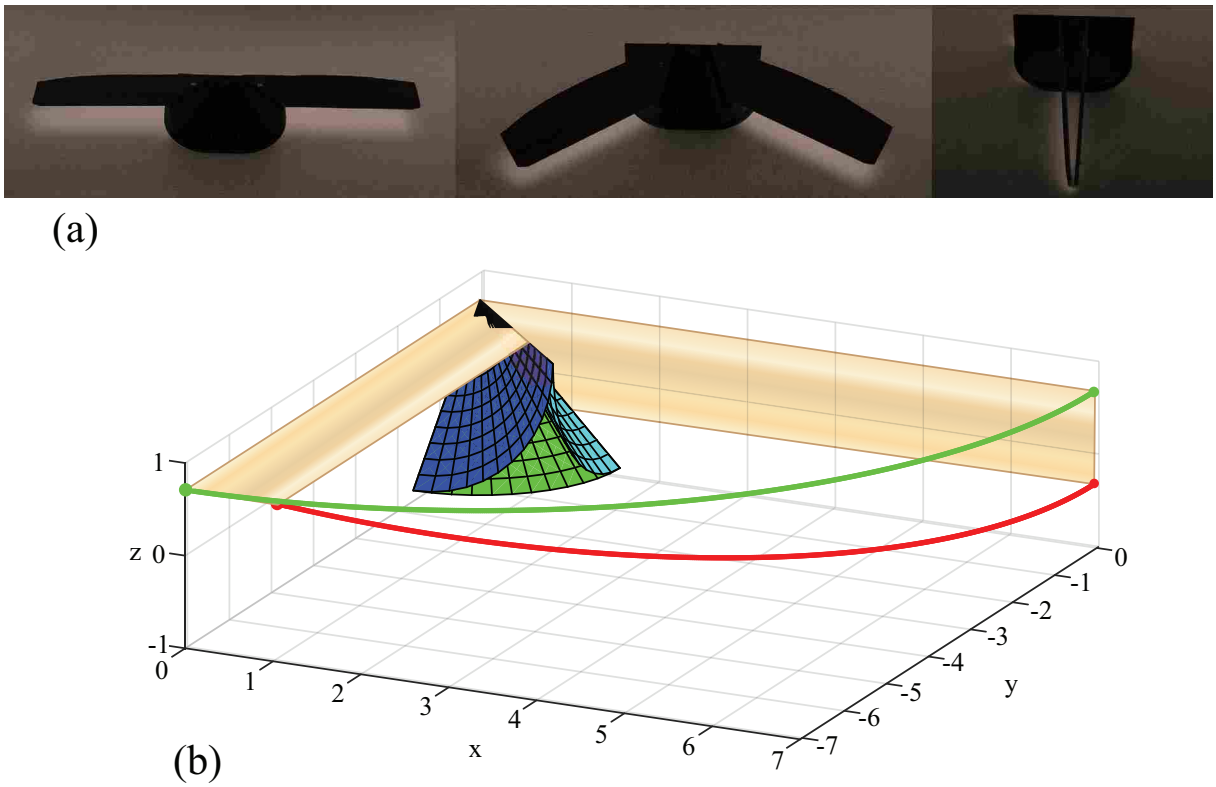

Figure 6.16: (a) 3D printed conical rolling-contact mechanism demonstrating the coupling of rotation and translation and (b) model of the rolling surfaces with the green surface being the grounded surface while the dark blue and light blue surfaces are the extreme rolling positions with the kinematic paths of the sheets endpoints shown for the entire rolling motion.

6.4.4 Sheet-Stowing Conical Rolling-Contact Mechanism

To demonstrate the unique coupling of rotation and translation into a single degree of freedom joint, two conical mechanisms were 3D printed with Tyvek bands and attached to flat sheets of balsa each 178 mm (7.0 in) in length. These conical mechanisms are composed of quarter cone rolling surfaces with constant ruling curvature and a cone height of 38.1 mm (1.5 in). Hardstops were incorporated into the rolling-contact mechanism design to prevent the rolling motion from being extended past the joint range limits. Figure 6.16(a) shows how the flat sheets of balsa are spread apart at one extreme in the joint's range of motion and compactly stored together at the other extreme. The kinematic paths of the endpoints of the sheets were calculated using the kinematics presented in the chapter and are shown in Fig. 6.16(b) with the rolling-contact surfaces and sheet for one half of the prototype.

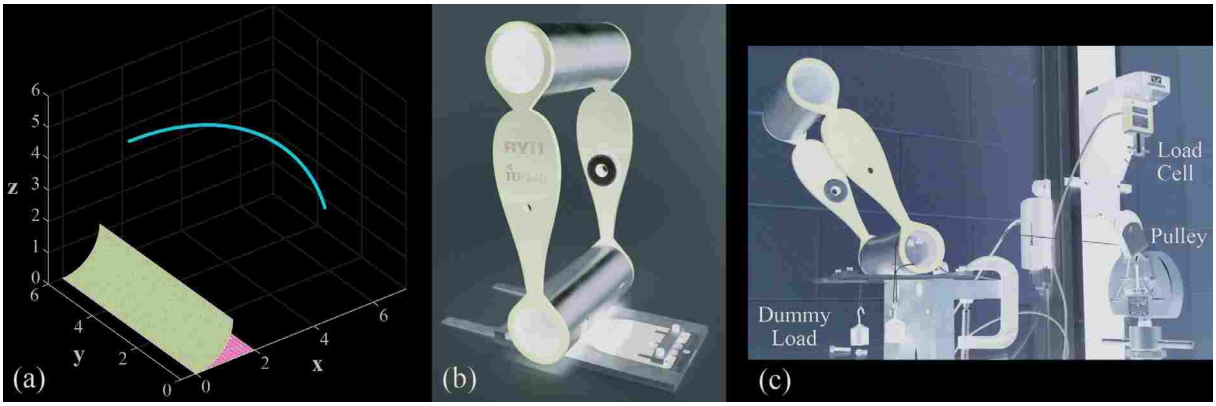

Figure 6.17: (a) The rolling-contact surfaces and kinematic path of the center of gravity of a rolling-contact mechanism designed to be statically balanced, (b) the constructed mechanism and (c) the test set up to measure the force response of the mechanism.

6.4.5 Statically Balanced Generalized Cylindrical Rolling-contact Mechanism

A statically balanced rolling-contact mechanism was designed, built, and is shown in Fig. 6.17. The weight of the moving arm of the mechanism was desired to be balanced throughout the motion. A circle and a plane were chosen as the rolling-contact surfaces. Three bands with no pre-curvature were used to hold the surfaces together during the rolling motion. Two of the bands were assumed to have negligible bending stiffness as they were made of thin steel shim stock. The other band made of spring steel also served to provide the stiffness response to counteract the weight of the rolling arm. The design process using the method developed in this chapter will be explained here.

The two rolling-contact surfaces were represented mathematically; the plane as

$$\mathbf{r}_g(s,v) = \begin{bmatrix} v \\ s \\ 0 \end{bmatrix} \tag{6.27}$$

and the quarter circle as

$$\mathbf{r}_1(s,v) = \begin{bmatrix} v \\ R\sin\frac{s}{R} \\ -R\cos\frac{s}{R}+R \end{bmatrix} \tag{6.28}$$

Alternatively the surfaces can be expressed using geodesic and ruling curvature functions as

$$\begin{cases} \kappa_g(s) = 0 \quad \kappa_r(s) = 0 & \text{(plane)} \\ \kappa_g(s) = 0 \quad \kappa_r(s) = 1/R & \text{(circle)} \end{cases} \tag{6.29}$$

For either representation we restrict $s \in [0, \frac{\pi R}{2}]$ for a quarter circle of rolling contact and $v \in [0,6]$.

The center of gravity of the 500 gram arm was selected to be 150 mm directly above the rolling-contact point when the arm is in a vertical position. The moment about the rolling-contact point caused by the weight of the arm was computed through the rolling motion. This was accomplished by using Eq. 6.15 to track the position of the rolling-contact point and the center of gravity enabling the length of the moment arm to be computed throughout the motion. The graph of the moment caused by the weight of the arm is plotted in Fig. 6.18 by the line for the analytical moment without balancing. The geometry of the steel band was computed such that the moment caused by gravity was to be balanced by the rolling mechanism. The Bernoulli-Euler relationship from Eq. 6.19 was used to relate the moment as a function of arc length of the band, s, to the second moment of area of the band as a function of arc length, $I(s)$. Further we know that for a circle of radius R, like was chosen for the rolling surface, the curvature is $\kappa = 1/R$, a constant. This along with a substitution of the second moment of area for a rectangular cross section where h is a constant height and b is the width varying with arc length of the band gives

$$\frac{b(s)h^3}{12} = \frac{MR}{E} \tag{6.30}$$

We can solve for function of the width of the band as it varies by arc length as

$$b(s) = \frac{12RM(s)}{Eh^3} \tag{6.31}$$

Our selection of the height h and radius for the circular surface R determine the maximum bending stress experienced in the beam independent of the value of b. This can be seen by taking the equation for bending stress

$$\sigma_b = \frac{Mz}{I} \tag{6.32}$$

where σ_b is the bending stress and z is the distance from the neutral axis to the point of interest in the cross section, solving for M and substituting into the Bernoulli-Euler relationship given by Eq. 6.19. Using the second moment of area for a rectangular beam in the equation, setting z to its maximum value, and simplifying gives

$$\sigma_b = \frac{Eh\kappa}{2} \tag{6.33}$$

where we can see the stress due to bending is independent of the width b. This relation gives us guidance in selecting an appropriate h and curvature to ensure the design will not yield the stiffness band.

The band was also adjusted at one end (by increasing b near this end) to create a small moment to keep the mechanism in an upright position. Once moved more than approximately 8 degrees from the vertical, the mechanism moves into a statically balanced state. This initial resistance to perturbations is shown by the sloped section in Fig. 6.18 at the left end of the line of the analytically expected moment.

A spring (visible in the bottom right of Fig. 6.17(b)) was added when anchoring the stiffness band to regulate the tension in all of the bands, though during motion this spring is inactive with the entire balancing force due to the stiffness band alone. The moment displacement response as the arm moves from a vertical to horizontal position and back was measured using a hydraulic tensile testing machine (Instron Model 1321 with a 22.3 N (5 lb) load cell). Several dummy moments ranging from $0 Nm$ to $5.51 Nm$ were applied to the mechanism for the testing as it can be difficult to measure zero force. This moment was applied by hanging weights across the bottom cylinder (which provides a constant moment arm if the distributed load from the string on the cylinder is considered negligible) and attaching the other end of the cable to the force gauge on the tensile tester. Using this set up the moment displacement response can be found and is plotted for several magnitudes of the dummy moments tested in Fig. 6.18. In this plot the dummy moment has been subtracted from the measured values to show deviation from the zero force response more clearly. The data shows limited hysteresis in the rolling-contact motion.

The plots show that while the stiffness band reduced the load, it did not provide enough of a counter moment to fully balance the mechanism. This behavior could be due in part to a

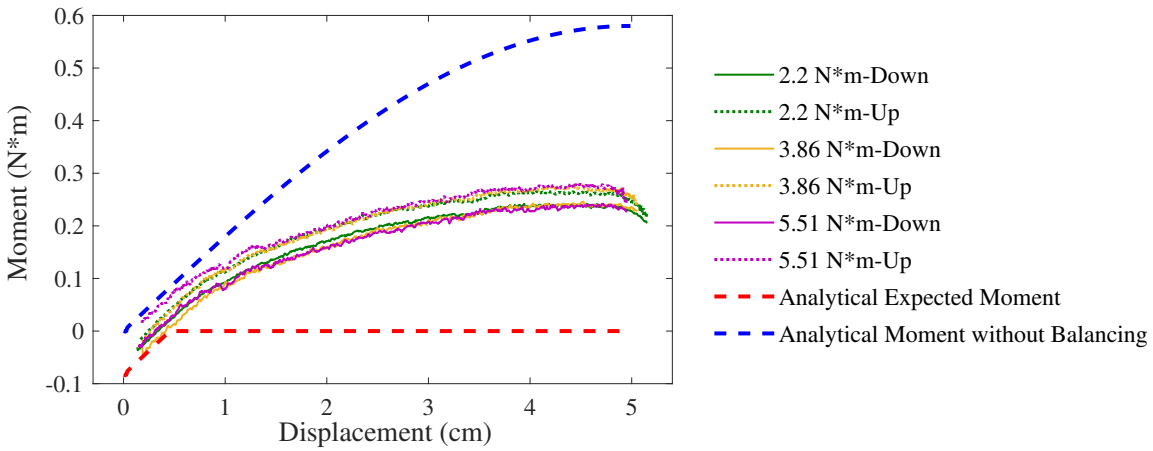

Figure 6.18: A graph of the moment occurring through a full cycle of motion (up and down) for various dummy moment loads with the dummy load subtracted from the measured data.

lifting-off effect occurring between the cylinder and plate it rolls on. The stiffness band wants to push the rolling cylinder off the flat plate. While this separating motion is resisted by the tension bands, the initial resistance to lift off is zero no matter how much initial tension is applied to the tension bands. This allows for some separation between the rolling bodies and decreases the curvature of the stiffness band. Since the curvature is proportional to the moment, a decrease in curvature is reflected in the graph as a decrease in the counter-moment to balance the mechanism. This lifting-off effect was not captured in the kinematic model presented. Further study is needed to characterize the impact of the lifting-off to appropriately implement it into a more refined and accurate kinetic model for rolling contacts with stiffness bands or mechanical means in the test set-up to eliminate the lifting effect.

Additional further study could be conducted to determine an approach for designing rolling-contact surfaces for desired motion paths and exploration of alternative connection methods which maintain a rolling constraint with or without compliant bands. While the theory presented should enable large ranges of statically balanced motion with rolling-contact mechanisms, further study could be conducted for particular rolling-contact mechanisms to achieve better force-response accuracy and to characterize the feasible limits of static balance.

6.5 Conclusions

This chapter has developed kinematic and kinetic models that enable the design of novel mechanisms from developable surfaces within the class of rolling-contact mechanisms. The measures of geodesic and ruling curvature of cross curves were emphasized to help designers see which combinations of developable surfaces can roll on each other. The possible paths of the compliant bands that create the rolling constraint between two bodies were analyzed. Several prototypes demonstrating the capabilities of this design method were constructed. One of these prototypes showed how stiffness bands can be added to these rolling mechanisms to create a tailorable force-displacement response. It is anticipated that a greater understanding of these rolling-contact mechanisms will lead to their use in applications where unique kinematic paths (particularly 3D paths) and kinetic responses are required.

CHAPTER 7. IMPLEMENTATION OF ROLLING CONTACTS FOR SORCE JOINTS

[1]In collaborative research carried out during work on this dissertation the use of curved rolling surfaces was leveraged to create a thickness-accommodation technique for straight-crease origami vertices [147]. This technique in particular and the other rolling-contact applications in the previous chapters highlight the need for a study investigating techniques to physically implement rolling contacts inspired from developable surfaces and curved-crease origami.

7.1 Introduction

Both ancient and contemporary origami art have produced folding patterns that can be employed in the design of deployable mechanisms and structures. Among other things, engineering has leveraged origami for applications where two states are desired, a compact folded state and deployed state. For example, origami designs have been employed in folding solar arrays [81], self folding robots [45], and deployable joints [57].

One of the challenges of using origami design in engineering applications is the accommodation of thickness of the panels. Various techniques have been developed to accommodate for thickness to move from an origami pattern, where the panels are modeled with zero-thickness, into a structure made of thick materials [111, 176, 177]. These techniques take advantage of methods such as trimming away material from panels [85], offsetting panels [178], introducing extra creases [179], and spacing panels on a flexible membrane [81] to facilitate the folding of thick material. Each of these techniques has strengths and limitations in regards to qualities such as preservation of the original origami kinematics, application to only certain crease patterns, and the ability to have parallel-stacked flat-folded states or planar-unfolded states. For example, the

[1]This chapter will be published in the conference proceedings for ReMAR 2018 as Nelson, T.G., Lang, R.J., Magleby, S.P., Howell, L.L., Implementation of Rolling Contacts for SORCE Joints, *4th IEEE/IFToMM International conference on Reconfigurable Mechanisms and Robots (ReMAR 2018)*, Delft, The Netherlands, June 20-22, 2018, Paper ID: 11 (accepted Mar 23, 2018)

membrane technique can be simple to manufacture, aligns all the panels in a single plane in an unfolded state and stacks panels parallel to each other in a flat-folded state; however, the membrane introduces extra freedom into the system during folding and unfolding.

The Synchronized-offset-rolling-contact element (SORCE) technique, has demonstrated the ability to combine many strengths of other thickness accommodation techniques while avoiding many of their limitations. This technique uses cam surfaces at each joint to maintain the zero-thickness origami-folding-model axis locations throughout the folding motion while simultaneously moving panels up or down to accommodate for thickness. In this way the SORCE technique preserves origami kinematics, is applicable to arbitrary crease patterns, has a planar unfolded state, and allows for parallel-stacked flat-folded states [147]. In addition, the SORCE technique imposes no constraints on the thickness of the panels. However, the limitation for this technique comes in the difficulty for physical implementation. Additionally, the Jacob's-ladder-like interwoven bands used originally on the SORCE technique do not allow for convex-concave rolling surfaces. This chapter explores how rolling contacts such as those used for the SORCE technique can be physically realized and gives some constraint methods for convex-concave rolling elements.

We present principles which can be used to effectively implement the SORCE technique and demonstrates these in the construction of several thick-panel origami vertices and structures. Fold-Angle Multipliers are used to characterize families of vertices which can be constructed using a single set of SORCE joints. Range control is shown by incorporating hard stops into the SORCE cams. Multiple methods of flexure assembly are explored and discussed. While this chapter specifically addresses rolling joints for the SORCE technique, many of the principles presented apply generally to rolling joints in their various forms and applications. These include biomimetic joints [104,165], multistable joints [94,180], joints for thick origami and folding structures [163,164,181], medical instruments [103], and rolling joints with spatial motions [166,167]. Cam-based linkages also present similar challenges in implementation and a large body of work addressing these challenges including force-closed and form-closed cams, custom follower geometries, and regulation of the pressure angle and normal force exists [150]. The principles presented here may also be useful in furthering cam-based-linkage implementation strategies. These principles are demonstrated in prototypes including the construction of two vertices with a shared fold-angle multiplier and a birds-foot array.

7.2 Background

7.2.1 The SORCE Technique

The SORCE technique for creating thick material origami vertices preserves the zero-thickness origami kinematic model during folding while simultaneously moving the thick panels vertically away from the zero-thickness model's panels to allow for stacking in the folded shape. The zero thickness model "moves through" the panels as they fold and become vertically offset from each other for stacking. Rolling contacts are a type of joint which can enable this axis shift with simultaneous rotation of the folding motion. These rolling cam surfaces enable the zero thickness model to be moved during the folding from one side of a panel to the other, or even off the panel to allow for other panels to stack between panels. Vector functions, $\mathbf{s}_l(t)$ and $\mathbf{s}_r(t)$ as shown in Fig. 7.1, are used to define the rolling-contact surfaces. The vector functions can be solved for using the kinematics of the zero-thickness origami vertex (specifically the fold-angle rates, $\gamma_i(t)$) and by choosing offset functions to describe how the panels move away from each other (z_i). Furthermore, offsets can be introduced into the zero thickness model by splitting the mechanism along a fold to produce a relative motion vector $\mathbf{d}(t)$ as shown in Fig. 7.1 both in the full vertex schematic and the detail view. Only summarized here, but treated fully in [147], the equations for determining the two rolling surfaces are given by

$$\mathbf{s}_l = \frac{1}{\gamma'}\left[z_r'\hat{\mathbf{u}}(\pi+\gamma) + z_l'\hat{\mathbf{u}}(0) + \mathbf{R}(\tfrac{\pi}{2})\cdot\mathbf{d}'\right] - z_l\hat{\mathbf{u}}(\tfrac{\pi}{2}) + \mathbf{d}, \tag{7.1}$$

$$\mathbf{s}_r = \frac{1}{\gamma'}\left[z_l'\hat{\mathbf{u}}(-\gamma) + z_r'\hat{\mathbf{u}}(\pi) + \mathbf{R}(\tfrac{\pi}{2}-\gamma)\cdot\mathbf{d}'\right] - z_r\hat{\mathbf{u}}(\tfrac{\pi}{2}) \tag{7.2}$$

where the explicit t dependence of the functions is dropped for brevity, and $\hat{\mathbf{u}}(\theta)$ is a unit vector given by

$$\hat{\mathbf{u}}(\theta) \equiv (\cos\theta, \sin\theta) \tag{7.3}$$

and $\mathbf{R}(\theta)$ is a counterclockwise rotation matrix given by

$$\mathbf{R}(\theta) \equiv \begin{pmatrix} \cos\theta & -\sin\theta \\ \sin\theta & \cos\theta \end{pmatrix}. \tag{7.4}$$

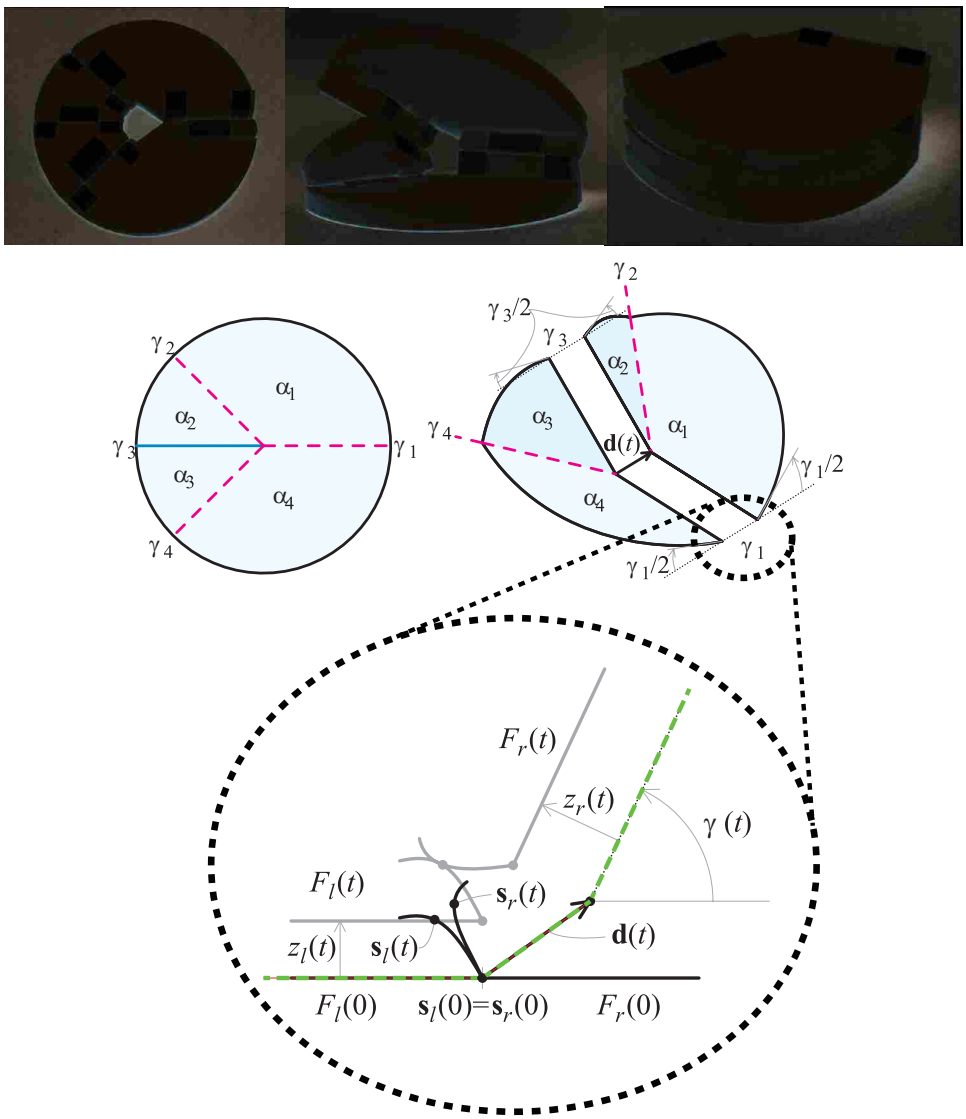

Figure 7.1: The SORCE technique: Using the kinematics of a zero-thickness origami vertex to create rolling surfaces at each fold line (such as the one shown in the dashed circle where the green dashed lines are the zero-thickness model plane) which allow for a vertex made of thick material to begin in a planar state and fold to a stacked state while preserving the zero-thickness kinematics.

7.3 Method

Principles are identified in this section to facilitate the physical implementation of the SORCE technique. A discussion of several current manufacturing techniques suitable to creating the custom surfaces required for the SORCE technique is also included.

7.3.1 Shared Fold-Angle Multipliers

For a flat-foldable degree-4 vertex the cam shapes depend on the panel offset functions $\{z_i(t)\}$ and the fold-angle functions $\{\gamma_i(t)\}$, and the latter can be expressed solely in terms of the fold-angle multiplier μ, and μ is the only place where the values of the sector angles enter into the analysis. That means that any set of four sector angles with the same fold-angle multiplier can make use of the same set of cams for a given panel thickness.

Suppose we have an initial set of flat-foldable sector angles satisfying the Kawasaki-Justin Theorem, $(\alpha_1, \alpha_2, \pi-\alpha_1, \pi-\alpha_2)$. The fold-angle multiplier μ is given in Equation (7.5),

$$\mu = \frac{\sin\frac{1}{2}(\alpha_1+\alpha_2)}{\sin\frac{1}{2}(\alpha_1-\alpha_2)}. \tag{7.5}$$

Now, if we change sector angle $\alpha_1 \to \alpha_1^*$ and wish to preserve μ, we must change $\alpha_2 \to \alpha_2^*$ with

$$\alpha_2^* = 2\cos^{-1}\left[2\sin\left(\frac{\alpha_1}{2}\right)\cos\left(\frac{\alpha_2}{2}\right)\cos\left(\frac{\alpha_1^*}{2}\right)\Big/ \sqrt{\cos(\alpha_2)\cos\left(\alpha_1^*\right)-\cos(\alpha_1)\left(\cos\left(\alpha_1^*\right)+\cos(\alpha_2)\right)+1}\right]. \tag{7.6}$$

So, for example, for the example vertex of Fig. 7.2 where

$$\alpha_1 = 120^\circ,\ \alpha_2 = 80^\circ,\ \alpha_3 = 60^\circ,\ \alpha_4 = 100^\circ,$$

the fold-angle multiplier μ is 2.8794, and if we change $\alpha_1 \to \alpha_1^* = 140^\circ$, then the vertex with the same fold-angle multiplier will have sector angles

$$\alpha_1^* = 140^\circ,\ \alpha_2^* = 106.165^\circ,\ \alpha_3^* = 40^\circ,\ \alpha_4^* = 73.835^\circ,$$

and the same rolling contact surfaces would give this vertex a single-DOF kinematic motion.

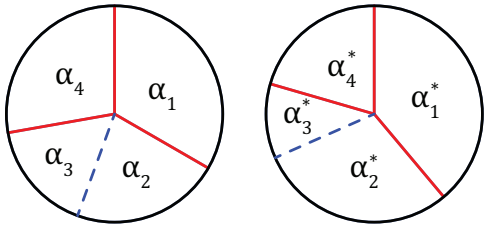

Figure 7.2: Two vertices related by a shared fold-angle multiplier of $\mu = 2.8794$ with mountain and valley folds shown by the red and blue dashed lines.

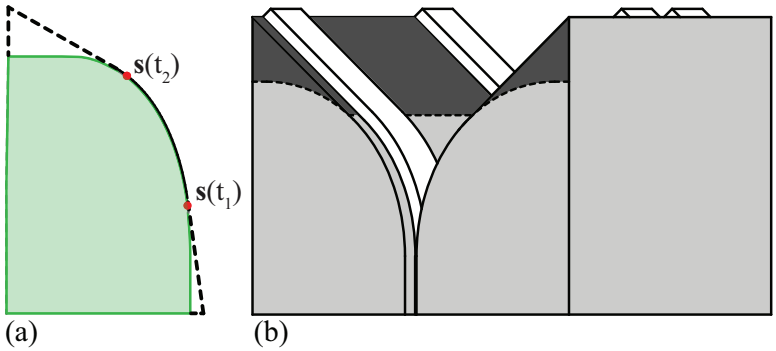

Figure 7.3: (a) Schematic diagram of how tangent lines can be used to control the folding angle range of a SORCE joint. (b) Hard stops incorporated into the cam design to limit the motion of the vertex to a certain angle.

7.3.2 Joint Range Control

The folding angle range of a vertex can be controlled by adjusting the geometry of the SORCE joint rolling surfaces. The following procedure describes how to construct a vertex with a particular folding angle range. Let t_1 and t_2 denote the fold parameters for $\gamma(t)$ corresponding to the two extreme angles of the desired folding angle range. The SORCE cam which enables this range of motion is created by extending lines tangent to the cam surfaces at the points $\mathbf{s}(t_1)$ and $\mathbf{s}(t_2)$ for both the left and right cam surfaces. These tangent lines will have slopes of $\mathbf{s}'(t_1)/\|\mathbf{s}'(t_1)\|$ and $\mathbf{s}'(t_2)/\|\mathbf{s}'(t_2)\|$ for the two extreme points and are shown in Fig. 7.3(a). The modified SORCE cams only allow motion up to the desired fold-angle range as portions of the surface corresponding to the tangent lines create hardstops. An example of a SORCE rolling joint that has been limited to a 90° fold angle is shown in Fig. 7.3(b).

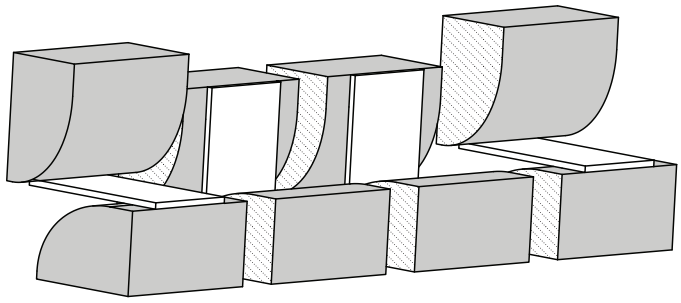

Figure 7.4: Cams can be split apart to facilitate assembly of the bands and then joined together on the cross-hatched faces.

7.3.3 Flexure assembly

Achieving the correct tension in each of the flexures joining the SORCE cams is important to create a rolling joint which avoids excess play, imbalance, or excessive stress in the flexures. Weaving the flexures between the SORCE cams and attaching them to the cam can be difficult so alternatives were explored.

One method which allows the bands to be tensioned effectively involves separating the SORCE cam into sections for assembly as shown in Fig. 7.4. In a SORCE joint, the two SORCE cams are held together by interwoven flexures which create balanced tensile forces that pull the cams together. Separating the cams into sections corresponding to the areas where the flexures pull the cams together in a single direction enables the flexures to be assembled in a relaxed state (no tension present). After the flexures are attached, the cams can be attached together effectively tensioning the opposing bands simultaneously.

Another method to facilitate cam assembly involves using contractile materials. Heat-activated contractile polymer (heat shrink) was investigated as a possible flexure material. This material allowed the joint to be assembled in loose configuration as shown in Fig. 7.5(a). Heat was used to contract the flexures and pull the cams together, creating the necessary tension for the joint to function. The joint after this contraction is shown in Fig. 7.5(b).

7.3.4 Sunken Flexures

While tensioning the flexures draws two convex rolling bodies together, if the curvature of the rolling bodies is small or one of the rolling bodies is planar it takes a negligible amount of

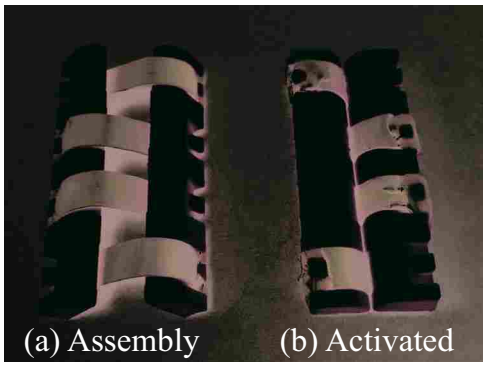

Figure 7.5: Heat-activated contractile polymer (heat shrink) can be used to facilitate assembly of the joint and then is activated to finalize the assembly.

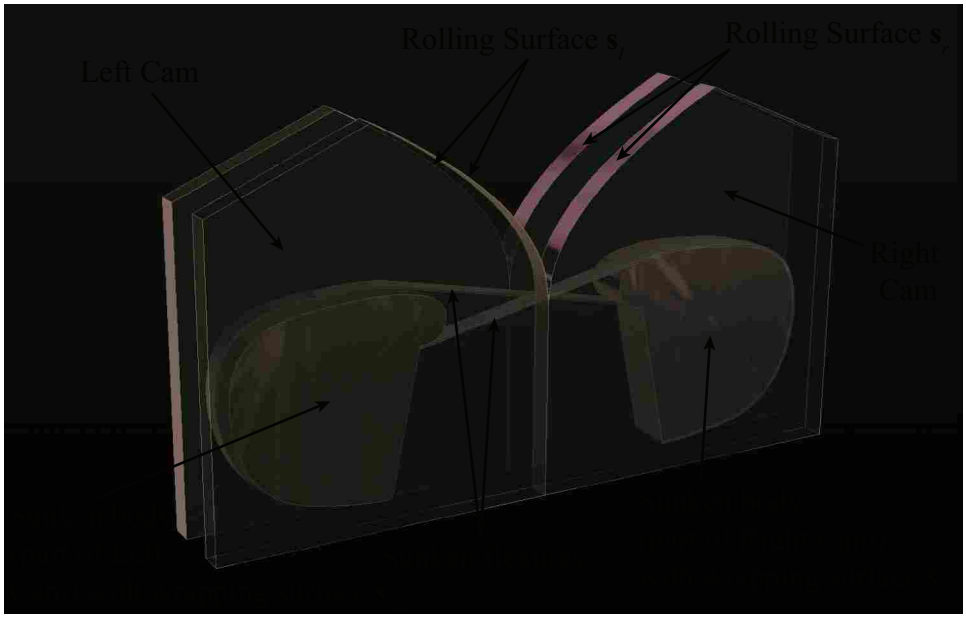

Figure 7.6: Labeled geometry of sunken flexures pulling together two rolling cams with the front panels of the rolling cams translucent.

force to initiate separation of the bodies regardless of the amount of tension in the flexures. To mitigate this effect for small curvature or planar surfaces, sunken flexures can be used. Sunken flexures are wrapped about surfaces set inside the rolling contact surface as shown in Fig. 7.6 and schematically in Fig. 7.7. The tension forces in sunken flexures have components of force normal to the rolling surfaces which draw the bodies toward each other.

Besides the special case of circular rolling surfaces, purely offsetting the rolling surfaces to create *wrapping surfaces* upon which the sunken flexures can wrap will result in the sunken

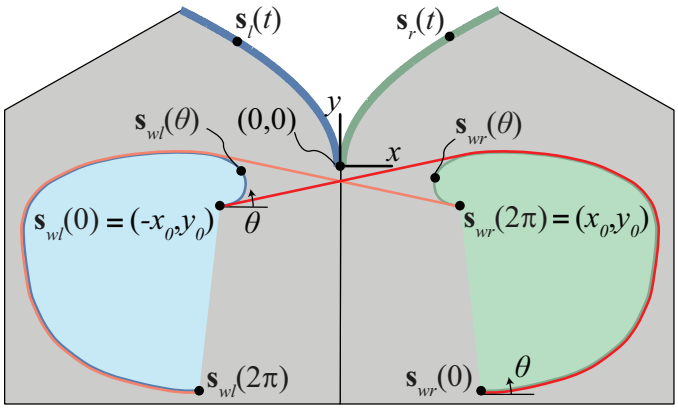

Figure 7.7: Schematic of sunken flexures on wrapping surfaces.

flexures having to stretch or even worse, go slack as the rolling motion occurs. This stretch or slack can be accommodated by incorporating a spring with sufficient travel to enable the extension and contraction of the sunken flexure length.

Alternatively, the wrapping surfaces upon which the sunken flexures wrap can be computed to minimize the stretch or slack during the rolling motion. While proving the existence of wrapping surfaces for arbitrary rolling surfaces which enable zero change of length in the sunken flexures is beyond the scope of this work, we present an optimization method which minimizes the change of length of the sunken flexures and show its performance on a prototype of two non-similar rolling surfaces. We first describe the geometry in a way that enables us to apply an optimization routine and then describe how the algorithm functions.

Geometry and Set-up for Optimization Algorithm

For any set of rolling-contact surfaces $\mathbf{s}_l(t)$ and $\mathbf{s}_r(t)$ (convex-convex or convex-concave pairs), the left and right wrapping surfaces, $\mathbf{s}_{wl}$ and $\mathbf{s}_{wr}$, are constrained to be convex surfaces which do not self-intersect and are symmetric about a vertical axis, the y axis of Fig. 7.7. Because of the symmetry, we first look at $\mathbf{s}_{wl}$. The convexity of the wrapping surface can be ensured by defining $\mathbf{s}_{wl}$ with a single function where the domain is the direction of the slope, θ, from 0 to 2π, and the range is the magnitude of the slope $M(\theta)$ with $M(\theta) > 0$. The function starts from a selected initial point, $(-x_0, y_0)$. From this information we can calculate

$$\frac{\mathrm{d}\mathbf{s}_{wl}(\theta)}{\mathrm{d}\theta} = (M(\theta)\cos\theta\ ,\ M(\theta)\sin\theta) \tag{7.7}$$

which can be integrated to

$$\mathbf{s}_{wl}(\theta) = \left(\int M(\theta)\cos\theta\ \mathrm{d}\theta + x_0, \int M(\theta)\sin\theta\ \mathrm{d}\theta + y_0 \right) \tag{7.8}$$

The right wrapping surface can be formulated as the reflection of $\mathbf{s}_{wl}(\theta)$ and we reverse the parametrization direction to maintain a counter-clockwise rotation as θ increases giving

$$\mathbf{s}_{wr}(\theta) = \begin{bmatrix} -1 & 0 \\ 0 & 1 \end{bmatrix} \mathbf{s}_{wl}(2\pi - \theta) \tag{7.9}$$

We can determine if a wrapping surface self intersects by putting the wrapping surface into polar coordinates (ϕ, r) and checking to see that the polar angle as a function of the slope direction θ, $\phi(\theta)$, is monotonic increasing. We numerically carry this out by stepping through the domain of θ and using a multi-valued inverse tangent function (i.e. atan2) to find ϕ as

$$\phi(\theta) = \mathrm{atan2}(y, x) \tag{7.10}$$

where $(x, y) = \mathbf{s}_{wl}(\theta)$.

If the polar angle decreases with any positive step in θ, it signifies that self-intersection has occurred. We later use this determination to impose a penalty constraint in our optimization routine for self-intersection.

The wrapping surfaces $\mathbf{s}_{wl}$ and $\mathbf{s}_{wr}$ are vector-valued functions given in the global xy frame shown in Fig. 7.7. However, once rolling starts to occur, the transformation relationships describing the rolling bodies and their surfaces are needed to analyze the sunken flexures joining the two rolling bodies. We can obtain this transformation information from $\mathbf{s}_l(t)$ and $\mathbf{s}_r(t)$. For simplicity we assume $\mathbf{s}_l$ is grounded while $\mathbf{s}_r$ rolls. The rotational component of the transformation is found using the composition of two rotations in the form of Eq. 7.4. The first rotates the global xy frame

about the z axis so the new y axis corresponds to the tangent vector at the point of contact, $\mathbf{s}_l'(t)$. The angle of rotation for this rotation is $\theta_{z1} = \text{atan2}(y_c, x_c) - \pi/2$ where (x_c, y_c) are the coordinates the point of contact, $\mathbf{s}_l(t)$. The second rotation is from the frame at the point of contact to the frame $x_R y_R$ at the initial point of the second rolling surface shown in Fig. 7.8. The angle of rotation for this rotation is $\theta_{z2} = \pi/2 - \text{atan2}(y_c, x_c)$. We can therefore write the rotational component as

$$\mathbf{R}(\theta_R) = \mathbf{R}(\theta_{z1} + \theta_{z2}) \tag{7.11}$$

where the explicit dependence of θ_R, θ_{z1}, and θ_{z2} on t has been dropped for brevity.

We can find the translational component, $\mathbf{q}(t)$, of the transformation by

$$\mathbf{q}(t) = \mathbf{s}_l(t) - \mathbf{R}(\theta_R)\mathbf{s}_r(t) \tag{7.12}$$

where $\mathbf{s}_l(t)$ and $\mathbf{s}_r(t)$ are the vectors to the point of contact shown in Fig. 7.8.

We can calculate the length of a sunken flexure at any rolling state t, (and as the wrapping surfaces are symmetric, the lengths of both sunken flexures are equivalent at any t) by

$$\ell(t) = \ell_l(t) + \ell_s(t) + \ell_r(t) \tag{7.13}$$

where ℓ_l is the length of the flexure wrapped on $\mathbf{s}_{wl}$, ℓ_s is the length of the straight tangent line segment of the flexure connecting $\mathbf{s}_{wl}$ and $\mathbf{s}_{wr}$, and ℓ_r is the length of the flexure wrapped on $\mathbf{s}_{wr}$. While this equation contains simple terms, some effort is required to evaluate it. We choose points to anchor the sunken flexures to the wrapping surfaces $\mathbf{s}_{wl}(a_1)$, $\mathbf{s}_{wr}(a_2)$, $\mathbf{s}_{wl}(a_3)$, and $\mathbf{s}_{wr}(a_4)$. These points are shown in Fig. 7.8 where they are chosen to be the extreme ends of the wrapping surfaces ($a_1 = a_2 = 0$, $a_3 = a_4 = 2\pi$). The sunken flexures connect $\mathbf{s}_{wl}(a_1)$ to $\mathbf{s}_{wr}(a_2)$ and $\mathbf{s}_{wl}(a_3)$ to $\mathbf{s}_{wr}(a_4)$.

Besides the four anchor points, we need to know four more points, $\mathbf{s}_{wl}(b_1)$, $\mathbf{s}_{wr}(b_2)$, $\mathbf{s}_{wl}(b_3)$, and $\mathbf{s}_{wr}(b_4)$ to determine the lengths of the sunken flexures at rolling state t. These points are shown in Fig. 7.8 for a specific rolling state t.

Because the sunken surfaces are symmetric we look at only one band as shown in Fig. 7.9. The straight portion of the band connecting the two rolling bodies is a diagonal tangent between the two convex wrapping surfaces. An optimization approach can be used to find the diagonal tangent and consequently points $\mathbf{s}_{wl}(b_1)$ and $\mathbf{s}_{wr}(b_2)$. We let θ_{wl} be our single free variable. Starting at

zero, we can incrementally increase this angle to minimize the distance δ between two parallel tangent vectors shown in gold. The tangent vector coming off the left wrapping surface has a slope of θ_{wl} and goes through point $\mathbf{s}_{wl}(\theta_{wl})$. The tangent vector coming off the right wrapping surface has a slope of $\theta_{wr} = \theta_{wl} + \pi - \theta_R$ going through point $\mathbf{s}_{wr}(\theta_{wr})$. If $\theta_{wr} > 2\pi$ we can decrease it by 2π (i.e. $\theta_{wr} = \theta_{wr} - 2\pi$) to keep it in the domain of $\mathbf{s}_{wr}(\theta)$. The distance between these two parallel lines is

$$\delta = \frac{|y_r - y_l + (x_l - x_r)\tan(\theta_{wl} + \pi)|}{\sqrt{1 + \tan^2(\theta_{wl} + \pi)}} \tag{7.14}$$

with

$$\begin{aligned} (x_l, y_l) &= \mathbf{s}_{wl}(\theta_{wl}) \\ (x_r, y_r) &= \mathbf{R}(\theta_R)\mathbf{s}_{wr}(\theta_{wr}) + \mathbf{q}(t) \end{aligned} \tag{7.15}$$

Minimizing the distance δ gives the diagonal tangent and angles b_1 and b_2 for a specific rolling state t. It is important to search by increasing from $\theta_{wl} = 0$ as δ will go to zero multiple times, but the first time will give the diagonal tangent we are interested in.

With the points $\mathbf{s}_{wl}(b_1)$ and $\mathbf{s}_{wr}(b_2)$ we can compute the terms in Eq. 7.13 using arc lengths and the magnitude of a vector as

$$\begin{aligned} \ell_l(t) &= \int_{a_1}^{b_1} \|\mathbf{s}'_{wl}(\theta)\| \, d\theta \\ \ell_r(t) &= \int_{a_2}^{b_2} \|\mathbf{s}'_{wr}(\theta)\| \, d\theta \\ \ell_s(t) &= \|(\mathbf{R}(\theta_R)\mathbf{s}_{wr}(b_2) + \mathbf{q}(t)) - \mathbf{s}_{wl}(b_1)\| \end{aligned} \tag{7.16}$$

With the ability to calculate the length of a flexure at a given rolling state t, we describe an optimization algorithm for finding the wrapping surfaces which provide constant length flexures.

Optimization Algorithm

We let the shape of $\mathbf{s}_{wl}$ vary with n free variables by choosing values $M_i = M(i(2\pi/n))$ for $i = 1$ to n and using cubic spline interpolation with these points to get $M(\theta)$. We select an

initial point $(-x_0, y_0)$ and use Eq. 7.7 and 7.8 to find an expression for $\mathbf{s}_{wl}(\theta)$. We check to make sure the surface does not self-intersect by using Eq. 7.10 and stepping through θ from 0 to 2π. If intersection occurs we impose a penalty (in our implementation, we set a value to cause an equality constraint to be false). We then use Eq. 7.9 to obtain $\mathbf{s}_{wr}(\theta)$.

We choose n_t values for t at which to compute the length of a flexure band. We find the transformation information $\mathbf{R}(\theta_R(t))$ and $\mathbf{q}(t)$ from the rolling surfaces $\mathbf{s}_l(t)$ and $\mathbf{s}_r(t)$ at these n_t values using Eq. 7.11 and 7.12. Note that this information need only be computed once and can be used for any iteration as it does not change with the free variables.

We compute the length of the band at each of the n_t values of t using the procedure explained previously with Eq. 7.13. We select one of these lengths to be our reference length, ℓ_{ref}. We subtract ℓ_{ref} from the computed band lengths to get changes in length $\Delta\ell$ for the n_t rolling states. We use this information to construct our objective function, $F(M_i)$, to minimize as

$$F(M_i) = \max(\Delta\ell) \tag{7.17}$$

where $\max(\Delta\ell)$ represents the largest change in length for the n_t rolling states checked.

We can use an optimizer (such as MATLAB's *fmincon*) to adjust the free variable M_i and iterate to converge to a solution that minimizes the change of length $\Delta\ell$ during rolling.

Note the choice of the initial point of the wrapping surfaces $(-x_0, y_0)$ largely affects the shape of the wrapping surfaces and can be adjusted if the wrapping surface found by the algorithm is not desirable. Further constraints could be added to the algorithm such as preventing the wrapping surfaces from extending beyond the rolling surfaces.

The algorithm described above was implemented with $n = 60$ and $n_t = 10$ for the surfaces shown in Fig. 7.10. The two rolling surfaces consisted of a section of a parabola and a quarter circle. The optimizer arrived at a solution with a maximum change in length of the sunken flexures during rolling of 0.5%. A physical prototype was created out of acrylic and tested which showed a maximum change in length of about 1.5%. This discrepancy could be to inaccuracies in fabrication and small amounts of slip occurring during testing.

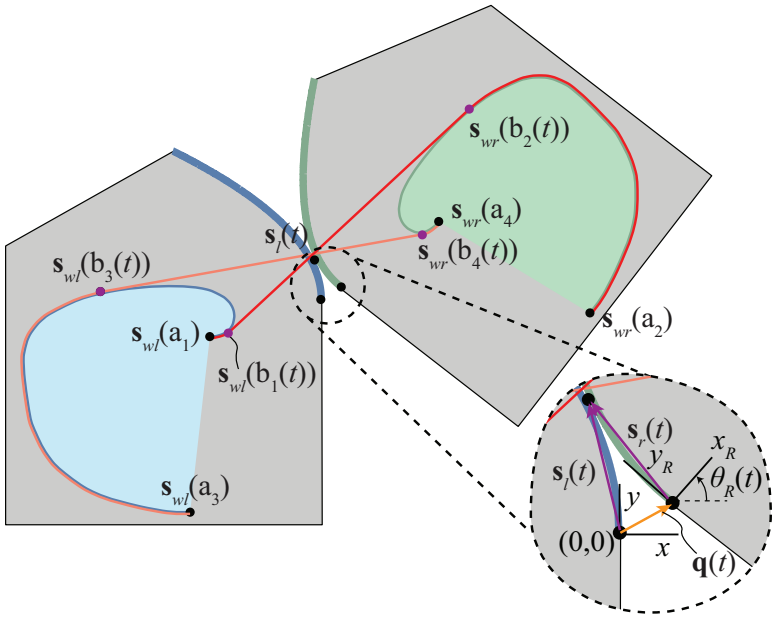

Figure 7.8: Sunken Flexures on wrapping surfaces at an arbitrary rolled state t.

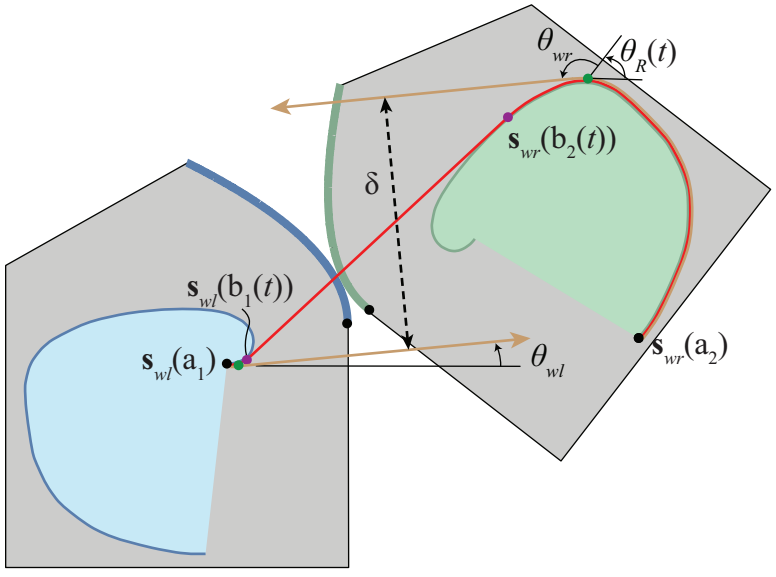

Figure 7.9: The process of finding a diagonal tangent line on convex hulls for an arbitrary rolled state t.

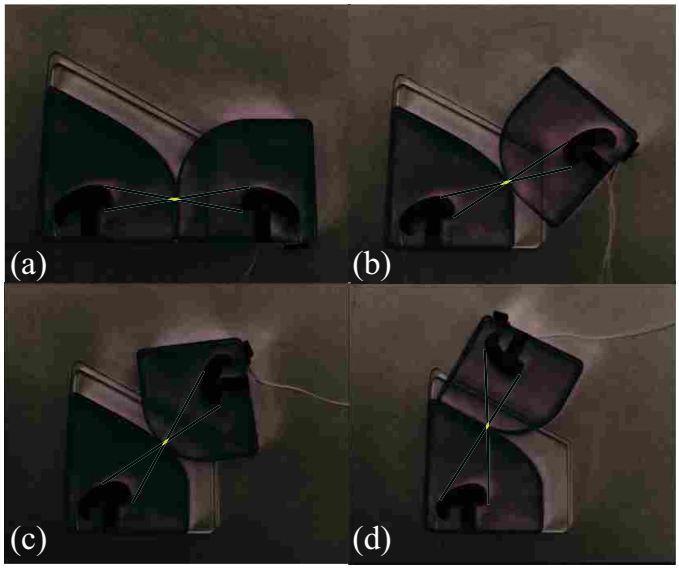

Figure 7.10: Prototype of a constant-length sunken flexure joint rolling from one extreme position (a) to the other (d) with dissimilar green rolling surfaces, white wrapping surfaces and dark green sunken flexures with straight regions highlighted in yellow for visibility.

7.3.5 Geared Teeth and flexure bands

Inaccuracies in flexure assembly and stretch in flexures can cause a decrease in the normal force and even slip between the two rolling bodies. Additional friction, or even geared teeth can be added to the rolling surfaces to create a no-slip rolling condition. Increasing the tension in the bands for sunken flexures will generate more normal force and may decrease the possibility of slip.

7.3.6 Form-Closed Rolling Joints

The traditional flexure-based architecture necessary for compliant rolling elements limits the design of SORCE cams to convex surfaces [147]. Like sunken flexures, form-closed rolling joints can provide architectures that allow these conditions to be relaxed. Analogous to the definition of form-closed traditional cams and followers, a rolling joint can be considered as form closed when geometric constraints hold the rolling surfaces together. This is in contrast to force-closed architectures, such as the flexure based architecture, where force elements keep the rolling surfaces together.

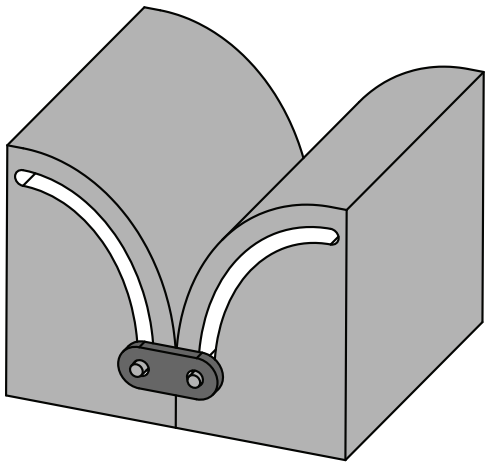

Figure 7.11: Roller tracks can be used instead of flexible bands to create form closed cams.

Roller Tracks

One method of creating a form-closed rolling joint is to cut grooves into two rolling cams such that two roller bearings joined by a link pull the two rolling cam faces together. This type of form-closed rolling joint is shown in Fig. 7.11. The grooves should maintain a constant offset from the cam surfaces corresponding to the length of the rigid link connecting the two roller bearings. This type of architecture for rolling joints enables cam surfaces to be joined where one of the rolling surfaces is convex while the other is concave with a smaller curvature than the convex surface. This mixing of convex and concave rolling surfaces enables the construction of SORCE joints for vertices who have surface functions that are difficult to make entirely convex.

Conjugate Cams

Conjugate cams create a geometric constraint that holds the two rolling surfaces together by introducing a conjugate surface for each rolling surface. These conjugate surfaces roll on a frame which constrains the two cam faces to be in contact. Figure 7.12 shows an example of symmetric rolling cams (green rolling surfaces) with their conjugate surfaces (blue surfaces) inside a frame.

We leave the development of an analytic or numerical technique to create conjugate cams as an open problem for further work.

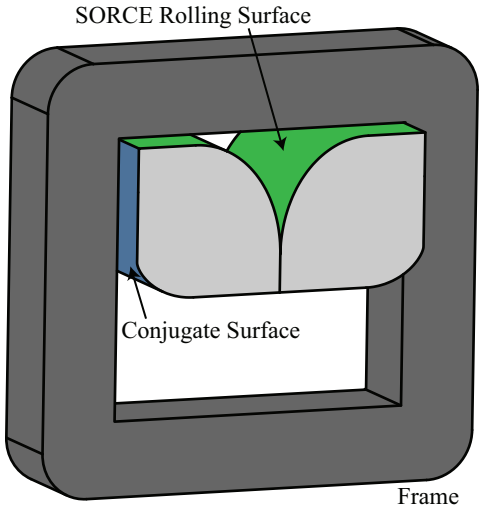

Figure 7.12: Conjugate surfaces can be created on the cams to enable the joint to roll within a frame to create a form closed cam.

7.3.7 Manufacturing Methods

The custom cam surfaces needed to implement SORCE technique are perhaps the most difficult elements of the joint to fabricate. Various manufacturing methods that are able to achieve custom 2D profiles can be used to achieve the cam surfaces including 3D printing, laser cutting, water jet, CNC mills, and wire electrical discharge machining (EDM). For high volume manufacturing injection molding and casting present suitable manufacturing methods. The growing commonality of 3D printing offers an economical way to manufacture the custom rolling cams required for the SORCE technique.

7.4 Examples

This section shows several examples of how the SORCE technique and principles discussed above can be implemented in thick origami applications.

7.4.1 Fold-Angle Multiplier Vertices

The pair of vertices with a shared fold-angle multiplier described in Fig. 7.2 were physically constructed using a sandwich panel, wooden cams, and flexible bands of Tyvek. Two sets of identical cams were used on these vertices to demonstrate that fold-angle multipliers can be

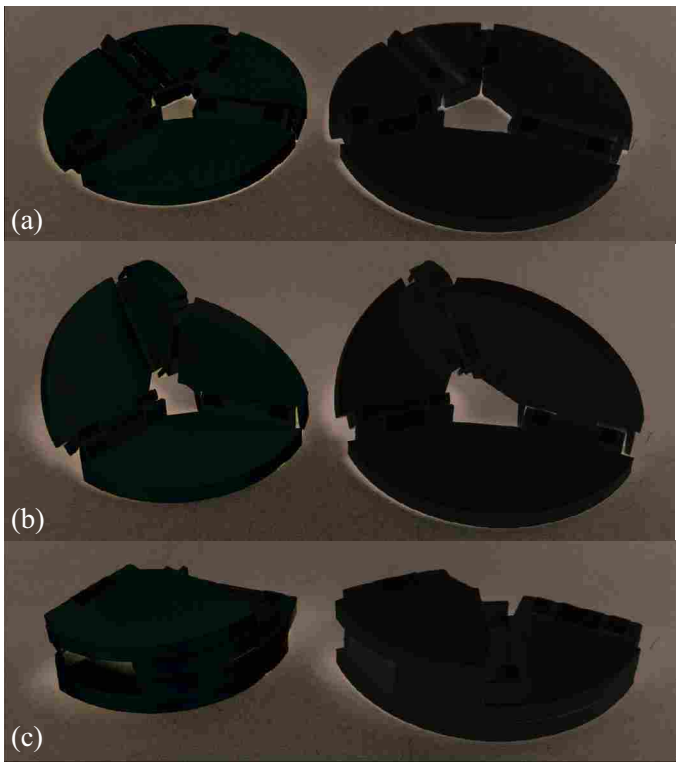

Figure 7.13: Physical prototypes of two vertices related by a shared fold-angle multiplier of $\mu = 2.8794$ shown (a) unfolded, (b) partially folded, and (c) fully folded.

used to find multiple vertex configurations which allow the same geometry of SORCE cams. The physically constructed vertices are shown in Fig. 7.13.

7.4.2 Birds-Foot tessellation

A multi-vertex birds-foot tesselation was created by repeating and connecting a vertex. This vertex consisted of sector angles of (135°, 45°, 45°, and 135°), similar to one of the vertices described in [147]. Also, the zero-thickness pattern of this vertex was split along its line of symmetry to obtain rolling surfaces better suited to the CORE architecture when accommodating thickness. 3D printing was used to create the rolling surfaces with flexible bands holding them together made of Tyvek. The panel facets were created from 1.016 cm (0.4 in) thick sandwich panel commercially available as Gatorboard. This Birds-foot tessellation is shown in Fig. 7.14.

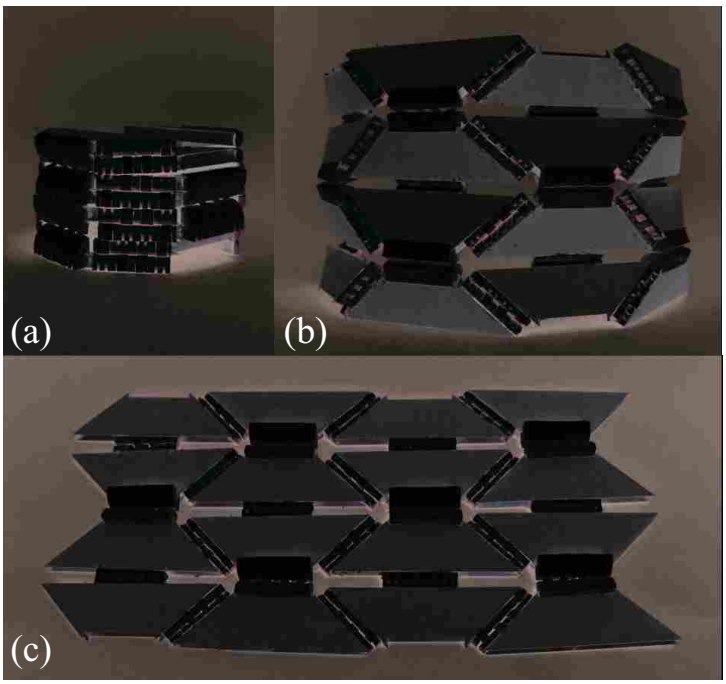

Figure 7.14: Birds-foot tessellation created with 3D printed cams with Tyvek flexures shown (a) fully folded, (b) partially folded, and (c) unfolded.

7.5 Conclusion

The principles presented in this chapter enable the use of the SORCE technique for thickness accommodation. They are also well suited for use in other areas where rolling joints are beneficial due to their unique qualities of a moving axis and low friction. These principles include using fold-angle multipliers to find shared rolling geometries for related origami vertices, various assembly techniques of the rolling joints, the use of sunken flexures, adding geared teeth, and form-closed possibilities. While some of the principles simplify manufacturing, such as the use of shared fold-angle multipliers and flexure assembly methods, other principles extend the capabilities of the SORCE technique. For example, sunken flexures present viable solutions to increasing the normal force between and preventing separation of rolling bodies that can occur with traditional interwoven flexures. These sunken flexures can enable convex-concave rolling surfaces, yet they come at the expense of increased complexity. With the ever increasing availability of custom manufacturing processes coupled with these principles, the barrier to using rolling joints can be lowered to enable innovative mechanisms and structures.

CHAPTER 8. CONCLUSIONS

In the previous chapters we have presented evidence that curved-crease origami with the developable surfaces that compose it can be used effectively in engineering challenges. Broadly put, the engineering applications that stand the most to gain from the work presented have certain attributes. These attributes include: 1. the presence of curved surfaces integral to the application's function, 2. the possibility to benefit from the ability to be deployed from a compact or planar state and 3. constraints on what manufacturing methods can be used such that planar operations and folding into the final shape may be desirable or even required.

Incorporating concepts from curved folding and developable surfaces can provide a pathway to using planar manufacturing processes with mechanisms and structures with curved surfaces and can also enable deployable mechanisms and structures with compact or flat storage. The particular concepts explored in this dissertation include the importance of ruling-line and hinge-axis alignment for creating deployable thick developable surfaces, the addition of curved creases to developable surfaces present in mechanisms and structures to create deployability, the unfolding of mechanisms and structures into a single plane to enable 2D manufacturing followed by assembly through folding, and the consideration of all classes of the developable surfaces to extend the design space for mechanisms and structures where developable surfaces are present. Multiple methods were employed to analyze and facilitate the incorporation of these concepts. These include analytic mathematical models (particularly trigonometry, vector-based, and differential geometry models), numerical simulations such as finite element models, optimization routines, pseudo-rigid body modeling, and graphical methods. This medley of approaches to implement 2D manufacturing followed by folding assembly or to create deployability characteristics from the concepts presented in the dissertation suggests the importance of examining each engineering application individually and selecting an appropriate methodology for what is desired. Further study is warranted to understand appropriate methodology selection for categories of applications.

Theory was presented for the synthesis of flexible, tailorable-property surfaces that can be used as thick curved-crease origami panels. This was accomplished through chaining together compliant elements. Particularly several types of lamina emergent mechanisms whose major rotational displacement came from distributed torsional members were utilized in the arrays. These networks of joints were used to locally decrease the stiffness along the ruling lines of a developable surface panel. Prototypes were built and tested to demonstrate moving curved-crease origami out of paper.

Further insight into the design and use of these thick flexible surfaces was gathered through the creation of shape factors to describe the effects of the array geometries on the effective properties of the flexing surface. These factors in conjunction with Ashby material property charts can provide designers with a material selection methodology for thick flexing panels.

The second part of this dissertation described and demonstrated how concepts from curved-crease origami and developable surfaces can be used in engineering design, particularly in the case study of rolling-contact joints. Elements of deployability and planar manufacturing were incorporated into a rolling-contact joint design using curved creases. A form of equations for developable surfaces, natural equations, was described that enables a designer to straightforwardly choose a developable surface of a single class with specific characteristics important to several engineering properties. This equation form was used to describe the entire family of single-class developable rolling-contact joints. Lastly some practical methodology of constructing these types of rolling joints was set forth.

Besides the contributions to the body of scholarly knowledge described above, this work has the capability to impact our broader society. As some of the chapters have begun to demonstrate, curved-origami-inspired mechanisms have applications in medical devices, deployable joints, efficient flexible solar arrays, morphing wings on aircraft, deployable emergency structures, airbag safety, and conformable body armor. Besides significant applications, this research will hopefully facilitate further cooperation and learning between two fields that often are viewed as separate: art and science. It has been a fruitful opportunity to work with artists and industrial designers on collaborative projects, where all have come away enlightened by the insights of the others. Such cooperation builds interest in the science, technology, engineering and math (STEM) fields from others and also gives those in the STEM an appreciation and value for work done outside of STEM.

Finally, this dissertation represents a step forward, but not a destination in the application of curved-crease origami and developable surfaces to engineering design. Many aspects of curved folding remain unexplored. Further mathematical characterization and design methodology is warranted to enable the understanding and intentional design of complex generalized developables. While one method for enabling the flexibility needed for thick panels in curved-origami-inspired mechanisms and structures was presented, alternative processes should be and are being explored to enable stronger, yet still flexible panels. Additionally methods of thickness-accommodation at the vertices where curved folds meet is needed. Though mainly rolling-contact joints were studied in this work, it is anticipated that future work will illuminate the breadth of engineering applications where curved-folding concepts form part of the path towards continuing innovation.

REFERENCES

[1] Koschitz, R. D., 2014. "Computational design with curved creases: David Huffman's approach to paperfolding." PhD thesis Massachusetts Institute of Technology.

[2] Sallas, J., 2010. *Gefaltete Schonheit*. Freiburg and Vienna.

[3] Wingler, H. M., 2015. *Bauhaus Weimar, Dessau, Berlin, Chicago*. The MIT Press.

[4] Ogawa, H., 1972. *Forms of Paper*. Van nostrand Reinhold (Trade).

[5] Londenberg, K., 1972. *Papier und Form: Design in der Papierverarbeitung*. Scherpe.

[6] Resch, R. D., 1974. "Portfolio of shaded computer images." *Proceedings of the IEEE,* **62**(4) pp. 496–502.

[7] Resch, R. D., 1974. "The space curve as a folded edge." In *Computer Aided Geometric Design: Proceedings of a Conference held at the University of Utah, Salt Lake City, Utah, March 18-21, 1974* Academic Pr p. 255.

[8] Huffman, D. A., 1976. "Curvature and creases: A primer on paper." *IEEE Trans. Computers,* **25**(10) pp. 1010–1019.

[9] Demaine, E. D., Demaine, M. L., Koschitz, D., and Tachi, T., 2011. "Curved crease folding: a review on art, design and mathematics." In *IABSE-IASS Symposium*.

[10] Struik, D. J., 1961. *Lectures on Classical Differential Geometry*. 2nd ed. Reading, Mass., Addison-Wesley Pub. Co.

[11] Pottmann, H., and Wallner, J., 2009. *Computational Line Geometry*. Springer Science & Business.

[12] Bo, P., and Wang, W., 2007. "Geodesic-controlled developable surfaces for modeling paper bending." *Computer Graphics Forum,* **26**(3) pp. 365–374.

[13] Rose, K., Sheffer, A., Wither, J., Cani, M.-P., and Thibert, B., 2007. "Developable surfaces from arbitrary sketched boundaries." In *Proceedings of the Fifth Eurographics Symposium on Geometry Processing* pp. 163–172.

[14] Solomon, J., Vouga, E., Wardetzky, M., and Grinspun, E., 2012. "Flexible developable surfaces." In *Computer Graphics Forum* Vol. 31(5) Wiley Online Library pp. 1567–1576.

[15] Fuchs, D., and Tabachnikov, S., 1999. "More on paperfolding." *American Mathematical Monthly* pp. 27–35.

[16] Duncan, J. P., and Duncan, J., 1982. "Folded developables." *Proceedings of the Royal Society of London. A. Mathematical and Physical Sciences,* **383**(1784) pp. 191–205.

[17] Mitani, J., and Igarashi, T., 2011. "Interactive design of planar curved folding by reflection." *Pacific Graphics (short paper)*.

[18] Mitani, J., 2011. Ori-ref: A design tool for curved origami based on reflection. September.

[19] Geretschlager, R., 2009. "Folding curves." *Origami*^{4} p. 151.

[20] Apostol, T. M., and Mnatsakanian, M. A., 2007. "Unwrapping curves from cylinders and cones." *American Mathematical Monthly,* **114**(5) pp. 388–416.

[21] Gattas, J. M., and You, Z., 2014. "Miura-base rigid origami: Parametrizations of curved-crease geometries." *Journal of Mechanical Design,* **136**(12) p. 121404.

[22] Kergosien, Y. L., Gotoda, H., and Kunii, T. L., 1994. "Bending and creasing virtual paper." *Computer Graphics and Applications, IEEE,* **14**(1) pp. 40–48.

[23] Kilian, M., Flöry, S., Chen, Z., Mitra, N. J., Sheffer, A., and Pottmann, H., 2008. "Curved folding." *ACM Transactions on Graphics,* **27**(3), Aug. pp. 75:1–75:9.

[24] Tachi, T., 2013. "Designing freeform origami tessellations by generalizing Resch's patterns." *Journal of Mechanical Design,* **135**(11) p. 111006.

[25] Jacobsen, J. O., Howell, L. L., and Magleby, S. P., 2007. "Components for the design of lamina emergent mechanisms." In *ASME 2007 International Mechanical Engineering Congress and Exposition* pp. 165–174.

[26] Jacobsen, J. O., Winder, B. G., Howell, L. L., and Magleby, S. P., 2010. "Lamina emergent mechanisms and their basic elements." *Journal of Mechanisms and Robotics,* **2**(1) p. 011003.

[27] Delimont, I. L., Magleby, S. P., and Howell, L. L., 2015. "Evaluating compliant hinge geometries for origami-inspired mechanisms." *ASME Journal of Mechanisms and Robotics,* **7**(1) p. 011009 (8 pages).

[28] Delimont, Isaac, L., 2014. "Compliant joints suitable for use as surrogate folds." Master's thesis Brigham Young University.

[29] Nelson, T. G., Lang, R. J., Pehrson, N. A., Magleby, S. P., and Howell, L. L., 2016. "Facilitating deployable mechanisms and structures via developable lamina emergent arrays." *Journal of Mechanisms and Robotics,* **8**(3), March pp. 031006–031006–10.

[30] Cajori, F., 1929. "Generalizations in geometry as seen in the history of developable surfaces." *American Mathematical Monthly* pp. 431–437.

[31] Lawrence, S., 2011. "Developable surfaces: Their history and application." *Nexus Network Journal,* **13**(3) pp. 701–14.

[32] Ushakov, V., 1999. "Developable surfaces in Euclidean space." *Journal of the Australian Mathematical Society (Series A),* **66**(03) pp. 388–402.

[33] Lang, R. J., 2013. "One ellipse to rule them all." *The Fold (Origami USA)*, November-December.

[34] Demaine, E., Demaine, M., and Koschitz, D., 2011. "Reconstructing David Huffman's legacy in curved-crease folding." *Origami,* **5** pp. 39–52.

[35] Demaine, E. D., Demaine, M. L., Huffman, D. A., Koschitz, D., and Tachi, T., 2014. "Designing curved-crease tessellations of lenses: qualitative properties of rulings." In *Proceedings of Origami*[6].

[36] Howell, L. L., 2001. *Compliant mechanisms*. John Wiley & Sons.

[37] Jacobsen, J. O., Chen, G., Howell, L. L., and Magleby, S. P., 2009. "Lamina emergent torsional (LET) joint." *Mechanism and Machine Theory,* **44**(11) pp. 2098–2109.

[38] You, Z., 2014. "Folding structures out of flat materials." *Science,* **345**(6197) pp. 623–624.

[39] Dureisseix, D., 2012. "An overview of mechanisms and patterns with origami." *International Journal of Space Structures,* **27**(1) pp. 1–14.

[40] Jamal, M., Bassik, N., Cho, J.-H., Randall, C. L., and Gracias, D. H., 2010. "Directed growth of fibroblasts into three dimensional micropatterned geometries via self-assembling scaffolds." *Biomaterials,* **31**(7) pp. 1683–90.

[41] Silverberg, J. L., Evans, A. A., McLeod, L., Hayward, R. C., Hull, T., Santangelo, C. D., and Cohen, I., 2014. "Using origami design principles to fold reprogrammable mechanical metamaterials." *Science,* **345**(6197) pp. 647–650.

[42] Lee, D.-Y., Kim, J.-S., Kim, S.-R., Koh, J.-S., and Cho, K.-J., 2013. "The deformable wheel robot using magic-ball origami structure." In *ASME IDETC/CIE 2013*.

[43] Ma, J., and You, Z., 2014. "Energy absorption of thin-walled square tubes with a prefolded origami pattern - part i: Geometry and numerical simulation." *Journal of Applied Mechanics,* **81**(1) p. 011003.

[44] Liu, Y., Boyles, J. K., Genzer, J., and Dickey, M. D., 2012. "Self-folding of polymer sheets using local light absorption." *Soft Matter,* **8**(6) pp. 1764–1769.

[45] Felton, S., Tolley, M., Demaine, E., Rus, D., and Wood, R., 2014. "A method for building self-folding machines." *Science,* **345**(6197) pp. 644–646.

[46] Saito, K., Pellegrino, S., and Nojima, T., 2014. "Manufacture of arbitrary cross-section composite honeycomb cores based on origami techniques." *Journal of Mechanical Design,* **136**(5) p. 051011.

[47] Miyashita, S., DiDio, I., Ananthabhotla, I., An, B., Sung, C., Arabagi, S., and Rus, D., 2015. "Folding angle regulation by curved crease design for self-assembling origami propellers." *Journal of Mechanisms and Robotics,* **7**(2) p. 021013.

[48] Chung, W., Kim, S.-H., and Shin, K.-H., 2008. "A method for planar development of 3D surfaces in shoe pattern design." *Journal of Mechanical Science and Technology,* **22**(8) pp. 1510–1519.

[49] Pottmann, H., Schiftner, A., Bo, P., Schmiedhofer, H., Wang, W., Baldassini, N., and Wallner, J., 2008. "Freeform surfaces from single curved panels." *ACM Transactions on Graphics,* **27**(3) p. 76.

[50] Eigensatz, M., Kilian, M., Schiftner, A., Mitra, N. J., Pottmann, H., and Pauly, M., 2010. "Paneling architectural freeform surfaces." *ACM Transactions on Graphics,* **29**(4) p. 45.

[51] Stevens, K. A., 1981. "The visual interpretation of surface contours." *Artificial Intelligence,* **17**(1) pp. 47–73.

[52] Young, W. C., Budynas, R. G., and Sadegh, A. M., 2012. *Roark's Formulas for Stress and Strain*. 8th ed. McGraw-Hill.

[53] Homer, E. R., Harris, M. B., Zirbel, S. A., Kolodziejska, J. A., Kozachkov, H., Trease, B. P., Borgonia, J.-P. C., Agnes, G. S., Howell, L. L., and Hofmann, D. C., 2014. "New methods for developing and manufacturing compliant mechanisms utilizing bulk metallic glass." *Advanced Engineering Materials,* **16**(7), July pp. 850–856.

[54] Ma, R. R., Belter, J. T., and Dollar, A. M., 2015. "Hybrid deposition manufacturing: Design strategies for multimaterial mechanisms via three-dimensional printing and material deposition." *Journal of Mechanisms and Robotics,* **7**(2) p. 021002.

[55] Kim, C., Espalin, D., Cuaron, A., Perez, M. A., Lee, M., MacDonald, E., and Wicker, R. B., 2015. "Cooperative tool path planning for wire embedding on additively manufactured curved surfaces using robot kinematics." *Journal of Mechanisms and Robotics,* **7**(2) p. 021003.

[56] Edmondson, B. J., Bowen, L. A., Grames, C. L., Magleby, S. P., Howell, L. L., and Bateman, T. C., 2013. "Oriceps: Origami-inspired forceps." In *ASME 2013 Conference on Smart Materials, Adaptive Structures and Intelligent Systems* p. V001T01A027.

[57] Nelson, T. G., Lang, R. J., Magleby, S. P., and Howell, L. L., 2016. "Curved-folding-inspired deployable compliant rolling-contact element (D-CORE)." *Mechanism and Machine Theory,* **96** pp. 225–238.

[58] Nelson, T. G., Bruton, J. T., Rieske, N. E., Walton, M. P., Fullwood, D. T., and Howell, L. L., 2016. "Material selection shape factors for compliant arrays in bending." *Materials & Design,* **110** pp. 865 – 877.

[59] Lamoureux, A., Lee, K., Shlian, M., Forrest, S. R., and Shtein, M., 2015. "Dynamic kirigami structures for integrated solar tracking." *Nature Communications,* **6**(8092).

[60] Song, Z., Wang, X., Lv, C., An, Y., Liang, M., Ma, T., He, D., Zheng, Y.-J., Huang, S.-Q., Yu, H., and Jiang, H., 2015. "Kirigami-based stretchable lithium-ion batteries." *Scientific Reports,* **5**(10988).

[61] Zhang, Y., Yan, Z., Nan, K., Xiao, D., Liu, Y., Luan, H., Fu, H., Wang, X., Yang, Q., Wang, J., Ren, W., Si, H., Liu, F., Yang, L., Li, H., Wang, J., Guo, X., Luo, H., Wang, L., Huang, Y., and Rogers, J. A., 2015. "A mechanically driven form of kirigami as a route

to 3D mesostructures in micro/nanomembranes." *Proceedings of the National Academy of Sciences,* **112**(38) pp. 11757–11764.

[62] Yang, S., Choi, I.-S., and Kamien, R. D., 2016. "Design of super-conformable, foldable materials via fractal cuts and lattice kirigami." *MRS Bulletin,* **41**(02) pp. 130–138.

[63] Lee, J., Kim, K., Ju, J., and Kim, D.-M., 2014. "Compliant cellular materials with elliptical holes for extremely high positive and negative poisson's ratios." *Journal of Engineering Materials and Technology,* **137**(1) p. 011001.

[64] Eidini, M., 2016. "Zigzag-base folded sheet cellular mechanical metamaterials." *Extreme Mechanics Letters,* **6** pp. 96 – 102.

[65] Zheng, X., Lee, H., Weisgraber, T. H., Shusteff, M., DeOtte, J., Duoss, E. B., Kuntz, J. D., Biener, M. M., Ge, Q., Jackson, J. A., Kucheyev, S. O., Fang, N. X., and Spadaccini, C. M., 2014. "Ultralight, ultrastiff mechanical metamaterials." *Science,* **344**(6190) pp. 1373–1377.

[66] Dey, V., Zani, G., Colombo, M., Prisco, M. D., and Mobasher, B., 2015. "Flexural impact response of textile-reinforced aerated concrete sandwich panels." *Materials & Design,* **86** pp. 187 – 197.

[67] Chen, B., Yin, D., Ye, W., Lin, S., Fan, J., and Gou, J., 2015. "Fiber-continuous panel-pillar structure in insect cuticle and biomimetic research." *Materials & Design,* **86** pp. 686 – 691.

[68] Gattas, J., and You, Z., 2016. "Design and digital fabrication of folded sandwich structures." *Automation in Construction,* **63** pp. 79–87.

[69] Mahshid, R., Hansen, H. N., and Hjbjerre, K. L., 2016. "Strength analysis and modeling of cellular lattice structures manufactured using selective laser melting for tooling applications." *Materials & Design,* **104** pp. 276 – 283.

[70] Wang, X.-T., Li, X.-W., and Ma, L., 2016. "Interlocking assembled 3D auxetic cellular structures." *Materials & Design,* **99** pp. 467 – 476.

[71] George, T., Deshpande, V. S., and Wadley, H. N., 2013. "Mechanical response of carbon fiber composite sandwich panels with pyramidal truss cores." *Composites Part A: Applied Science and Manufacturing,* **47** pp. 31 – 40.

[72] Ullah, I., Brandt, M., and Feih, S., 2016. "Failure and energy absorption characteristics of advanced 3D truss core structures." *Materials & Design,* **92** pp. 937 – 948.

[73] Klett, Y., and Drechsler, K., 2011. "Designing technical tessellations." *Origami*^{5} pp. 305–322.

[74] Ohshima, T., Tachi, T., Hiroya, T., and Yamaguchi, Y., 2015. "Analysis and design of elastic materials formed using 2D repetitive slit pattern." In *International Association for Shell and Spatial Structures (IASS) Symposium 2015*.

[75] Isobe, M., and Okumura, K., 2016. "Initial rigid response and softening transition of highly stretchable kirigami sheet materials." *Scientific Reports,* **6**(24758).

[76] Ashby, M., 1991. "Overview no. 92: Materials and shape." *Acta Metallurgica et Materialia,* **39**(6) pp. 1025 – 1039.

[77] Pasini, D., 2007. "Shape transformers for material and shape selection of lightweight beams." *Materials & Design,* **28**(7) pp. 2071 – 2079.

[78] Singh, J., Mirjalili, V., and Pasini, D., 2011. "Integrated shape and material selection for single and multi-performance criteria." *Materials & Design,* **32**(5) pp. 2909–2922.

[79] Ashby, M. F., 2011. *Materials Selection in Mechanical Design*. 4th ed. Elsevier.

[80] Amany, A., and Pasini, D., 2009. "Material and shape selection for stiff beams under non-uniform flexure." *Materials & Design,* **30**(4) pp. 1110 – 1117.

[81] Zirbel, S. A., Lang, R. J., Thomson, M. W., Sigel, D. A., Walkemeyer, P. E., Trease, B. P., Magleby, S. P., and Howell, L. L., 2013. "Accommodating thickness in origami-based deployable arrays." *Journal of Mechanical Design,* **135**(11) p. 111005.

[82] Quaglia, C., Dascanio, A., and Thrall, A., 2014. "Bascule shelters: A novel erection strategy for origami-inspired deployable structures." *Engineering Structures,* **75** pp. 276–287.

[83] Aten, Q. T., Jensen, B. D., Burnett, S. H., and Howell, L. L., 2014. "A self-reconfiguring metamorphic nanoinjector for injection into mouse zygotes." *Review of Scientific Instruments,* **85**(5) p. 055005.

[84] Gantes, C. J., Connor, J. J., Logcher, R. D., and Rosenfeld, Y., 1989. "Structural analysis and design of deployable structures." *Computers & Structures,* **32**(3) pp. 661–669.

[85] Tachi, T., 2011. "Rigid-foldable thick origami." In *Origami*^{5}. CRC Press pp. 253–264.

[86] Weaver, P., and Ashby, M., 1997. "Material limits for shape efficiency." *Progress in Materials Science,* **41**(1) pp. 61 – 128.

[87] Birmingham, R., and Jobling, B., 1996. "Material selection: Comparative procedures and the significance of form." In *International Conference on Lightweight Materials in Naval Architecture* The Royal Institution of Naval Architects.

[88] Tolman, S. S., Delimont, I. L., Howell, L. L., and Fullwood, D. T., 2014. "Material selection for elastic energy absorption in origami-inspired compliant corrugations." *Smart Materials and Structures,* **23**(9) p. 094010.

[89] Delimont, I. L., Magleby, S. P., and Howell, L. L., 2015. "A family of dual-segment compliant joints suitable for use as surrogate folds." *Journal of Mechanical Design,* **137**(9) p. 092302.

[90] Timoshenko, S., and Goodier, J., 1969. *Theory of elasticity*. McGraw-Hill classic textbook reissue series. McGraw-Hill.

[91] Callister, W. D., and Rethwisch, D. G., 2007. *Materials Science and Engineering: an Introduction*. Vol. 7 Wiley New York.

[92] Norton, R. L., 2006. *Machine Design: An Integrated Approach*. 3rd ed. Pearson, Prentice Hall pg. 176.

[93] Iman, R. L., 2008. *Latin Hypercube Sampling*. John Wiley & Sons, Ltd.

[94] Halverson, P. A., Howell, L. L., and Magleby, S. P., 2010. "Tension-based multi-stable compliant rolling-contact elements." *Mechanism and Machine Theory,* **45**(2) pp. 147–156.

[95] Dai, J. S., and Jones, J. R., 1999. "Mobility in metamorphic mechanisms of foldable/erectable kinds." *Journal of Mechanical Design,* **121**(3) pp. 375–382.

[96] , 1889. "Jacob's ladder." *Scientific American* October 12, 1889 Issue.

[97] Ding, X., Yang, Y., and Dai, J. S., 2011. "Topology and kinematic analysis of color-changing ball." *Mechanism and Machine Theory,* **46**(1) pp. 67–81.

[98] Wilkes, D. F., 1967. Rolamite: A new mechanical design concept, unclassified No. SC-RR-67-656 Sandia Corporation.

[99] Cadman, R. V., 1970. Rolamite: geometry and force analysis, Tech. rep. Sandia Corporation.

[100] Thornton, A., and Predecki, P., 1973. "Design considerations in a Rolamite knee joint prosthesis." *Journal of Biomedical Materials Research,* **7**(3) pp. 419–433.

[101] English, C., and Russell, D., 1999. "Implementation of variable joint stiffness through antagonistic actuation using Rolamite springs." *Mechanism and Machine Theory,* **34**(1) pp. 27–40.

[102] Halverson, P. A., Bowden, A. E., and Howell, L. L., 2012. "A compliant-mechanism approach to achieving specific quality of motion in a lumbar total disc replacement." *The International Journal of Spine Surgery,* **6**(1) pp. 78–86.

[103] Nai, T. Y., Herder, J. L., and Tuijthof, G. J., 2011. "Steerable mechanical joint for high load transmission in minimally invasive instruments." *Journal of Medical Devices,* **5**(3) p. 034503.

[104] Moon, Y.-M., 2007. "Bio-mimetic design of finger mechanism with contact aided compliant mechanism." *Mechanism and Machine Theory,* **42**(5) pp. 600–611.

[105] Wei, G., and Dai, J. S., 2014. "Origami-inspired integrated planar-spherical overconstrained mechanisms." *Journal of Mechanical Design,* **136**(5) p. 051003.

[106] Qin, Y., Dai, J. S., and Gogu, G., 2014. "Multi-furcation in a derivative queer-square mechanism." *Mechanism and Machine Theory,* **81** pp. 36–53.

[107] Qiu, C., Aminzadeh, V., and Dai, J. S., 2013. "Kinematic analysis and stiffness validation of origami cartons." *Journal of Mechanical Design,* **135**(11) p. 111004.

[108] Zhang, K., and Dai, J. S., 2014. "A kirigami-inspired 8R linkage and its evolved overconstrained 6R linkages with the rotational symmetry of order two." *Journal of Mechanisms and Robotics,* **6**(2) p. 021007.

[109] Francis, K., Blanch, J., Magleby, S., and Howell, L., 2013. "Origami-like creases in sheet materials for compliant mechanism design." *Mechanical Sciences,* **4**(2) pp. 371–380.

[110] Tolley, M. T., Felton, S. M., Miyashita, S., Aukes, D., Rus, D., and Wood, R. J., 2014. "Self-folding origami: shape memory composites activated by uniform heating." *Smart Materials and Structures,* **23**(9) p. 094006.

[111] Chen, Y., Peng, R., and You, Z., 2015. "Origami of thick panels." *Science,* **349**(6246) pp. 396–400.

[112] Filipov, E. T., Paulino, G. H., and Tachi, T., 2016. "Origami tubes with reconfigurable polygonal cross-sections." *Proc. R. Soc. A,* **472**(2185).

[113] Mu, J., Hou, C., Wang, H., Li, Y., Zhang, Q., and Zhu, M., 2015. "Origami-inspired active graphene-based paper for programmable instant self-folding walking devices." *Science Advances,* **1**(10).

[114] Hernandez, E. A. P., Hartl, D. J., Akleman, E., and Lagoudas, D. C., 2016. "Modeling and analysis of origami structures with smooth folds." *Computer-Aided Design,* **78** pp. 93 – 106.

[115] Vergauwen, A., Laet, L. D., and Temmerman, N. D., 2017. "Computational modelling methods for pliable structures based on curved-line folding." *Computer-Aided Design,* **83** pp. 51 – 63.

[116] Saito, K., Tsukahara, A., and Okabe, Y., 2016. "Designing of self-deploying origami structures using geometrically misaligned crease patterns." *Proc. R. Soc. A,* **472**(2185).

[117] Lee, N., and Close, S., 2013. "Curved pleat folding for smooth wrapping." *Proc. R. Soc. A,* **469**(2155).

[118] Lang, R. J., Nelson, T. G., Magleby, S. P., and Howell, L. L., 2017. "Kinematics and discretization of curved-fold mechanisms." In *ASME 2017 IDETC/CIE* pp. DETC2017–67439.

[119] Li, C.-Y., Wang, R.-H., and Zhu, C.-G., 2013. "An approach for designing a developable surface through a given line of curvature." *Computer-Aided Design,* **45**(3) pp. 621 – 627.

[120] Shen, L., and Pérez-Díaz, S., 2015. "Determination and (re)parametrization of rational developable surfaces." *Journal of Systems Science and Complexity,* **28**(6) pp. 1426–1439.

[121] Hwang, H.-D., and Yoon, S.-H., 2015. "Constructing developable surfaces by wrapping cones and cylinders." *Computer-Aided Design,* **58** pp. 230 – 235.

[122] Zhao, H., and Wang, G., 2008. "A new method for designing a developable surface utilizing the surface pencil through a given curve." *Progress in Natural Science,* **18**(1) pp. 105 – 110.

[123] Gattas, J., and You, Z., 2015. "The behaviour of curved-crease foldcores under low-velocity impact loads." *International Journal of Solids and Structures,* **53** pp. 80 – 91.

[124] Yates, R., 1947. "A handbook on curves and their properties (JW Edwards, Ann Arbor, MI).".

[125] Euler, L., 1741. "De constructione aequationum ope motus tractorii aliisque ad methodum tangentium inversam pertinentibus (E51)." *Comm. Acad. Sci. Petrop,* **8** pp. 66–85 presented 1735.

[126] Whewell, W., 1849. "Of the intrinsic equation of a curve, and its application." *Transactions of the Cambridge Philosophical Society,* **8**.

[127] Cesàro, E., 1896. *Lezioni di geometria intrinseca*. Tipografia della R. Accademia delle scienze.

[128] Ruffa, A. A., 2007. "A novel solution to the Frenet-Serret equations.".

[129] Frenet, F., 1852. "Sur les courbes à double courbure." *Journal des Mathématiques Pures et Appliquées,* **17** pp. 437–447.

[130] Serret, J.-A., 1851. "Sur quelques formules relatives à la théorie des courbes à double courbure.." *Journal de Mathématiques pures et appliquées* pp. 193–207.

[131] O'Neill, B., 2006. *Elementary Differential Geometry*. Academic press.

[132] Do Carmo, M. P., 1976. *Differential geometry of curves and surfaces*. Prentice-hall Englewood Cliffs.

[133] Abbena, E., Salamon, S., and Gray, A., 2006. *Modern differential geometry of curves and surfaces with Mathematica*. CRC press.

[134] Weisstein, E. W., 2002. *CRC concise encyclopedia of mathematics*. CRC press.

[135] Weatherburn, C. E., 1926. "Some new theorems in geometry of a surface." *The Mathematical Gazette,* **13**(180) pp. 1–6.

[136] Pressley, A. N., 2010. *Elementary Differential Geometry*. Springer Science & Business Media.

[137] Tang, C., Bo, P., Wallner, J., and Pottmann, H., 2016. "Interactive design of developable surfaces." *ACM Transactions on Graphics,* **35**(2), Jan. pp. 12:1–12:12.

[138] Leopoldseder, S., 2001. "Algorithms on cone spline surfaces and spatial osculating arc splines." *Computer Aided Geometric Design,* **18**(6), Jul pp. 505–530.

[139] Leopoldseder, S., 2002. "Cone spline surfaces and spatial arc splines – a sphere geometric approach." *Advances in Computational Mathematics,* **17**(1) pp. 49–66.

[140] Şentürk, G. Y., and Yüce, S., 2015. "Characteristic properties of the ruled surface with Darboux frame in E^3." *Kuwait Journal of Science,* **42**(2).

[141] Kreyszig, E., 1968. *Introduction to Differential Geometry and Riemannian Geometry*. Vol. 16 University of Toronto Press.

[142] Leopoldseder, S., 1998. "Cone spline surfaces and spatial arc splines." PhD thesis Technische Universitt Wien.

[143] Wang, W., Jüttler, B., Zheng, D., and Liu, Y., 2008. "Computation of rotation minimizing frames." *ACM Transactions on Graphics,* **27**(1), Mar. pp. 2:1–2:18.

[144] Janbaz, S., Hedayati, R., and Zadpoor, A. A., 2016. "Programming the shape-shifting of flat soft matter: from self-rolling/self-twisting materials to self-folding origami." *Materials Horizons,* **3** pp. 536–547.

[145] Jobin, J.-P., Buddenberg, H. S., and Herder, J. L., 2004. "An underactuated prosthesis finger mechanism with rolling joints." In *ASME 2004 IDETC/CIE* pp. 549–559.

[146] Jeanneau, A., Herder, J. L., Laliberte, T., and Gosselin, C., 2004. "A compliant rolling contact joint and its application in a 3-dof planar parallel mechanism with kinematic analysis." In *ASME 2004 IDETC/CIE* pp. 689–698.

[147] Lang, R. J., Nelson, T. G., Magleby, S. P., and Howell, L. L., 2017. "Thick rigidly foldable origami mechanisms based on synchronized offset rolling contact elements." *Journal of Mechanisms and Robotics,* **9**(2) p. 021013.

[148] Khonsari, M. M., and Booser, E. R., 2008. *Applied Tribology: Bearing Design and Lubrication*. Vol. 12 John Wiley & Sons.

[149] Li, S., 2018. "A mathematical model and numeric method for contact analysis of rolling bearings." *Mechanism and Machine Theory,* **119** pp. 61 – 73.

[150] Norton, R., 2009. *Cam Design and Manufacturing Handbook*. Industrial Press.

[151] Radzevich, S. P., and Dudley, D. W., 1994. *Handbook of practical gear design*. CRC press.

[152] Cannon, J. R., Lusk, C. P., and Howell, L. L., 2005. "Compliant rolling-contact element mechanisms." In *ASME 2005 IDETC/CIE* pp. 3–13.

[153] Montierth, J. R., Todd, R. H., and Howell, L. L., 2011. "Analysis of elliptical rolling contact joints in compression." *Journal of Mechanical Design,* **133**(3) p. 031001.

[154] Kuntz, J. P., 1995. *Rolling link mechanisms*. TU Delft, Delft University of Technology.

[155] Dijksman, E. A., 1976. *Motion geometry of mechanisms*. CUP Archive.

[156] Hillberry, B., and Hall, A., 1976. Rolling contact prosthetic knee joint, Mar. 23 US Patent 3,945,053.

[157] Slocum, A., Goodman, D., Eilenberg, M., Titarelli, J., and Meyer, L., 2014. Rolling-contact knee prosthesis, Feb. 20 US Patent App. 13/968,224.

[158] Etoundi, A. C., Burgess, S. C., and Vaidyanathan, R., 2013. "A bio-inspired condylar hinge for robotic limbs." *Journal of Mechanisms and Robotics,* **5**(3) p. 031011.

[159] Slocum Jr, A. H., 2013. "Rolling contact orthopaedic joint design." PhD thesis Massachusetts Institute of Technology.

[160] Gini, G., Scarfogliero, U., and Folgheraiter, M., 2007. "Human-oriented biped robot design: Insights into the development of a truly anthropomorphic leg." In *Proceedings 2007 IEEE International Conference on Robotics and Automation* pp. 2910–2915.

[161] Jelínek, F., Pessers, R., and Breedveld, P., 2014. "Dragonflex smart steerable laparoscopic instrument." *Journal of Medical Devices,* **8**(1) p. 015001.

[162] Herder, J. L., Horward, M. J., and Sjoerdsma, W., 1997. "A laparoscopic grasper with force perception." *Minimally Invasive Therapy & Allied Technologies,* **6**(4) pp. 279–286.

[163] Jianguo, C., 2016. "Kinematic analysis of foldable plate structures with rolling joints." *Journal of Mechanisms and Robotics,* **8**(3) p. 034502.

[164] Watt, A. M., and Pellegrino, S., 2002. "Tape-spring rolling hinges." In *Proceedings of the 36th Aerospace Mechanisms Symposium* pp. 15–17.

[165] Sancisi, N., and Parenti-Castelli, V., 2011. "Strip-driven devices for the spatial motion guidance of human joints." In *Engineering in Medicine and Biology Society, EMBC, 2011 Annual International Conference of the IEEE* pp. 632–635.

[166] Nardini, F., Sancisi, N., and Castelli, V. P., 2015. "Analytical stiffness analysis of a family of spatial strip-driven devices." In *Proceedings of the 14th IFToMM World Congress* pp. 319–326.

[167] Kimura, N., and Iwatsuki, N., 2017. "Spatial rolling contact pair generating the specified relative motion between links." In *Mechanism and Machine Science: Proceedings of ASIAN MMS 2016 & CCMMS 2016* Springer pp. 307–316.

[168] Cui, L., and Dai, J. S., 2015. "From slidingrolling loci to instantaneous kinematics: An adjoint approach." *Mechanism and Machine Theory,* **85** pp. 161 – 171.

[169] Montana, D. J., 1988. "The kinematics of contact and grasp." *The International Journal of Robotics Research,* **7**(3) pp. 17–32.

[170] Li, Z., and Canny, J., 1990. "Motion of two rigid bodies with rolling constraint." *IEEE Transactions on Robotics and Automation,* **6**(1), Feb pp. 62–72.

[171] Cai, C., and Roth, B., 1987. "On the spatial motion of a rigid body with point contact." In *Robotics and Automation. Proceedings. 1987 IEEE International Conference on* Vol. 4 pp. 686–695.

[172] Cui, L., and Dai, J. S., 2009. "A coordinate-free approach to instantaneous kinematics of two rigid objects with rolling contact and its implications for trajectory planning." In *Robotics and Automation, 2009. ICRA'09. IEEE International Conference on* pp. 612–617.

[173] Herder, J. L., 2001. *Energy-free Systems. Theory, conception and design of statically balanced spring mechanisms*.

[174] Stapel, A., and Herder, J. L., 2004. "Feasibility study of a fully compliant statically balanced laparoscopic grasper." In *ASME 2004 IDETC/CIE* pp. 635–643.

[175] Kuleshov, A., Hubbard, M., Peterson, D., and Gede, G., 2011. "Motion of the oloid on the horizontal plane." *Nelin. Dinam.,* **7**(4) pp. 825–835.

[176] Hoberman, C., 1988. Reversibly expandable three-dimensional structure, United States Patent No. 4,780,344.

[177] Hoberman, C., 1991. Reversibly expandable structure, United States Patent No. 4,981,732.

[178] Edmonson, B. J., Lang, R. J., Magleby, S. P., and Howell, L. L., 2014. "An offset panel technique for thick rigidly foldable origami." In *Proceedings of the ASME 2014 IDETC/CIE* no. DETC2014-35606.

[179] Ku, J. S., and Demaine, E. D., 2015. "Folding flat crease patterns with thick materials." In *ASME 2015 IDETC/CIE* pp. V05BT08A056–V05BT08A056.

[180] Jianguo, C., Yuhang, Z., Jian, F., and Yixiang, X., 2017. "A bistable rolling joint for multi-stable structures." *Mechanics Research Communications,* **79** pp. 1 – 6.

[181] Tolman, K. A., Lang, R. J., Magleby, S. P., and Howell, L. L., 2017. "Split-vertex technique for thickness-accommodation in origami-based mechanisms." In *ASME 2017 IDETC/CIE* pp. V05BT08A054–V05BT08A054.

APPENDIX A. DERIVATIONS AND EXPLANATIONS FOR CHAPTER 5

A.1 Derivations and Explanations

This section contains derivations and explanations referred to in Chapter 5.

A.1.1 Derivation for Eq. 5.11

This derivation shows how the ruling curvature of any cross curve for a generalized cylinder relates to the radius of an osculating cylinder as expressed in Eq. 5.11.

Let a generalized cylinder be parametrized in the form of Eq. 5.8 such that $\mathbf{r}(t, v_c)$ with v_c being an arbitrary constant is the cross curve in a 3D state. The ruling curvature of the cross curve is expressed by Eq. 5.10 and the unit normal vector $\mathbf{U}(t)$ found from Eq. 5.7.

Similar to how a circle has constant curvature and can be used as a osculating shape for a planar curve, a right circular cylinder has a constant non-zero principal curvature and can be correlated to the ruling curvature for any cross curve of a generalized cylinder to create an osculating cylinder. Let us look at how the radius of a right circular (osculating) cylinder is related to the ruling curvature.

As Euclidean transformations can be used to align a right circular cylinder to a given ruling line without affecting the ruling curvature or maximum principal curvature along a ruling line, let us consider a right circular cylinder located at a convenient location expressed in the canonical parameterization specified by Eq. 5.8 as

$$\mathbf{r}(t, v) = \begin{bmatrix} R\cos\frac{t}{R} \\ R\sin\frac{t}{R} \\ v \end{bmatrix} \tag{A.1}$$

where R is the radius of the right circular cylinder.

Using Eq. 5.7 to compute an expression for the unit normal gives

$$\mathbf{U}(t) = \begin{bmatrix} \cos(\frac{t}{R}) \\ \sin(\frac{t}{R}) \\ 0 \end{bmatrix} \tag{A.2}$$

and using Eq. 5.10 we find the ruling curvature is

$$\kappa_r(t) = -\frac{1}{R} \tag{A.3}$$

However, we must be careful here as Eq. A.1 can be modified slightly by adding a negative to the y term. This results in a normal that points in the same direction as the curvature of the cylinder making $\kappa_r(t)$ positive. This ambiguity results from the ability to define an osculating shape using two different orientations of the surface normal. Because of this we denote $R(t)$ as $\pm 1/\kappa_r(t)$ giving us Eq. 5.11.

A.1.2 Derivation for Eq. 5.12

This derivation relates the ruling curvature of a generalized cone to the opening angle of an osculating right cone as expressed by Eq. 5.12.

Let a generalized cone be parametrized in the form of Eq. 5.8 such that $\mathbf{r}(s, v_c)$ is the cross curve. The ruling curvature is expressed by Eq. 5.10.

An osculating cone with matching variation of principal curvature along a ruling line can be designated for each ruling line of the generalized cone. The osculating cone's apex and apex of the generalized cone will also be the same. As the principal curvature variation depends on just the opening angle of the cone when both apexes are the same, we will relate the opening angle of a right circular cone to the ruling curvature. As with the first derivation Euclidean transformations can be used to align the right circular cone to a given ruling line without affecting the ruling curvature or maximum principal curvature, so we will assume a convenient location to express a right circular cone in the form of Eq. 5.8 with the cross curve at $\mathbf{r}(t, v_c)$ as

$$\mathbf{r}(t,v) = \begin{bmatrix} v\sin(\phi)\cos\frac{t}{v_c\sin(\phi)} \\ v\sin(\phi)\sin\frac{t}{v_c\sin(\phi)} \\ v\cos(\phi) \end{bmatrix} \tag{A.4}$$

where ϕ is the angle between the cone axis and the cone's ruling lines.

We find the unit normal using Eq. 5.7 resulting in

$$\mathbf{U}(t) = \begin{bmatrix} \cos(\phi)\cos\frac{t}{v_c\sin(\phi)} \\ \cos(\phi)\sin\frac{t}{v_c\sin(\phi)} \\ -\sin(\phi) \end{bmatrix} \tag{A.5}$$

and using Eq. 5.10 we get the ruling curvature in terms of the opening angle of the cone and v_c as

$$\kappa_r(t) = \frac{-\cot(\phi)}{v_c} \tag{A.6}$$

Rewriting this equation yields Eq. 5.12. As with the cylinder, we can change the direction of the normal and still have an osculating cone by starting with Eq. A.4 with an added negative on the y term. However, to preserve continuity with signs in other equations with the way we defined the sign of v_c (being the same as the sign of κ_g) we will select the sign choice from Eq. A.5.

A.1.3 Derivation for Eq. 5.13

This derivation relates the ruling curvature of a tangent developable to the ratio of the radius and pitch of an osculating tangent developable helical surface.

Let a tangent developable surface be parametrized in the form of Eq. 5.8 such that $\mathbf{r}(t, c_v(t))$ is the cross curve. The ruling curvature is expressed by Eq. 5.10.

To find the osculating helical tangent developable for each ruling line we want to know the ruling curvature that corresponds to a helical tangent developable with a constant radius, a, and constant pitch between the windings, $2\pi b$. This results in a helical tangent developable that has matching variation of principal curvature along a ruling line for a specific ruling line of the tangent developable. As with the first two derivations a convenient location to express a helical tangent developable characterized by a and b will be selected as Euclidean transformations do not

affect the curvature of the osculating shape. We will write a helical tangent developable in the form of Eq. 5.8 for a reverse tangent developable with $\mathbf{r}_r(t, c_v(t))$ describing a cross curve (we could straightforwardly repeat this derivation using the forward parametric representation). To accomplish this we first write the parametric equation in the form of Eq. 5.8 for helical tangent developable where $\mathbf{r}(s_e, 0)$ is the edge of a regression (a helix specified by parameters a and b and s_e is the arc length of the edge of regression). This equation is

$$\mathbf{r}_r(s_e, v) = \begin{bmatrix} a\cos\frac{s_e}{\sqrt{a^2+b^2}} - \frac{a}{\sqrt{a^2+b^2}} v \sin\frac{s_e}{\sqrt{a^2+b^2}} \\ a\sin\frac{s_e}{\sqrt{a^2+b^2}} + \frac{a}{\sqrt{a^2+b^2}} v \cos\frac{s_e}{\sqrt{a^2+b^2}} \\ \frac{bs_e}{\sqrt{a^2+b^2}} + \frac{bv}{\sqrt{a^2+b^2}} \end{bmatrix} \tag{A.7}$$

Instead of writing this parametric equation such that the edge of regression is arc-length parametrized we would like a cross curve to be arc-length parametrized to make the calculation of the curve speed $\dot{s}$ trivial. This is done by using Eq. 5.30 to relate the arc length s_e to the geodesic curvature of the cross curve. Further, since the cross curve is an involute of the edge of regression when developed to a plane, and for a helical tangent developable the edge of regression when developed to a plane is a circle, we know that the geodesic curvature of the cross curve is the curvature of the involute of a circle. The curvature of the involute of a circle and thus geodesic curvature of the cross curve for this reverse parametrization is

$$\kappa_g(t) = \frac{1}{(2a't)^{1/2}} \tag{A.8}$$

where t is the arc length of the cross curve and a' is the radius of the planar circle (and developed helix). We relate the planar circle with radius a' to the radius of a formed helix (the edge of regression of a helical tangent developable) by noting that the curvature of a formed helix is equal to the geodesic curvature of a helical tangent developable. This results in the expression

$$a' = \frac{a^2+b^2}{a} \tag{A.9}$$

We use Eqs. 5.30, A.8, and A.9 to write

$$s_e = \left(2t\left(\frac{a^2+b^2}{a}\right)\right)^{1/2} \tag{A.10}$$

and substitute this equation into Eq. A.7 to find the parametric equation written with the cross curve arc-length parametrized as

$$\mathbf{r}_r(t,v) = \begin{bmatrix} a\cos\left(\left(\frac{2t}{a}\right)^{1/2}\right) - \frac{a}{\sqrt{a^2+b^2}} v \sin\left(\left(\frac{2t}{a}\right)^{1/2}\right) \\ a\sin\left(\left(\frac{2t}{a}\right)^{1/2}\right) + \frac{a}{\sqrt{a^2+b^2}} v \cos\left(\left(\frac{2t}{a}\right)^{1/2}\right) \\ b\left(\frac{2t}{a}\right)^{1/2} + \frac{bv}{\sqrt{a^2+b^2}} \end{bmatrix} \tag{A.11}$$

We find the unit normal of this parametric equation using Eq. 5.7 resulting in

$$\mathbf{U}(t) = \frac{1}{\sqrt{a^2+b^2}} \begin{bmatrix} -b\sin\left(\left(\frac{2t}{a}\right)^{1/2}\right) \\ b\cos\left(\left(\frac{2t}{a}\right)^{1/2}\right) \\ -a \end{bmatrix} \tag{A.12}$$

An arc-length parametric equation of the cross curve itself can be found using Eq. A.8 and Eq. A.11 as

$$\mathbf{C}(t) = \mathbf{r}_r\left(t, \frac{-1}{\kappa_g(t)}\right) \tag{A.13}$$

We can take the derivative of this expression to find $\mathbf{T}(t)$ and use Eq. 5.10 to get the ruling curvature, but the equations become complex quickly.

Instead to find the ruling curvature we take magnitude of the derivative of Eq. A.12 with respect to arc length t and note that the sign is positive as the unit normal points in the direction the reverse parametrized surface curves to find the ruling curvature in terms of a, b, and t as

$$\kappa_r(t) = \frac{b}{\left(2at\left(a^2+b^2\right)\right)^{1/2}} \tag{A.14}$$

Using Eqs. A.8, A.9, and A.14 we can find that

$$\frac{\kappa_r(t)}{\kappa_g(t)} = \frac{b(t)}{a(t)} \tag{A.15}$$

We also know that for a helix the parameters a and b are related to the curvature and torsion of the helix by [131]

$$\begin{aligned} \kappa &= \frac{a}{a^2+b^2} \\ \tau &= \frac{b}{a^2+b^2} \end{aligned} \tag{A.16}$$

Rearranging and substituting these expressions into Eq. A.15 give Eq. 5.13.

A.1.4 Derivation for Eq. 5.14

This derivation shows how an osculating cone can be the equivalent of an osculating helical tangent developable for a tangent developable surface and derives the relationship given in Eq. 5.14.

If the variation of the principal curvature along a ruling line is equivalent for a particular osculating cone as it is for an osculating helical tangent developable we can conclude that the two shapes can be interchanged as the osculating shape. Using Eq. 5.16 and Eq. 5.17 we see that the principal curvature variation along a ruling line for both an osculating cone and helical tangent developable is $1/v$ multiplied by a constant written in terms of the geometry of the osculating shapes. By equating these constants we can relate the geometry of the osculating cone to the osculating helical tangent developable as

$$\cot\phi = \frac{-\kappa_r(t)}{\kappa_g(t)} \tag{A.17}$$

which can be rearranged to get Eq. 5.14.

A.1.5 Derivation for Eqs. 5.15, 5.16, 5.17, and 5.18,

This derivation shows how to find the variation of the principal curvature along a ruling line for generalized cones and tangent developables. We leverage osculating shapes to write expressions for the variation of the principal curvature.

We will find the variation of principal curvature of the osculating shape (which will be the same as the variation of the principal curvature of the generalized shape along the ruling line of

interest). For generalized cones let the osculating shape be parametrized as Eq. A.4. We use the first and second fundamental forms with this parametrization to find the principal curvatures (one of which will be zero). This process is described in [141] where the principal curvatures are the roots of a characteristic equation formed from the fundamental forms. The result of this process is that the principal curvatures are indeed zero and Eq. 5.16. It is straightforward substitution from Eq. 5.12 into Eq. 5.16 to get Eq. 5.15.

The same process is used for tangent developables surfaces where the osculating shape is parametrized as Eq. A.7 and we use the fundamental forms and characteristic equation to find Eq. 5.18. It is again a straightforward substitution from Eq. 5.13 into Eq. 5.18 to get Eq. 5.17.